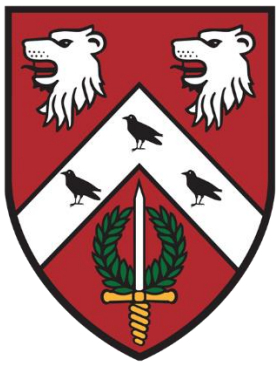
Novel Zirconium Alloys for Fusion Applications

Bradley Young

St Anne's College





Supervised by Professor Chris Grovenor and Professor David Armstrong

Abstract

Magnetic-confinement fusion power plants promise to provide a baseload, clean energy supply if a suitable breeder blanket design can be realised. There are no candidate structural materials for the breeder blanket without significant drawbacks to their selection due to the harsh operating environment in this application. Zirconium alloys have been suggested as potential candidate structural materials for the fusion breeder blanket due to their low thermal neutron absorption cross-section, but insufficient relevant data are available to enable serious consideration of their potential. The advantage of zirconium's low thermal neutron cross-section has the potential to improve the neutron efficiency of the breeder blanket component, and therefore enable a suitable tritium breeding ratio to be achieved, a key success criterion for the component, and the fusion system as a whole.

Three major chapters are presented for the assessment of zirconium alloys for fusion applications. Firstly, in section 4, following identification of the most promising binary zirconium-based alloy systems as part of the literature review, alloys were cast and processed. Zr-Mo alloys were not investigated further after brittle behaviour was observed in processing. However, alloys of the Zr-Al, Zr-Ta and Zr-V systems were successfully processed to produce samples with microstructures representative of in-service engineering alloys. These materials were tested experimentally to assess their microstructure and mechanical strength at temperatures relevant to the fusion breeder blanket environment, indicating performance which matched or exceeded the performance of alternative candidate materials.

Following this, in sections 5 and 6, the stability of the alloy microstructures was assessed following exposure to operationally relevant environmental conditions. In section 5,

alloy samples were exposed to both extended isothermal and transient ageing conditions, designed to be representative of in-service conditions. Whilst some microstructural instability was observed following exposure to the elevated temperature conditions, including precipitate coarsening and recrystallisation for some alloys, a number of alloys showed promising stability. These findings of microstructural stability were supported by evidence of relatively consistent mechanical properties as measured before and after the ageing treatments. Results of microstructural stability were also shown to be favourable in comparison with an alternative candidate material for the application, Eurofer.

Their corrosion resistance in liquid lithium was also assessed as this is a leading design option as the breeder material with which the structural material must be compatible. An experimental assembly was constructed as part of this study to enable the exposure of specimens to liquid lithium at temperatures of 500 °C for analysis. The microstructures of the corroded surface following exposure were examined to ascertain the dominant corrosion mechanisms in the system along with their overall level of resistance to corrosion. Results of this testing demonstrated improved corrosion resistance in comparison with advanced steel candidate structural materials for the fusion breeder blanket.

The results presented show particularly promising behaviour of alloys of the Zr-Al and Zr-Ta systems, suggesting that further development and optimisation of zirconium alloys may produce an advantageous product compared with other candidate materials for fusion breeder blanket design. This possibility has the potential to help realise the production of a successful liquid lithium breeder blanket design, thereby enabling electricity generation by fusion power.

Acknowledgements

There are so many people who have helped me get to this stage and deserve more thanks than a few lines here could ever do justice to. I've enjoyed the last four years at Oxford so much, both in the labs and outside of them, and I am so grateful to everyone who has played a part in that.

Chris and Dave, thank you both so much for the opportunity to work with you and your groups over the last few years, the advice, guidance and opportunities that you've given me have been so valuable.

To everyone in the department who has helped me during my time here, Tony Wheeler, Pete Flaxman, Ash Brown, Phani Karamched, Tony Tang, Becs Bradford, Simon Hills, Nicola Flanagan, Ian Sutton, Diana Passmore, and so many others, it's been such a pleasure to work with you all and thank you for so kindly lending your time and expertise.

I am also extremely grateful to all the people I've collaborated with at other institutions who have contributed to this work. The processing at Imperial with Thomas Kwok, Sam Rogers and David Dye; the transient heating at Bristol with Hannah Tipping and James Hargreaves; and the neutron scattering at ISIS with Dirk Honecker and Steve King have all contributed massively to this work and it wouldn't have been the same without their input and experience.

I've been so lucky to work with fantastic people at Oxford who have all become great friends during this project. I'd like to thank everyone who's been part of the Oxford

Micromechanics & Microstructure Group (OMG) over the last few years for being so great to work with, and equally everyone from our smaller zirconium group (James, Junliang, Guanze, Jack, Ben, Rajat, Wenyu, Kay, and Zhexin). Our office group in 21BR18.02 has been such a joy to work in for the last few years and they have been such a source of support through the everyday challenges of a DPhil project, and the tougher times that life throws at us; Pedr, Jack, Ben, Robin, Rob, Keivan, Johann and Anna, thank you for being there for me.

Outside of the materials department, I'd like to thank the team at Oxford Sigma for the exposure to the fusion industry which you've given me and the perspective which that has given me on my research. I'd also like to thank all of the people from OUHC and OUO who have given me the most welcome distractions from work and made my hobbies so enjoyable.

To Alice, thank you for putting up with me and this research for the last four years, and for all of your support and encouragement. I love you and I love all of the time we spend together, and I look forward to spending much more time with you.

And lastly, my family. Your support of everything I have ever done has been exceptional and unwavering. There is no chance I would have got to this point without you and I will never be able to express how grateful I am.

Contents

Abstract **1-2**
Acknowledgements **1-4**
Contents **1-6**
1 Introduction **1-11**
1.1 Research Objectives 1-11
1.2 Thesis outline 1-13
2 Literature Review **2-14**
2.1 World energy crisis 2-14
2.1.1 Nuclear energy 2-16
2.1.2 Major challenges facing fusion development 2-19
2.2 Breeder blanket design concepts 2-21
2.3 Material selection 2-23
2.3.1 Breeder blanket requirements and material selection 2-24
2.3.2 Steels 2-25
2.3.3 Vanadium 2-28
2.3.4 Tungsten 2-29
2.3.5 Molybdenum, Niobium, Tantalum, Chromium 2-30
2.3.6 Ceramic composites 2-31
2.3.7 Titanium 2-31
2.3.8 Zirconium 2-32
2.3.9 Summary of materials selection 2-33
2.4 Zirconium metallurgy and alloy design 2-34
2.4.1 Introducing zirconium 2-34
2.4.1.1 Zirconium alloys for fusion applications 2-37
2.4.2 Alloying elements for study 2-39
2.4.2.1 Low abundance elements (Pd, Ru, Os) 2-40
2.4.2.2 Zr-Be 2-40
2.4.2.3 High diffusion elements (Cr, Cu, Fe, Ni) 2-40
2.4.2.4 Elements with fabricability difficulties (W, Mn) 2-41
2.4.2.5 Previously researched alloys (Nb, Sn) 2-41

2.4.2.6 Zr-HEAs 2-42
2.4.2.7 Zr-Hf 2-43
2.4.2.8 Zr-Y 2-44
2.4.2.9 Zr-Al 2-45
2.4.2.10 Zr-Ta 2-46
2.4.2.11 Zr-V 2-48
2.4.2.12 Zr-Mo 2-49
2.4.2.13 Summary of alloying elements 2-50
2.4.2.14 Similar research being undertaken 2-51
2.5 Liquid Lithium Compatibility of Structural Materials 2-51
2.5.1 Mechanistic and qualitative evaluation of samples 2-52
2.5.2 Corrosion studies at lower temperatures (~300 °C) 2-53
2.5.3 Corrosion studies at breeder blanket temperatures (500-700 °C) 2-53
2.6 Processing 2-54
2.6.1 Zirconium processing 2-55
3 Methodology 3-57
3.1 Polishing 3-57
3.2 Electro-Thermal Mechanical Testing (ETMT) 3-57
3.2.1 Sample preparation 3-57
3.2.2 Sample heating 3-58
3.2.3 Inert atmosphere 3-60
3.2.4 Stress and strain measurement 3-60
3.3 Nanoindentation 3-61
3.3.1 Calculation of indentation stress 3-64
3.3.2 Tip shape calibration 3-65
3.3.3 Calculation of indentation strain 3-66
3.3.4 Production of averaged flow curves 3-67
3.3.5 Heating method 3-69
3.4 Optical Microscopy (OM) 3-70
3.5 Scanning Electron Microscopy (SEM) 3-71
3.5.1 EDX data analysis 3-71
3.5.2 EBSD data analysis 3-72
3.6 X-ray Diffraction 3-74

4 Production, Processing and Assessment of Novel Zirconium Alloys 4-75
4.1 Aim 4-75
4.2 Novel alloy production 4-75
4.2.1 Composition selection 4-75
4.2.2 Casting 4-76
4.2.3 Chemical analysis 4-78
4.2.4 Homogenisation 4-81
4.2.5 Hot Rolling 4-83
4.2.5.1 Phase transformation temperature determination 4-84
4.2.5.2 Rolling method 4-87
4.2.5.3 Exclusion of ZrMo alloys from further study 4-88
4.2.5.4 Examination of rolled samples 4-91
4.2.6 Annealing 4-97
4.3 Processing stages summary and microstructure predictions 4-99
4.4 Examination of the annealed alloys – aims 4-104
4.5 Microstructural analysis results 4-105
4.5.1 Pure zirconium 4-105
4.5.2 Zirconium-aluminium 4-107
4.5.3 Zirconium-vanadium 4-114
4.5.4 Zirconium-tantalum 4-118
4.5.5 Zirconium-niobium 4-124
4.6 Mechanical property testing results 4-127
4.6.1 ETMT 4-127
4.6.2 Nanoindentation 4-134
4.6.3 Creep 4-145
4.7 Discussion of the microstructural and mechanical analysis of the new alloys 4-147
4.7.1 Microstructures 4-147
4.7.2 Mechanical properties 4-151
4.8 Conclusions from the microstructures and mechanical properties of novel alloys ... 4-153
4.9 Estimations of the contribution of microstructural effects to alloy strengthening ... 4-154
4.9.1 Solid solution strengthening in the alloys 4-155
4.9.1.1 Calculations of the extent of solute solubility 4-155
4.9.1.2 Calculating the atomic misfits of the solutes 4-157

4.9.2 Precipitation strengthening in the alloys 4-158
4.9.2.1 Calculating the precipitate spacing 4-159
4.9.3 Zr-Al alloy predicted strengthening mechanisms 4-160
4.9.4 Zr-Ta alloy predicted strengthening mechanisms 4-160
4.9.5 Zr-V alloy predicted strengthening mechanisms 4-161
4.9.6 Considerations for creep deformation resistance 4-162
5 Analysis of Thermal Treatments of Novel Zirconium Alloys 5-164
5.1 Aim 5-164
5.2 Thermal conditions and simulation method 5-164
5.2.1 Isothermal ageing 5-164
5.2.2 Transient heating 5-166
5.3 Results 5-168
5.3.1 Zirconium-vanadium 5-169
5.3.2 Zirconium-tantalum 5-177
5.3.2.1 Transient heating testing 5-187
5.3.3 Zirconium-aluminium 5-193
5.3.3.1 Analysis of nano-scale precipitates 5-203
5.3.3.2 Nanoindentation analysis 5-213
5.4 Conclusions 5-216
5.5 Further work 5-217
6 Liquid Lithium Corrosion 6-219
6.1 Aim 6-219
6.2 Method 6-219
6.3 Discussion of the relevance of mass change in liquid lithium corrosion 6-226
6.4 Results of post-corrosion analysis of candidate structural steels 6-229
6.4.1 Results from Eurofer steel sample 6-229
6.4.2 Results from Castable Nanostructured Alloy steel sample 6-231
6.4.3 Results from 14YWT ODS steel sample 6-234
6.5 Discussion of the corrosion analysis results for steel samples 6-236
6.5.1 The effect of corrosion on precipitates 6-236
6.5.2 The effect of corrosion on grain boundaries 6-240
6.5.3 The appearance of surface particles on the corroded samples 6-242
6.5.4 The appearance of crystallographic terracing on the corroded samples 6-243

6.6 Results of post-corrosion analysis of novel zirconium alloys 6-243
6.6.1 Selection of zirconium alloy samples for testing 6-243
6.6.2 Results from the Pure Zr sample 6-244
6.6.3 Results from the Zr1V sample 6-246
6.6.4 Results from the Zr2.5Al sample 6-252
6.6.5 Results from the Zr2.5Ta sample 6-257
6.7 Discussion of the corrosion analysis results for zirconium alloy samples 6-265
6.7.1 The effect of corrosion on precipitates 6-265
6.7.2 The effect of corrosion on grain boundaries 6-267
6.7.3 The appearance of surface particles on the corroded samples 6-268
6.7.4 The appearance of crystallographic terracing on the corroded samples 6-268
6.8 Conclusions of observations of liquid lithium corrosion 6-270
6.9 Further work suggested in this area 6-272
7 Summary, Conclusions, and Further Work 7-275
7.1 Summary and Conclusions 7-275
7.2 Further Work 7-277
7.2.1 Further material development 7-277
7.2.2 Addressing material requirements 7-278
8 Appendix: Aqueous corrosion of Zr2.5Al and Zr2.5Ta 8-281
9 Appendix: Publication plans 9-284
10 References 10-285
11 List of Figures 11-344
12 List of Tables 12-369
13 Copyright Permission Endnotes 13-371

1 Introduction

1.1 Research Objectives

The objective of this study was to identify zirconium alloys which may offer improved high-temperature properties than the current commercial zirconium alloys used in the nuclear fission industry. The overall aim was to explore whether zirconium-based alloys have potential for application as the structural material of a breeder blanket in a nuclear fusion reactor.

The key benefit of zirconium alloys' low thermal neutron absorption cross-section, which makes them attractive as a fuel cladding material in fission applications [1], [2], may also provide significant benefits in fusion structural materials where neutron efficiency is important to achieve sufficient tritium breeding in the reactor. However, other materials property requirements, such as high temperature strength, creep resistance and corrosion resistance, differ sufficiently between the applications that alternatives to the current commercial alloys used in the fission industry will be necessary for the new application in fusion [3].

The research included in this thesis was designed to explore the feasibility of dilute zirconium alloys with alloying elements not commonly used in commercial products to achieve materials properties which would indicate promise for their use as structural material in the environment of the fusion breeder blanket. The available literature to assess the capability of potential alloys in this area is sparse, despite the promise which has been identified [3], [4]. The output of this research is intended to enable a more

informed assessment of the potential of zirconium alloys for application in the expected environment of a fusion breeder blanket, along with analysis which may enable future compositional and microstructural alloy optimisation.

The research demonstrated in this work provides a benchmarked comparative assessment of different alloying compositions of the primary solute elements in zirconium deemed most likely to be suitable for the application. An assessment of this type has not previously been presented for zirconium alloys having undergone thermo-mechanical treatments representative of those which would likely be used industrially to produce an engineering alloy.

Identified alloy compositions of interest were cast and processed to allow for experimental evaluation of key properties and microstructural features to inform future decision-making regarding alloy development and material selection for fusion breeder blankets.

In addition, an apparatus to enable exposure of materials to static liquid lithium at temperatures greater than 400 °C was developed for this study to assess corrosion resistance in this environment. This is relevant as circulating liquid lithium is a leading design as a breeder/coolant material in fusion breeder blankets [5]. The development of this apparatus is thought to be significant as, prior to its assembly, it is not thought that a similar capability was currently available in the UK, nor the rest of western Europe. However, since its development and presentation of initial findings, at least four similar facilities have subsequently been developed in the UK which have taken learnings from its implementation and operation.

1.2 Thesis outline

This thesis begins with a review of the current literature, including the design concepts of breeder blankets for nuclear fusion and the material selection challenges which this leads to, the prior work on zirconium alloying elements which may be used to select promising candidates, and the processing methods used to produce zirconium alloys for nuclear applications.

The experimental methods used are described and explained in chapter 3, followed by reporting on the production and processing of novel zirconium alloys in chapter 4. Initially, the microstructure and mechanical properties of the alloys were evaluated for their suitability to their application as a fusion breeder blanket structural material.

In the following sections, other important material properties for this application are assessed and discussed, including the stability of the microstructure of the alloys under the thermal conditions expected in-service in chapter 4, and their resistance to corrosion by liquid lithium, which may be used as the breeder/coolant fluid, in chapter 5.

Conclusions about alloy suitability for this application and suggestions of further work are given throughout the experimental chapters, and are summarised with overall conclusions at the end of the thesis.

There is also a short appendix in which the aqueous corrosion resistance of the most promising alloying elements is assessed.

2 Literature Review

2.1 World energy crisis

Significant changes in the global climate have occurred in the industrial era – since 1950 [6]. The scientific consensus attributes this change to human activity, specifically increases in the levels of gases in the atmosphere which contribute to the greenhouse effect [6]. The dominant cause of greenhouse gas emissions is energy supply (35.2%) [7] which is forecast to increase by almost 50% between 2018 and 2050 [8]–[14]. Transport is also a significant contributor (14%) [7]; and as this sector moves towards electrification, its direct greenhouse gas emissions will fall dramatically but place an increased burden on electricity supply [15].

The polluting effects of energy generation as well as its reliance upon finite natural resources to supply the increasing global population lead to the global energy crisis. This crisis has not only environmental impacts but also economic and political consequences [6]. Options for alternative energy sources to fossil fuels include renewable energy sources such as wind, tidal, and solar power, as well as low-carbon energy sources such as nuclear. Whilst it may be possible for the UK to achieve its goals in relation to reduction of greenhouse gas emissions through the deployment of renewable energy sources alone [16], this presents a significant challenge and would not be such a reasonable proposition for parts of the world with less favourable geography and higher population densities [17], [18]. Therefore, a baseload power supply is crucial, which may be provided by nuclear power, fossil fuels, hydro-electric power, or geothermal power. Therefore, nuclear power is the only alternative to fossil fuels which doesn't rely on regional geographic features.

As shown in Figure 2-1 [19], energy produced by nuclear is estimated to have the lowest greenhouse gas emission intensity of any energy source, as well as being one of the safest despite the fear evoked by memories of disasters at Three Mile Island, Chernobyl, and Fukushima [20]–[23]. Additionally, the contribution of nuclear power to the non-fossil-fuel energy mixture is expected to significantly reduce the cost associated with energy production whilst achieving minimised greenhouse gas emissions as the need for substantial energy storage capabilities is averted [24].

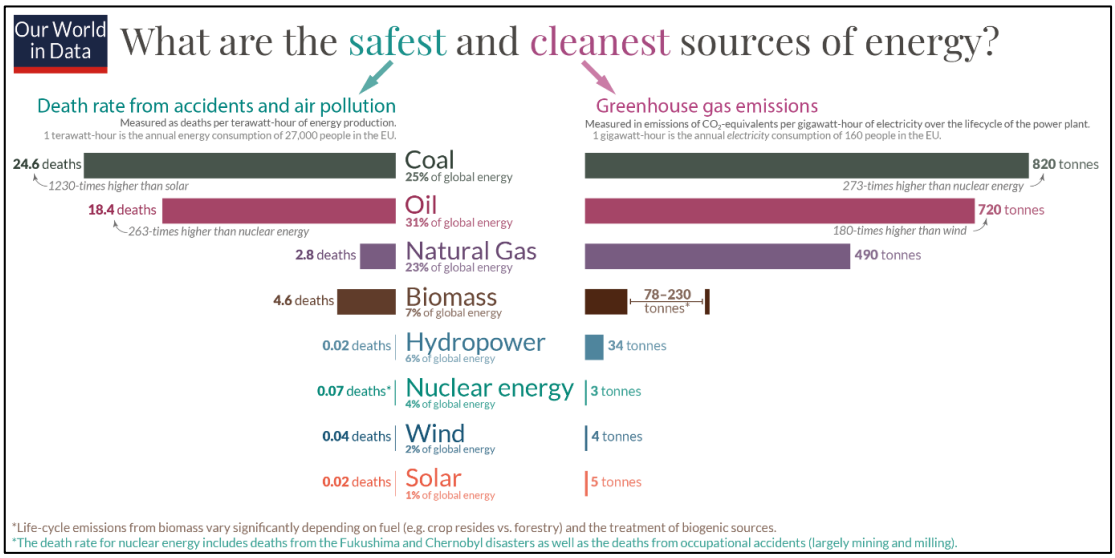


Figure 2-1: Chart showing the death rate and greenhouse gas emissions associated with various sources of energy per unit of energy produced, showing how nuclear energy compares to renewable and non-renewable energy sources [19]. *Credit: Hannah Ritchie and Max Roser /* CC-BY-4.0

The production of long-lived radioactive waste is a legitimate concern associated with nuclear power. However, there already exist stringent protocols for the classification, management, and disposal of radioactive waste products in the UK [25]. There is also a strong international agreement on radioactive waste management to protect the environment and human health [26].

2.1.1 Nuclear energy

Nuclear energy is produced by converting the potential energy stored within atomic nuclei in to electricity via a nuclear reaction. Nuclear reactions involve reorganising atomic nucleons in to new nuclei in which their average binding energy per nucleon is lower. Therefore, the excess energy is released by the momentum of the resultant nuclei and heat.

Nuclear fission is the technology currently used in reactors worldwide and occurs when a large nucleus breaks apart to form two smaller nuclei. The most commonly exploited fission reaction involves impacting a Uranium-235 nucleus with a neutron to form an unstable Uranium-236 nucleus which then decays in to two lighter nuclei [27]. This process results in two-to-three high-energy neutrons which can go on to instigate further fission reactions making a self-propagating power plant achievable [28]. This self-propagating reaction has the potential to lead to reactor meltdown [29]. Fuel cladding materials which do not absorb these neutrons, such as zirconium, are imperative to ensure that the chain reaction may be achieved and to increase the reactor efficiency.

Nuclear fusion is the other type of nuclear reaction that may be used to produce electricity, but this process has only been achieved in experimental reactors to date [30], [31]. Fusion involves combining two light atomic nuclei to form one larger nucleus, releasing excess energy in the form of neutrons and heat. The most promising reaction for fusion to output energy is the reaction between deuterium and tritium to produce helium [32], [33] due to the high reaction cross-section at relatively low particle energies [34]. Deuterium is a readily available resource in the world's oceans in the form of heavy water [35] and tritium (^{3}H) may be bred within the reactor, as shown in Figure 2-2, using

the reaction of neutrons with lithium [36], where ^{6}Li has a higher neutron absorption cross-section for instigation of this reaction than ^{7}Li [37].

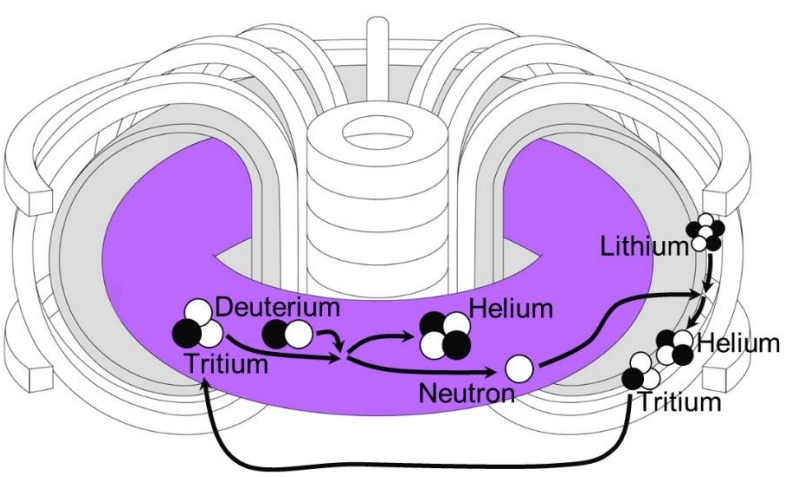


Figure 2-2: Schematic diagram showing atomic reactions that are likely to occur within a nuclear fusion reactor. After [38]*, reproduced with permission from Oxford Sigma Ltd., modified*

There are major advantages to this proposed fusion approach over the existing fission reaction. Firstly, each atomic reaction releases significantly more energy due to the variation in atomic binding energies shown in Figure 2-3. Fusion fuels (deuterium and lithium) are also far safer and more abundant than the uranium needed for fission power [39]–[41]. Finally, the fission reaction creates an amount of long-lived high-level radioactive waste that may take millennia to be safely disposed of [42], [43]. On the other hand, the fusion reaction leads to only helium-4 (an inert gas). Although the structural components of fusion reactors, like fission reactors, will be activated during operation, leading to intermediate-level or low-level waste, it is anticipated that a fusion reactor will not lead to any high-level radioactive waste [44] provided that the radioactive tritium fuel is entirely consumed or recycled.

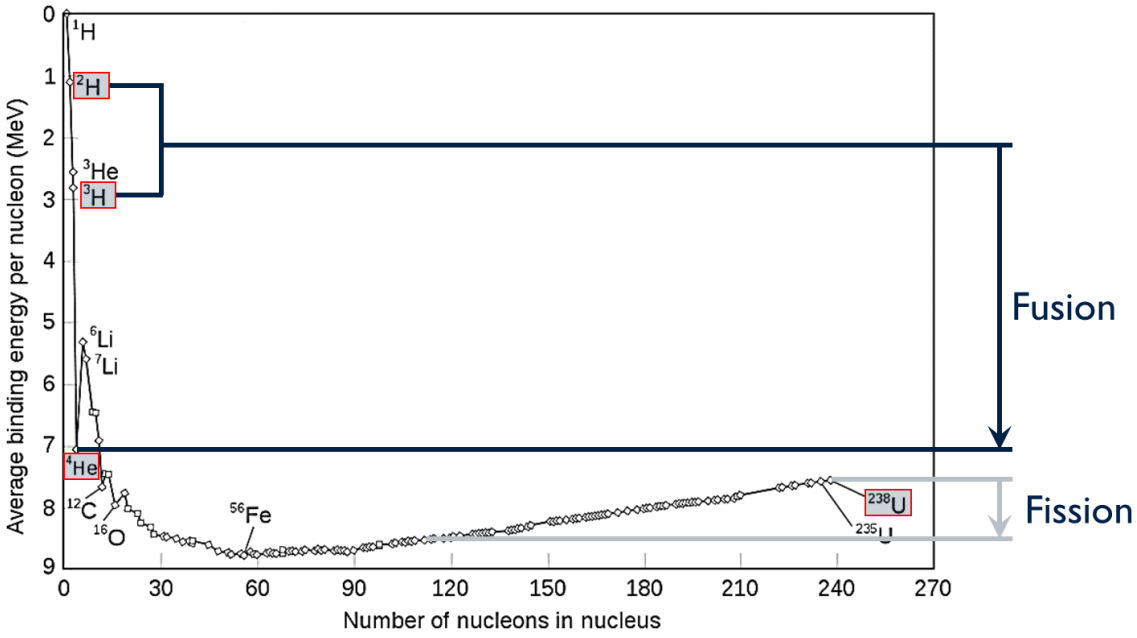


Figure 2-3: Diagram showing how each fusion atomic reaction releases more potential energy than each fission atomic reaction. Credit: User:Bdushaw / Wikimedia Commons / CC-BY-SA-4.0 / modified

The main barrier to achieving the commercially viable fusion reaction is the necessary confinement of the plasma to overcome the electromagnetic repulsion between the deuterium and tritium ions. Magnetic Confinement Fusion (MCF) is the leading design idea amongst atomic energy agencies and private companies worldwide [45], and hence is the basis for the international experimental collaboration reactor ITER [46]. In these designs, the plasma operates at extremely high temperatures, low densities, and for relatively long periods of time (seconds/minutes) confined by magnetic fields [47]. Inertial Confinement Fusion (ICF), the main competitor process [45], works by rapidly compressing the fusion fuel using a pulse of energy so that the pressure and temperature of the fuel increase rapidly and fusion occurs [48]. This is a principle being developed by First Light Fusion Ltd in the UK, among others worldwide [32], [45], [49]–[51]. Other organisations are developing hybrid magneto-inertial designs [45], such as the Magnetized Target Fusion (MTF) design of General Fusion in Canada [52].

This project is aimed at developing a structural material for the breeder blanket modules of an MCF tokamak. This has been chosen as the MCF tokamak design is currently the most advanced design of a fusion reactor due to international collaboration since the 1960s [53], [54]. There is current UK interest in small MCF reactors shown by the £220M STEP project [55], and the private company Tokamak Energy [56]. The breeder blanket section of the fusion reactor is responsible for breeding the necessary tritium to supply the reactor as well as cooling the reactor and hence extracting the energy produced [57].

2.1.2 Major challenges facing fusion development

Fusion technology is now defined as being in the 'delivery era' [58], meaning that there is high confidence that reactors that are being built will be able to output energy. This being said, there are still major challenges to overcome to build a functioning power plant. The UK Atomic Energy Authority (UKAEA) have identified six key challenges facing the deployment of fusion as an energy source [Figure 2-4][59]. 'Removing excess heat' and 'Fuel self-sufficiency' are two of the six challenges associated with the design of the breeder blanket section of the reactor. The breeder blanket surrounds the toroidal plasma and is within the vacuum vessel and magnetic coils [Figure 2-5]. Within the breeder blanket, heat must be extracted for conversion to electricity, and tritium fuel must be bred and extracted to maintain the reaction [57].

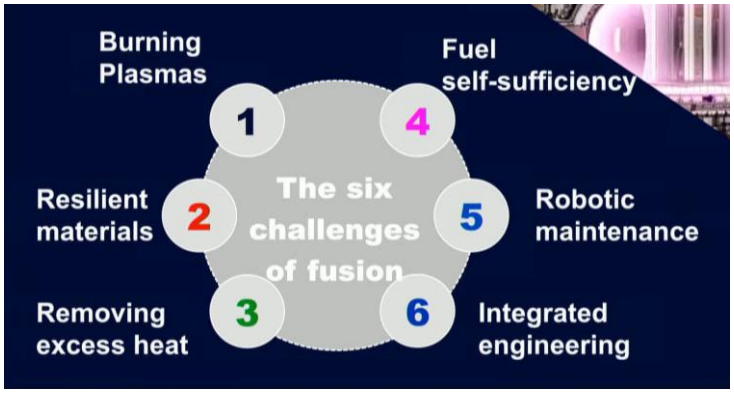


Figure 2-4: The six key challenges to nuclear fusion becoming an energy source, as identified by the UK Atomic Energy Authority [59] *Credit: TED / CC-BY-NC-ND-4.0*

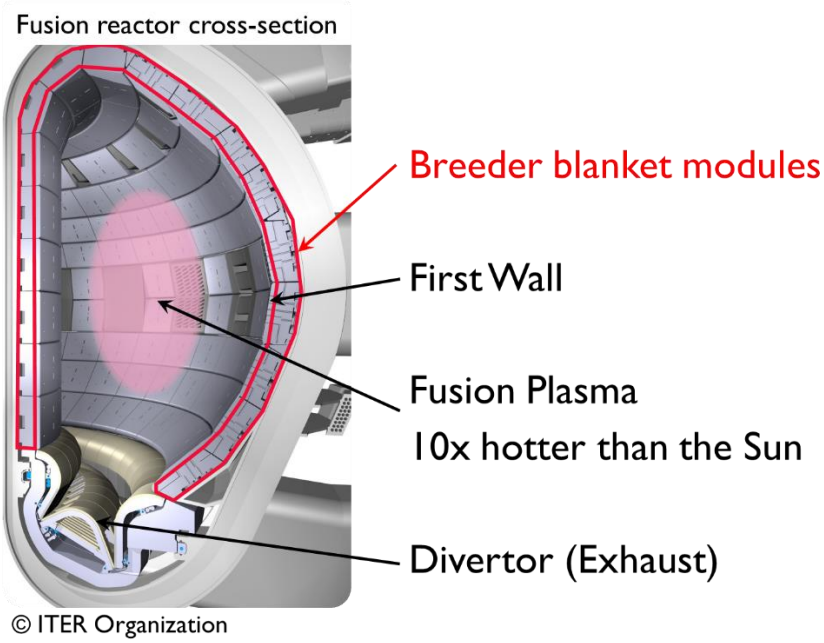


Figure 2-5: Cross-section diagram of a nuclear fusion tokamak, breeder blanket modules highlighted in red. Credit: ITER Organization

'Resilient materials' is another of the six key challenges identified by UKAEA [59] and this is especially important within the breeder blanket. Although breeder blanket materials are protected from the harshest plasma environments by the first wall materials [Figure 2-5], they will still face harsh operating conditions. These include steady-state temperatures of between 500-700 °C [3], temperature surges well above this level due to plasma instability [60], [61], and the corrosive environment of whatever coolant is used.

2.2 Breeder blanket design concepts

As with the design concept for the nuclear fusion reaction itself, there are a number of competing ideas to fulfil the requirements of the breeder blanket. Most of these involve separate systems to breed tritium and cool the reactor. The tritium breeding ratio (TBR, ratio of tritium bred to tritium consumed in the reactor) describes the success of tritium production. The TBR of the reactor as a whole must be greater than one to ensure that enough tritium is produced to fuel further operations. Realistic losses in transport and storage necessitate a TBR significantly greater than one for practical reactor operation, therefore TBR values of approximately 1.1-1.3 have been suggested [5], [62]–[64].

Tritium breeding may be achieved by lithium in the solid state in a lithium-containing ceramic such as lithium orthosilicate or lithium metatitanate [65]. These compounds are the ones selected for experimental development as part of the ITER programme, although octalithium compounds have been proposed which would increase the atomic concentration of lithium significantly [66], [67]. However, it is more attractive to use lithium in the liquid state (molten metal) as this will allow a higher ^{6}Li concentration, pumping and easier subsequent removal of the tritium from the reactor [68]. Lead may also be included with lithium in the liquid state to act as a neutron multiplier to achieve the desired tritium production, most likely at the eutectic 83Pb-17Li atomic composition so that tritium extraction may be performed within the liquid state at low temperatures [69]. Neutron multiplication can be achieved by the reaction of lead-208

with a neutron to produce 2 neutrons and lead-207 (^{208}Pb(n,2n)^{207}Pb) [70], [71]. Liquid-state breeding may be more desirable in order to achieve a suitable TBR for a number of reasons. Firstly, the current generation of lithium-containing ceramics are naturally limited to around 40 at% lithium concentration and the pebble-bed sphere-packing construction leads to large volumes of unoccupied space necessary for tritium diffusion. Alongside this, the decay of lithium and removal of tritium from the ceramic will lead to volume loss over time, potentially leaving dangerous 'windows' through which neutrons will be able to pass unhindered and causing the reactor to 'leak' radiation [72].

Reactor cooling and heat extraction may be performed using helium gas or high-pressure water (~15 MPa) [73]. Helium gas may also be used to dissolve and remove tritium from lithium-containing ceramics [72], necessary due to tritium inventory limits imposed by the regulator [74].

Combining the need for breeding and cooling leads to designs such as HCPB (helium-cooled pebble-bed: lithium-containing ceramic breeder with helium cooling and tritium removal), HCLL (helium-cooled lithium-lead: helium coolant with lithium-lead tritium breeding and removal), and WCLL (water-cooled lithium-lead: water coolant with lithium-lead tritium breeding and removal) [62], [75].

Molten metal may also be used as a coolant within the reactor to extract heat. A self-cooled lithium or lithium-lead breeder blanket is particularly attractive due to its design efficiency, however the high flow velocities needed for adequate cooling are likely prohibitive [76]. Currently the DCLL (dual-cooled lithium-lead) breeder blanket is a design possibility which utilises both helium and liquid metal as coolants whilst the liquid metal also generates and removes tritium [77].

2.3 Material selection

The desire to utilise liquid metal, specifically molten lithium or lithium-lead, within the breeder blanket of a fusion reactor presents the first key design consideration for the structural material due to the corrosive nature of these fluids. The breeder blanket module design in Figure 2-6, although in this case for a solid breeder, shows the approximate arrangement of structural material which would be needed for a breeding module. Another key consideration for the structural material is the temperature of operation of the component. This figure is not certain due to the lack of firm design decisions, although performance in the 500-750 °C range is expected [78]. Within the nuclear power plant, the structural material will also be exposed to irradiation by 14 MeV neutrons for extended periods of operation [79]. The structural material is expected to maintain its integrity under these conditions for at least two full power years [80].

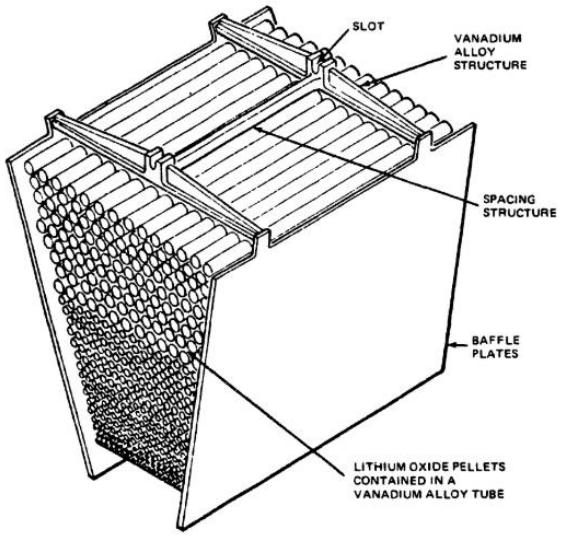


Figure 2-6: Model of a solid breeder blanket module for the MARS reactor showing where structural material would be needed, vanadium alloys were proposed in this case: tubes, structure, spacing structure, and baffle plates. [81], [82] *© copyright 1983, reprinted by permission of Informa UK Limited, trading as Taylor & Francis Group, http://www.tandfonline.com*

Alongside these design requirements, minimisation of tritium retention within all the functional and structural materials is vital in order to remain beneath the threshold tritium inventory of the facility imposed by the regulator [83]. It is also desirable, although not essential, for the structural material to be low-activation following its use in order to minimise the costs and difficulties of disassembly and disposal.

Operation of any material under fusion reactor conditions is relatively unexplored due to the difficulties associated with recreating the necessary conditions [78], [84]. Therefore, bespoke testing of materials performance under appropriate temperature, mechanical load and neutron-flux conditions is required, and it is likely that new materials will have to be developed as this is a condition quite unlike any in which materials have been required to operate before, therefore materials optimisation approaches have not been thoroughly carried out [85].

2.3.1 Breeder blanket requirements and material selection

There is currently no material that is widely accepted as a clear choice for the structural components of the breeder blanket. In order to develop new alloys for breeder blanket structural materials, the UKAEA have specified a list of "target properties and performance characteristics" that will need to be assessed. These are: [80]

- Strength and ductility at ambient and operating temperatures
- Phase stability at operating temperature
- Effects of irradiation on strength, ductility, and phase stability
- Hydrogen isotope retention and hydriding behaviour
- Operating creep and fatigue performance

- Long-term activation
- Thermal neutron absorption
- Compatibility and corrosion behaviour with coolant fluid and breeding material

This combination of criteria is unique to the nuclear fusion environment, so there is little previous research which can inform materials selection decisions. A number of the potential materials for this application [86] will now be critically discussed.

2.3.2 Steels

Of all the potential materials for fusion components, steel is in the most advanced stage of research [87]. This is mostly due to the very large database of knowledge about steel gathered since the 18th century in western Europe [88], its use in an almost endless list of industries [89], its relatively low cost [90], and availability in tonnage quantities [91]. Good fabricability and mechanical properties has led to partners in the ITER project proposing various steel structures for their breeder blanket modules [57]. Ferritic/Martensitic (FM) steels developed for fission requirements have been the starting point for developments of steels for fusion, and this has led to the development of reduced activation ferritic/martensitic (RAFM) steels such as Eurofer97 and CLAM [87], and more recently the UKAEA NEURONE project [92]. RAFM steels are to be used as the breeder blanket module structural materials by five out of the six major partner countries of ITER (China, Europe, India, Korea, USA) due to their good, well-understood mechanical properties at the relevant high temperatures of operation [93]. The martensitic phase of FM steels is not an equilibrium phase and therefore significant phase changes could occur and dramatically alter the material properties if sufficient temperatures are experienced to enable this transformation.

However, it is likely that the high-temperature properties of this steel would limit its operating temperature to 500 °C [86], [94], which is at the lower end of the desired breeder blanket operating temperature [3], [78]. There are also concerns about embrittlement caused by helium and irradiation [86] which would be undesirable for a structural material in which ductility is preferred. The ferromagnetic nature of FM steels could also cause significant problems relating to the magnetohydrodynamics of a liquid metal breeder or coolant [95].

Although there is extensive experience with joining steels, welding may lead to localised phase transformations which may have significant detrimental effects on the mechanical properties of the structural components [96].

There has been some research in to the corrosion behaviour of various steels in a lithium environment. The general conclusion from these is that reaction products containing high concentrations of alloying elements such as nickel and chromium form on the surface, suggesting leaching of alloying elements from the bulk of the material towards the surface [97]. This will have a large effect on the bulk material properties due to depletion of alloying elements. Lithium compatibility of candidate structural materials is addressed in more detail in section 2.5.

The extensive research history on steels has led to it being the go-to structural material for the breeder blanket. However, this also means that it is unlikely that future research will lead to significant improvements in the performance of Fe-based alloys in operating conditions. Oxide dispersion strengthening (ODS) [98] and coatings [99] are the two main current areas of research to improve the performance of steels for fusion.

Coatings such as yttria, erbia, alumina, and aluminium nitride have the potential to provide protection to steels from lithium corrosion. Ceramic coatings also have the advantage of forming an electrically insulating barrier between the steel and the flowing liquid metal which can mitigate MHD effects and potentially mitigate the permeation of tritium in to the structural materials. The major concern with coatings such as these is their difference in thermal expansion coefficient compared to steel, leading to the formation of cracks or spallation of the ceramic coating, and therefore significantly reducing the protection they offer [100]. Therefore, it is necessary for the underlying material to also display sufficient resistance to corrosion. The extent and implications of coating degradation by thermal expansion and corrosion are not well understood and research is ongoing at Oxford University and elsewhere in this area. It has been suggested that the use of multi-layered coating may mitigate the deleterious effect of cracking [101]. Currently, there does not appear to be overlap between those coatings which are effective for reducing MHD effects and those which are effective at preventing lithium corrosion [99], [102]–[106].

ODS steels have shown potential to increase the operating temperatures of steel significantly [107] by pinning grain boundaries in order that grain growth does not occur at elevated temperatures. The high density of nano-oxides in these materials also improve strength, creep resistance and radiation damage tolerance as the nano-oxides act as sinks for the recombination of irradiation-induced defects [108]–[113]. The high temperature strengthening effects and increased irradiation-induced damage resistance conferred by the microstructure of ODS steels makes them attractive as a structural material for fusion in which high temperature strength and resistance to irradiation damage are desirable properties.

Because these alloys are produced using powder processing of insoluble oxide phases, microstructural features occur on a very fine scale meaning that advanced techniques such as atom probe tomography must be used to characterise and understand them [114]. As a result, microstructural characterisation is still ongoing to determine their suitability for fusion applications. There are also issues related to the scalability of this technology to produce material on an engineering scale [115]. ODS technology is not limited to steels and may also be applied to improve the properties of other metal alloys [116]–[121].

2.3.3 Vanadium

Vanadium alloys, especially the V-Cr-Ti system, are of interest due to their corrosion resistance in lithium [122]. These alloys have the potential to accommodate operating conditions up to 600 °C [123] and are also likely to be able to be classified as low-level radioactive waste following service [124]. Despite this, significant improvements are needed in order for vanadium alloys to be realistic design considerations. The main issue relates to the low oxidation resistance of vanadium which leads to difficulties with fabricability [125]. Vanadium can also retain large volumes of hydrogen isotopes which may cause a problem with tritium inventory limits of a power plant and the structural integrity [126]. There are also concerns over the irradiation-induced microstructural evolution of vanadium alloys in-service, leading to embrittlement, swelling, and creep as shown in Figure 2-7 [126]. In addition, vanadium can be used as a neutron absorbing material [127], which would have detrimental consequences for achieving a good tritium breeding ratio, and vanadium alloys are also currently expensive and have a poorly developed supply chain [128]. [126], [129], [130]

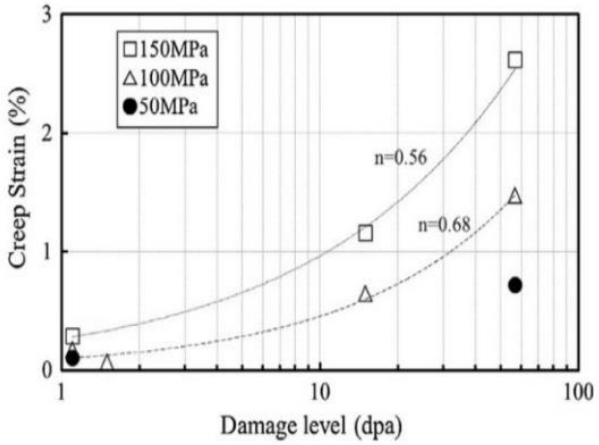


Figure 2-7: Effective irradiation creep strain as a function of neutron dose for V-4Cr-4Ti alloys irradiated at 450 °C [131] [i].

Relatively little is known about the in-service performance of vanadium alloys, as they currently have few applications [132]. This also leads to issues with availability of suitable quantities to build large-scale nuclear reactors. Only 100,000 tonnes of vanadium is produced each year [133] of which a significant proportion is ferrovanadium. Ferrovanadium is a commonly produced 'raw material' form of vanadium which has a high iron content [134]. Therefore, it is suitable for application in adding vanadium to steels, which accounts for 85% of all vanadium applications [132], but not suitable for producing vanadium-based alloys without further purification methods to isolate the vanadium.

2.3.4 Tungsten

Tungsten is a material that is extensively researched for fusion applications, specifically for use as a plasma-facing material [135], due to its extremely high melting point. Such a high melting temperature, however, leads to significant issues with manufacturing and joining [136]. Tungsten also has issues with low ductility which causes

design concerns for structural applications [136], and the fact that the ductile-to-brittle transition temperature (DBTT) increases with irradiation damage [137]. The high density leads to heavy bulk components which increases structural stresses and its neutron shielding effect is undesirable .

There has been research showing a relatively good compatibility of tungsten with liquid lithium, although mass loss measurements in this environment suggest that it is not completely resistant to corrosion [97].

2.3.5 Molybdenum, Niobium, Tantalum, Chromium

Alloys of these refractory metals are exciting due to their potentially high operating temperatures and compatibility with lithium [97], [138], [139]. However, poor fabricability and low ductility mean that it is very unlikely that molybdenum, tantalum and chromium, or their alloys, will be used for structural applications [86]. Although niobium and its alloys may be more favourable in terms of fabricability and ductility, concerns about its activation levels following service leading to waste issues likely prohibit its use [79], [86].

Despite not being used themselves, these elements may prove useful to support other materials. An example of this is chromium coatings on zirconium alloys for fission applications, currently being widely researched to improve the oxidation resistance [140]–[142].

2.3.6 Ceramic composites

SiC_f/SiC is the leading material in this category, and ceramics are very attractive due to their extremely high strength, creep resistance, and high operating temperature [86]. For application as a structural material in a liquid lithium breeding system, it is thought that the corrosion of the carbon interlayer of SiC_f/SiC is likely to greatly affect its mechanical properties [143], [144]. In addition, the lack of material availability – only 22 tonnes of SiC fibres are produced annually [145] – means that the prospect of large-scale engineering projects would be challenging. However, if the demand for this material arose, it is likely that production could be scaled-up.

The major problem with any ceramic is its inherent brittle nature, an issue in structural applications where toughness is important, and this issue is enhanced by radiation damage to the material [146]. In terms of engineering considerations, SiC_f/SiC is very difficult to join and even with developments with brazing technology, joints still account for most of the failures [86]. Swelling due to He and H generation, coupled with low permeability, presents another engineering concern due to the potential for crack initiation [147].

2.3.7 Titanium

Titanium has a long history in aerospace and medical applications. Therefore, low density, corrosion resistant alloys with excellent mechanical properties at high temperature (up to approximately 600 °C) have been developed [148]. A further result of the aerospace application of titanium alloys is that fabrication and microstructural control are well understood [149]. Whilst good high temperature mechanical properties are

desirable for a breeder blanket structural material, the density and environment-specific corrosion resistance are less important for fusion.

Nuclear-specific properties for titanium are not well understood. It is thought that hydrogen may diffuse readily into titanium causing issues with embrittlement and tritium retention. The level of irradiation swelling likely in Ti-alloys are likely to be high and may not be tolerable for the application. A final consideration is that, above 600 °C, titanium absorbs its own oxide and therefore loses its natural protective barrier from the environment. [78]

2.3.8 Zirconium

Zirconium alloys have been widely applied as reactor internals in the nuclear industry due to the low thermal neutron absorption cross-section of pure zirconium [1], [2]. Therefore, extensive research has been performed in order to optimise alloy microstructure for performance at approximately 350 °C in an irradiation environment with aqueous corrosion, and to reduce hydrogen uptake and swelling. Although hydrogen uptake is a known issue for zirconium alloys, extensive work has been undertaken to mitigate its effects [150]. Manufacturability and joining procedures have been successfully developed to support the use of zirconium in fission applications [151]. The prevalence of zirconium alloys in the fission industry ensures that a suitable quantity of the material would be available for the realisation of a fusion power plant, 90% of 900,000 metric tons of zirconium produced annually worldwide is used in the nuclear industry [152], [153]. The major concerns related to zirconium are its mechanical properties (especially creep resistance) at high temperatures and its resistance to liquid metal corrosion [80], [84].

Alloying elements for zirconium in alloy development for fission applications have been selected mainly due to their ability to improve the corrosion resistance to the high temperature H_2O environment (water or steam). As a result, a number of alloying elements which are not compatible with the fission environment have been rejected and, therefore, their potential to increase the high temperature mechanical performance of zirconium has not been assessed [4], [154], [155]. Due to zirconium being metallurgically similar to titanium, it is anticipated that knowledge from titanium alloy developments in the aerospace sector may be applied to development of zirconium alloys for high temperature applications thus accelerating the development of high-performance alloys, although this expectation still requires experimental verification [78]. The corrosion resistance of any zirconium alloy in a liquid metal environment is essentially unknown [84], [156]. It would not be unreasonable to hope that zirconium would have similarly promising liquid lithium corrosion resistance to other refractory metals, its neighbours in the periodic table.

2.3.9 Summary of materials selection

In summary, there is no ideal candidate material for structural components for the breeder blanket. This is due to one or more of; irradiation swelling, irradiation embrittlement, liquid metal compatibility, fabricability, toughness, and high temperature mechanical integrity. Some of these characteristics are summarised in Figure 2-8. Toughness is not included in this figure which presents concerns for SiC/SiC, tungsten, chromium, niobium, tantalum, and molybdenum.

Zirconium alloys may be viable candidates for breeder blanket components as discussed in the previous section and in the literature [3], [4], [155]. However, liquid metal

compatibility will need to be assessed and high temperature mechanical properties, especially creep resistance, would need to be improved above the performance of commercial nuclear fission alloys [80], [84].

Therefore, the scope of this study is to investigate the potential of novel zirconium alloys for application as structural materials for a liquid lithium breeder blanket design.

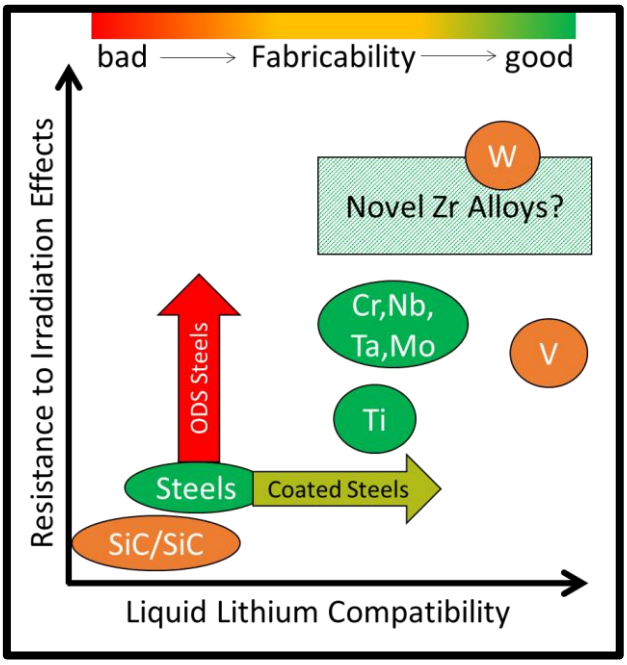


Figure 2-8: Schematic figure summarising the properties of materials relevant to their application as a breeder blanket structural material. Toughness is an important factor not indicated in this figure but discussed above. The region shown for novel zirconium alloys is an educated guess due to the lack of availability of data.

2.4 Zirconium metallurgy and alloy design

2.4.1 Introducing zirconium

Zirconium is a refractory metal that exists in its hexagonal close-packed (hcp) alpha (α-Zr) structure at room temperature and pressure. This is shown in the allotropic

phase diagram in Figure 2-9. At higher temperatures, zirconium exhibits a body-centred cubic (BCC) crystal structure, β-Zr. At standard pressure this temperature is around 865 °C in pure zirconium. Alloying elements can stabilise either the α-Zr or β-Zr, raising or lowering the transition temperature respectively. Niobium and molybdenum are examples of β-Zr stabilising elements, whereas tin and aluminium are examples of α-Zr stabilising elements. Zirconium also presents an omega phase (ω-Zr) which is metastable at standard pressure [157]. The formation of this phase is affected by cooling rates from temperatures in the β-Zr region, and also by the presence of certain alloying elements [158], [159]. Pure zirconium has a melting temperature of 1855 °C [160].

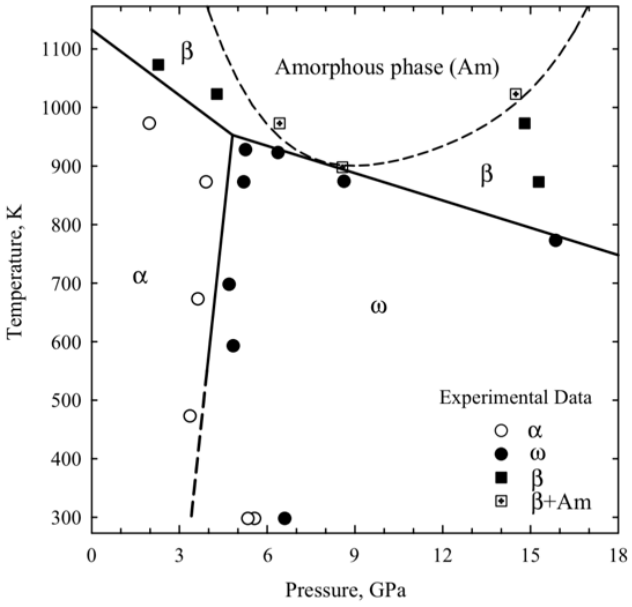


Figure 2-9: Allotropic phase diagram of zirconium [157] [ii]

Zirconium is almost always used in its hcp (α-Zr) form as this is the thermodynamically stable crystal structure at room temperature. The c/a ratio of α-Zr is 1.593 as opposed to the ideal value of the hcp structure: 1.633. This 'squat' unit cell leads to deformation primarily by first order prismatic slip, and basal slip at elevated temperatures [161]. Due to the hcp crystal structure, the mechanical properties of

zirconium can be very anisotropic, this is particularly prevalent following processing stages which lead to crystallographic alignment (texture) throughout a sample, such as rolling [162]–[164]. This anisotropy has led to large disparities between reported measured properties within literature. A table summarising key properties is shown below.

Table 2-1: Mechanical properties data for zirconium [165]–[167]

Modulus of Elasticity (GPa)	96 - 100
Yield Strength (MPa)	276 - 345
Tensile Strength (MPa)	350 - 483
Elongation (%)	28.7 - 32.2
Hardness (GPa)	1.9 - 2.3

The key property of zirconium, which has led to its widespread use in the nuclear fission industry, is its remarkably low thermal neutron absorption cross-section [1] of approximately 0.18 barns [168]. This low neutron cross-section allows the neutrons produced in a fission reaction to interact with other fuel atoms rather than being absorbed by the material. This was noticed by Admiral H.G. Rickover who was leading nuclear research for the US Navy in 1947 upon a visit to Oak Ridge National Laboratory. It had been discovered that the majority of the neutron absorption of zirconium was due to the hafnium mining impurities contained within it. Upon learning that the hafnium was removable within a laboratory, it was immediately decided to pursue zirconium as a reactor material. Ever since this point, zirconium has had extensive research and development, focussed on the design requirements and environment in nuclear fission reactors. [2]

This history has resulted in a number of commercial alloys which are optimised for conditions (aqueous corrosion and temperatures up to 350 °C) which are very

different to those which are likely to exist in the breeder blanket of a fusion reactor. A low neutron absorption rate is equally attractive for a fusion reactor in order to achieve a high tritium breeding ratio. Although the high energy, 14 MeV, neutrons that are produced by a fusion reaction are likely to easily pass through most materials, the transparency of the structural material to lower energy neutrons is necessary to improve the tritium breeding ratio due to the increased cross-section of the $^{6}Li(n,^{4}He)^{3}H$ reaction at lower neutron energies for tritium production. Therefore, there is the potential for new alloys that are optimised for fusion reactor conditions.

Nuclear regulation may introduce a barrier to the acceptance of new alloys, however this should not discourage innovation due to recent experience gaining acceptance for new fabrication techniques [80]. This shows that it is possible for the use of novel materials to be approved by the nuclear regulator, and therefore the potential for innovation in this area should be explored.

2.4.1.1 Zirconium alloys for fusion applications

In order to assess whether a zirconium alloy system may be feasible for application in nuclear fusion, the most important aspect is the increased operating temperature that is likely to be experienced (approximately 500-700 °C [80]) and the corrosive nature of the environment. The potential of zirconium alloys for applications within fusion has long been overlooked by the research community despite analysis indicating their potential [4], [155], and therefore a very large number of potential binary alloy systems may be considered. This is compounded by the fact that the limited research that does exist is impossible to inter-compare due to experimental differences - such as microstructure and

experimental conditions – which could have significant influences on results and conclusions.

Additionally, it has been shown that the activation characteristics of zirconium under fusion-relevant neutronic environments are similar or better than other candidate elements such as iron or vanadium [3], [169]. An example of this is shown in Figure 2-10 which indicates the activation level of elements 10 years after 2 full-power-years (fpy) of operation in the vacuum vessel position of the DEMO reactor design [170].

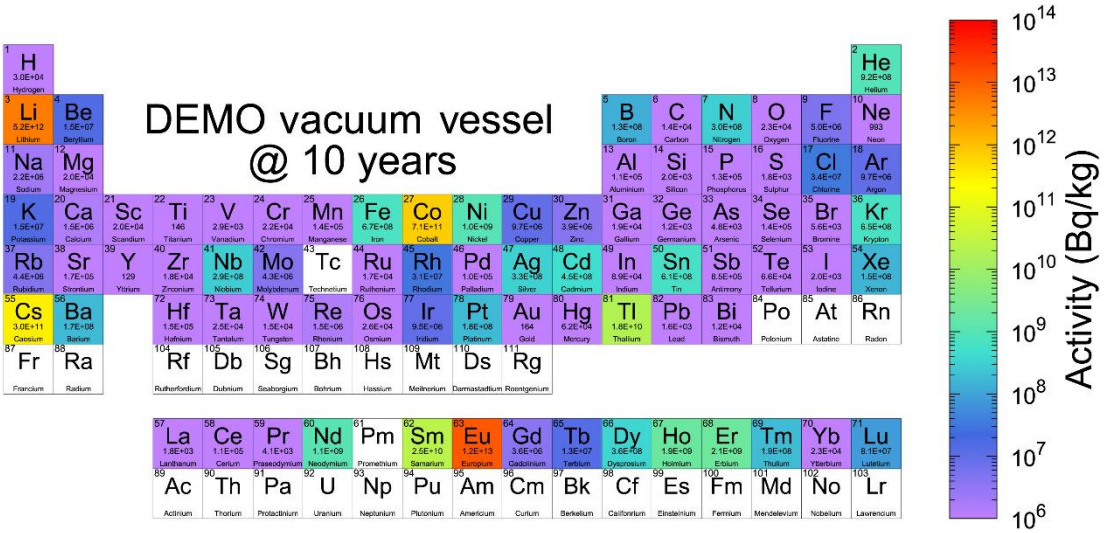


Figure 2-10: Periodic table showing the total becquerel activity from each element after 10 years of decay cooling following a 2-fpy irradiation in a DEMO vacuum vessel environment. The colour of each element reflects the activity according to the Bq/kg legend, but the absolute values are also given beneath each element symbol. From [169]. *Credit: M. R. Gilbert et al. /* CC-BY-NC-ND-4.0

The aim of this study was to produce binary zirconium alloys with maximised strength at the high temperatures associated with breeder blanket structures of fusion reactors. It is also necessary for alloys to display phase stability in service at these temperatures. As a result, binary alloy systems of interest have been assessed using the limited data available and published phase diagrams which may give an indication of

retention of good properties at high temperature. The strategy was to identify binary systems which displayed the highest possible α-β phase transformation temperature which would therefore minimise the pseudo-homologous temperature of the operational conditions. This strategy was expected to yield alloys with the greatest microstructural stability at the elevated testing temperatures which would therefore maintain their strengthening microstructural features. In addition, phase diagrams were sought which gave an indication that alloy strengthening may be imparted by the solute due to either solid solution or second phase mechanisms. (In this case, the concept of a pseudo-homologous temperature is used to describe the ratio of a temperature to the temperature of the material solid-state phase transformation, rather than the accepted definition of homologous temperature which relates to a material's solid-liquid phase transformation temperature.)

2.4.2 Alloying elements for study

A selection of alloying elements of interest in zirconium, where some data existed to review their potential benefits, were evaluated to determine which may be most likely to contribute to high temperature strengthening and other desirable properties for operation in the fusion breeder blanket environment. A similar, thorough review of an array of potential alloying elements was conducted in [3], [85]. In this section, alloying elements of specific interest are identified and discussed, along with some themes where similar reasons for exclusion of a collection of alloying elements has been identified.

2.4.2.1 Low abundance elements (Pd, Ru, Os)

Palladium, ruthenium, rhenium and osmium are all potentially interesting alloying elements for zirconium. However, their low global abundance, and therefore their high price, is likely to prohibit their commercial use.

Alongside this, osmium has a highly toxic oxide (OsO_4) and palladium may present issues with high hydrogen isotope retention. [85], [171], [172]

2.4.2.2 Zr-Be

Beryllium presents advantages such as its neutron multiplication effects and studies appear to show good mechanical properties at elevated temperatures when alloyed with zirconium. The toxicity of beryllium presents a significant concern, and microstructural characterisation shows that the intermetallic $ZrBe_2$ phase simply decorates α-Zr grain boundaries. Therefore, although beryllium may be an advantageous alloying element in small concentrations, it will not form part of this study. [85], [173]

2.4.2.3 High diffusion elements (Cr, Cu, Fe, Ni)

Chromium, copper, iron, and nickel have all been investigated as alloying elements in zirconium, and some of these are already used in commercial alloys [85]. Despite this, the high diffusivity of these elements in zirconium is likely to bar them from being major alloying elements for a fusion alloy as this property is likely to lead to increased creep and precipitate coarsening in-service [174]. Additionally, the inclusion of iron, chromium and titanium as alloying elements has been shown to give minimal strengthening effects

compared with other alloying elements considered, although this research was performed only on quenched and tempered alloys [175].

Nickel also presents issues due to its solubility in liquid lithium and Pb-Li which would reduce compatibility with these coolants [176], [177].

2.4.2.4 Elements with fabricability difficulties (W, Mn)

Tungsten and manganese are both potentially beneficial alloying elements, however both of these present fabrication difficulties. The high vapour pressure of manganese means that it will cause large contamination to a plasma arc furnace when casting the alloy [178]. Tungsten's high melting temperature also presents difficulties with casting [85], [136], [179].

2.4.2.5 Previously researched alloys (Nb, Sn)

Niobium and tin additions have formed the basis for the vast majority of commercial nuclear zirconium alloys [150]. Therefore, additional research in this study is unlikely to add any new information to the literature. Despite this, the production of comparison alloys with similar compositions to commercial alloys, but produced by the same method as the novel alloys in this study, would be of use to appropriately benchmark the novel candidates. Alloys of nominal composition Zr-1at%Nb and Zr-2.5at%Nb are used in this study for this purpose.

The strengthening mechanisms associated with Zr-Nb-based commercial fission alloys are derived from several microstructural features. Firstly, the limited extent of substitutional solid solubility of niobium in zirconium has a limited strengthening effect

caused by the misfit strains. A fine and quite continuous β-Nb phase forms at the boundaries of the fine α-Zr phase grain structure which aids the creep resistance of the material by inhibiting grain boundary sliding mechanisms [180]. In addition, complex Laves second phase precipitates (SPPs) are observed to form, consisting of zirconium and niobium as well as elements of lower concentration in the alloy including iron and chromium, strengthening the alloy via conventional incoherent intragranular precipitate strengthening mechanisms [181].

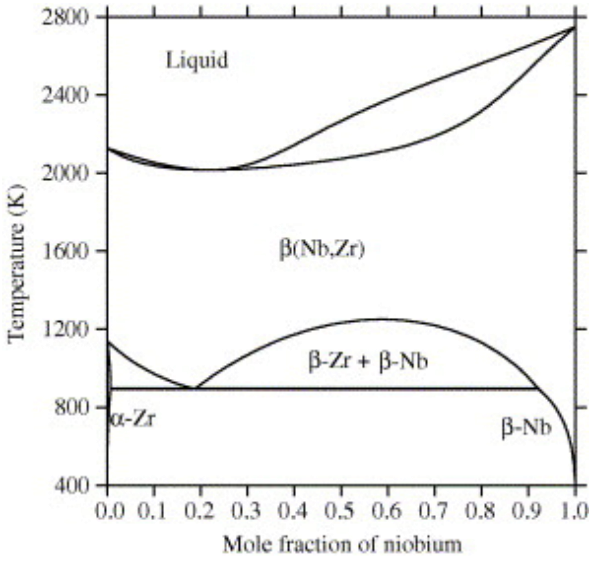


Figure 2-11: Zirconium-Niobium phase diagram [182] [iii]

2.4.2.6 Zr-HEAs

Zirconium-based high entropy alloys (HEAs) have demonstrated favourable properties at room temperature [183]. Due to the high number of components, microstructural changes are very significant when aged for long periods of time, and therefore mechanical properties of the alloys are likely to change over the lifetime of the reactor. This is likely to be unacceptable for a structural material. There are also concerns that the ductility of these alloys will be low, presenting a further problem with their

utilisation as a structural material [183]. The use of HEAs also negates some of the benefits of zirconium-based alloys such as the extensive knowledge base developed over years of research on dilute zirconium alloys for fission reactors, and the low neutron absorption of zirconium. Despite hopes that HEAs display good resistance to irradiation effects, the only study of Zr-HEAs provided inconclusive results and provided evidence of non-crystalline features, suggesting that amorphisation had occurred [184].

Development of HEAs may lead to their suitability for application, however the conclusion drawn in the UKAEA report [85] that "Zr HEAs are the superior Zr alloy choice as a structural material" is based on significant assumptions and is hard to justify given that high temperature data is "severely lacking" [85] for all zirconium alloys. It is possible that some author bias has affected this conclusion as both of the authors have extensively researched and published papers about HEAs including the Nb-Ti-V-Zr system [184]–[191]. The report, however, also states that there are significant prospects to develop new binary zirconium alloys [85]. In addition, the peer reviewed journal article which followed the report presents a more balanced view, including the limitations of low ductility and increased thermal neutron absorption of Zr-HEAs, and recommendations of dilute zirconium alloy systems of interest [3].

2.4.2.7 Zr-Hf

Hafnium is a good α-Zr stabiliser but its effect on neutron absorption is well known [2]. This is likely to negate the low neutron absorption advantage of zirconium, and therefore Zr-Hf alloys are unlikely to be ideal structural materials for the breeder blanket.

2.4.2.8 Zr-Y

Yttrium is considered to be immiscible with zirconium [192]. This means that the α-β transus temperature of the alloy system remains the same as for pure zirconium at around 865 °C as shown in the phase diagram in Figure 2-12. The immiscibility of the elements and lack of intermetallic formation means that the microstructure is likely to resemble that of Zr-Nb alloys, with a second phase forming on the grain boundaries of the predominant α-Zr grain structure. This may provide a benefit for creep resistance at high temperature, and a strengthening effect by the addition of Y to Zr has been previously observed [193]. Inevitable inclusion of oxygen in the alloy is likely to lead to the formation of strengthening Y_2O_3 precipitates as indicated by [194].

Although this alloy system shows some promise for fusion applications, and the mechanical properties must still be evaluated, it was not investigated in this study due to lesser strengthening effects seen by yttrium in comparison with other potential alloying elements in a previous study [195].

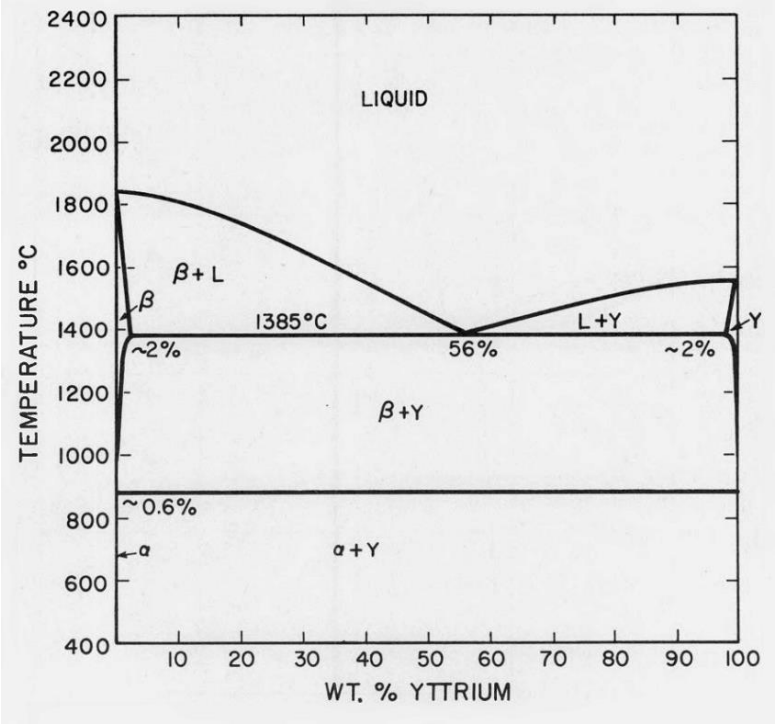


Figure 2-12: Zirconium-Yttrium phase diagram [196]

2.4.2.9 Zr-Al

Aluminium is a commonly used alloying element with titanium [197], however it behaves quite differently with zirconium; although it is still an α-phase stabilising element, its solid solubility in the α-phase is lower in zirconium and the intermetallics exist with different crystal structures as shown in Figure 2-13 [198]–[200]. The reported ductility of the Zr_3Al intermetallic has created great excitement for the potential use of the compound as a structural material [201]. However, this ductility reduces significantly with any surface defects or irradiation [202]–[204]. Although dilute Zr-Al alloy studies have been carried out, there is very little consistency between studies and microstructures have been formed which are unlikely to be stable at operational temperatures [205], [206]. Despite this, reasonable mechanical properties at room temperature and elevated temperature have been displayed. As a result, this alloy system appears to have promise, and further

investigation will be useful to provide insight in to its potential for application in the breeder blanket environment.

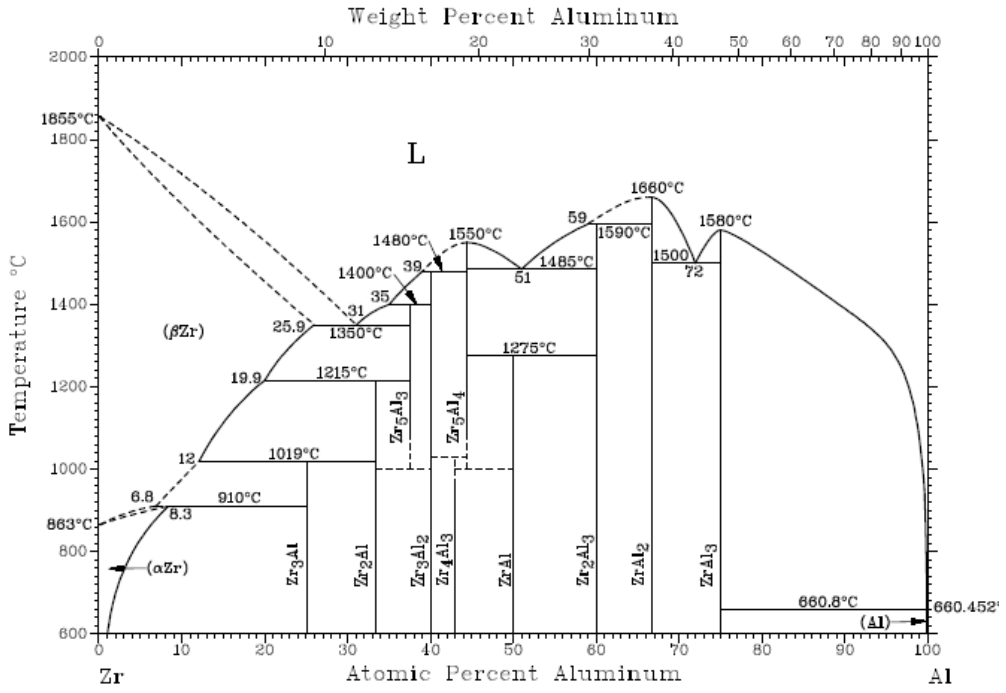


Figure 2-13: Zirconium-Aluminium phase diagram [198], [207] *Reproduced with permission from Springer Nature*

2.4.2.10 Zr-Ta

Zirconium-tantalum alloys were discarded from fission research efforts due to their relatively high thermal neutron absorption compared with other zirconium alloys [208]. However, it is likely that these alloys could still provide an improvement in neutron absorption over steels. There are distinct similarities between the monotectoid-type Zr-Ta and Zr-Nb phase diagrams shown in Figure 2-14 and Figure 2-11 respectively, as well as similarities of the corrosion resistance in aqueous and gaseous conditions [208]. It is possible that, due to the increased transition temperatures in the Zr-Ta system, that mechanical properties of Zr-Ta alloys will be retained to higher temperatures than Zr-Nb alloys which, as previously discussed, are commonly in commercial use in nuclear fission.

There is some evidence of good high temperature creep resistance of Zr-Ta alloys, but this research was performed only on quenched and tempered alloys [175]. One report suggests that lack of ductility of the microstructure may be an issue [85] but there is no justification offered for this view. For this study, it is anticipated that a microstructure similar to that produced in Zr-Nb alloys will be possible due to the similarities of the phase diagrams and therefore the production of similarly ductile materials.

As a result of this review, I concluded that this alloy system shows some promise and therefore was chosen for examination in this study.

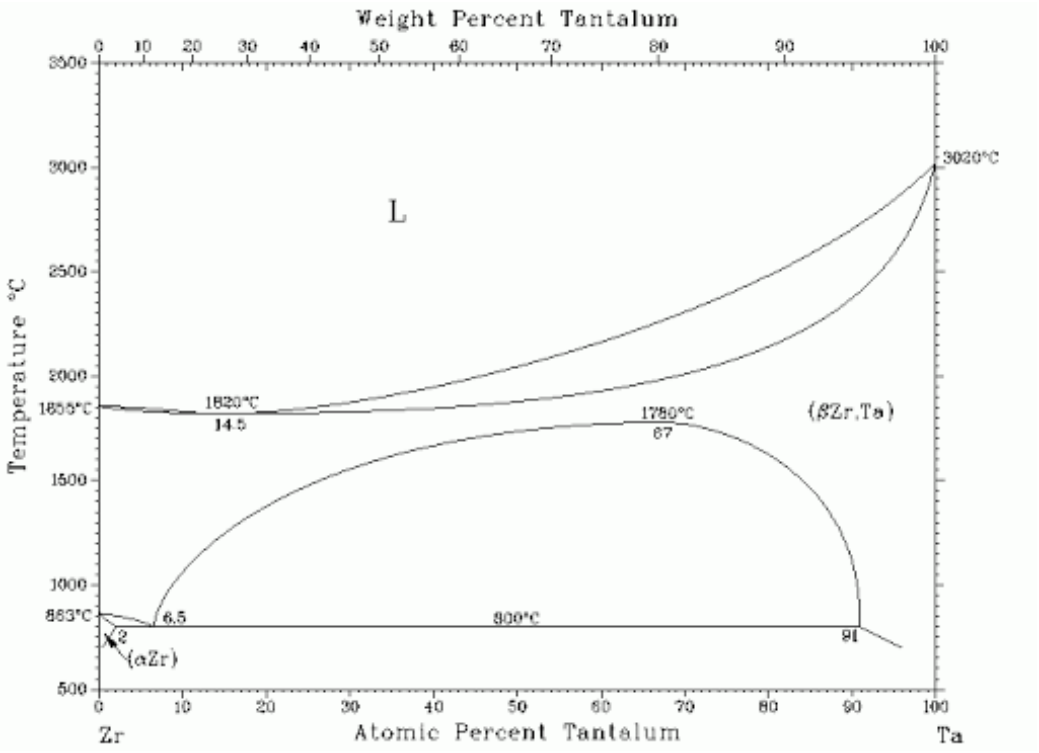


Figure 2-14: Zirconium-Tantalum phase diagram [209] *Reproduced with permission from Springer Nature*

2.4.2.11 Zr-V

An elevated α-β transus temperature of the Zr-V systems suggests that the α-Zr system will be stable at the predicted fusion breeder blanket operating temperatures. Limited solubility of vanadium in zirconium as shown in Figure 2-15 suggests that solid solution strengthening is unlikely to be a large effect, but precipitation strengthening by the ZrV_2 phase is likely. Zr-V alloys containing β-Zr phase have been mechanically tested, but this microstructure will not be stable under operating conditions and therefore the data provided by the study is not useful for applications in the breeder blanket [210].

Research has also been undertaken in to the superconducting properties of the Zr-V system [211]. Whilst this may provide some microstructural information, the data is not relevant to support or contradict the possibility of this alloy system being suitable for fusion applications.

There is very limited examination of this alloy system and there does not appear to be any suggestion of properties that would prevent its use in fusion applications. Although the neutron cross-section of a Zr-V alloy may be relatively high compared to other zirconium alloys [127], this alloy system was also chosen for examination in this study.

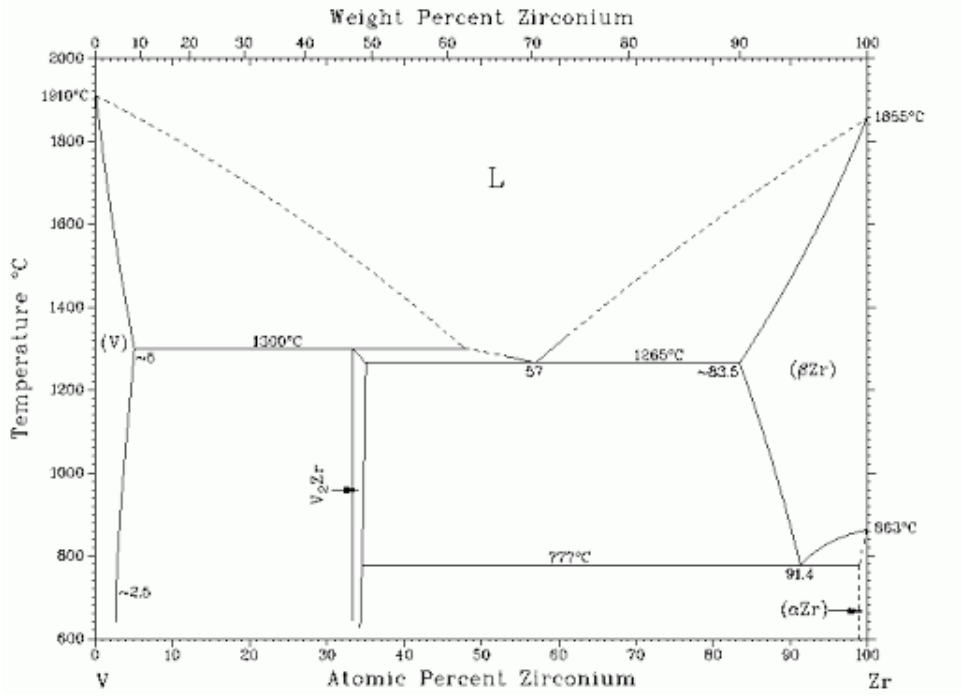


Figure 2-15: Zirconium-Vanadium phase diagram [212] *Reproduced with permission from Springer Nature*

2.4.2.12 Zr-Mo

There is some discrepancy in the reported α-β transus temperature of the Zr-Mo system, lying between 730-777 °C. This is acknowledged in a number of reports and it is suggested that the higher temperature is the more reliable figure [213], [214]. The Zr-Mo system phase diagram appears very similar to the Zr-V system [Figure 2-15,Figure 2-16]. Like the Zr-V system, limited solid solubility of Mo in α-Zr means that precipitation strengthening by $ZrMo_2$ is likely to be the dominant strengthening effect. The metastable ω-Zr phase can appear in Zr-Mo alloys upon casting and the presence of this is likely to be problematic for the fusion application due to its metastable nature [158], [159].

Some study of this alloy system has been undertaken for biomedical applications, however this involved very little alloy processing and no data that may inform suitability for the fusion environment [158]. It has been shown that alloying with molybdenum may

increase the strength of pure zirconium at 400 °C and higher temperature properties will need to be assessed [215]. The neutron absorption cross-section of a Zr-Mo alloy is likely to remain low. It is also thought that $ZrMo_2$ may decrease hydrogen isotope retention within the material, although this may not be accurate due to possible inclusion of β-Zr in the samples tested [216].

Although the presence of ω-Zr will need to be overcome, Zr-Mo may be a good candidate and, therefore, was also chosen for investigation.

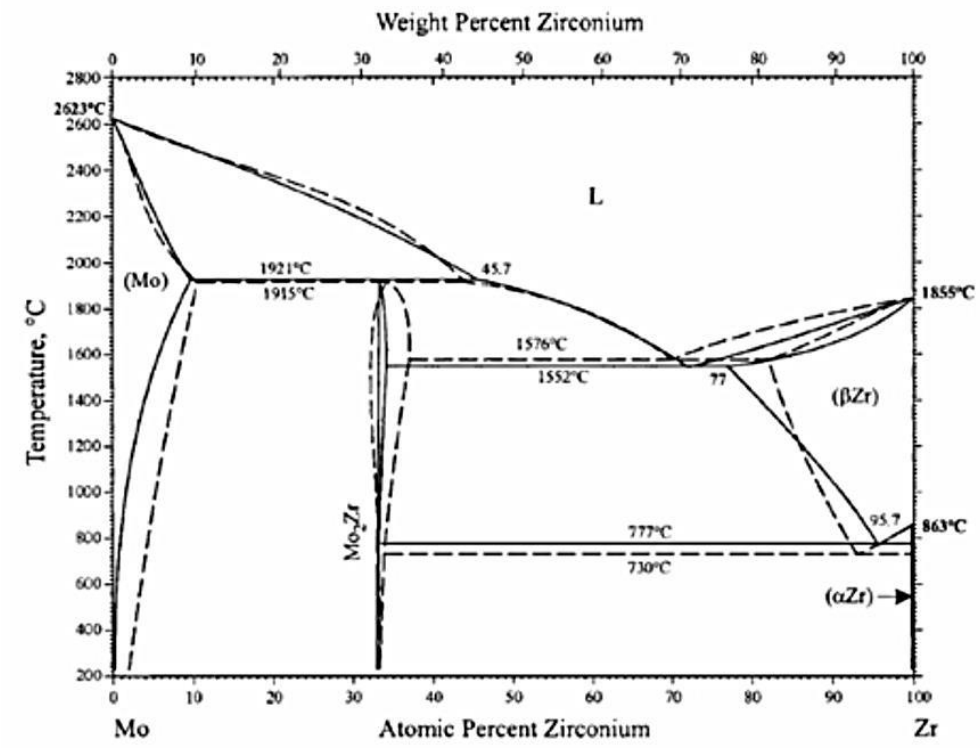


Figure 2-16: Zirconium-Molybdenum phase diagram showing discrepancies between research [214]. *More reliable data is shown in solid lines* [213]. *Credit: K.F.Ahmmed /* CC-BY-4.0

2.4.2.13 Summary of alloying elements

The result of this analysis was the identification of aluminium, molybdenum, vanadium, and tantalum as elements with promise for favourable high temperature

properties. The strengthening mechanisms expected in these alloys, and therefore the logic behind their design, is presented and discussed in section 4.3. Other elements were disregarded from this study due to aspects such as toxicity (beryllium), high diffusion rates in zirconium (chromium and iron), extensive previous research as a solute in zirconium (tin and niobium), and fabrication challenges (tungsten and manganese).

2.4.2.14 Similar research being undertaken

In parallel with this study, work has been ongoing at the University of Birmingham with similar aims of developing zirconium-based alloys with higher operating temperature capabilities than current commercial fission alloys. The approach taken has been to design novel zirconium alloys by analogy to near-α titanium alloys developed for aerospace applications. This has yielded alloys of the Zr-Al-Sn-(Si,Cr,V) system with mechanical testing showing greatly improved mechanical performance relative to conventional zirconium alloys, with measurements of creep resistance indicating especially promising performance in comparison with other candidate materials at temperatures relevant to fusion breeder blanket design [217].

2.5 Liquid Lithium Compatibility of Structural Materials

For a liquid lithium breeder blanket design to be achieved, a key challenge which will need to be addressed is the corrosion of the structural material by the liquid lithium [82], [93], [218]. Given that this has been identified as one of the major design challenges for the realisation of a successful breeder blanket, research in to this area remains surprisingly scarce and further investigation is needed [219].

2.5.1 Mechanistic and qualitative evaluation of samples

Due to its potential as a coolant for nuclear reactors, significant research output was produced between the 1950s and 1980s focussed on understanding the potential corrosion mechanisms in liquid lithium and preliminary assessments of the corrosion resistance of different classes of materials [138], [220]–[224]. This kind of assessment is often limited to qualitative descriptions of the observations, with limited characterisation presented from which to draw firm conclusions as to the corrosion resistance potential of the materials [138], [225]. The identified mechanisms from this research include: the simple dissolution of material elements soluble in lithium; mechanisms involving the reactions of interstitial elements (nitrogen, carbon and oxygen [226], [227]) with lithium; thermal gradient mass transfer in a non-isothermal loop; erosion; grain boundary penetration; liquid metal embrittlement, and induced phase changes due to compositional alterations as a result of corrosion. The occurrence of some of these mechanisms and their dependence on the state of the flowing liquid are shown in Figure 2-17. The corrosion mechanism of reactions involving interstitial elements has been shown to have a strong dependence on the concentration of these elements within the system, with higher levels leading to an enhanced corrosion rate, and a threshold level below which this mechanism appears to be halted [228]–[230].

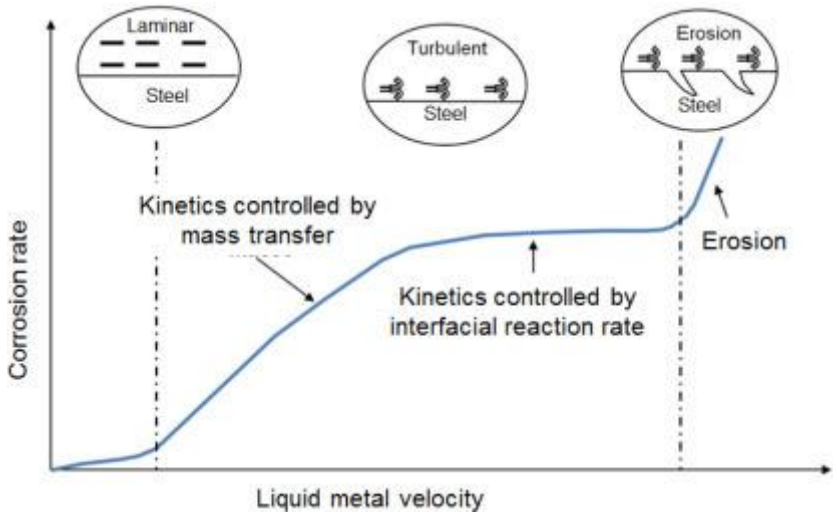


Figure 2-17: Schematic representation of corrosion rate evolution as a function of liquid alloy velocity. From [219] [iv]

2.5.2 Corrosion studies at lower temperatures (~300 °C)

Since approximately 2010, there has been renewed interest in the corrosion effects of liquid lithium in the fusion industry as, along with application as a breeder/coolant medium, liquid lithium is also considered for use as a plasma-facing material and as a fusion neutron source for materials testing [231]–[234]. These alternative applications necessitate a liquid temperature of approximately 300 °C and whilst there have been significant corrosion studies performed in this temperature regime, these results are not applicable to the corrosion of liquid lithium in a breeder blanket application (500-700 °C) due to the unknown effect of increased temperature [78], [80], [221], [235]–[238].

2.5.3 Corrosion studies at breeder blanket temperatures (500-700 °C)

There has been very limited study of the lithium corrosion behaviour of candidate structural materials for the breeder blanket at relevant application temperatures. Where studies have been performed they show significant surface morphology effects, alloy embrittlement and leaching of alloying elements under static and thermal convection

conditions [106], [239]–[242]. No studies could be found in to the corrosion resistance of advanced steels for fusion applications (such as Eurofer or ODS steels). This is also the case for zirconium and its alloys, with the exception of qualitative findings mentioned previously, as confirmed by the findings of other authors [3], [84], [138], [225].

2.6 Processing

It is well known that the microstructure of a material affects its properties [78], [84], [243], [244]. Therefore, in order to draw any reasonable experimental conclusions about a material, microstructural control is of the utmost importance, and processing is key when trying to achieve a good balance of materials properties. This is especially true when trying to compare the potential of a novel alloy against alloys that have had years of characterisation and optimisation [245]. Despite this, a number of papers have tried to assess the properties of novel zirconium alloys in the quenched and tempered state [175] or an as-cast state [159], [246]. These previous studies [159], [175], [246] all make use of material which is shown to have, or is likely to have, the martensitic form of zirconium (α'-Zr) [247], [248]. This phase tends to produce a microstructure of micron-scale lath-shaped HCP grains. This phase is metastable in the zirconium system and forms upon rapid cooling from the high temperature β-Zr (BCC) phase. As a result, regardless of its properties, this structure would not be stable under service conditions, and is therefore unsuitable for the stated application. The stable phase at service temperatures would be the HCP α-Zr phase and therefore a processing method to produce that phase is necessary to produce a potentially suitable alloy.

It would be beneficial to the research community to obtain and test samples with microstructures similar to those of an engineering alloy before drawing conclusions about the potential of an alloy system.

2.6.1 Zirconium processing

The α-Zr phase requirement stated above is equivalent to the requirement for zirconium alloys used in nuclear fission applications and therefore an analogous processing route may be applied to novel alloys to achieve the desired phase composition. In addition, the processing route considered was intended to achieve a relatively fine and equiaxed grain structure as is the case for commercial fission alloys. The purpose of this is to mirror the general structure of engineering alloys in which the length scale of the grain structure is around or below the order of 10 μm [249], [250]. The effect of this grain size is to maximise the benefit of Hall-Petch strengthening whilst maintaining a stable grain structure that does not undergo significant coarsening in service due to the effects of high interfacial free energy at grain boundaries.

To achieve the desired grain structure, it is expected that the produced alloys will need to be worked. One working method which is common for zirconium alloys is rolling. It has been shown that cold rolling a novel zirconium alloy sample can have substantial impacts on its mechanical properties [195]. It is also necessary to perform heat treatments between rolling stages in order to stress-relieve the material. Information has been gathered from UK, US and European patent databases, with individual patents detailing the processing route of a number of commercial zirconium alloys used in the nuclear fission industry. In general, these begin with a quench from a homogenisation step in the β-Zr region followed by hot working within the α-Zr region. The material is then

alternately annealed in the α-Zr region and cold worked approximately three times until the desired microstructure is achieved. There is then a final annealing step. This processing route is shown schematically in Figure 2-18 with rolling indicated as the hot and cold working deformation mechanism as this is the methodology which was available for use in this study. [84], [251]–[268]

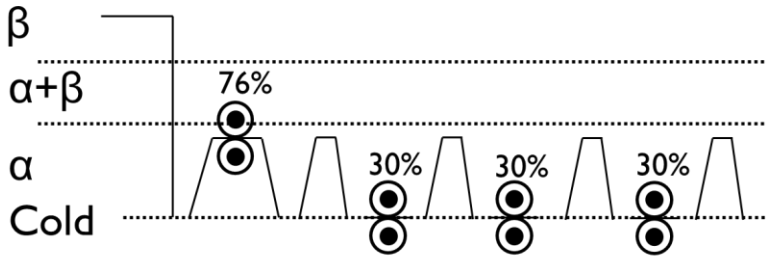


Figure 2-18: Diagram showing the processing stages of a zirconium alloy for fission applications obtained through analysis of patents for commercial alloys.

There is a slight adjustment to this processing procedure for commercial alloys based on the Zr-Nb system as their hot rolling stage can occur in the α-Zr/β-Zr dual phase region, a schematic of which is shown in Figure 2-19. This is of particular note for processing novel alloys such as Zr-Ta which possess similar monotectoid-type phase diagrams to the Zr-Nb system. [252], [253], [255]

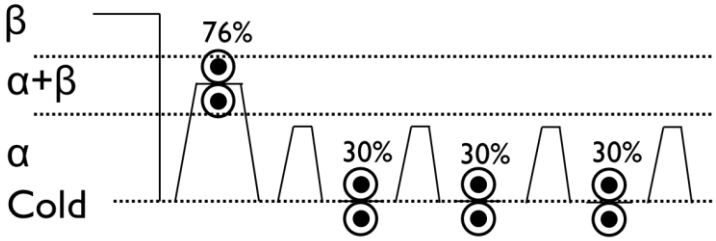


Figure 2-19: Diagram showing the alteration of the processing route shown in Figure 2-18 specifically for commercial zirconium-niobium alloys displaying a monotectoid-type binary phase diagram.

3 Methodology

This chapter gives details of the experimental methods and techniques used for analysis of the material samples throughout the study. These techniques include sample preparation, mechanical testing, and microstructural characterisation.

3.1 Polishing

Samples were cut using a cut-off saw with a diamond blade and surfaces were then prepared for examination by microscopy, X-ray diffraction (XRD) or indentation. This was achieved by grinding of the surface using progressively finer grades of SiC grit paper between grades 400 to 4000. Grinding was performed in 2 perpendicular directions using each grade of grit paper to remove the scratches introduced from the grade before and the sub-surface region of plastic deformation. Following this, samples were polished on a Kemet Chem-H polishing pad using a 1:4 volume ratio mixture of hydrogen peroxide and 0.09 μm colloidal silica suspension respectively for approximately 2-3 hours. This was found to be sufficient to produce a mirror-finish surface.

3.2 Electro-Thermal Mechanical Testing (ETMT)

3.2.1 Sample preparation

Samples of the shape shown in Figure 3-1 were required for compatibility with the Instron ETMT machine available. This shape was cut using Electrical Discharge Machining (EDM) by Simon Hills through the thickness of a bar of the sample material,

and EDM was then used again to produce slices of 1 mm thickness to be used as the final sample. The EDM method produces damage on the surfaces of the sample which needs to be removed before testing to avoid stress concentrations within the sample. This was achieved by grinding the flat surfaces on both sides of each specimen with progressively finer grades of SiC grit paper between grades 600 to 4000. Both edges of the test section between the curved shoulders were initially ground using an abrasive attachment with a Dremel tool before final grinding with 4000-grade SiC grit paper.

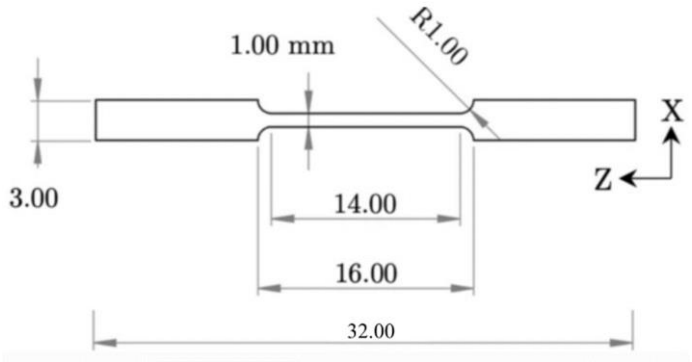


Figure 3-1: Engineering drawing of the shape of samples produced for ETMT with dimensions marked in millimetres

3.2.2 Sample heating

ETMT is capable of testing samples at room temperature and at elevated temperatures. This is achieved by Joule heating caused by passing a direct current through the sample. A K-type thermocouple is made by spot welding the tips of a Chromel and an Alumel wire together and spot welding this to the centre of the gauge length of the sample as shown in Figure 3-2. This thermocouple is connected to the machine control software and is used in a feedback control loop which controls the current being applied to the sample to maintain the desired testing temperature.

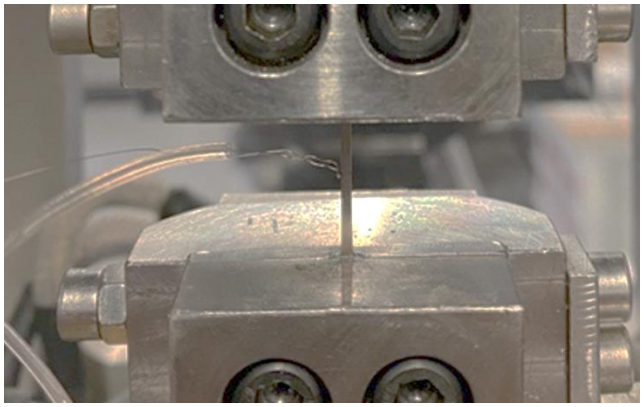


Figure 3-2: Image of an ETMT sample held between the loading grips with a thermocouple attached to the centre of the sample. The scale of this image may be ascertained from the dimensions shown in Figure 3-1

When heating the sample by this method, the temperature is not constant across the length of the manufactured gauge length. Instead, a maximum temperature is observed in the centre of the sample, where the thermocouple is located, and the temperature decreases away from the centre of the sample, towards the grips. Therefore, the deformation of the sample should be most concentrated in the centre of the manufactured gauge length where the temperature is highest, with the assumption that deformation is maximal in the region of highest temperature in the sample. A smaller gauge length is identified in the centre of the sample over which the temperature profile is approximately constant and within which the sample strain can be measured. Previous work on this instrument has shown that a 3 mm long section in the centre of the sample is the appropriate length [269]–[271]. Therefore, the strain measurements described in section 3.2.4 are taken within this shorter gauge length at the centre of the sample for any testing at elevated temperatures.

Necking of the sample during deformation causes an increase in the current density within the necked region, leading to localised overheating of the sample above the

intended test temperature at the latter stages of each test. As a result, data collected from the ETMT method should only be considered reliable up until the point of ultimate tensile stress (UTS), and a meaningful strain to failure measurement is not possible for heated samples.

3.2.3 Inert atmosphere

Zirconium is known to oxidise significantly at elevated temperatures [272] and therefore an inert atmosphere was required to test the samples because an oxidising environment such as air is not expected in-service in fusion machines. An environmental chamber is installed on the ETMT around the testing section. This allows the chamber to be sealed and pumped to vacuum levels of 0.2 mbar, however this vacuum can apply a force on the loading bars which run through the top and bottom of the environmental chamber. Therefore, the tests were run at ambient pressure conditions with an argon supply used to achieve an inert atmosphere within the chamber. Three cycles of evacuation to 0.2 mbar and backfilling to ambient pressure with argon were completed for each test, to ensure an inert environment for the material testing.

3.2.4 Stress and strain measurement

Crosshead displacement is not a reliable measurement of sample extension due to compliance within the system outside of the designated gauge length. Therefore, digital image correlation (DIC) was used to accurately determine the extension of each sample using iMetrum Video Gauge software with a resolution of 0.05%. To enable this, a speckle pattern was needed on the sample surface to track its deformation. Heat resistant spray paint (VHT flame-proof paint) was used to cover one face of the samples in white so that

a second spray of black heat resistant paint from further away could be used to produce a speckle pattern with high contrast. Using this feedback, the machine was capable of maintaining a constant strain rate of each sample during deformation, which was set at a rate of 10^{-3} s^{-1} as is common procedure for use of this equipment [273].

A camera and external lighting source were set up and focussed on the centre of each sample so that two small regions of the speckle pattern within the gauge length could be selected. The testing software was then used to track the change in distance between the two selected regions over the course of the test, and therefore a strain measurement could be calculated and cross-referenced to the applied stress on the sample at the same time.

The width and thickness of each sample was calculated using the average of at least three measurements taken using a micrometer screw gauge. This was used to calculate the cross-sectional area of the gauge necessary for calculating the applied stress on the sample from the load cell data produced by the ETMT.

3.3 Nanoindentation

Nanoindentation was utilised to allow for the investigation into the mechanical response of the sample at both ambient and elevated temperatures. The particular benefits offered by this technique are the relatively low volume of material required for testing, including repeats for data assurance, and the relative ease of sample preparation, including cutting and surface finishing, in comparison with tensile methods such as ETMT.

Nanoindentation was performed in this study using two instruments of different design and capability. On completion of testing, output data of applied normal load (N), the normal displacement (m), and the corresponding contact stiffness (N/m) of the sample was exported from the instrument software for post-processing and analysis.

An MTS XP nanoindenter was used which was capable of performing continuous stiffness measurement (CSM) to provide dynamic measurement of load, displacement, and contact stiffness during the full indentation loading cycle.

A MicroMaterials NanoTest Extreme capable of performing quasi-static indentation at elevated temperature was also used. Due to the lack of dynamic measurement capability, a loading method was implemented which included partial unloading to 60% of the maximum load to evaluate stiffness at set intervals during the indentation load cycle. The number of intervals were limited by the machine to a maximum of 100 partial unloading cycles per indent, leading to a lower maximum resolution of load, displacement, and contact stiffness data points than was possible with the CSM method.

Following export of the data, examples of which are shown in Figure 3-3(a,b), it was necessary to determine an accurate zero-point (the point at which the indenter tip begins applying load to the material surface) for the tip displacement channel to correspond to the start of the indent loading cycle. This is achieved by plotting the applied load raised to the power of ⅔ against the displacement to give a linear region in the elastic loading portion of the indent as determined by Hertzian contact theory [274], [275] as shown in Figure 3-3(c,d). This linear region is manually identified and extrapolated to find the point of intersection with the axis where applied load is zero. This intersection is then

defined as the surface of the sample and displacement values are calculated relative to this point to give an indentation depth (h). Load (P) and contact stiffness (S) values for each data point are unchanged by this calculation.

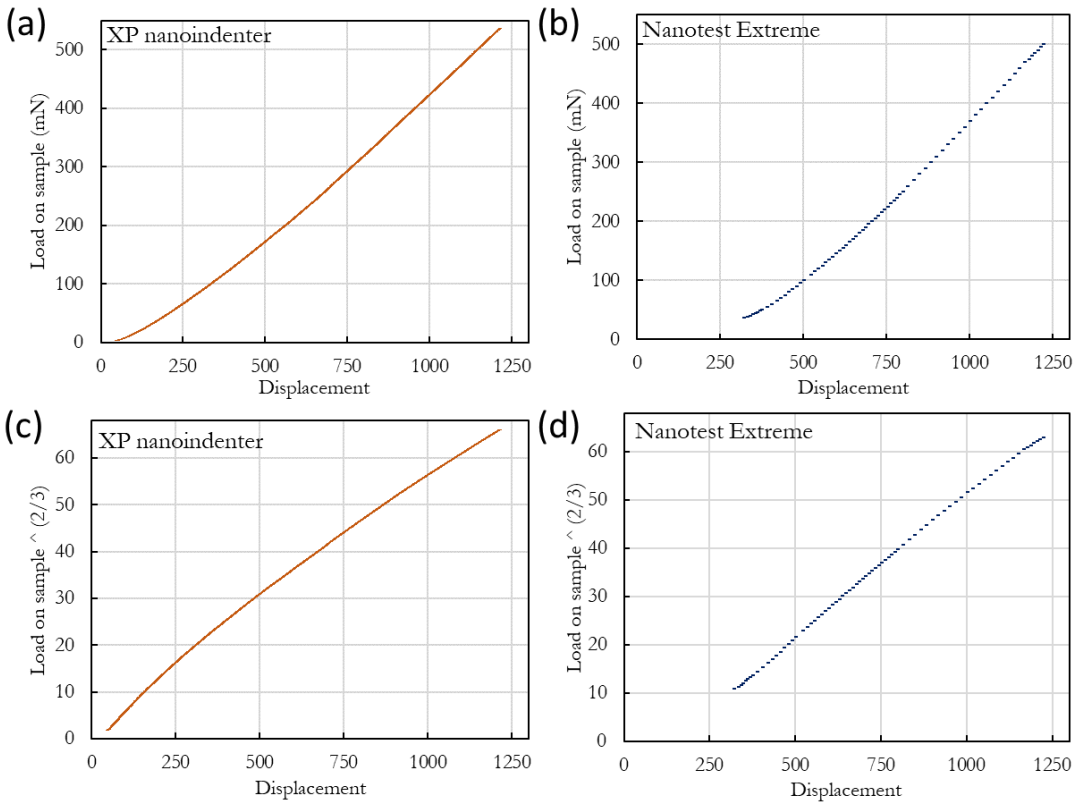


Figure 3-3: (a,b) Example data from the two nanoindenter machines used in this study for the annealed Zr2.5Ta alloy at room temperature. (c,d) show the same data as in (a,b) but with the 'Load' channel raised to the power of ⅔ for determination of the elastic loading portion.

To assess and compare the mechanical behaviour of various samples, indentation flow curves were used. Indentation with a spherical-shaped tip generates an increasing effective strain as a function of indentation depth, allowing the extraction of stress and strain measurements during deformation in both the elastic and plastic deformation regimes [276]. Small-scale measurements are significantly affected by the local microstructure and plasticity scaling effects. To minimise the influence of this, a relatively large tip, of nominally 50 μm radius, was chosen to increase the volume of material under

load and to provide mechanical behaviour that may be more indicative of the sample as a whole rather than that of individual crystallographic orientations [277], [278]. It is estimated that under the maximum load on the samples, the hemisphere of stressed material under the tip had a radius of approximately 50 μm as shown by the 2D isotropic elastic-perfectly plastic finite element analysis model in Figure 3-4 by Charlotte Wheatley.

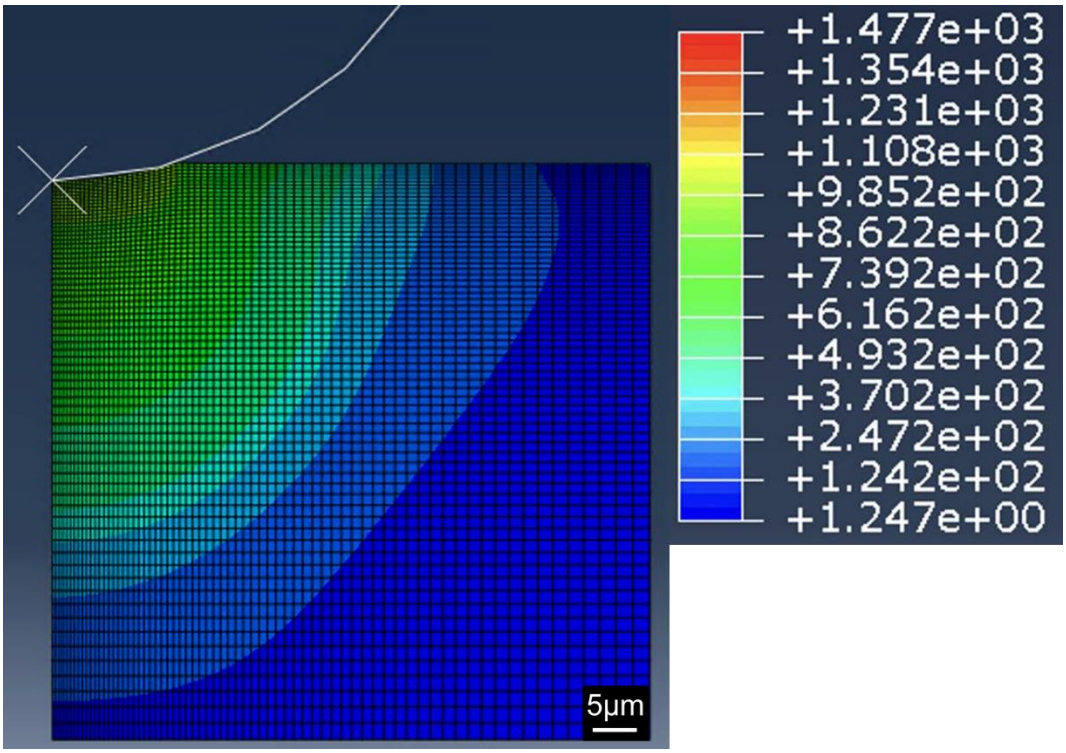


Figure 3-4: 2D isotropic elastic-perfectly plastic finite element analysis model of the Von Mises stress (shown in MPa in the scale) distribution below a 2 μm deep indentation using the commercial software ABAQUS by Charlotte Wheatley.

3.3.1 Calculation of indentation stress

A method of producing a flow curve in which indentation stress is plotted against indentation strain was used which is derived from accepted practice in the literature [274], [275], [279]. The indentation stress (σ_i) is defined by Equation 3-1 in terms of the applied

load (P) and the projected contact area (A_c) [274], [275]. This is equivalent to the definition of hardness [280].

Equation 3-1 $$\sigma_i = {}^{P}/_{A_c}$$

In the case where the indenter tip is a perfect sphere of radius R, the projected contact area (A_c) is defined geometrically in terms of the contact depth (h_c) as shown in Equation 3-2 [279].

Equation 3-2 $$A_c = 2 \cdot \pi \cdot R \cdot h_c - \pi \cdot {h_c}^2$$

The contact depth (h_c), as used to define contact area (A_c) in Equation 3-2, is calculated using the indentation depth (h) following zero-point correction as discussed earlier and the measured values of applied load (P) and contact stiffness (S) as shown in Equation 3-3. The geometric constant, β, is equal to 0.75 for a sphere [279].

Equation 3-3 $$h_c = h - \beta \cdot {}^{P}/_{S}$$

3.3.2 Tip shape calibration

Manufacturing difficulties of such tips necessitates the modification of Equation 3-2 to accurately define the contact area due to imperfections in the tip shape. Leitner [279] proposed Equation 3-4 to achieve this in which B_0, B_1, and B_2 are experimentally determined constants for a specific indenter tip. These constants are determined by indenting a material of known reduced modulus (E*), such as polycarbonate or fused silica which were used in this study, and adjusting the constants such that the reduced modulus measurements calculated using Equation 3-5 [279] are relatively constant with indent depth and match the known values.

Equation 3-4

$$A_c = B_0 \cdot {h_c}^{B_1} - B_2 \cdot {h_c}^2$$

Having collected data from a reference material, the optimisation of the constants B_0, B_1, and B_2 for the tips used in this study was done by Dr Anna Kareer and Dr Kay Song to give the values shown in Table 3-1. This was achieved through numerical methods of parameter optimisation using MATLAB, such that the output data matched the expected reduced modulus for the material.

Equation 3-5

$$E^* = \sqrt{\pi} \cdot S \Big/ 2 \cdot \sqrt{A_c}$$

Table 3-1: Summary of nanoindentation tip calibration constants

Indenter compatible with tip	**Nominal tip curvature radius (μm)**	**Tip-shape constants**		
		B_0 (m)	**B_1**	**B_2**
MTS XP	50	1.08E-3	1.11	3.44
MicroMaterials NanoTest	50	7.26E-5	0.926	2.83
[Ideal Case]	[50]	[3.14E-4]	[1]	[3.14]

3.3.3 Calculation of indentation strain

The indentation strain (ε_i) is defined in Equation 3-6 in terms of the indentation depth (h) and the contact radius (a_c) [274], [275], [279].

Equation 3-6

$$\varepsilon_i = {}^{4 \cdot h}/_{3 \cdot \pi \cdot a_c}$$

The contact radius (a_c) can be determined due to its geometrical relationship with contact area (A_c) as shown in Equation 3-7 given that the contact area is circular for a spherical tip.

Equation 3-7

$$A_c = \pi \cdot {a_c}^2$$

3.3.4 Production of averaged flow curves

Having calculated indentation stress according to Equation 3-1 and indentation strain according to Equation 3-6 for each data point, a flow curve for each indent performed can be plotted. These flow curves may still have some influence of local crystallographic anisotropy, and a more general indication of the mechanical strength of the material is desirable. Therefore, following exclusion of individual flow curves that appear anomalous and are therefore deemed unsuccessful, flow curves obtained from the same sample are averaged to give an overall flow curve for the material.

Data points from a minimum of three successful flow curves were segregated in to bins of fixed size based on their value of indentation strain. The average and standard deviation of the indentation stress values within a bin were then taken to give a single value of indentation stress for a given indentation strain and an indication of the error margin involved. An example of this process is shown in Figure 3-5.

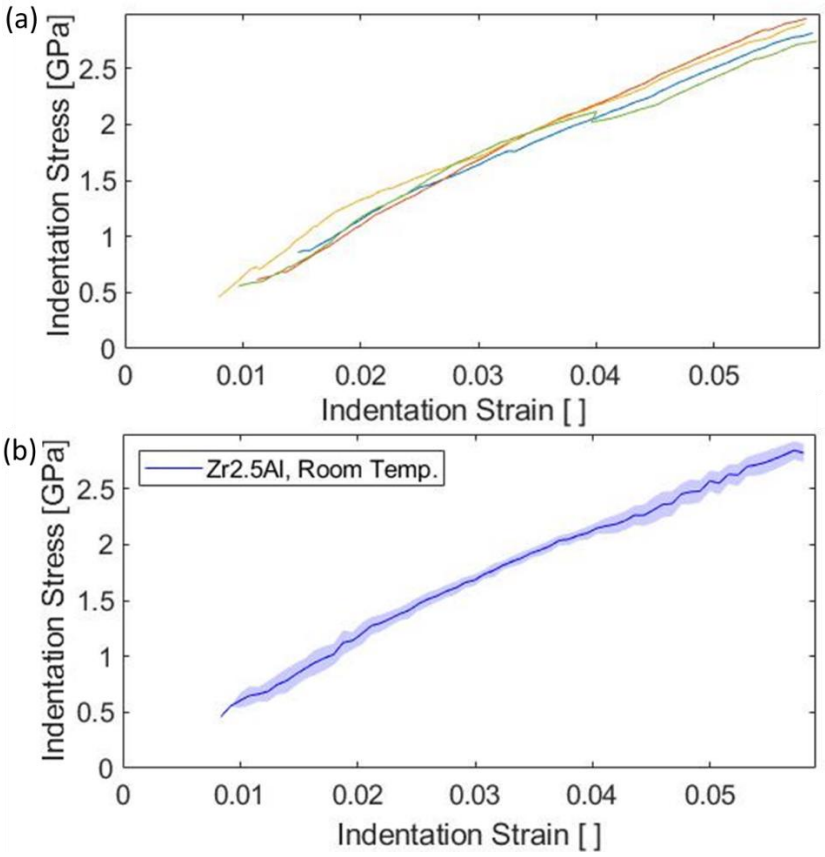


Figure 3-5: An example of the representation of individual indentation flow curves, (a), with an averaged flow curve (b), using the method described above using the data from the annealed Zr2.5Al alloy with the MicroMaterials machine at room temperature.

When only one data point is available within a bin, no error margin may be indicated but the error may be inferred from the scatter in consecutive data points instead. This effect occurs more frequently in tests at elevated temperatures as greater strain increases are observed as the load on the sample is increased, and the size of the loading increments was limited by the equipment. An example of this is shown in Figure 3-6 and it can be seen that, although serrations are seen in the averaged data (Figure 3-6(b)), this is not representative of the smooth curve of the data seen for individual indents in Figure 3-6(a). By plotting these averaged flow curves, comparisons between the strength of different samples may be analysed.

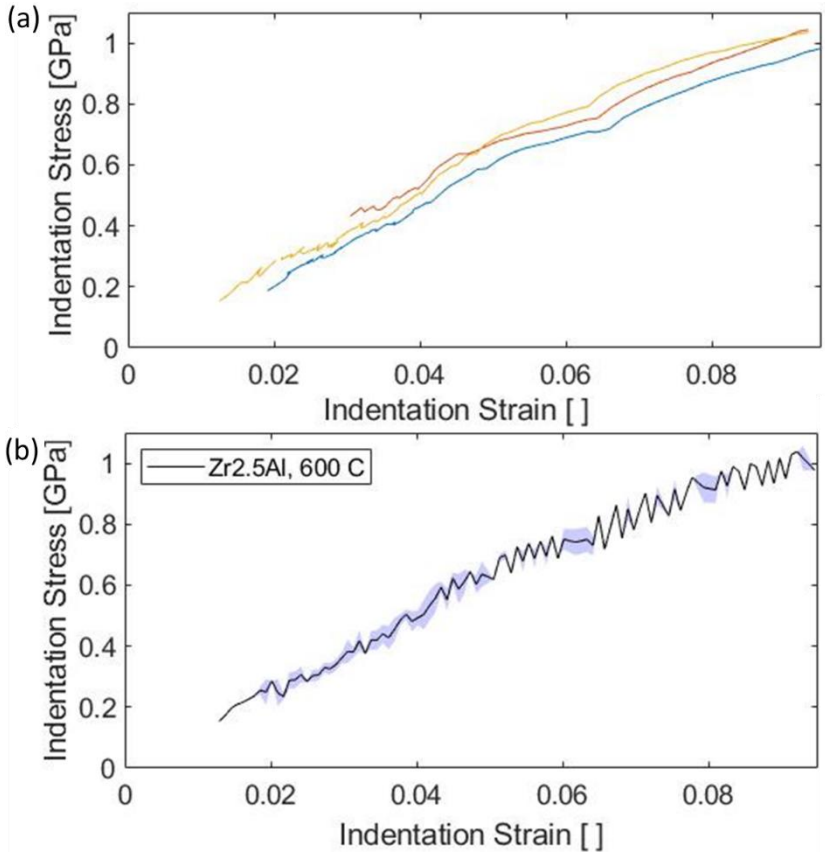


Figure 3-6: An example of the representation of individual indentation flow curves, (a), with an averaged flow curve (b), using the method described above using the data from the annealed Zr2.5Al alloy with the MicroMaterials machine at 600 °C.

3.3.5 Heating method

The MicroMaterials NanoTest Extreme instrument was capable of performing indentation experiments at elevated temperature. This was achieved by securing the samples to a stage with high temperature cement and also using this cement to secure a thermocouple to the side of the sample near to the surface of the sample that was to be indented. Having been loaded in to the machine, the stage could be heated to increase the temperature of the samples. Once the samples reached the set temperature, they were held for a period prior to indentation to allow the temperature to equilibrate and minimise any thermal drift effects. This period was between 5 and 40 hours depending on the

stability of the temperature readings and the order in which the samples were tested. This presents a significant difference to the high temperature testing by the ETMT method, in which samples more rapidly achieved their set temperature and were held for much shorter periods (<10 minutes) prior to commencing the test.

The stage required heating above the desired test temperature in order to achieve the desired temperature at the indentation surface of the sample measured by the attached thermocouple. The indenter tip is also heated to match the temperature of the surface of the sample to avoid thermal drift caused by a temperature mismatch between the sample and indenter in contact. Prior to the test indents on the sample, a series of more rapid indents were performed to check the extent to which thermal drift was occurring. The set temperature of the indenter tip was then altered to minimise this. As a result, not all indents were performed at precisely the chosen temperature but the measured temperature was always within 4 °C of the target temperature.

Any testing at elevated temperature was performed whilst the chamber containing the indenter and sample was held under vacuum to avoid oxidation of any parts of the machine and of the sample surface which could affect the results. The residual pressure in the system was approximately 10 μTorr.

3.4 Optical Microscopy (OM)

The optical anisotropy of the HCP crystal structure, common in the samples analysed, results in birefringence. This means that optical microscopy may make use of polarised light with crossed polarising filters to give contrast in the resultant image of a sample depending on the crystallographic orientation of individual grains [281], [282].

This technique was used widely as part of this study to observe the grain structure of samples using a Zeiss Axiophot optical microscope with polarisation capability.

3.5 Scanning Electron Microscopy (SEM)

Electron microscopy was performed on a Tescan Mira 3 field emission source analytical SEM throughout this study, making use of standard techniques for the characterisation of metallic material samples. Secondary electron (SE) and back-scattered electron (BSE) detectors were used to obtain micrographs in both imaging modes. The SE imaging mode allows for observation primarily of the surface topology of the material. Atomic number contrast is enhanced in the BSE imaging mode.

In addition, electron backscatter diffraction (EBSD) and energy dispersive X-ray spectroscopy (EDX or EDS) within the SEM were used to observe the crystallographic orientations and the distribution of elements within the sample respectively. Analysis was performed using an Oxford Instruments Symmetry EBSD detector and an Oxford Instruments Ultim Max 100 EDS detector.

Further details and backgrounds on these techniques can be found in [283].

3.5.1 EDX data analysis

Analysis of the EDX data collected was performed using the Oxford Instruments AZtec software. Using this software, the background counts could be subtracted from the raw data and a k-factor (or k-ratio) correction [283] was performed on all collected data by the software. Having done this, an estimation of the atomic percentage

composition at each data point may be reported. EDX data was generally collected using a 20 kV accelerating voltage due to microscope calibration availability at this value.

Throughout this study, "apparent concentration" is often reported from EDX results; this data has been processed in the same way but it has been deemed that the atomic percentage figures are unnecessary or misleading to report, often due to the presence of carbon contamination on the sample surface and within the microscope chamber leading to an artificially increased recording of its concentration. In these cases, the relative enrichment or depletion of species over the measured region is prioritised over a quantitative analysis of composition.

3.5.2 EBSD data analysis

EBSD data was collected and analysed using the Oxford Instruments AZtec software, with further processing performed using the opensource MTex software to plot the recorded EBSD data and obtain quantitative crystallographic measurements. The data is plotted so that pixels are coloured based on the crystallographic direction which is aligned according to the plot shown in Figure 3-7.

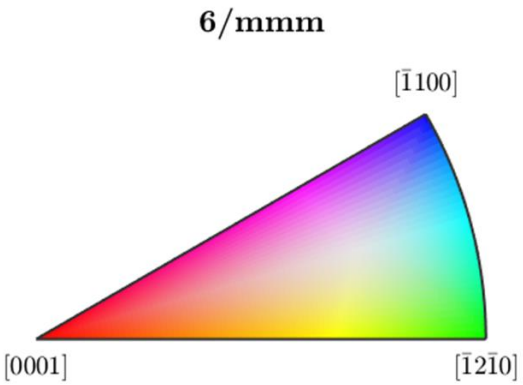


Figure 3-7: Inverse pole figure colour map indicating how the colours shown in EBSD plots of the HCP α-Zr structure in this study are related to the local crystallographic orientation of the sample surface.

The MTex software was able to calculate the Kearns factors of the measured sample. Kearns factors are commonly used in the zirconium industry to give a simplified measurement of the degree of crystallographic texture within the material [284]–[286]. Kearns factors can be measured by multiple methods, but here EBSD has been used [287], [288]. Three factors are denoted as f_{ND}, f_{TD}, and f_{RD} to represent the extent of the alignment of the [0001] direction with the normal, transverse, and rolling direction respectively. The three factors will always sum to 1.

A measurement of the grain size was also possible using EBSD. MTex functions were used to calculate the boundaries between grains given an input of a minimum value of misorientation. The enclosed areas of the calculated grains were then calculated having excluded regions containing below a threshold number of pixels, and the median grain area could be determined. By assuming a circular shape, an approximation of the median grain size could then be made using the relationship between the diameter and area of a circle, with the understanding that this will always be an underestimate of the observed grain size due to the non-circular nature of the grains. EBSD data was plotted for this

study using the original pixels coloured by their identified orientation, with white lines overlaid to show the identified grain boundaries.

3.6 X-ray Diffraction

X-ray diffraction allows for analysis of the phase structure of materials due to the diffraction of incident X-rays from a copper source emitting $K\alpha_1$ radiation of wavelength 0.15406 nm. $K\alpha_2$ radiation of wavelength 1.5444 nm was also present leading to peak splitting phenomena in the data. This was excluded when analysing the data such that the $K\alpha_1$ peaks were used to determine lattice parameters. A Rigaku MiniFlex was used in this study which included a filter to remove copper Kβ radiation. A detector is used to measure the intensity of the diffracted X-ray radiation as the diffraction angle is varied. Peaks in intensity are observed when the scattering angle (2θ) produces constructive interreference as a result of diffraction by crystallographic planes of spacing 'd' according to Bragg's Law, as shown in Equation 3-8 where 'λ' is the wavelength of the X-rays and 'n' is a positive integer.

Equation 3-8 $$n \cdot \lambda = 2 \cdot d \cdot sin(\theta)$$

The samples analysed by XRD had a surface are of approximately 6 x13 mm and were not spun during the test. The data was collected over a 2θ range of 20° - 100° over a period of approximately 40 minutes.

In order to analyse XRD data, literature crystal structures were obtained from the International Crystal Structure Database (ICSD) and compared with the experimental pattern observed using the CrystalDiffract software.

4 Production, Processing and Assessment of Novel Zirconium Alloys

4.1 Aim

The aim within this section of the study is to produce binary novel zirconium alloys using the primary alloying elements selected in section 2.4.2.13 and to perform preliminary assessments of their suitability for application as a structural material for a fusion breeder blanket. These alloys should have a microstructure representative of that which might be used in the engineering context discussed in section 2.6, and then be assessed to examine their microstructure and mechanical properties under relevant conditions.

4.2 Novel alloy production

4.2.1 Composition selection

Following a review of the literature, aluminium, molybdenum, tantalum, and vanadium were selected for examination as potential primary alloying elements with zirconium for the reasons identified and discussed in section 2.4.2.

Having chosen binary alloy systems, alloying element concentrations were selected. Current commercial zirconium alloys for nuclear fission, including Zircaloy-2, Zircaloy-4, B166, X2, M5, E110, and Zirlo, a contain between 1-2.5% of their principal alloying element, either niobium or tin. Therefore, binary zirconium alloys containing 1% and 2.5% of each of the selected solute elements were chosen for casting and subsequent testing and analysis. Due to the increased level of solid solubility of aluminium in zirconium it was decided that, in addition, Zr-5at%Al would be cast in order that a Zr-Al alloy with an increased volume fraction of second phase precipitation could be available for analysis. An increased concentration of aluminium within the alloy is less problematic in terms of maintaining the low thermal neutron absorption cross-section of the alloy than increased concentrations of the other potential elements, due to the relatively low thermal neutron absorption cross-section of aluminium [3].

Throughout the analysis presented in this study, focus is placed upon the alloys containing 2.5 at% of the primary alloying element both because this is a composition which could be compared for all of the alloys, and the higher amount of alloying addition resulted in increased microstructural effects allowing for easier observation.

4.2.2 Casting

To make alloys of the desired compositions, pure pellets of elemental raw metal were obtained from Goodfellow Cambridge Limited and weighed out using an Adam Equipment Luna LPB423i balance with a readability of 0.001 g and a repeatability of 0.002 g to produce the necessary target composition to an accuracy of ±0.001 at% when melted. The stated purity of the material received was a minimum of 99.9 wt% with the exceptions of the raw vanadium (99.6 wt%) and the raw zirconium (99.2 wt% with known

hafnium inclusions). Once weighed out, metals were melted in an Arcast200 plasma arc furnace in order to synthesise the new alloys for evaluation. The elements were added to the water-cooled oxygen-free copper crucible before sealing the chamber and evacuating it to a pressure equal to or less than 25 mTorr using a vacuum pump. Following this, the chamber was backfilled with argon so that melting occurred at -10±3 inHg. Argon gas was added to achieve a pressure at the bottom of this range at the start of melting to account for the increase in pressure in the chamber during melting caused by the heating of a fixed volume of gas. Once the chamber was prepared, power was applied to the permanent tungsten electrode (initially in contact with the tungsten strike pin on the edge of the crucible) to create a plasma arc between the electrode and the material to be melted. Sufficient power, up to an applied current of 650 A, was used to fully melt all of the metal, and electromagnetic stirring of the liquid was employed each time the metal was melted to improve the macroscale chemical homogeneity of the produced alloy. In addition to the stirring, the solidified alloy was flipped and remelted at least four times prior to final casting.

Having achieved what was intended to be a homogenous alloy, the metal was melted one final time in the crucible and, rather than solidifying in-place, the crucible was tilted whilst the metal was still molten so that the liquid poured into a copper mould attached to the side of the crucible. This mould cast the alloy into a rod shape of approximate length 90 mm and diameter 13 mm whilst applying a suction force to the opposite end of the mould from the opening using the vacuum pump to reduce casting porosity in the product as shown in Figure 4-1. The suction hole was drilled out to remove the casting from its mould and the excess metal which remained after filling the mould was cut off using a diamond blade cut-off saw to produce the cast rod. The offcuts were

collected so that a mass loss as a result of the casting process could be calculated to ensure that there was no significant loss of material as a result of evaporation during casting. It was found that across all the samples cast there was a maximum of 0.077 % mass loss with the exception of the Zr-2.5at%Mo in which a mass loss of 0.302 % or 0.709 g was measured. The higher mass loss in this sample indicates that it is not likely to be as a result of evaporation during the casting process and instead is more likely to be caused by the loss of a small piece of material that became detached from the casting during the transfer between the furnace and the balance or that escaped the crucible during the melting process.

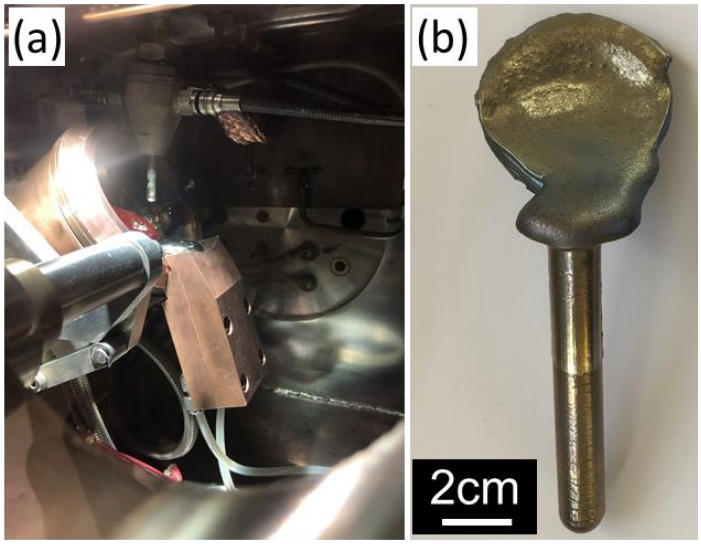


Figure 4-1: Images of alloy casting with (a) showing the tilted crucible with attached mould (copper-coloured), the solidifying alloy sample material (silver-coloured with some red-hot), and the tungsten electrode above the alloy. The polymer pipe connected to the vacuum pump can be seen attached to the bottom of the mould. An image of an extracted alloy sample is shown in (b).

4.2.3 Chemical analysis

Control and measurement of the purity of the alloy product is necessary for appropriate reporting of results, and to avoid artificial strengthening as a result of

excessively high levels of interstitial elements [289]. The raw materials obtained for this study limit the ultimate purity obtainable for the final alloy products. In order to assess this, the predominant raw material (nominally 99.2 wt% pure zirconium pellets) used for casting were sent for X-ray Fluorescence (XRF) analysis to determine elemental concentrations by AMG Analytical (AMG Superalloys UK Limited) under UKAS accreditation. This yielded a result of 138 ppm carbon, 35 ppm nitrogen, and 1149 ppm oxygen by weight. Following casting of the alloys, samples were sent for the same XRF testing to observe the accuracy of the target solute concentrations and any increase in impurity content caused by the casting process. One of the products was made without the addition of any alloying elements to act as a baseline test of "Pure Zr", as this allows for direct comparison with the raw materials to observe the effect of the melting process alone on impurity levels. The measured levels after melting and casting the zirconium raw material were 211 ppm carbon, 60 ppm nitrogen, and 1223 ppm oxygen by weight. Whilst all of these values are increased in comparison to the raw material, the increases were not considered significant. The results are shown in Table 4-1, and the general conclusion from this analysis is that the casting process has not contributed in any significant way to an increase in impurity content of the metal and that the process has been relatively successful in producing alloys of the nominal composition. A notable exception is shown in the ratios achieved for the Zr-Mo alloys in which the measured molybdenum concentration is around 15% lower than targeted, however further research on these alloys was discontinued at a relatively early stage of this study.

Table 4-1: Results of X-Ray Fluoresence analysis showing the measured compositions of the cast alloys. 'Primary Solute' refers to the main alloying element used to create the zirconium alloy, e.g. aluminium in the case of Zr1Al. The ratio between the atomic percentages of the two most abundant elements in the alloy is also shown for direct comparison with the intended ratio described by the alloy name.

Alloy Name	Zr/Primary Solute at% concentration ratio	Atomic% measurements of elements within the alloy							Parts per million by weight		
		Zr	Primary Solute	Hf	Fe	Cr	Sn	W	O	N	C
Zr	-	98.72	-	0.23	0.11	-	0.04	-	1223	60	211
Zr1Al	99.09/ 0.91	97.57	0.90	0.23	0.10	-	-	-	1262	48	267
Zr2.5Al	97.49/ 2.51	96.26	2.48	0.23	0.13	0.09	0.04	-	1195	34	118
Zr5Al	94.94/ 5.06	93.41	4.98	0.22	0.09	0.08	-	-	1735	47	328
Zr1V	99.05/ 0.95	97.72	0.94	0.24	0.10	-	-	-	1308	93	271
Zr2.5V	97.54/ 2.46	96.33	2.43	0.23	0.10	-	0.04	-	1272	48	178
Zr1Ta	99.00/ 1.00	97.78	0.99	0.24	0.10	-	-	-	1200	97	185
Zr2.5Ta	97.57/ 2.43	96.19	2.39	0.23	0.10	0.25	-	0.03	1117	39	178
Zr1Mo	99.13/ 0.87	97.89	0.86	0.24	0.10	-	-	-	1278	39	220
Zr2.5Mo	97.92/ 2.08	96.61	2.05	0.22	0.10	-	-	-	1442	110	168
Zr1Nb	99.02/ 0.98	97.59	0.96	0.23	0.10	0.09	-	-	1161	33	471
Zr2.5Nb	97.60/ 2.40	96.02	2.36	0.23	0.16	0.10	0.04	-	1344	42	393

4.2.4 Homogenisation

Patent literature for the processing of commercial zirconium alloys in nuclear fission applications was reviewed in section 2.6.1, and some general trends were identified. The outcome of this analysis was to proceed with thermo-mechanical processing of the alloys in this study according to the procedures shown in Figure 2-18 and Figure 2-19. Due to the success of the application of zirconium alloys in this industry, a similar process is expected to yield engineering-relevant microstructures in alloys of novel compositions.

The first stage of the processing route identified was to homogenise and quench the cast samples. Heating into the β-Zr phase region allows diffusion to create a uniform distribution of solute elements throughout the alloy samples. This was achieved in this study by holding the samples at 1200 °C for 48 hours in a box furnace before removing them and quenching to room temperature using a bucket of water. The act of quenching the samples makes the formation of the martensitic α'-Zr phase likely. The lenticular microstructure observed in Figure 4-2 is common across the alloys, and is indicative of the β-Zr→α'-Zr transformation [247], [290], [291]. Martensitic α'-Zr is an unfavourable phase as previously discussed in section 2.6, but subsequent processing stages are designed to remove this phase. The quenching step is designed to be readily repeatable to allow for exact replication of the material microstructure prior to the subsequent processing stages that would generate the final microstructure.

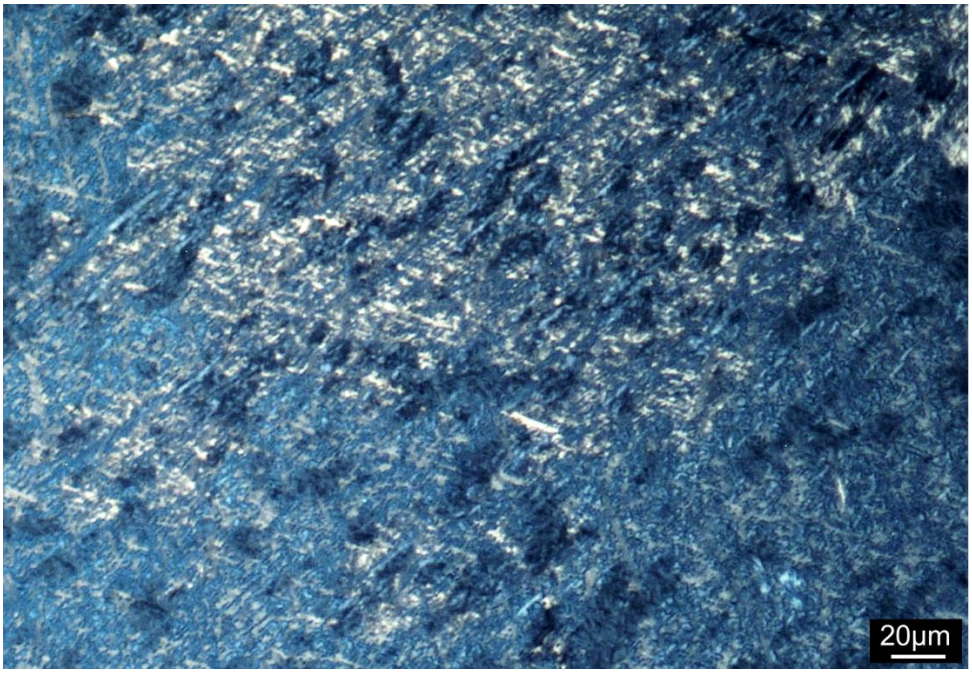


Figure 4-2: Optical micrograph with crossed polarising filters of the Zr2.5Al alloy following quenching after a homogenisation treatment as described above

If the homogenisation and quenching stages were performed in air, the zirconium samples would oxidise heavily. In order to mitigate this, the samples were contained within silica tubes which were evacuated to a maximum pressure 1 µTorr before being backfilled with argon gas and then sealed. As a result, the samples remain relatively shiny following the homogenisation and quenching treatment, as can be seen in Figure 4-3 indicating an insignificant level of surface oxidation.

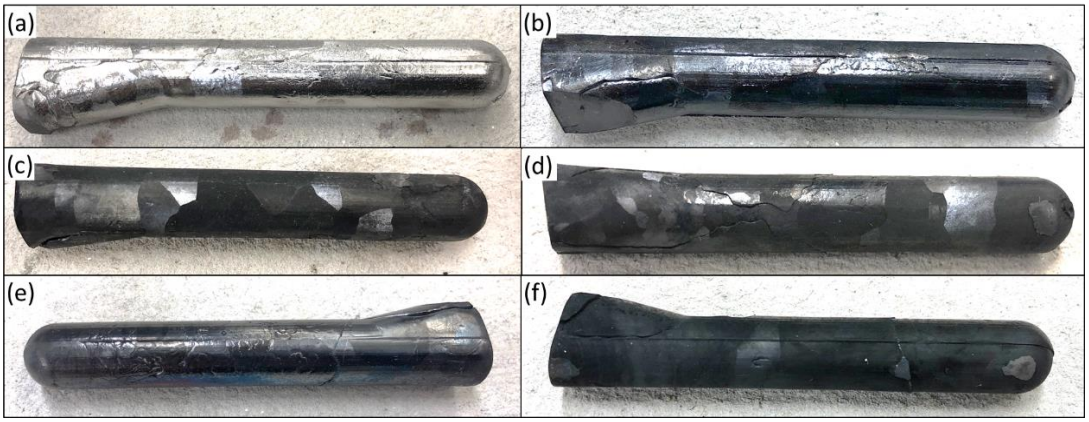


Figure 4-3: Optical images of alloy bars following the homogenisation and quenching treatment. (a) pure zirconium, (b) Zr2.5Ta, (c) Zr2.5V, (d) Zr2.5Nb, (e) Zr2.5Al, (f) Zr2.5Mo. For scale, the length of each bar imaged is approximately 9 cm.

4.2.5 Hot Rolling

The next stage in the processing of commercial zirconium alloys is deformation at elevated temperature, which was achieved in this study by rolling. Prior to commencement of hot rolling, suitable temperature choices were required to fulfil the processing routes identified previously and shown in Figure 2-18 and Figure 2-19. For the pure zirconium sample and the samples of Zr-Al, Zr-Mo, and Zr-V systems (which do not display a monotectoid-type binary phase diagram), a rolling temperature of 700 °C was selected. This temperature was chosen as it is within the α-Zr phase region and comfortably below the transus temperature of any of the alloys indicated in the phase diagrams shown in section 2.4.2, whilst it was felt that this remained a sufficiently elevated temperature. Whilst a rolling temperature of 700 °C was also desired for alloys of the ZrMo system, a soak temperature of 600 °C was used for operational reasons. This was necessary to match the required temperature of other alloys being processed and ensure that all samples could be processed within the available timeframe of the equipment. A summary of soak temperatures used for the rolling treatment is shown in Table 4-3.

4.2.5.1 Phase transformation temperature determination

The ZrTa alloy system displays a monotectoid-type binary phase diagram as shown in Figure 2-14, similar to the one for the ZrNb system as shown in Figure 2-11. ZrNb-type commercial alloys are commonly processed with a hot deformation stage at a temperature within the two-phase α+β region of the phase diagram, and therefore it was decided to mirror this for the processing of ZrTa alloys and for the production of ZrNb control alloys. Therefore, the temperature window of the two-phase region had to be defined.

The binary phase diagrams for these alloy systems give a good indication of the phase transformation temperatures, but the inclusion of other elements (especially oxygen) in the alloy as shown by the XRF analysis in Table 4-1 can affect these temperatures. It was proposed that oxygen would affect the transformation temperatures of the alloys to the same extent that it affects pure zirconium. This effect can be estimated from the Zr-O binary phase diagram shown in Figure 4-4. For example, the inclusion of 0.63 at% oxygen (the value of oxygen measured in the Zr2.5Ta sample by XRF shown previously) to pure zirconium increases the α→α+β transformation temperature by approximately 11 °C and the α+β→β transformation temperature by 55 °C. By applying this shift to the temperature window of the two-phase region of Zr-2.5at%Ta predicted by the phase diagram shown in Figure 2-14, the two-phase temperature window would change from 800-846 °C to 811-901 °C. It was desirable to confirm this by measurement of the phase transformation temperatures of the samples, and an appropriate method was sought.

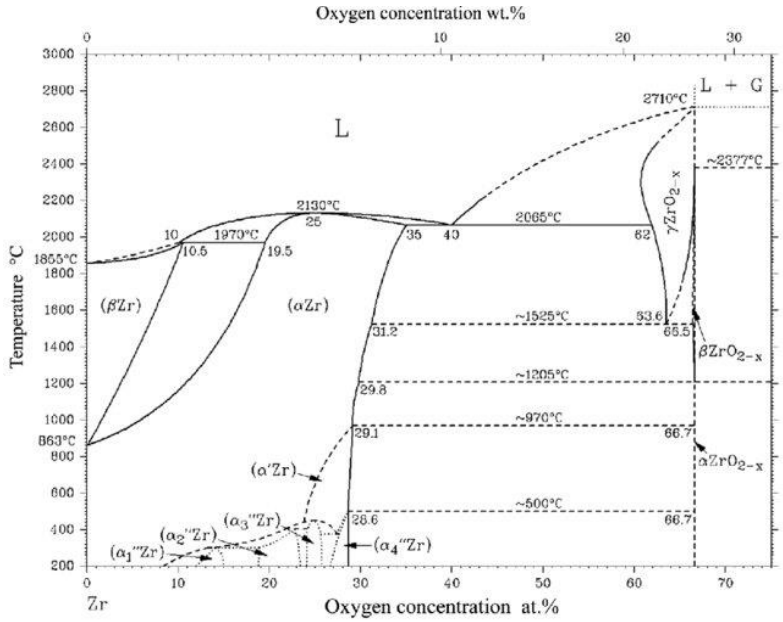


Figure 4-4: Zirconium-Oxygen phase diagram [292], [293] *Reproduced with permission from Springer Nature*

The most appropriate equipment available was a Perkin-Elmer Pyris 1 Thermogravimetric Analysis (TGA) machine. Whilst TGA was not required, this machine also measured the rate of heat flow required to maintain the constant rate of increase of temperature of the sample as defined by the user. If no phase changes of the material occurred, this measurement would have resulted in a smooth curve when heat flow rate (mW/minute) was plotted against sample temperature (°C). The initiation of a phase change would normally result in a heartbeat-type deviation to this heat flow rate curve, first in the positive direction then in the negative direction before returning to the initial trend. The data collected for a specimen of the Zr2.5Ta sample is shown in Figure 4-5, which indicates phase transformation temperatures at approximately 810 °C and 900 °C. This is in remarkable agreement with the estimate stated previously where the two-phase temperature window was predicted to be between 811 and 901 °C. Therefore, this method was used to calculate the two-phase temperature windows available for processing all of the Zr-Ta and Zr-Nb alloys in this study, as shown in Table 4-2.

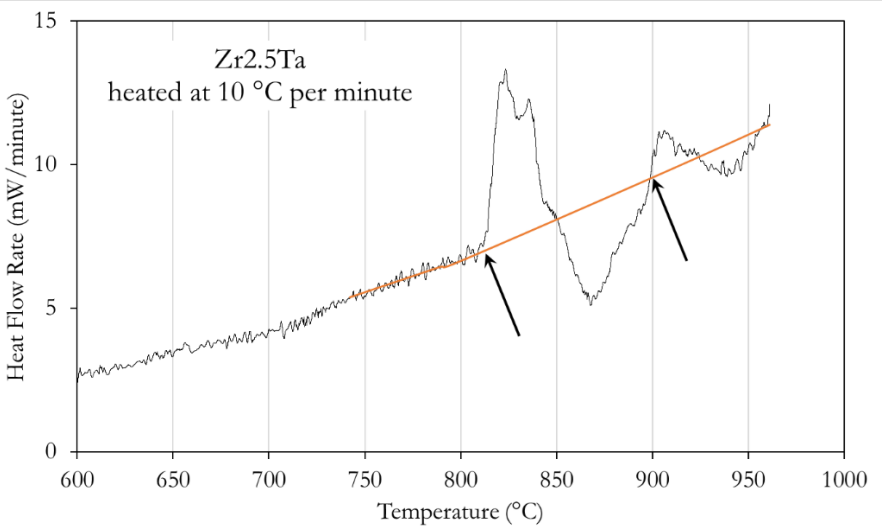


Figure 4-5: Thermometric analysis of Zr-2.5at%Ta sample to determine phase transformation temperatures. The black line indicates the measured heat flow rate data from the constant heating rate test. The orange line represents the anticipated trend of heat flow rate without any phase changes of the material and the black arrows indicate the observed onset points of phase transformations ($\alpha \rightarrow \alpha+\beta$ at approximately 810 °C and $\alpha+\beta \rightarrow \beta$ at approximately 900 °C).

Table 4-2: Summary of two-phase temperature window analysis informing choice of soak temperature for hot rolling processing.

Alloy	Oxygen level from XRF measurement (at%)	Two-phase temperature window (°C)		Chosen soak temperature for hot rolling (°C)
		From binary phase diagram	Calculated including effect of oxygen	
Zr1Nb	0.66	622 – 840	633 – 898	840
Zr2.5Nb	0.76	622 – 813	635 – 880	840
Zr1Ta	0.69	826 – 857	838 – 917	870
Zr2.5Ta	0.63	800 – 846	811 – 901	870

4.2.5.2 Rolling method

A mechanically driven rolling mill with adjacent furnace facilities at the Department of Materials, Imperial College London shown in Figure 4-6 was kindly offered for this stage of alloy processing. The expertise of the regular operators of this facility was consulted to optimise the choices necessary, and their help was gratefully received to complete the three-person process. Having chosen the target rolling temperatures shown in Table 4-2, a box furnace was set to the soak temperature for the specific alloy to be rolled. The samples were placed in the furnace at that temperature for 30 minutes prior to the first pass through the rollers. The sample thicknesses were initially measured with callipers prior to rolling, and for the first pass the separation of the rollers was set to approximately this thickness, nominally a 'sizing pass'. For each pass through the rolling mill, samples were removed from the furnace and immediately fed in to the rollers using tongs, the sample was received after passing through the rollers by a second operator, passed back to the first operator and the new sample thickness measured with callipers before being returned to the furnace. Soaking steps in the furnace between rolling passes were performed for 5 minutes.



Figure 4-6: Image of zirconium alloy sample (red) being hot rolled.

A thickness reduction target of 76 % true strain was set for all the samples. For the purposes of efficiency, two or three alloys with the same soak temperature were processed concurrently. Therefore, the roller separation distance set had to be the same for each of the samples in the set, and it was not possible to achieve the target thickness reduction perfectly. The total true strains achieved for each sample are shown in Table 4-3. Additionally, it was decided that four passes would be best to achieve the final total true strain required. Roller separation distances for each pass were decided based on the most recent measurement of the sample thickness and the desire to maintain a relatively constant value of true strain per pass of 19 % which was achieved within a ±4 % margin. Following the fourth and final pass, the samples were returned to the furnace for a final soak for 5 minutes and then removed from the furnace and air cooled with each end rested on a mullite brick to ensure a homogenous cooling rate of the sample.

Table 4-3: Showing details of the hot rolling processing of the alloys including the soak temperature set on the furnace and the total true strain achieved

Alloy	Soak temperature (°C)	Total true strain (%)	Alloy	Soak temperature (°C)	Total true strain (%)
Zr	700	71.0	Zr1Ta	870	77.9
Zr1V	700	71.3	Zr2.5Ta	870	80.1
Zr2.5V	700	69.9	Zr1Nb	840	77.0
Zr1Al	700	72.8	Zr2.5Nb	840	76.4
Zr2.5Al	700	74.8	Zr1Mo	600	76.5
Zr5Al	700	73.5	Zr2.5Mo	600	75.5

4.2.5.3 Exclusion of ZrMo alloys from further study

ZrMo alloys were rolled with a soak temperature of 600 °C as shown in Table 4-3 for operational reasons, and despite the change in temperature it is believed that this should yield comparable results to rolling with a soak temperature of 700 °C. All samples

other than those of ZrMo alloys emerged from the rolling processing with relatively little evidence of macroscopic rolling defects as can be seen in Figure 4-7.



Figure 4-7: Optical images of 2.5 at% alloy bars directly following the hot rolling procedure. (a) pure zirconium, (b) Zr2.5Ta, (c) Zr2.5V, (d) Zr2.5Nb, (e) Zr2.5Al

Conversely, significant defects were observed in the Zr2.5Mo sample following rolling including sample bending and edge-cracking as shown in Figure 4-8.



Figure 4-8: Optical images of the Zr2.5Mo sample following hot rolling

The reduction in ductility observed during rolling is thought to result from the presence of the ω-Zr phase identified in the sample prior to rolling as shown in Figure

4-9 which is known to more brittle than the α-Zr phase [294]. Although the ω-Zr and β-Zr give rise to similar spectra in XRD analysis, ω-Zr can be confidently identified in this sample due to the peaks above the background at 2θ values of 71° and 99° which are expected for the ω-Zr phase and not for the β-Zr phase.

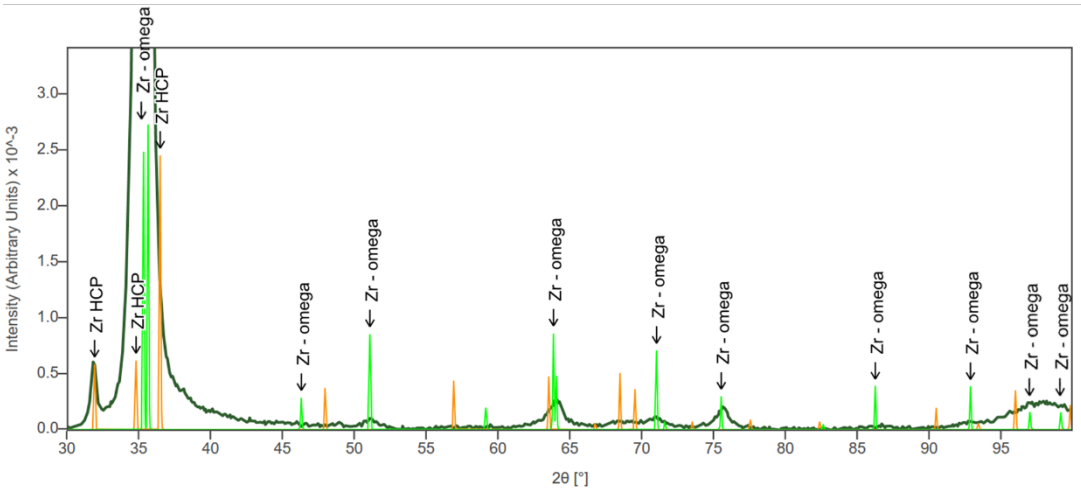


Figure 4-9: XRD data of the Zr2.5Mo sample prior to hot rolling with a simulated pattern of the ω-Zr phase indicated along with peak positions of α-Zr, from [295].

Despite the elevated temperature during rolling, the reduced ductility would suggest that the ω-Zr phase remains present and contributes deleteriously to the mechanical properties. This is supported by the XRD analysis following hot rolling shown in Figure 4-10 in which, as expected, increased fraction of α-Zr phase is observed when compared with the data before hot rolling shown in Figure 4-9. Evidence of the ω-Zr phase remains, and the peaks correlated with this phase are observed at slightly increased values of 2θ compared with their position before hot rolling, which is consistent with an increased concentration of molybdenum within the ω-Zr phase due to its smaller atomic radius than zirconium [296]. This distribution of molybdenum is consistent with the lack of peaks from the $ZrMo_2$ Laves phase which would be predicted as the primary equilibrium second phase in this alloy from the phase diagram shown in Figure 2-16.

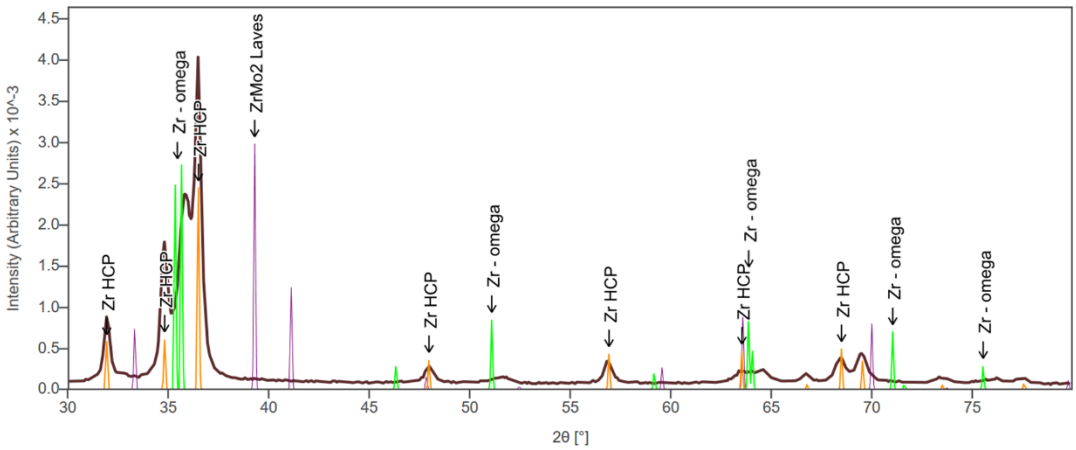


Figure 4-10: XRD data of the Zr2.5Mo sample after hot rolling with a simulated pattern of the ω-Zr phase indicated along with peak positions of α-Zr from [295] *and of $ZrMo_2$ from* [297].

The presence of the undesirable ω-Zr phase which is believed to contribute to a lack of ductility, leads to challenges when processing the material. This observation, along with the lack of the desirable $ZrMo_2$ Laves phase for alloy strengthening, led to the decision to discontinue more research on this alloy system because these preliminary results led to the conclusion that molybdenum is unlikely to be a promising binary alloying element for novel zirconium alloys. Despite this, molybdenum may be beneficial as a minor alloying element in lower concentrations as has previously been predicted [85].

4.2.5.4 Examination of rolled samples

Microscopy of the successfully rolled samples was used to examine their microstructures to understand the grain morphology and length scales that had been produced. A more thorough microstructural analysis of all the alloys presented in this section will follow in section 4.5, but preliminary observations are shown below.

OM employing polarised light was used to observe the grain structure of the pure zirconium and Zr2.5Al samples as shown in Figure 4-11. The grain structure visible in

these micrographs is approximately equiaxed and the grain diameter is of the order of 10 µm. The grain sizes appear smaller in the Zr2.5Al sample than in the pure zirconium sample, as would be expected with the addition of an alloying element that may create second phases to pin grain boundaries.

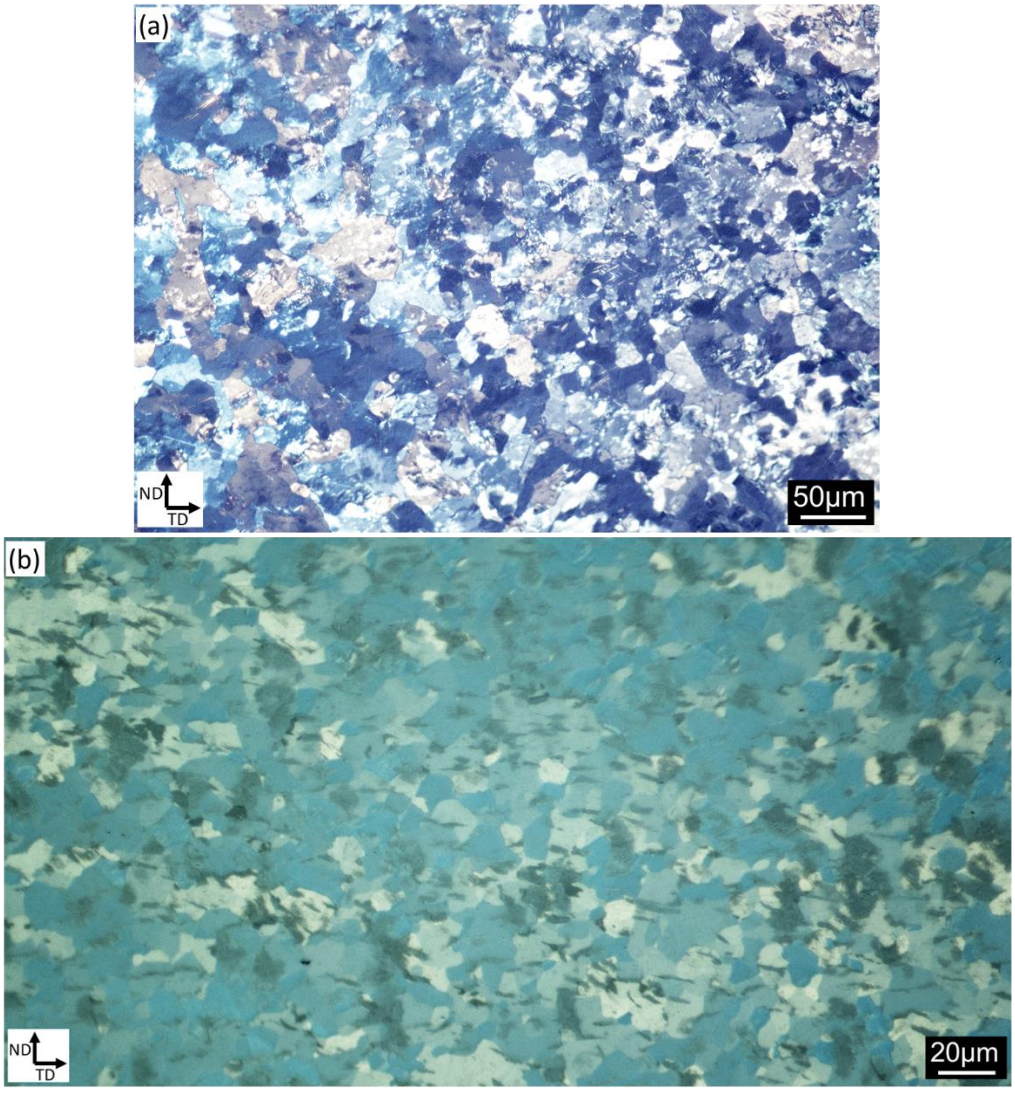


Figure 4-11: Optical micrograph with crossed polarising filters of the (a) pure zirconium and (b) Zr2.5Al alloy following hot rolling as described above. The arrows labelled ND and TD represent the normal and transverse rolling directions respectively.

XRD data, taken from the same surface of the alloys shown in Figure 4-11, indicates that the α-Zr phase dominates, as is the case for all alloys presented in this

section, and is expected from the processing temperature selected. A portion of this XRD data is shown in Figure 4-12, which also indicates a strong crystallographic texture in the α-Zr phase for both samples when compared with the predicted relative peak heights from literature. This indicates a strong alignment of the [001] crystallographic direction perpendicular to the rolling direction which agrees with the split basal texture following hot rolling previously observed in zirconium [162], [298]–[300]. Finally, a small peak just below a 2θ value of 33° is consistent with the presence of the ZrH phase [301]. This is the common γ-hydride phase and is widely observed in zirconium alloys since zirconium is a material known to be prone to hydrogen pick-up [2], [302]. This, along with some surface oxidation is thought to lead to the darker areas in the optical micrographs, especially visible in Figure 4-11(b) and Figure 4-13(a).

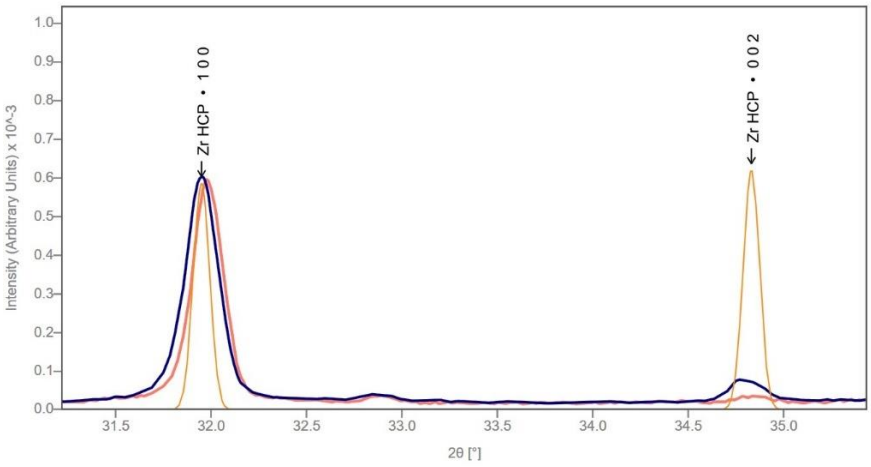


Figure 4-12: XRD data of the pure zirconium sample (shown in blue) and the Zr2.5Al sample (shown in red) after hot rolling, along with a literature spectrum of α-Zr from [295].

In contrast to the equiaxed grain structure observed in Figure 4-11, Figure 4-13(a) appears to show a much more elongated grain morphology in the Zr2.5V alloy sample following hot rolling. Upon further examination using SEM, shown in Figure 4-13(b), a more equiaxed grain structure appears to be visible on a finer length scale due to electron

channelling contrast from different crystallographic orientations. A thin lift-out sample of the same alloy was produced by Dr Junliang Liu by focussed ion beam (FIB) milling, shown in Figure 4-13(c), and an SE micrograph was taken which shows the grain structure of this alloy with increased contrast giving confidence in the identification of a roughly equiaxed grain structure with grain diameter of the order of 1 μm. This is noticeably finer than the pure zirconium and Zr2.5Al samples presented in Figure 4-11.

Reconciliation of the equiaxed structure observed in SEM and the larger elongated structure observed in OM is thought to be as a result of the phenomenon of macrotexture which is common in titanium alloy processing [303], [304] and results from the orientation relationship of the α phase to the crystallographic orientation of the β phase region from which it forms.

The dark spots observed in the SE micrographs of Figure 4-13(b,c) may indicate precipitates, and this will be discussed further in section 4.5.3.

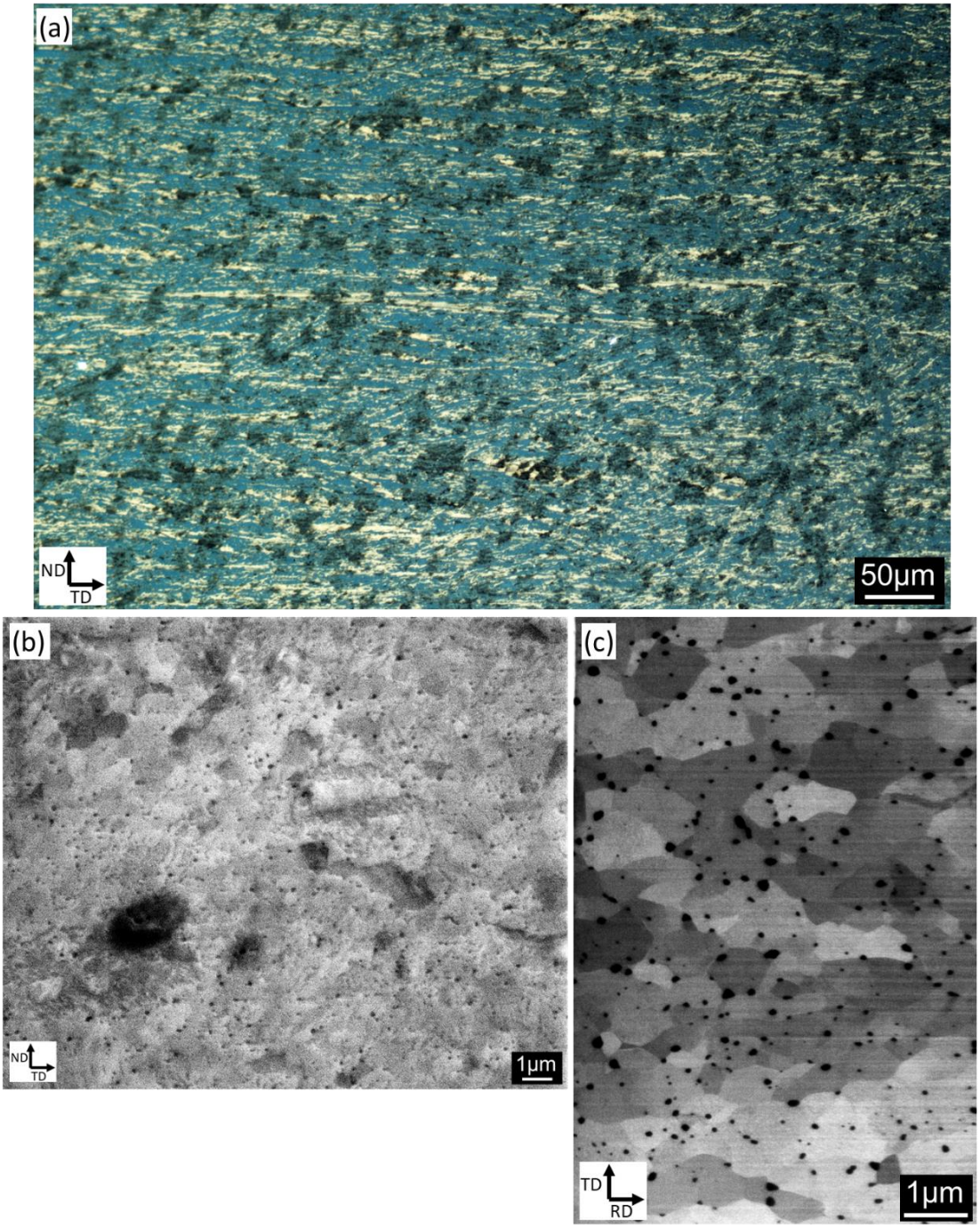


Figure 4-13: (a) Optical micrograph with crossed polarising filters, (b) SE micrograph, and (c) SE micrograph of a thin lift-out by Dr Junliang Liu of the Zr2.5V alloy following hot rolling. The arrows labelled ND, TD and RD represent the normal, transverse, and rolling directions, respectively, with respect to the rolling treatment.

As observed for the other alloys, fine and roughly equiaxed microstructures can also be observed for the Zr2.5Ta and Zr2.5Nb alloys in the polarised optical micrographs shown in Figure 4-14 and Figure 4-15(a), respectively. Figure 4-14 shows grain sizes of around 5 μm in the Zr2.5Ta alloy following hot rolling, whilst it is more difficult to determine grain size for the Zr2.5Nb alloy in Figure 4-15(a) as it appears finer.

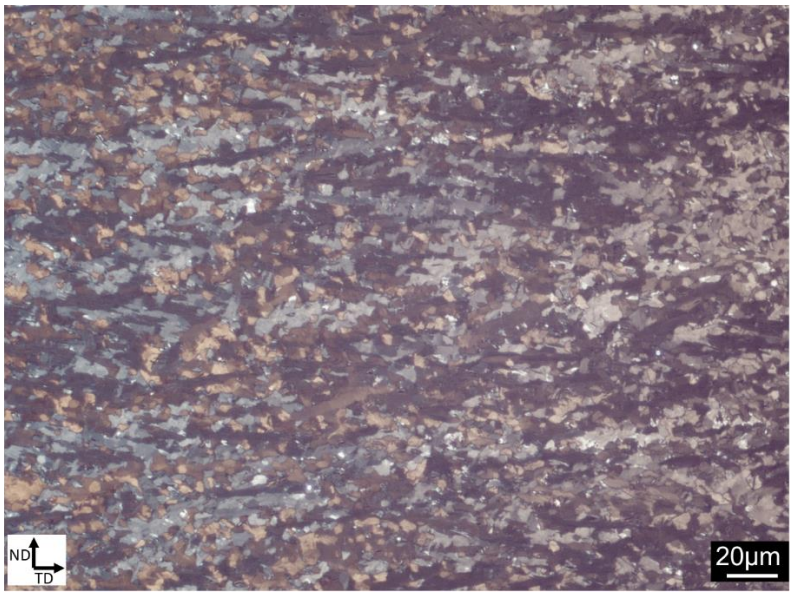


Figure 4-14: Optical micrograph with crossed polarising filters of the Zr2.5Ta alloy following hot rolling. The arrows labelled ND and TD represent the normal and transverse directions respectively with respect to the rolling treatment.

An SE micrograph of the Zr2.5Nb alloy is shown in Figure 4-15(b) which confirms the approximately equiaxed structure and reveals a length scale of approximately 2 μm. This is visible partially due to the surface relief of different grains caused by polishing but also by the presence of a lighter coloured second phase which is present at the boundaries between grains, as will be discussed in more detail later.

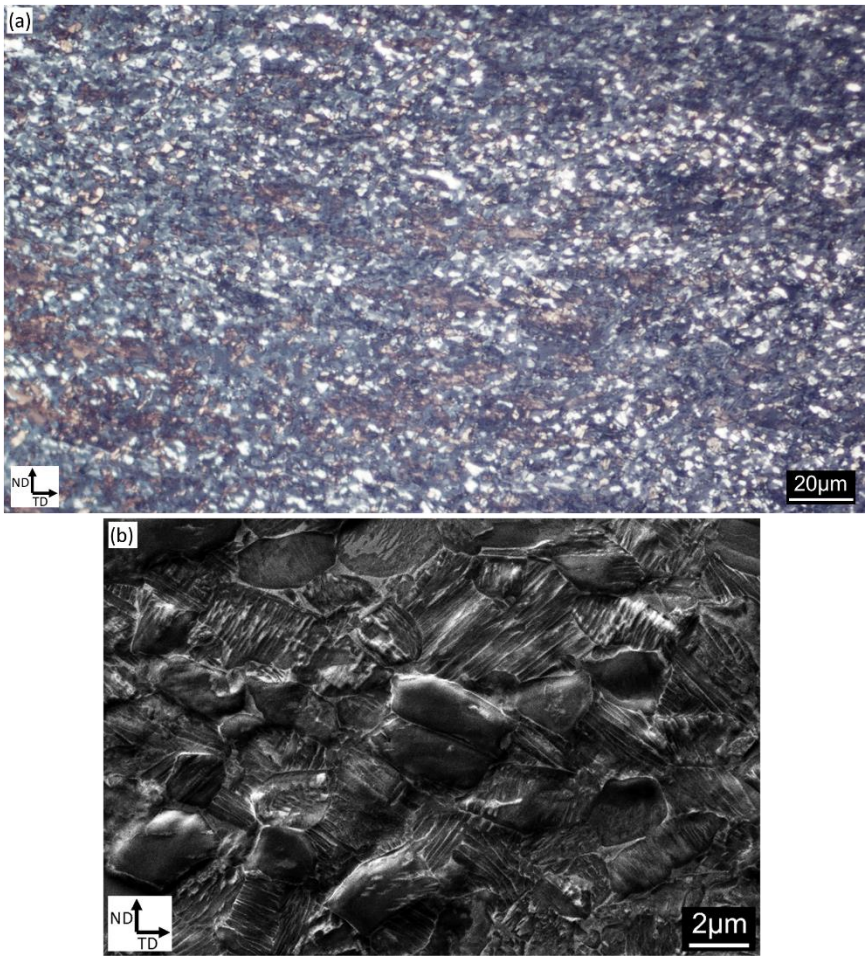


Figure 4-15: (a) Optical micrograph with crossed polarising filters and (b) SE micrograph of the Zr2.5Nb alloy following hot rolling. The arrows labelled ND and TD represent the normal and transverse directions respectively with respect to the rolling treatment.

4.2.6 Annealing

Having examined the microstructures produced in the alloys following hot rolling, it was deemed that the alloy microstructures had been sufficiently refined such that they appeared to resemble that of an engineering structural material as discussed in section 2.6.1. Following high temperature deformation, commercial zirconium alloys undergo a series of alternating stages of heat treatment and cold deformation stages before a final annealing step is performed, as discussed in section 2.6.1. Due to the suitable

microstructures already achieved after the hot rolling stage, it was decided that no further microstructural refinement was necessary by cold deformation and therefore the alloys were taken directly to a final annealing stage.

During rolling, the material undergoes significant deformation which leads to the presence of a high dislocation density within the microstructure. As a result, they should undergo an annealing treatment to reduce dislocation density and relieve internal stresses prior to application or testing in order that an artificially increased strength is not measured as a result of forest hardening. For commercial zirconium alloys in the fission industry, an elevated temperature which remains within the α-Zr phase region (most commonly around 580 °C) is chosen for annealing as discussed in section 2.6.1. Therefore, a temperature of 700 °C was chosen as it is suitable for all the alloys in this study as an elevated temperature below the β-Zr transition temperature as demonstrated by the phase diagrams in section 2.4.2. This is with the exception of the Zr-Nb alloys included for comparison, for which 700 °C would be within the β-Zr phase region. A temperature of 580 °C was used for these to mirror reported commercial processes for Zr-Nb alloys [253], [254], [258]–[261].

The annealing time period for zirconium alloys varies widely commercially, perhaps due to the varying sizes of component produced and the need for the heat to equilibrate throughout. A time of 2 hours was deemed suitable for this study due to the relatively small volume of material produced.

The propensity of zirconium to oxidise heavily in an air environment at elevated temperatures for extended periods necessitated the employment of an inert argon atmosphere for annealing. This was achieved by making use of a box furnace which was

contained within an argon-atmosphere glovebox with an oxygen level maintained below 1 ppm. The samples were introduced to a pre-heated furnace at the stated temperature and removed after the required time period and air cooled to ambient temperature whilst suspended between two ceramic blocks to ensure a homogenous cooling rate for the whole sample.

4.3 Processing stages summary and microstructure predictions

The alloy compositions cast and thermo-mechanically processed for investigation are summarised below including brief details. Full details are contained in the preceding sections (4.2.2 – 4.2.6).

Pure Zr, Zr1Al, Zr2.5Al, Zr5Al, Zr1V and Zr2.5V (with solute concentration indicated in atomic%) were cast, homogenised at 1200 °C and quenched. They were then hot rolled with a soak temperature of 700 °C and annealed at 700 °C for 2 hours. The compositions of these alloys at the 700 °C temperature of soak for rolling treatment and annealing is marked on the respective phase diagrams in Figure 4-16 and Figure 4-17. The 1200 °C homogenisation temperature is also marked on the diagrams.

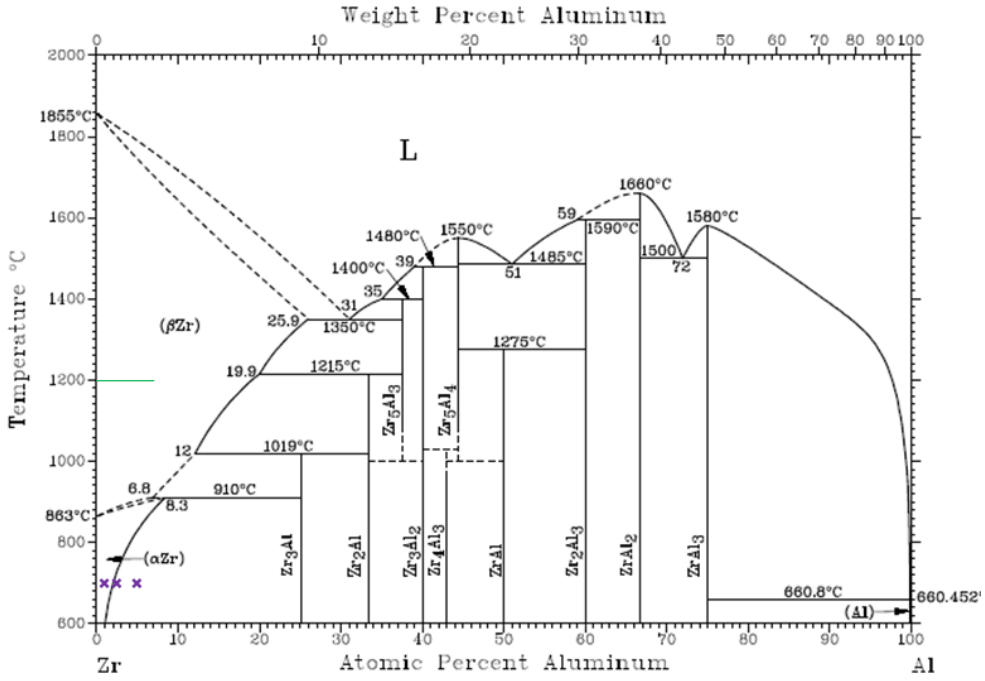


Figure 4-16: Zirconium-Aluminium phase diagram [198], [207] *with alloy compositions and thermo-mechanical treatment temperatures marked by purple crosses, and the homogenisation temperature marked by a green line*

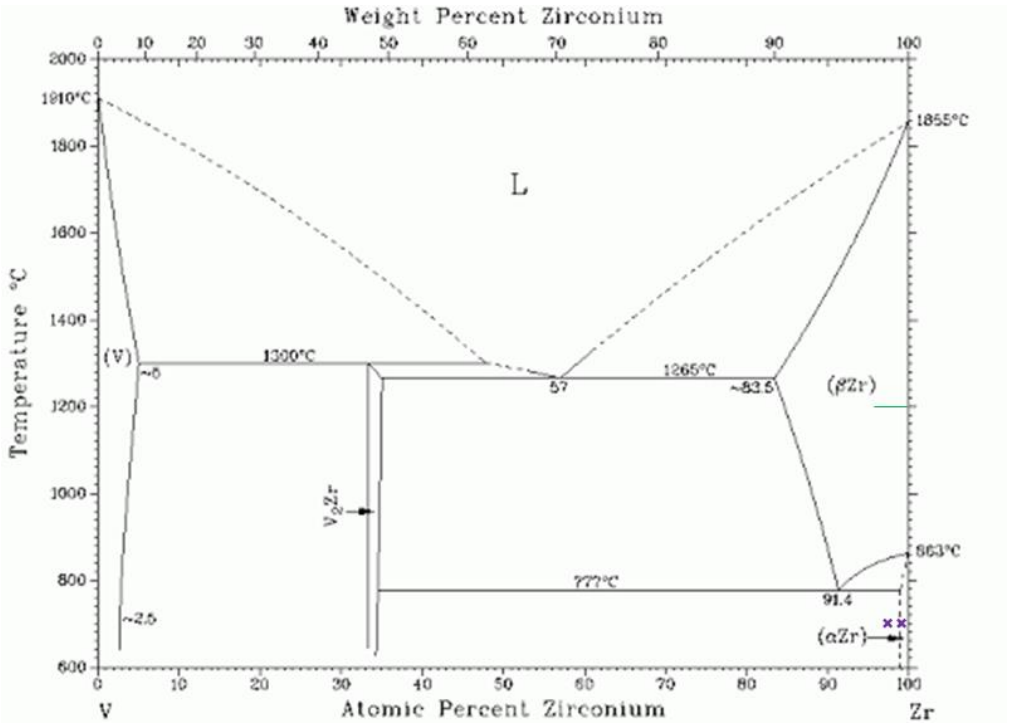


Figure 4-17: Zirconium-Vanadium phase diagram [212] *with alloy compositions and thermo-mechanical treatment temperatures marked by purple crosses, and the homogenisation temperature marked by a green line*

From examination of the phase diagrams in Figure 4-16 and Figure 4-17, it is expected that the alloys will be thermo-mechanically processed outside of the range of solubility of the solute in the α-Zr phase, with the exception of the Zr1Al alloy. Therefore, in the Zr1Al alloy, a single-phase microstructure may be expected, with substitutional solid solution strengthening mechanisms exhibited. Alternatively, the precipitation of second phase particles may be expected for the Zr1V, Zr2.5V, Zr2.5Al and Zr5Al alloys as they are processed in the α-Zr+ZrV_2 phase region in the case of the Zr-V alloys and the α-Zr+Zr_3Al phase region in the case of the Zr-Al alloys. The microstructure of these alloys may be expected to consist of micron-scale intergranular and intragranular intermetallic precipitates, surrounded by an α-Zr matrix phase.

Zr1Ta and Zr2.5Ta were cast, homogenised at 1200 °C and quenched. They were then hot rolled with a soak temperature of 870 °C and annealed at 700 °C for 2 hours. The compositions of these alloys at the 870 °C temperature of soak for rolling treatment (purple) and the 700 °C temperature of annealing (green) is marked on the phase diagram shown in Figure 4-18. The 1200 °C homogenisation temperature is also marked on the diagram.

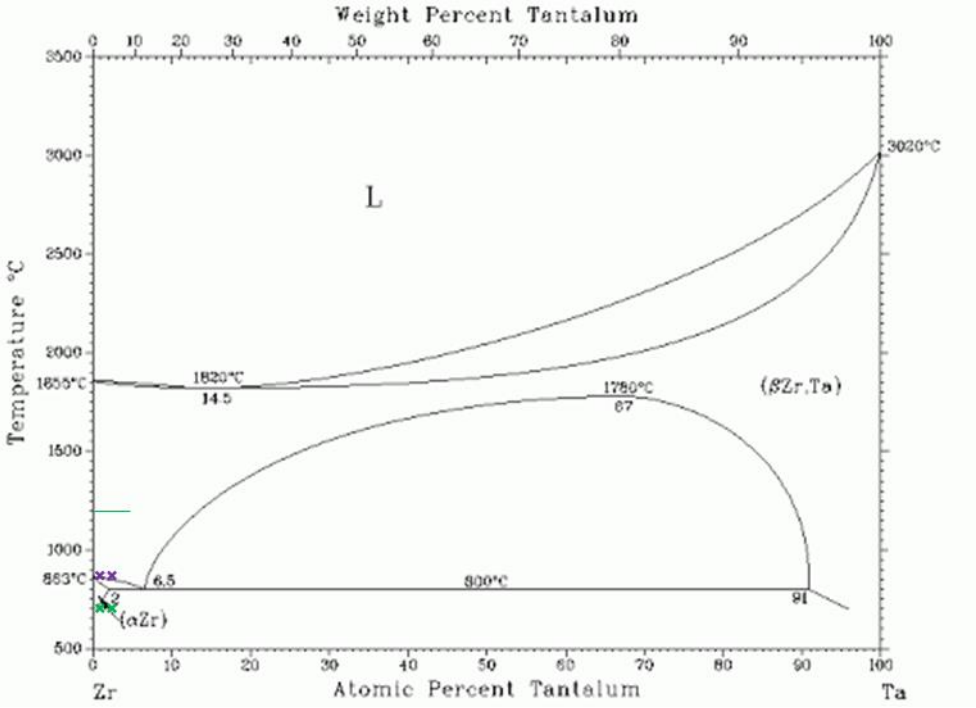


Figure 4-18: Zirconium-Tantalum phase diagram [209] *with alloy compositions and thermo-mechanical treatment temperatures marked by purple and green crosses, and the homogenisation temperature marked by a green line*

Zr1Nb and Zr2.5Nb were cast, homogenised at 1200 °C and quenched. They were then hot rolled with a soak temperature of 840 °C and annealed at 580 °C for 2 hours. The compositions of these alloys at the 840 °C temperature of soak for rolling treatment (purple) and the 580 °C temperature of annealing (green) is marked on the phase diagram shown in Figure 4-19. The 1200 °C homogenisation temperature is also marked on the diagram.

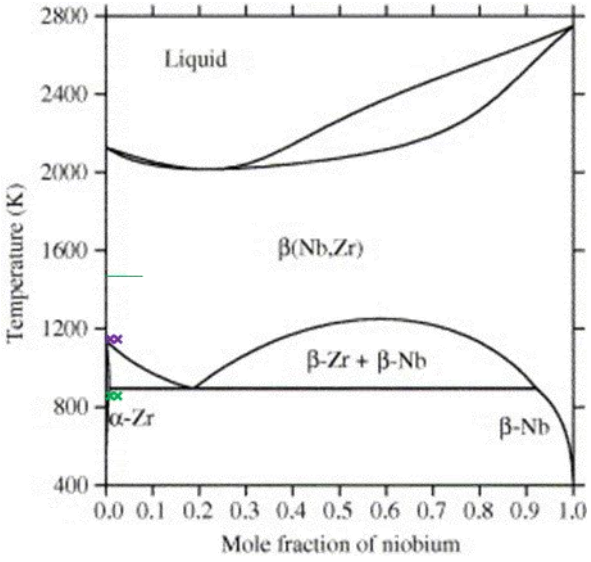


Figure 4-19: Zirconium-Niobium phase diagram [182] *" with alloy compositions and thermo-mechanical treatment temperatures marked by purple and green crosses, and the homogenisation temperature marked by a green line*

From examination of the phase diagrams in Figure 4-18 and Figure 4-19, a similar microstructure may be expected in both the Zr-Ta and Zr-Nb alloys. Although the rolling soak temperature marked on the diagrams is slightly above the α-Zr + β-Zr→β-Zr transformation indicated, the combination of the effects of increased transformation temperature due to oxygen contents (as discussed in section 4.2.5.1) and specimen cooling as it is removed from the furnace for rolling means that it is expected that the alloys were rolled at a temperature in the α+β phase region.

Processing at this temperature is expected to cause a bimodal microstructure by the formation of grains of both α-Zr and β-Zr phase at the hot rolling temperature, where the solute element has a significant solubility in the β phase but not in the α phase. The lower solubility of the solute element in the α phase may be expected to cause segregation of the solute to the grain boundaries, leading to the formation of a second phase (β) in these regions. As the alloy cools from its processing temperature and in to the α-Zr region

of the phase diagram, the β-Zr grains may be expected to undergo a phase transformation to the α phase in which the solubility of the dissolved solute is greatly reduced. Therefore, partitioning of the excess solute may occur to form second phase β precipitates in the prior-β grains.

Following thermo-mechanical processing, samples of all the alloys listed above (with the exception of the Zr-Nb alloys) were further isothermally aged at 700 °C for periods of both 200 and 1343 hours. Section 5 contains further discussion of the methodology and results of this ageing treatment.

4.4 Examination of the annealed alloys – aims

Following the completion of alloy processing, microstructural characterisation and evaluation of mechanical properties was carried out. Various characterisation techniques were employed to determine the microstructural effects that the alloying elements have had on the zirconium and the strengthening mechanisms which they may give rise to.

In order to fulfil the engineering requirements, the key mechanical properties of strength, stiffness, and ductility should be evaluated for the alloys to determine their potential structural effectiveness at both room temperature and up to the projected operating temperature. The mechanical properties of zirconium alloys at temperatures above 400 °C is identified as a knowledge gap [84]. In addition, an indication of the resistance or susceptibility to creep deformation would be valuable [84] as it is thought that this may be a life-limiting factor for the deployment of zirconium alloys in-service [80].

The microstructural stability with respect to the elevated temperature environment, and the compatibility of the material with the corrosive environment of the breeder/coolant fluid used in the design are also important considerations when assessing the applicability of a material. These are examined and discussed in more detail later in this study (sections 5 and 6 respectively).

4.5 Microstructural analysis results

4.5.1 Pure zirconium

Figure 4-20 shows the grain structure of the pure zirconium benchmarking material, which may be compared to the similar structure observed prior to annealing shown in Figure 4-11(a). The structure appears approximately equiaxed with a length scale of the order of 10 μm and no grains appear to have a dimension significantly larger than 50 μm. The line intersection method for determining grain size was used to give an approximate quantification of the grain size according to the methods detailed in [305], [306] with at least 4 different measurements taken and averaged, with error estimated by the standard deviation of the measurements. By this method, a grain size of 32.9 ±2.7 μm was measured for the microstructure of annealed pure zirconium shown in Figure 4-20.

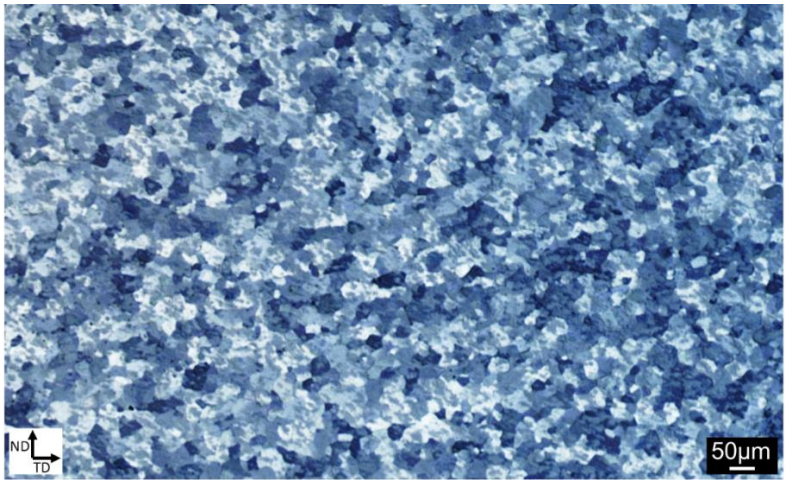


Figure 4-20: Optical micrograph with crossed polarising filters of the pure zirconium following annealing. The arrows labelled ND and TD represent the normal and transverse directions respectively with respect to the rolling treatment.

The microstructure is identified to consist of the HCP α-Zr phase this is the only phase identified in the XRD data shown in Figure 4-21, with the exception of an indication of the γ-ZrH phase as discussed previously in relation to Figure 4-12.

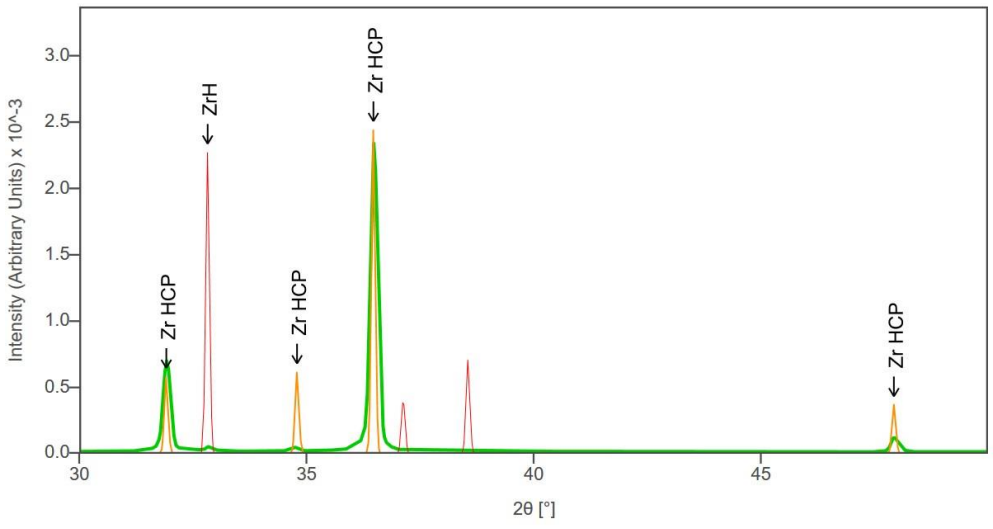


Figure 4-21: XRD data of the pure zirconium sample after annealing, along with a peak positions from literature of the α-Zr phase from [295] *and the γ-ZrH phase from* [301].

This microstructure is expected to be broadly similar for the zirconium alloys produced, with microstructural modifications due to the addition of secondary phases which may refine the microstructure. The results of microstructural analysis of the alloys are presented next.

4.5.2 Zirconium-aluminium

Optical microscopy of the Zr2.5Al alloy following annealing in Figure 4-22 reveals a similar morphology and length scale of grain structure as is observed for the alloy prior to annealing as shown in Figure 4-11(b).

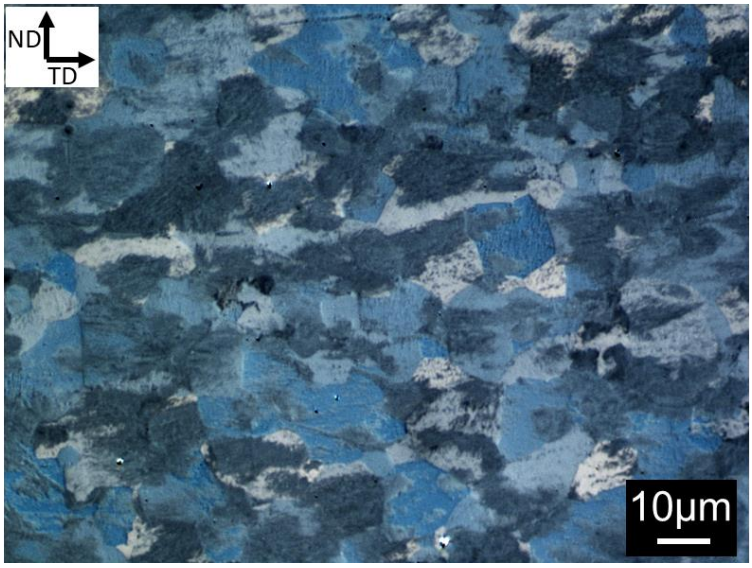


Figure 4-22: Optical micrograph with crossed polarising filters of the Zr2.5Al alloy following annealing. The arrows labelled ND and TD represent the normal and transverse directions respectively with respect to the rolling treatment.

Observation of this grain structure with optical microscopy at lower magnifications is challenging due to the dark patches on the sample surface which are thought to be caused by surface oxidation. This is also seen in the SE micrographs shown in Figure 4-23(a,b) where dark patches are visible which do not appear to be part of the

underlying microstructure. The oxidised nature of these areas is confirmed by the EDX analysis shown in Figure 4-23(c) where a significantly increased oxygen concentration is correlated with the dark areas on the surface.

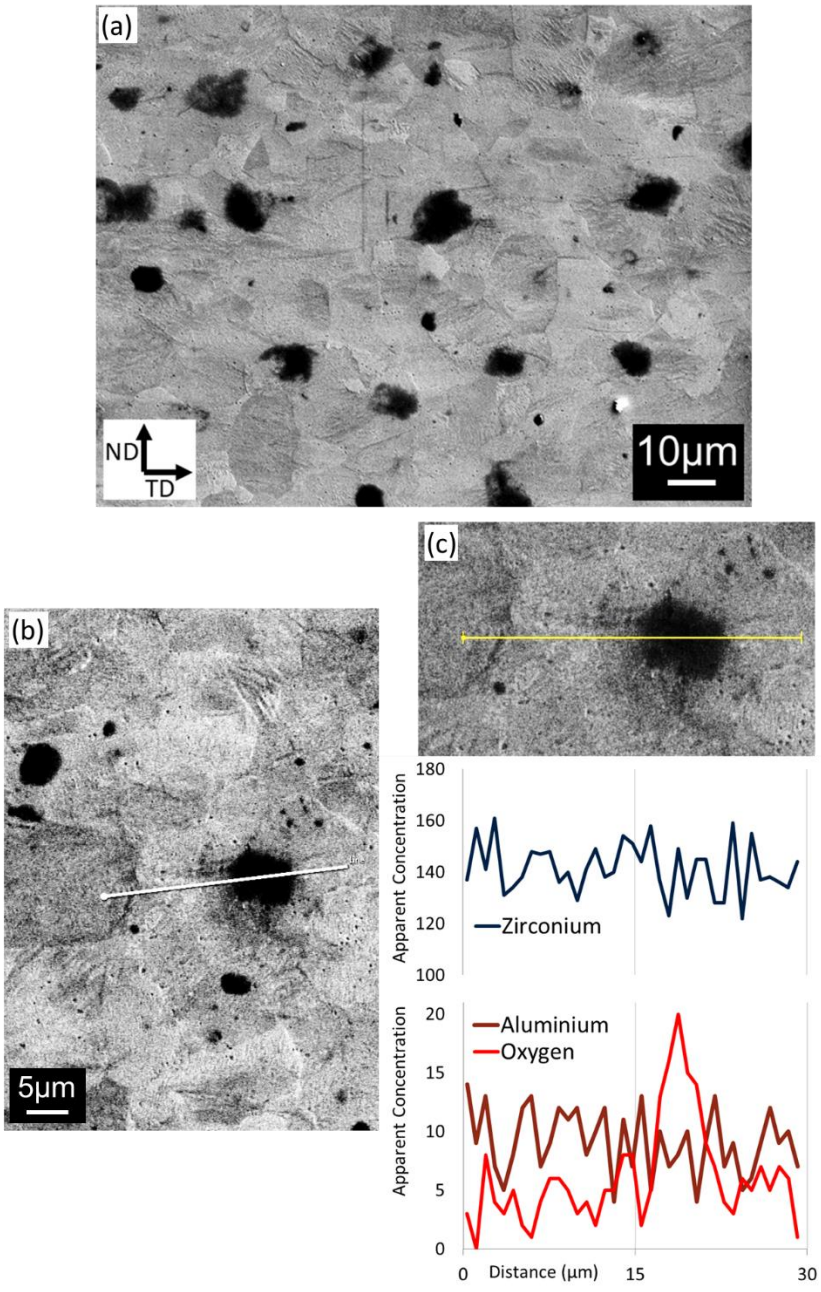


Figure 4-23: (a,b) SE micrographs of the annealed Zr2.5Al sample and (c) EDX linescan analysis across one of the black patches seen in (b) with indications of apparent concentration variations of the indicated elements.

BSE micrographs shown in Figure 4-24 confirm the grain structure observed in Figure 4-22 due to electron channelling contrast in grains of different orientations. Also visible in these micrographs is the presence of small black dots which are identified as precipitates within the microstructure of the alloy.

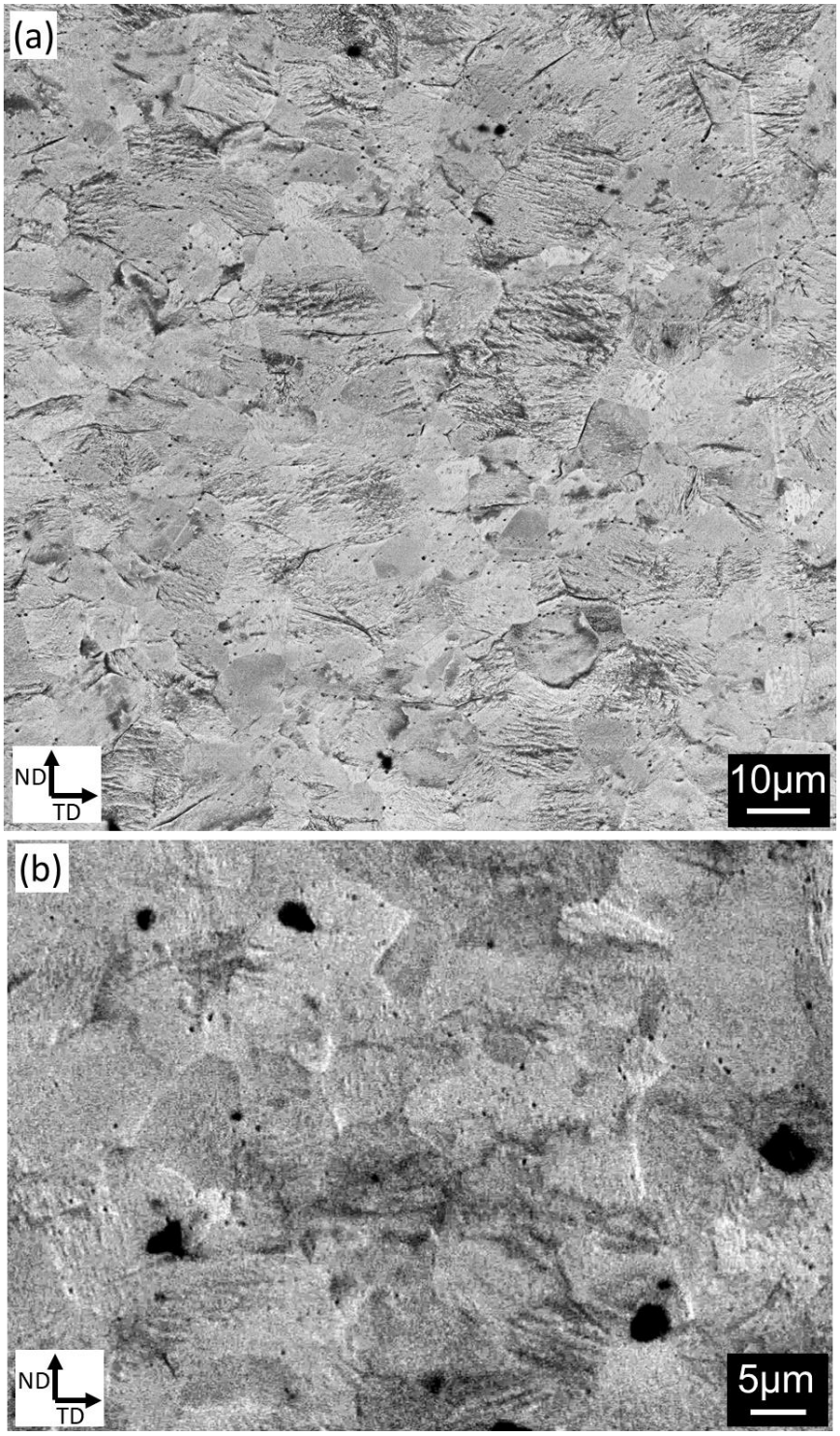


Figure 4-24: BSE micrographs of the annealed Zr2.5Al alloy with dark spots indicating the presence of precipitates within the microstructure. The arrows labelled ND and TD represent the normal and transverse directions respectively with respect to the rolling treatment.

EDX analysis of the dark spots identified as precipitates in the microstructure of the Zr2.5Al alloy is shown in Figure 4-26, with an enrichment in aluminium associated with the precipitates. XRD data in Figure 4-25 indicates the presence of the Zr_3Al intermetallic phase with the $L1_2$ crystal structure in the material, as may be expected from the phase diagram shown in Figure 2-13. Given the presence of this phase and the aluminium enrichment identified with EDX, the dark spots are identified as precipitates of Zr_3Al with a size of a few hundred nanometres.

Also identified in the XRD analysis shown in Figure 4-25 is the γ-ZrH phase as has been identified and discussed previously in relation to Figure 4-12. Needle-shaped dark regions visible in Figure 4-26(a,b) do not show elemental segregation with EDX analysis and therefore it is thought that these may be identified as the γ-ZrH phase within the microstructure as low atomic number elements such as hydrogen cannot be detected by EDX.

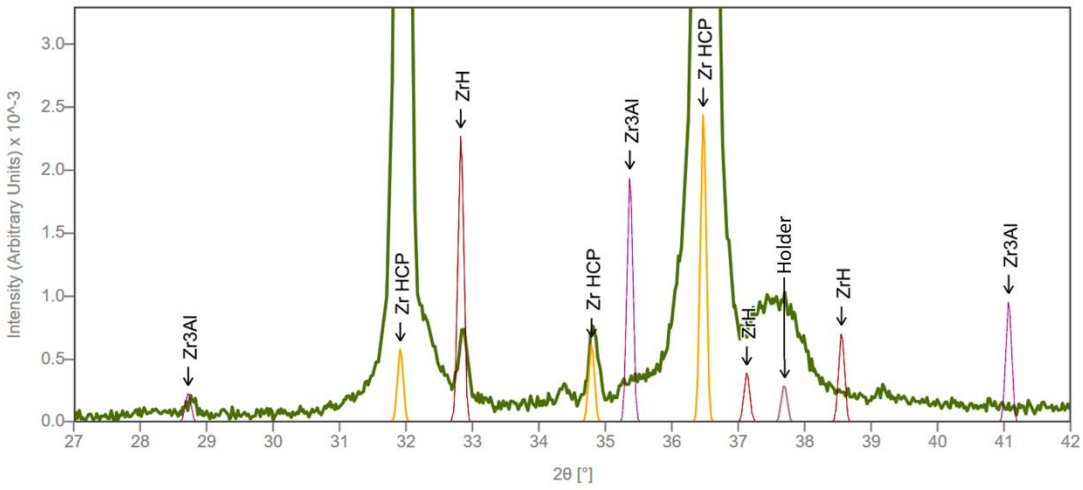


Figure 4-25: XRD data of the Zr2.5Al sample after annealing, along with a peak positions from literature of the α-Zr phase from [295]*, the $L1_2$ structure Zr_3Al phase from* [307]*,and the γ-ZrH phase from* [301].

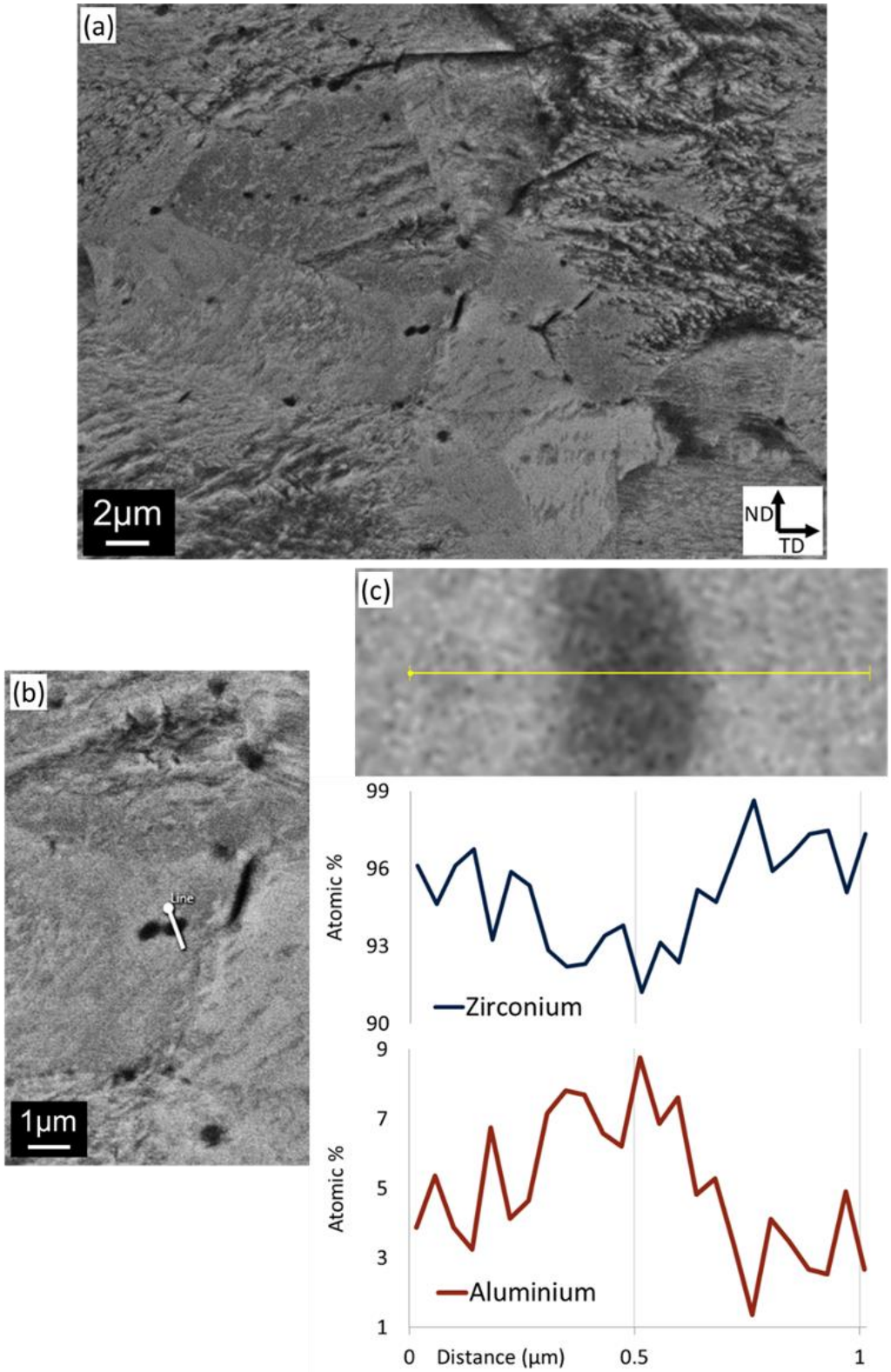


Figure 4-26: (a,b) BSE micrographs of the annealed Zr2.5Al sample and (c) EDX linescan analysis across one of the dark spots seen in (b) with indications of apparent concentration variations of the indicated elements.

EBSD data from the Zr2.5Al alloy was obtained and processed as described in 3.5.2 and is shown in Figure 4-27. The diffraction pattern quality was not sufficient for successful indexing of all grains, potentially due to residual strain within the material. This confirms grain size estimations made by observation of the other result in this section with a calculated median grain diameter of 6.5 μm using the method described in section 3.5.2 with a misorientation threshold of 3° and a minimum pixel threshold of 8. In addition, Kearns factors for this sample were calculated from the data shown in Figure 4-27 as f_{ND}=0.73, f_{TD}=0.12, f_{RD}=0.15.

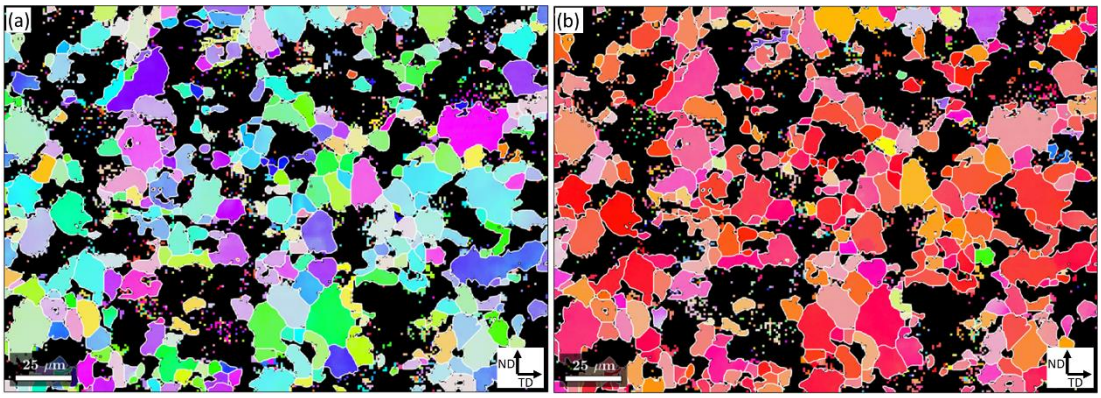


Figure 4-27: EBSD data of the annealed Zr2.5Al sample showing the crystallographic alignment of measured pixels with (a) the rolling direction and (b) the normal direction with reference to the colour scale shown in Figure 3-7 with calculated grain boundaries overlaid in white.

Alloy strengthening by nano-scale precipitates has previously been observed in Ti-Al alloys [308], [309] and it is thought that this may also occur in Zr-Al alloys due to the similarities between zirconium and titanium. However, it is known that these two metals do not interact with aluminium in exactly the same way due to the differences in their respective binary phase diagrams [198], [310]. Visual and statistical analysis of an Atom Probe Tomography (APT) dataset from the annealed Zr2.5Al sample produced by Kieran Rivers, shown in Figure 4-28, does not indicate the presence of nano-scale precipitates in this alloy following annealing.

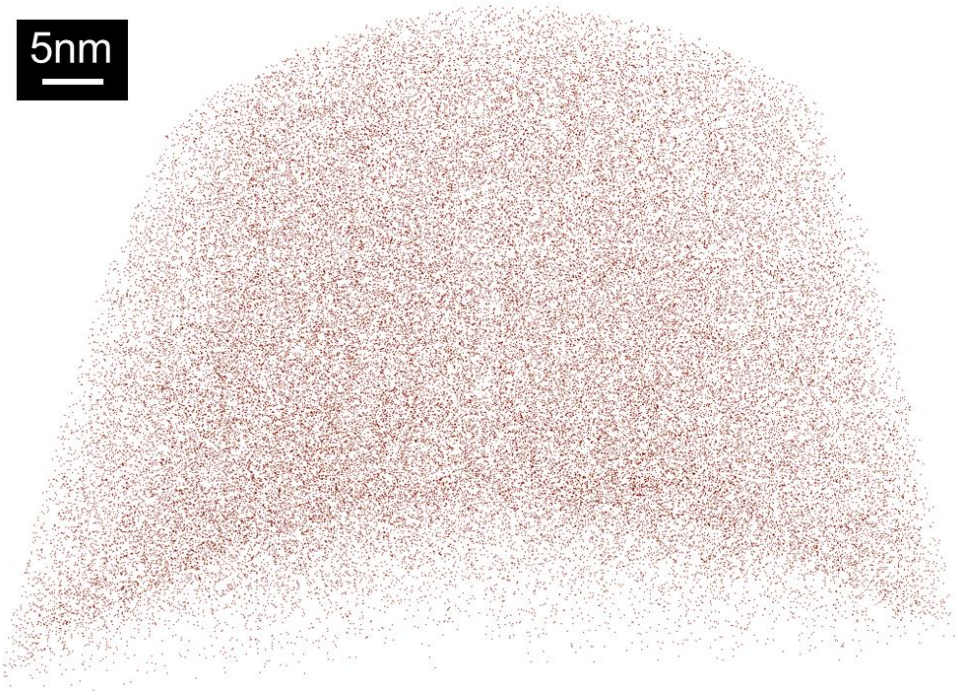


Figure 4-28: APT analysis of data taken by Kieran Rivers from a sample of annealed Zr2.5Al showing Al ions as red dots indicating a homogenous distribution of aluminium within the sample volume.

4.5.3 Zirconium-vanadium

As was shown for the Zr2.5V alloy prior to annealing in Figure 4-13, electron microscopy is necessary to observe the fine grain structure of this alloy. The grain structure following annealing can be seen in the SE micrographs shown in Figure 4-29, and it is much more obvious in the micrograph of the FIB lift-out taken by Dr Junliang Liu in Figure 4-29(b). This reveals a roughly equiaxed grain structure and the scale of the grain diameters is of the order of 1 μm as was the case prior to annealing. Black circles are also visible within the microstructure which appear to be precipitates.

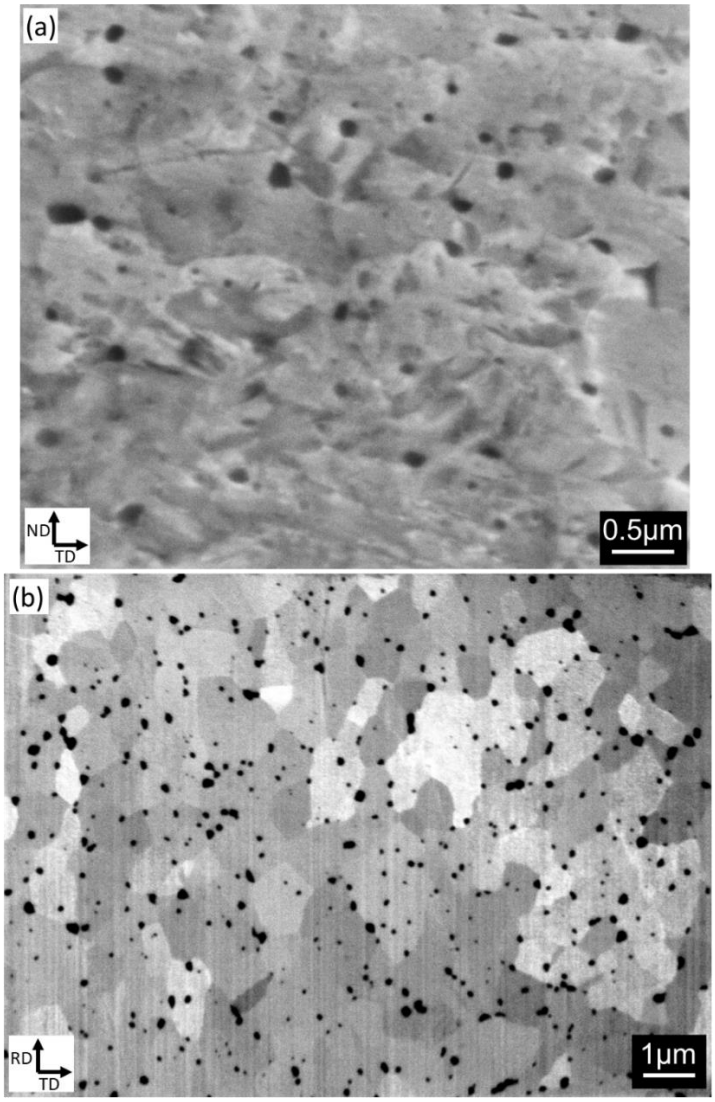


Figure 4-29: (a) surface SE micrograph and (b) SE micrograph of a thin lift-out by Dr Junliang Liu of the Zr2.5V alloy following annealing. The arrows labelled ND, TD and RD represent the normal, transverse, and rolling directions respectively with respect to the rolling treatment.

EDX analysis in the SEM was unable to conclusively resolve the chemical variation associated with these precipitates in comparison with the matrix. However, EDX in the TEM by Dr Junliang Liu shown in Figure 4-30 was more successful in indicating a depletion of zirconium and an enrichment of vanadium, and in some cases iron, associated with the precipitates. Iron is a known impurity within the alloy as shown in Table 4-1, and strong segregation of this element to precipitates is expected due to its low solubility in zirconium as demonstrated by the phase diagram in Figure 2-15.

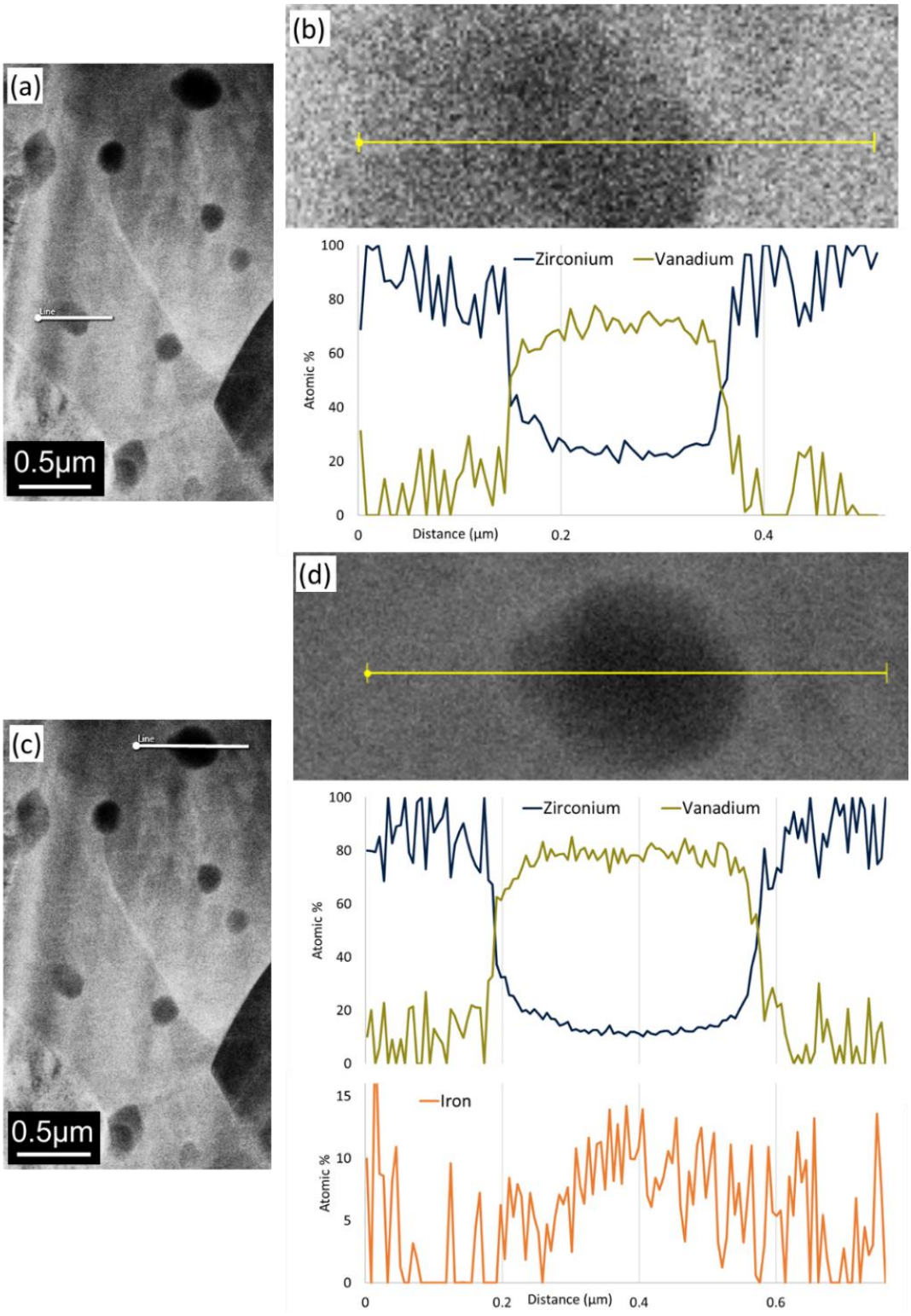


Figure 4-30: (a,c) TEM micrographs by Dr Junliang Liu showing the Zr2.5V alloy and the region in this image from which EDX linescan data was taken across an area of darker contrast. EDX linescan data is shown in (b,d) with graphs displaying the relative concentrations of the three elements indicated and how these vary along the length of the line.

X-ray diffraction data was collected from the same surface of the sample as was imaged in Figure 4-29(a) to determine the phases present in the material, and is shown in Figure 4-31. The peaks in this data indicate good agreement with the α-Zr and ZrV_2 Laves phases. There is also a peak attributed to the γ-ZrH phase and the presence of this phase within the alloys has been discussed previously in relation to Figure 4-12. The combination of this XRD data and the EDX analysis shown in Figure 4-30 provides confidence in the identification of ZrV_2 Laves phase precipitates in the microstructure of Zr2.5V.

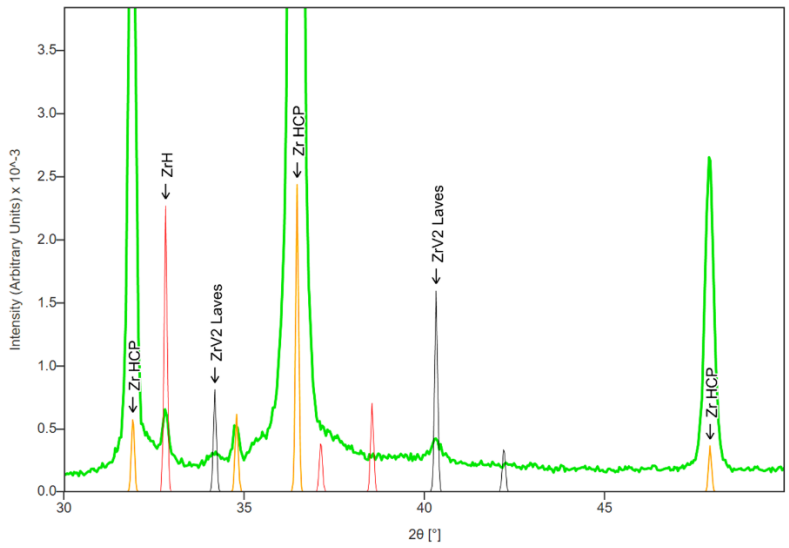


Figure 4-31: XRD data of the Zr2.5V sample after annealing, along with a peak positions from literature of the α-Zr phase from [295]*, the Laves ZrV_2 phase from* [311]*,and the γ-ZrH phase from* [301].

EBSD data was obtained from the sample as shown in Figure 4-32. This confirms grain size estimations made by observation of Figure 4-29, with a calculated median grain diameter of 1.5 µm using the method described in section 3.5.2 with a misorientation threshold of 0.8° and a minimum pixel threshold of 8. In addition, Kearns factors for this

sample were calculated from the data shown in Figure 4-32 as f_{ND}=0.61, f_{TD}=0.24, f_{RD}=0.15.

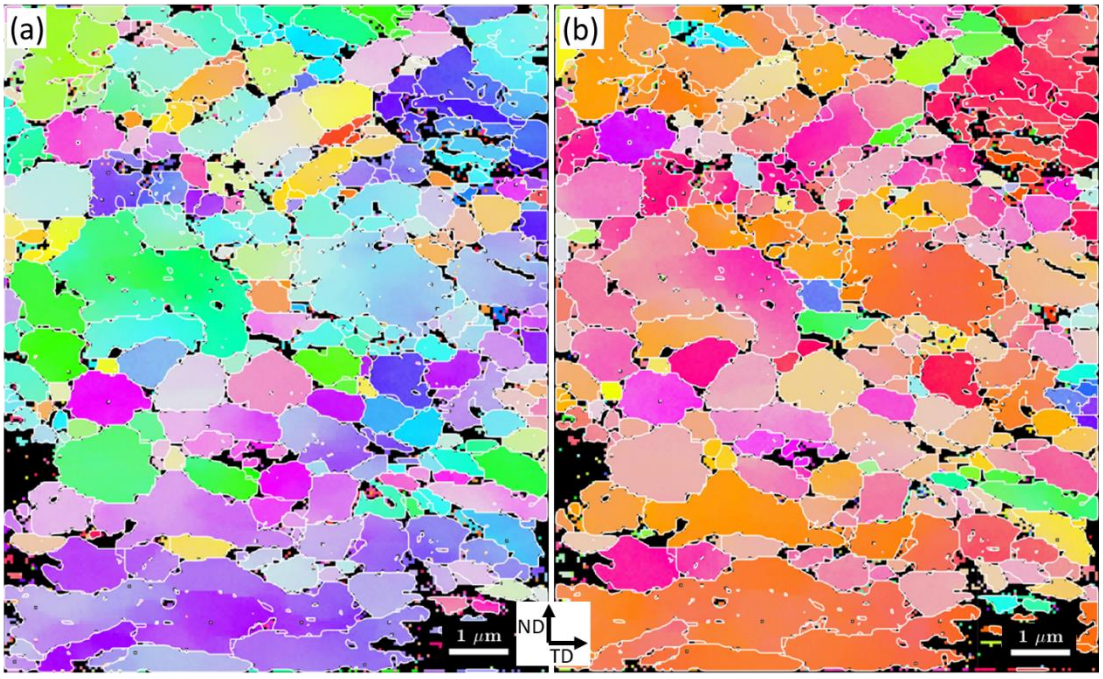


Figure 4-32: EBSD data of the annealed Zr2.5V sample showing the crystallographic alignment of measured pixels with (a) the rolling direction and (b) the normal direction with reference to the colour scale shown in Figure 3-7 with calculated gran boundaries overlaid in white.

4.5.4 Zirconium-tantalum

The microstructure of Zr2.5Ta prior to annealing as shown in Figure 4-14 appears relatively unchanged following annealing, as shown in Figure 4-33 where a microstructural length scale of the grain size is shown to be around 5 μm. The BSE micrograph in Figure 4-33(b) reveals a bimodal microstructure where some grains are dark with a lighter phase decorating the grain boundary whilst other grains contain a lighter phase both decorating the grain boundary and within the grain.

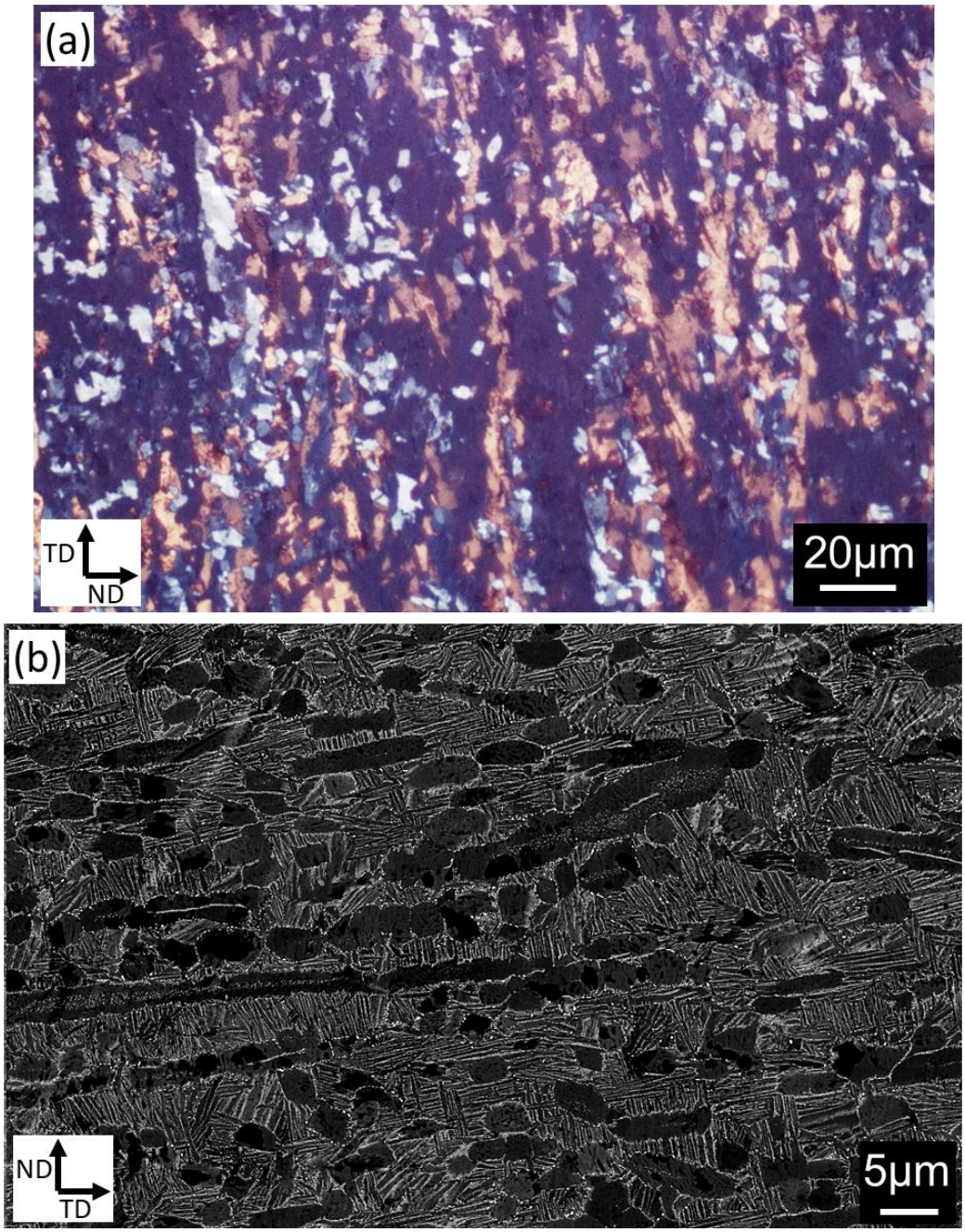


Figure 4-33: (a) Optical micrograph with crossed polarising filters and (b)BSE micrograph of the Zr2.5Ta alloy following annealing. The arrows labelled ND and TD represent the normal and transverse directions respectively with respect to the rolling treatment.

Further analysis of the microstructure using the BSE micrographs in Figure 4-34 reveals that the second phase appears as discrete precipitates both when they are along grain boundaries and within grains where they are aligned as bands.

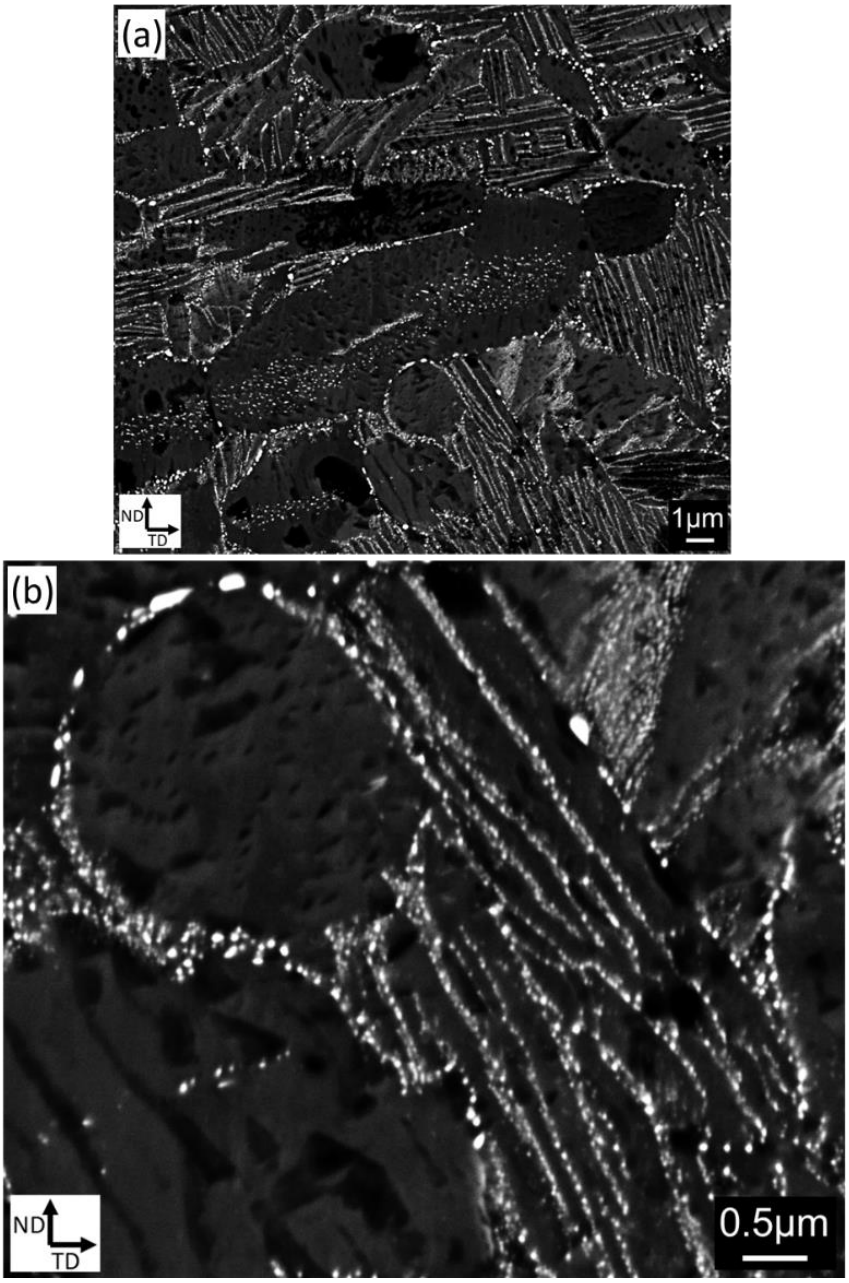


Figure 4-34: BSE micrographs of the Zr2.5Ta alloy following annealing. The arrows labelled ND and TD represent the normal and transverse directions respectively with respect to the rolling treatment.

As would be expected from the lighter contrast in the BSE images, the chemical analysis shown in Figure 4-35 indicates an enrichment of tantalum within the precipitates identified in the microstructure.

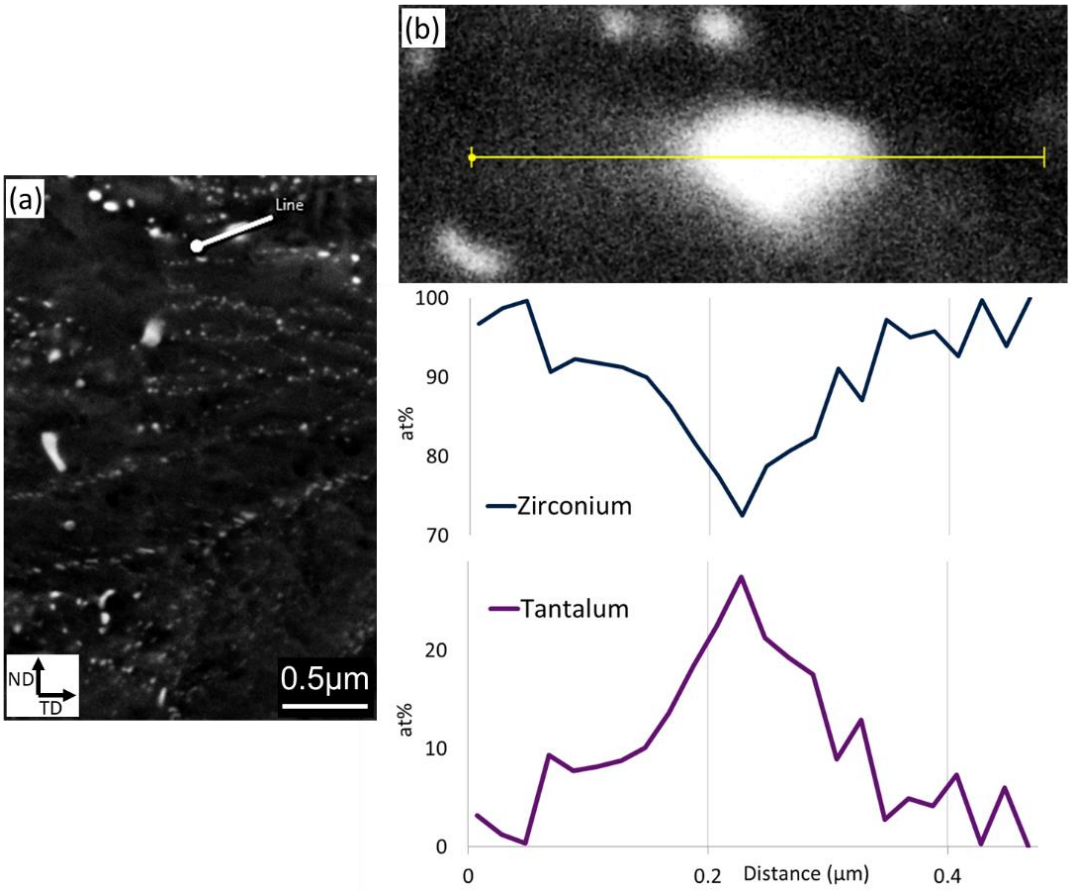


Figure 4-35: (a) BSE micrograph of the annealed Zr2.5Ta sample and (b) EDX linescan analysis across one of the light areas seen in (a) with indications of apparent concentration variations of zirconium and tantalum.

EDX analysis in Figure 4-35(b) indicates a maximum of less than 30 at% concentration of tantalum in the precipitate, however this measurement is likely to be affected by the surrounding zirconium matrix due to the small size of the precipitate. In contrast, chemical analysis of a precipitate identified in an atom probe tip which was measured by Wenyu Zhang indicates a concentration of up to 80 at% tantalum in the precipitate as shown in Figure 4-36. This figure also indicates a segregation of iron which appears to be located at the interface between the matrix and the precipitate.

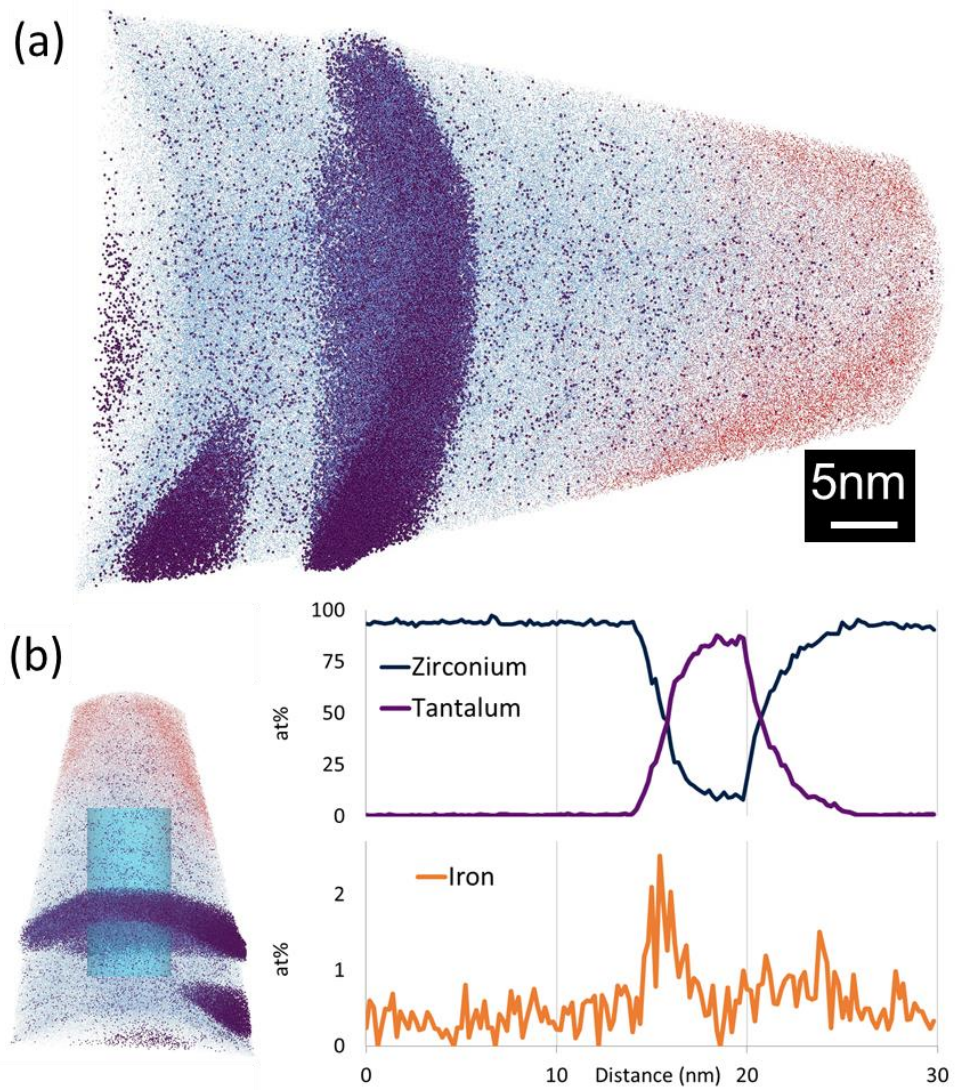


Figure 4-36: Analysis of APT data by Wenyu Zhang of a sample of annealed Zr2.5Ta including a precipitate with red points indicating ZrO ions, blue indicating Zr ions, and purple indicating Ta ions. Chemical analysis is shown in (b) from top to bottom of the cylindrical region indicated, showing the segregation of species associated with the precipitate.

XRD allowed for further analysis of the microstructure, revealing a predominance of the α-Zr phase with a weak indication of the γ-ZrH phase as has been observed for the previous alloys analysed in this section. In contrast to previous alloys, some indication of an oxide phase is identified which is thought to be caused by a surface oxide layer as no microstructural features have been identified which display an associated enrichment of oxygen. The diffraction peak at a 2θ value of approximately 38.5° is identified as

representative of the BCC structure β-Ta phase. This identification is consistent with the high atomic concentration levels measured in the precipitates by APT analysis in Figure 4-36, therefore suggesting that the tantalum-rich precipitates in the microstructure are β-Ta.

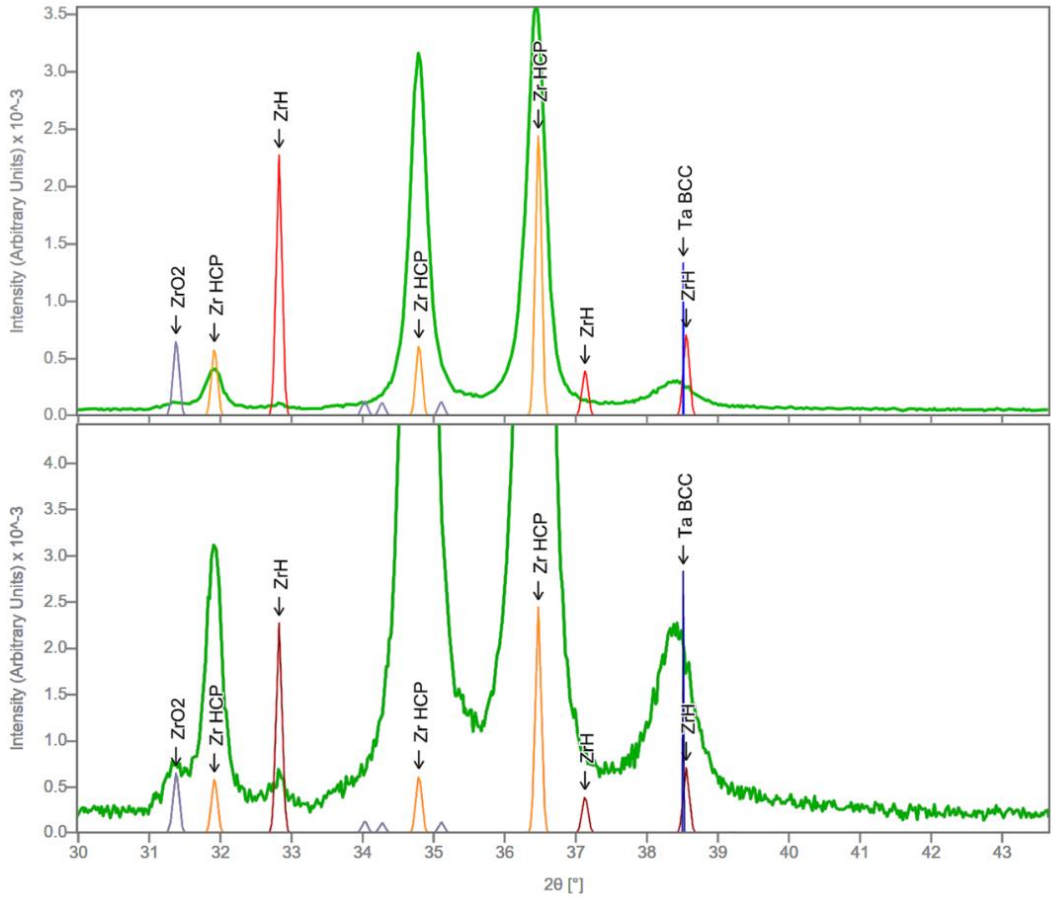


Figure 4-37: Two views of the same XRD data of the Zr2.5Ta sample after annealing, along with a peak positions from literature of the α-Zr phase from [295]*, the β-Ta BCC phase from* [312]*, the ZrO_2 zirconium oxide phase from* [313]*, and the γ-ZrH phase from* [301].

As for previous alloys, EBSD data from the Zr2.5Ta alloy, shown in Figure 4-38, was obtained and processed as described in section 3.5.2. This analysis yielded a calculated median grain diameter of 3.4 μm using the method described in section 3.5.2 with a misorientation threshold of 3° and a minimum pixel threshold of 8. Kearns factors for

this sample were calculated from the data shown in Figure 4-38 as f_{ND}=0.0.31, f_{TD}=0.19, f_{RD}=0.50. This result indicates a preferential alignment of the basal pole to the rolling direction, contrary to the expected alignment of the basal pole towards the transverse direction as has been observed for rolling processes in the α+β regime in titanium and Zr-Nb alloys [162].

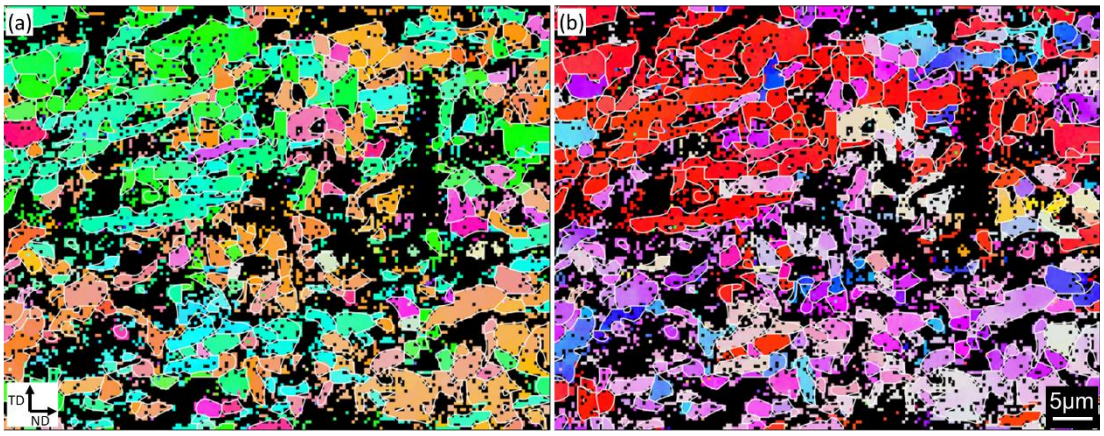


Figure 4-38: EBSD data of the annealed Zr2.5Ta sample showing the crystallographic alignment of measured pixels with (a) the normal direction and (b) the rolling direction with reference to the colour scale shown in Figure 3-7 with calculated grain boundaries overlaid in white.

4.5.5 Zirconium-niobium

Analysis of the microstructure of the Zr2.5Nb prior to annealing, shown in Figure 4-15, indicated a fine microstructure of grains with a secondary phase which appears lighter in electron imaging. These observations are repeated in Figure 4-39 with a microstructural length scale which appears unchanged compared with before the annealing treatment, as shown in Figure 4-15(b). A second phase lighter in colour is also observable in both Figure 4-39 and Figure 4-15(b), and appears to occur both along boundaries between grains and within some of the grains, appearing as a banded structure crossing the grains.

Also just visible in Figure 4-39 are small, light circular features which can be identified as remnants of polishing media used in the surface preparation, and therefore should be disregarded for evaluation of the microstructure.

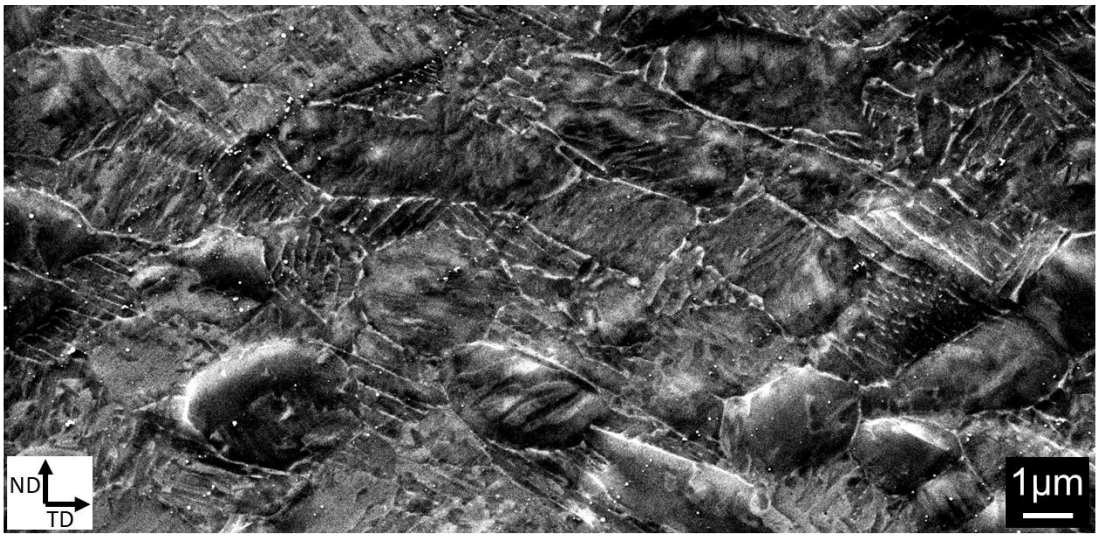


Figure 4-39: SE micrograph of the annealed Zr2.5Nb alloy with lighter regions indicating the presence of a second phase within the microstructure. The arrows labelled ND and TD represent the normal and transverse directions respectively with respect to the rolling treatment.

In order to identify the second phase observed in Figure 4-39, EDX analysis was used to identify chemical segregation which occurs in this phase. This is shown in Figure 4-40, and indicates an enrichment of niobium in the second phase which agrees with the contrast in the micrographs due to niobium's higher atomic number than zirconium.

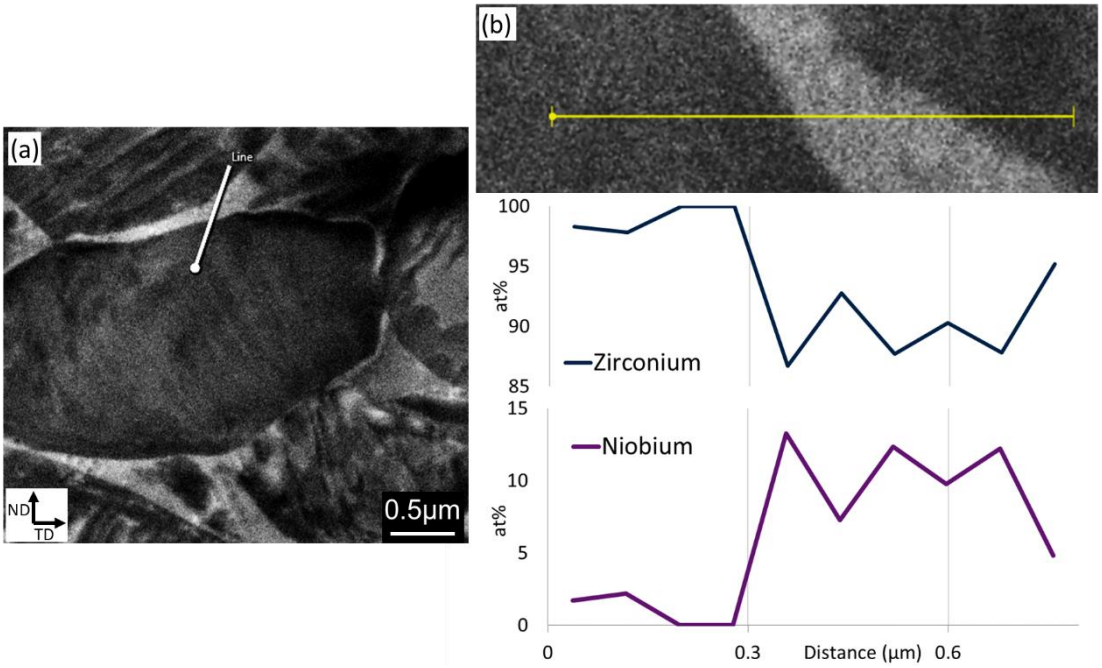


Figure 4-40: (a) SE micrograph of the annealed Zr2.5Nb sample and (b) EDX linescan analysis across one of the light regions seen in (a) with indications of apparent concentration variations of zirconium and niobium.

To confirm the crystal structure of the second phase, XRD data was taken from the surface of the sample shown in Figure 4-39, and shown in Figure 4-41. This analysis indicates a predominance of the α-Zr phase, with some γ-ZrH also present, as is the case for the alloys previously examined following annealing. A second phase with BCC structure containing both zirconium and niobium shows good agreement with the observed diffraction peak at a 2θ position of approximately 52°. This is consistent with the chemical analysis shown in Figure 4-40 and the expected phases from the binary phase diagram shown in Figure 2-11.

This microstructural analysis provides confidence in the identification of the microstructure as α-Zr grains with a β-ZrNb secondary phase with BCC structure occurring along grain boundaries and also within some, but not all, grains. Correlation of this microstructure with commercial alloys will be discussed in section 4.7.1

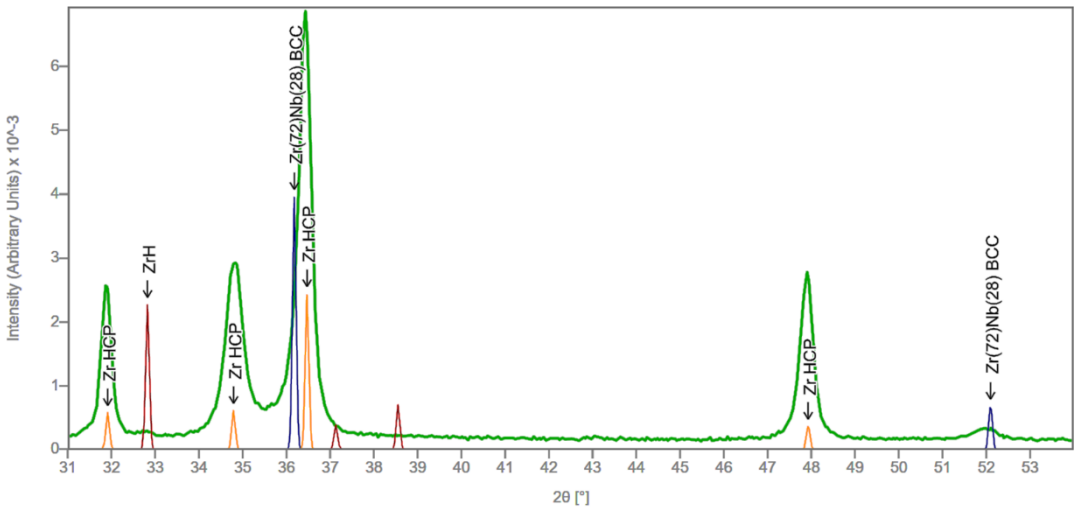


Figure 4-41: XRD data of the Zr2.5Nb sample after annealing, along with a peak positions from literature of the α-Zr phase from [295]*, the ZrNb BCC phase from* [314]*,and the γ-ZrH phase from* [301].

4.6 Mechanical property testing results

As well as examination of the microstructures to observe the behaviour of the alloying elements, it is important to determine the extent to which the alloying elements and the microstructures which they create enhance the mechanical properties of the material so that we can judge if it may be useful as structural material.

4.6.1 ETMT

The stress state induced in the sample during electro-thermal mechanical testing (ETMT) is relatively simple and well explored, as uniaxial tension is the standard geometry for testing the mechanical properties of materials [315]. Because of the relatively small volumes of material produced, this test was chosen to give reliable determination of the strength, stiffness, and ductility of the sample materials at three different temperatures, with overall sample dimensions of 32 x 3 x 1 mm as shown in Figure 3-1. The

temperatures chosen for testing were ambient room temperature, 300 °C and 600 °C as this elevated temperature is representative of the design temperature for fusion breeder blanket components as discussed in section 2.3. Testing at this temperature was performed under an inert atmosphere, as discussed in section 3.2.3, to mitigate the effects on the results of sample oxidation which would not be expected in-service. In addition, an intermediate testing temperature of 300 °C was chosen in order to give more idea about the trend of how mechanical properties change with temperature. Also, 300 °C is approximately the in-service operating temperature of zirconium alloys within nuclear fission reactors, and so provides a useful testing baseline against which to compare the novel alloys, aligning with the aims set out in section 4.1. Whilst this method was an ideal for the determination of properties, the relatively high material quantity demands for the sample geometry and the lack of availability of the testing equipment for larger numbers of tests means that a relatively small selection of samples could be tested in this way. A testing method which allows for wider comparison of the samples is presented in section 4.6.2.

The data collection method is set out in section 3.2, and yielded a set of discrete stress and strain data points which could be plotted. Stiffness of the material was evaluated by manual selection of the initial linear portion of the stress-strain data collected, and then employing a linear fitting function in MATLAB to calculate the relevant gradient and produce a quantitative measurement of Young's Modulus. In order to determine other materials properties, it was useful to obtain a continuous data line rather than a series of discrete data points. This was achieved using the spline fitting function within MATLAB to fit the data with a fitting parameter of 0.9999. The results of this are shown in Figure

4-42 along with indications of the material properties calculated from data processing that will be described in the following paragraphs.

Having calculated this continuous, smoothed data profile, various methods for calculating the strength of the material were possible. Firstly, the ultimate tensile strength of the material was calculated by identifying the maximum stress value reached in the spline smoothed data series. The smoothed data is used for this method to exclude any small error which may be introduced by a singular erroneous measurement. Secondly, a value of 0.2% proof stress is identified as the intersection point between the line representing the smoothed data and a line constructed with the same gradient as the identified linear portion of the data and a strain-axis intercept value of 0.2%.

Whilst 0.2% proof stress values can provide a reliable and repeatable estimation of the yield stress of the material, a more accurate method was sought which identified a stress closer to the point where the stress-strain relationship visibly deviated from linearity. The most appropriate method identified to achieve this was to calculate the second derivative of stress with respect to strain of the smoothed data line, which is then plotted against strain. This allows for identification of the point in the resultant profile where a substantial minimum turning point is observed which gives a good estimation of the first point where the stress-strain profile initially deviates from linear behaviour. Due to the imprecise nature of accurately identifying a minimum turning point, the position of this point was approximately identified and then confirmed by identifying the point where the third derivative of stress with respect to strain line crosses the strain axis. This method is used to calculate the value labelled as yield stress in this study.

The final material parameter extracted from the data is the strain to failure which gives an indication of the material ductility. This is manually identified by selecting the final measured data point before a significant drop in measured stress value. Identification of this point is unambiguous in room temperature tests as a result of the sudden failure of the material. As previously discussed in section 3.2.2, due to material overheating associated with necking, strain to failure cannot be identified accurately for tests at elevated temperatures using this method.

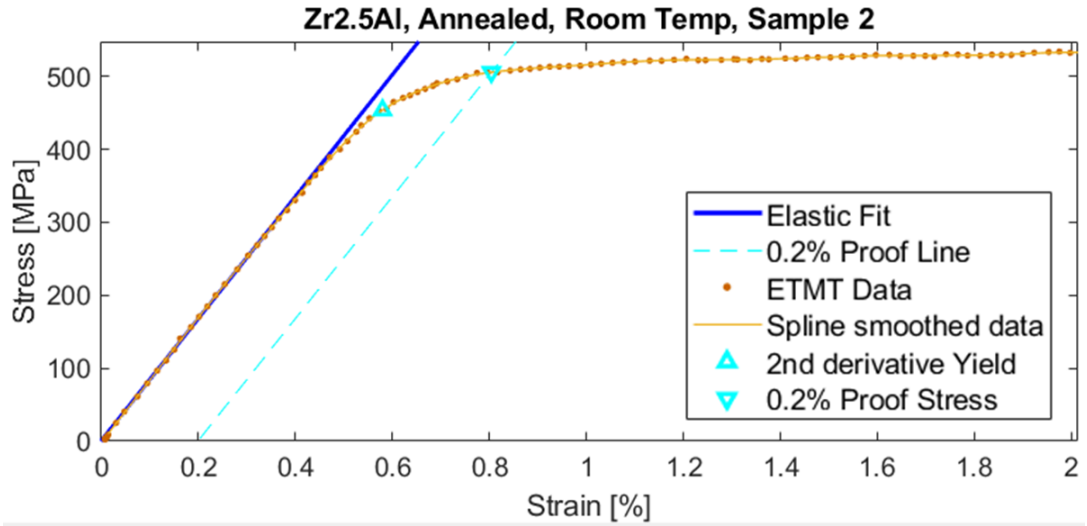


Figure 4-42: An example of the stress-strain data collected by ETMT, with a section of the data collected from Zr2.5Al at room temperature shown. The collected data points are shown as orange circles with the spline smoothing of this data shown by the orange line. Analysis of the data is described in this section with indications of the fitting of the linear region, proof stress method, and yield stress identification shown.

The samples tested in this study were the 2.5% alloys of the Zr-Al, Zr-Ta, and Zr-V systems. In addition, benchmark materials were tested for comparison with the novel alloys. The first benchmark material sample is from the bar of pure zirconium which was cast and processed in parallel with the novel alloys. Secondly, samples of Zircaloy-4, which is a common zirconium-based commercial alloy in the nuclear fission industry,

provided by Rolls-Royce and previously examined by Murray [250], were tested. All samples were tested in the same orientation such that the uniaxial tensile axis was aligned with the rolling direction of the sample. The values of material properties calculated from the data collected are shown in Table 4-4.

The strain to failure values shown in Table 4-4 indicate reasonable ductility of all the novel alloys produced, with Zr2.5Al displaying notably good ductility, comparable to Zircaloy-4 and the pure zirconium.

Visualisation of some of the numerical data shown in Table 4-4 is shown in Figure 4-43 which shows the variation of 0.2% proof stress, and Figure 4-44 which shows the variation of yield stress (calculated by the method described above) between samples and at different temperatures.

Discussion of these mechanical testing results, in the context of the microstructures observed throughout section 4.5, follows in section 4.7.

Table 4-4: Numerical results of analysis of ETMT data by the methods described in sections 3.2 and 4.6.1. Data presented is an average of at least two tests with the standard deviation of the results shown in brackets. Strain to failure is not given at elevated temperatures due to limitations of the testing technique.

Material	Temperature	Modulus (GPa)	Yield Stress (MPa)	0.2% Proof Stress (MPa)	UTS (MPa)	Strain to Failure (%)
Zircaloy-4	Room	89.7 (1.3)	315.0 (5.4)	380.1 (0.9)	545.6 (1.6)	24.4 (0.8)
	300 °C	60.9 (2.2)	94.9 (19)	133.0 (5.1)	236.2 (4.8)	-
	600 °C	35.6 (1.6)	57.2 (5.6)	64.6 (0.4)	76.1 (0.1)	-
Pure Zr	Room	76.6 (2.8)	268.1 (16.2)	371.68 (2.1)	466.2 (5.1)	25.4 (6.7)
	300 °C	60.0 (5.2)	70.3 (9.6)	95.59 (4.2)	155.0 (0.7)	-
	600 °C	21.4 (3.0)	29.1 (5.0)	38.0 (0.1)	43.0 (1.4)	-
Zr2.5Ta	Room	87.2 (7.2)	534.3 (24.9)	590.5 (13.0)	696.9 (10.5)	16.0 (7.5)
	300 °C	76.0 (2.6)	191.0 (2.0)	291.2 (9.6)	353.6 (1.3)	-
	600 °C	41.1 (5.4)	95.3 (3.5)	154.0 (27.2)	175.6 (30.9)	-
Zr2.5V	Room	81.7 (1.9)	427.7 (42.0)	531.2 (1.5)	642.5 (6.2)	9.3 (0.1)
	300 °C	62.3 (2.2)	164.3 (6.0)	243.7 (0.6)	307.8 (1.3)	-
	600 °C	25.9 (2.7)	81.8 (2.8)	103.8 (8.5)	126.7 (9.8)	-
Zr2.5Al	Room	84.1 (0.6)	449.1 (6.6)	502.7 (4.4)	580.3 (7.5)	23.0 (3.3)
	600 °C	38.2 (3.1)	111.0 (3.3)	121.7 (2.0)	131.0 (4.2)	-

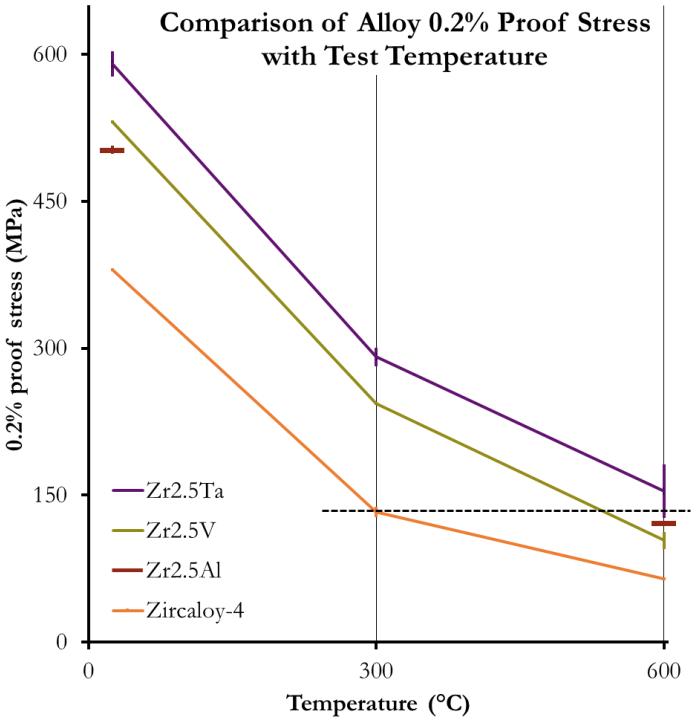


Figure 4-43: Graph comparing the 0.2% proof stress of novel zirconium alloys with Zircaloy-4 across temperatures as measured by ETMT

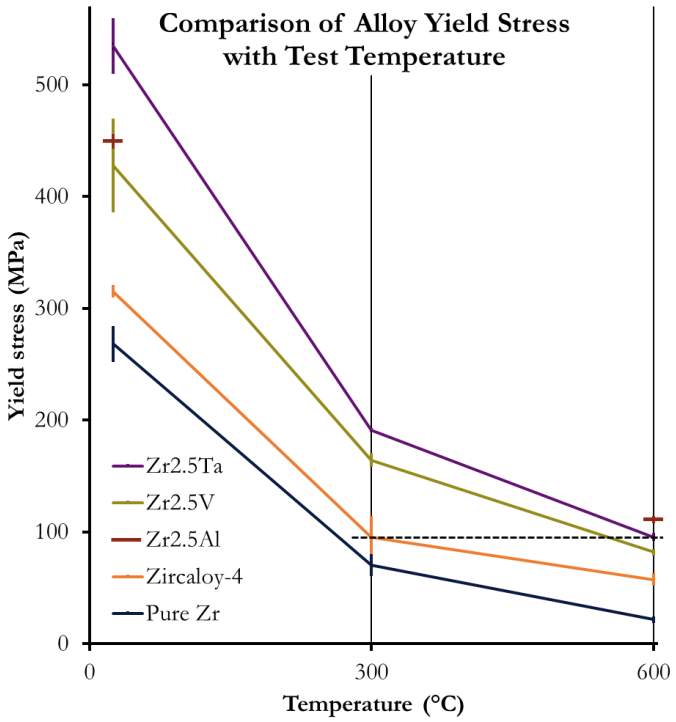


Figure 4-44: Graph comparing the yield stress of novel zirconium alloys with Zircaloy-4 across temperatures as measured by ETMT and determined via a method utilising the second derivative of the stress-strain curve

4.6.2 Nanoindentation

Whilst the ETMT results shown are intended to give accurate measures of key materials property parameters, the nanoindentation results presented in this section, collected and analysed as discussed in section 3.3, are intended to give a more qualitative comparison between sample strengths. This is because the more complex nature of the stress field associated with the spherical indentation method makes it challenging to extract property values, but a measurement of the stress required for varying amounts of strain deformation may be visualised by the plotting of indentation flow curves. It should also be noted that the indentation stress and strain values indicated on the flow curves should not be interpreted as equivalent to the stress and strain values which would be extracted from a uniaxial tensile test. The nature of the nanoindentation method, and its lower requirement of sample material volume compared with ETMT, allows for the testing of a greater number of samples, to give a wider comparison of material performance. Room temperature, 300 °C and 600 °C were chosen as testing temperatures for the same reasons as stated for the ETMT testing in the previous section, and to ensure easy comparison of the results.

Comparison of the nanoindentation results with the ETMT data shown above may be demonstrated by Figure 4-45. The data shown indicates how the hardness (indentation stress), which may be correlated with material strength [316], varies as the indentation strain applied to the material increases. The trend of decreasing strength with the increasing temperature at which the test was performed in Figure 4-45, shows comparable behaviour to the same effect seen in ETMT testing, as shown in Figure 4-43 and Figure 4-44 for the same materials. Further comparison of the behaviour of the different materials is shown below.

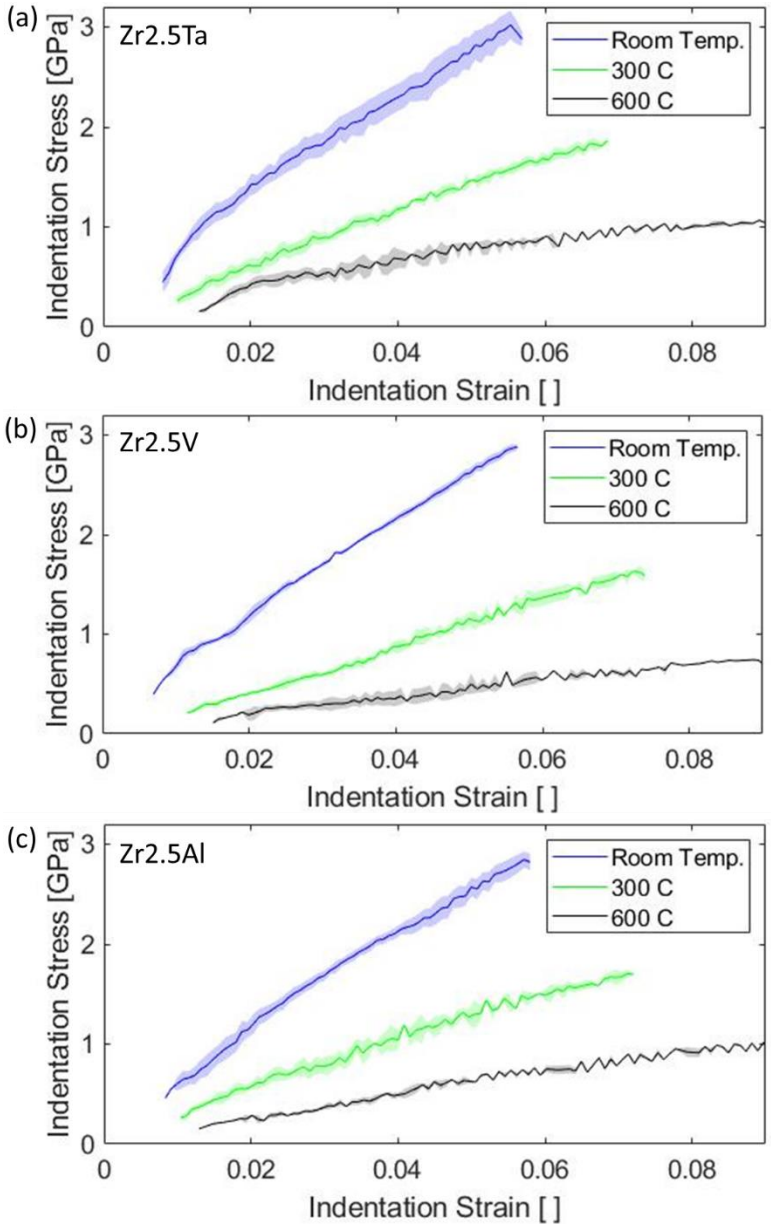


Figure 4-45: Averaged indentation flow curve comparisons between tests performed at room temperature, 300 °C and 600 °C on (a) Zr2.5Ta, (b) Zr2.5V, and (c) Zr2.5Al.

In Figure 4-46, the flow curves obtained from annealed zirconium and the three zirconium alloy materials with 2.5 at% composition, which were all tested with the ETMT method, are compared at these three temperatures. At room temperature, in Figure 4-46(a), the three alloys display broadly similar strengths, with the Zr2.5Ta alloy being the strongest. At increased temperatures, in Figure 4-46(b,c), the alloy strengths differ more. The Zr2.5Ta alloy generally displays the greatest strength at all temperatures in Figure

4-46, with Zr2.5Al only slightly below at 600 °C in Figure 4-46(c). Zr2.5V displays the lowest strength of the three alloys at 600 °C in Figure 4-46(c). This data shows good agreement in general trends when compared with the ETMT data in Table 4-4, and visualised in Figure 4-43 and Figure 4-44. This general agreement in trends is shown in Figure 4-47.

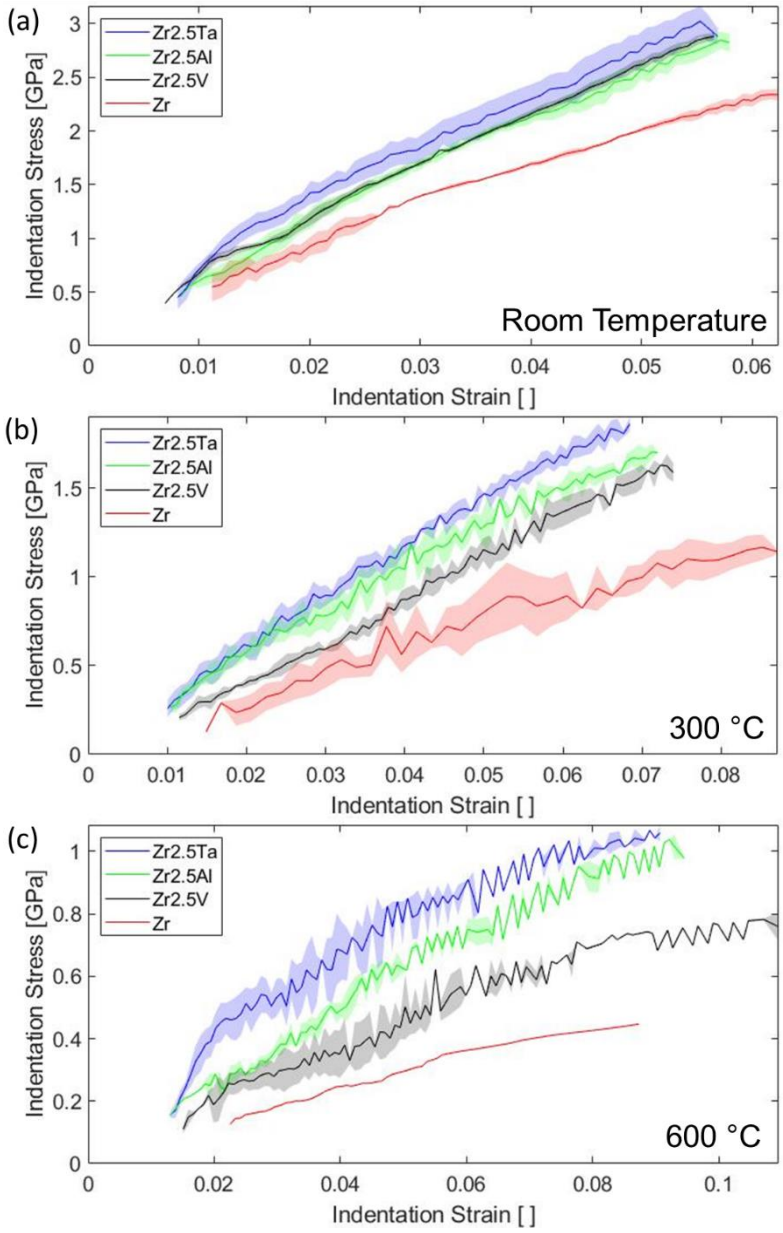


Figure 4-46: Averaged indentation flow curve comparisons between zirconium, Zr2.5V, Zr2.5Al, and Zr2.5Ta at (a) room temperature, (b) 300 °C, and (c) 600 °C.

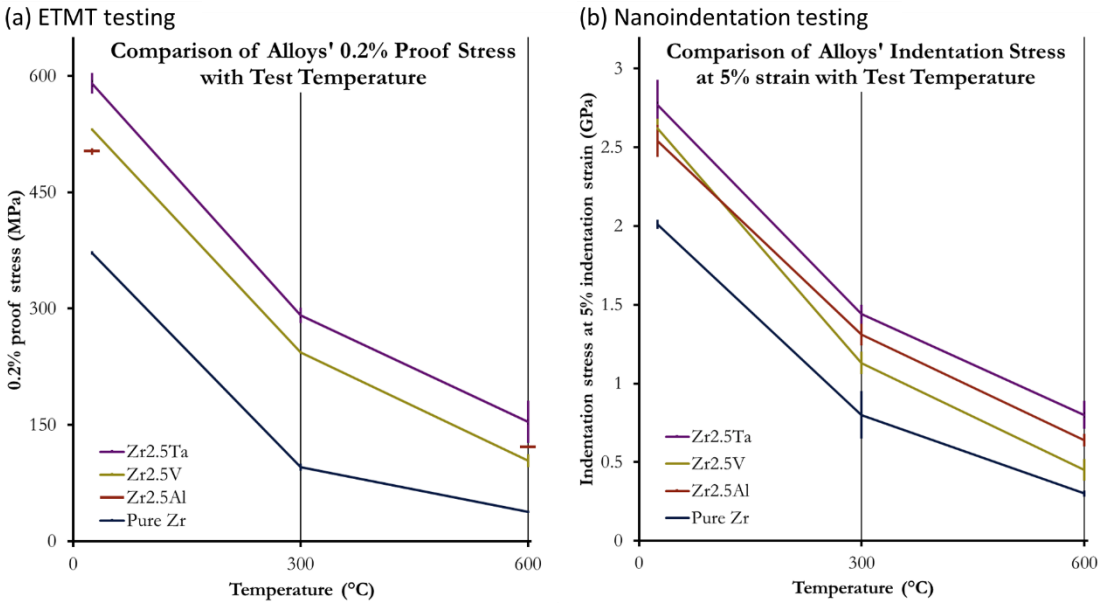


Figure 4-47: Graphs showing the trends of alloy strength with increasing testing temperature for two different testing methods. (a) shows the 0.2% proof stress as measured by ETMT and shown previously in Figure 4-43, and (b) shows the indentation stress measured at 5% indentation strain by nanoindentation testing shown in Figure 4-46.

It is also encouraging to see that a similar trend is followed for the three alloy systems with 1 at% alloying, as shown in Figure 4-48. As would also be expected, the strength levels of the alloys with lower alloying additions appears lower than with 2.5 at% alloying, as may be directly compared in Figure 4-48 and Figure 4-46(c). This will be more thoroughly examined in the following figures.

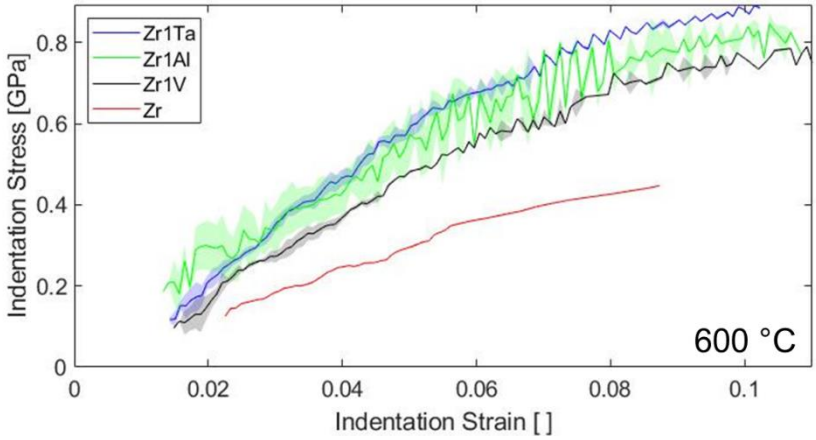


Figure 4-48: Averaged indentation flow curve comparisons between zirconium, Zr1V, Zr1Al, and Zr1Ta at 600 °C.

Comparison of alloy strengths at 600 °C with increasing alloying percentages in the Zr-Al and Zr-Ta systems is shown in Figure 4-49 to confirm that strength increases as alloying content increases. The extent of increased strengthening between Zr2.5Al and Zr5Al at this elevated temperature appears significant.

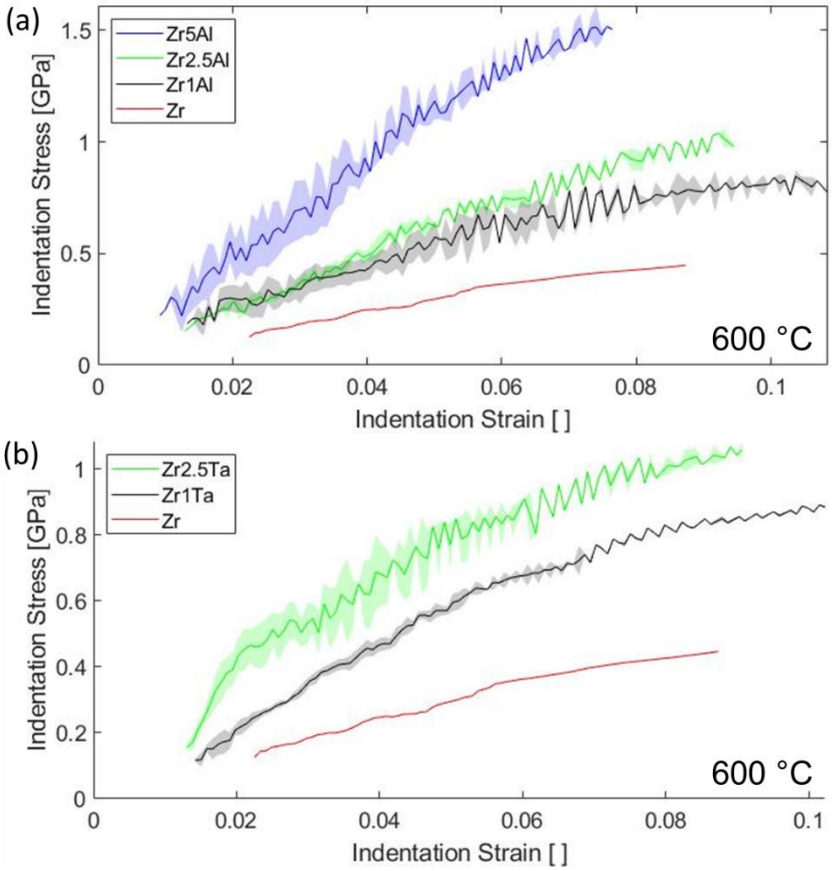


Figure 4-49: Averaged indentation flow curve comparisons of different solute percentage compositions in (a) the ZrAl system and (b) the ZrTa system, both at 600 °C.

In contrast with the expected strengthening increments seen for the Zr-Al and Zr-Ta systems in Figure 4-49, the equivalent comparison for the Zr-V system at 600 °C is shown in Figure 4-50(b) which indicates that the strength of the Zr1V alloy and Zr2.5V alloy are approximately equivalent at 600 °C. The trend is similar at 300 °C as shown in Figure 4-50(a), indicating that increasing the vanadium content of the alloy does little to increase its strength.

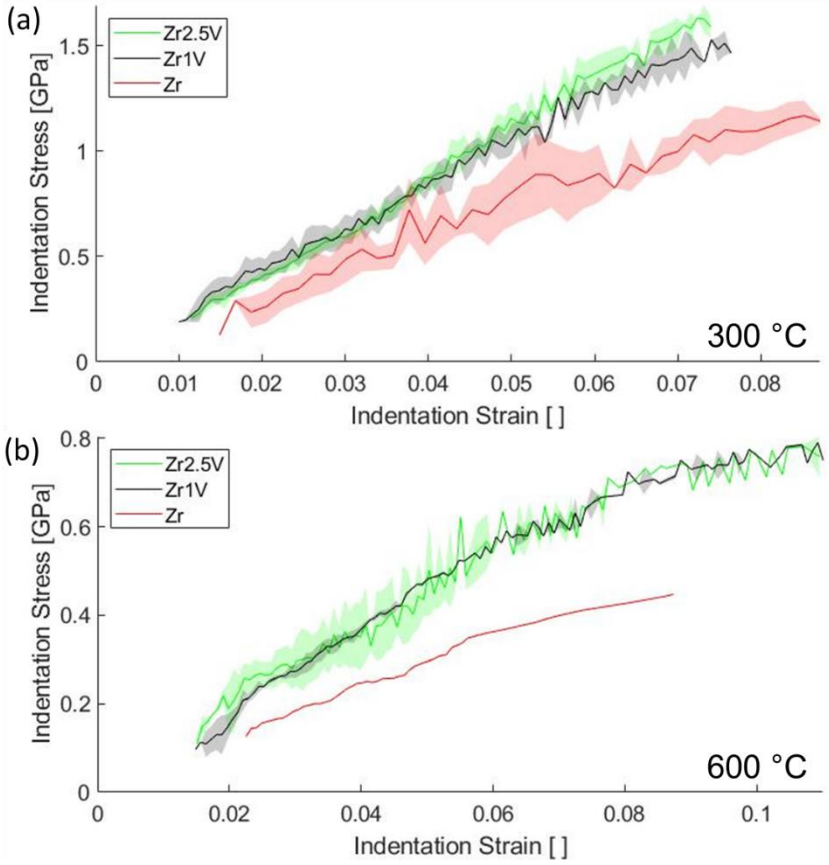


Figure 4-50: Averaged indentation flow curve comparisons of different solute percentage compositions in the ZrV system at (a) 300 °C and (b) 600 °C.

The ZrTa and ZrNb alloy systems both display monotectoid-type binary phase diagrams and were subject to equivalent processing routes resulting in comparable microstructures as shown in sections 4.5.4 and 4.5.5. Therefore, the comparable strength of the Zr2.5Nb and Zr2.5Ta alloys at room temperature, as shown in Figure 4-51(a), agrees with the relative strengths which may have been expected for the alloys. In contrast, at elevated temperatures the relative strengths differ substantially, as shown in Figure 4-51(b,c). ZrNb alloys of approximately the same composition as the alloy in this study are applied in the nuclear fission industry with operating temperatures in the region of 300 °C. Testing at this temperature shown in Figure 4-51(b) indicates that the Zr2.5Nb alloy retains a greater strength than the Zr2.5Ta alloy, although this trend is reversed in the testing performed at 600 °C (Figure 4-51(c)) which is thought to be more

representative of the in-service temperature in the fusion breeder blanket environment. However, it is thought that the results recorded for the strength of Zr2.5Nb at 600 °C may be erroneous as a strength less than that of the pure zirconium sample tested was measured as shown in Figure 4-51(c). Whilst the data collected for the Zr2.5Nb sample at 600 °C was consistent, it is possible that microstructural instability of the sample at 600 °C, as evidenced by the phase transformation at approximately the same temperature displayed in the phase diagram shown in Figure 2-11, may have resulted in the measurement of reduced strength. A similar phenomenon of microstructural instability affecting the results of high temperature nanoindentation data is discussed later in section 5.3.1 for the Zr2.5V alloy.

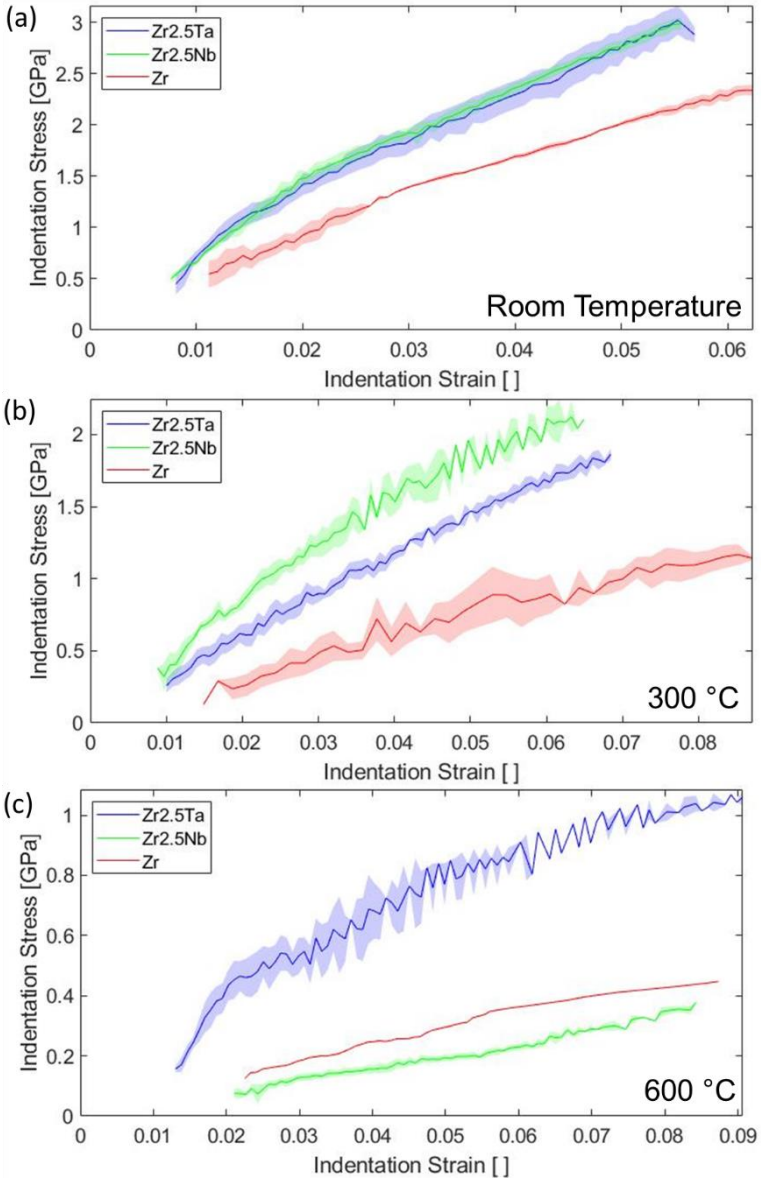


Figure 4-51: Averaged indentation flow curve comparisons between zirconium, Zr2.5Ta and Zr2.5Nb at (a) room temperature, (b) 300 °C, and (c) 600 °C.

Due to the potentially erroneous nature of the result above, the comparative strengths of the Zr1Nb and Zr1Ta alloys are useful. This is shown in Figure 4-52 where a similar trend may be observed. At 300 °C, the 1 at% alloys in Figure 4-52(a) display similar strengths. This is comparable to the 2.5 at% alloys tested at 300 °C in Figure 4-51(b), although the strengths of the alloys are not as similar in that case. At 600 °C, in Figure 4-52(c), the Zr1Nb alloy shows increased strength compared with pure zirconium,

as would be expected. This gives confidence in the data shown in Figure 4-52(c), which also indicates significantly increased strength of the Zr1Ta alloy in comparison with the Zr1Nb alloy at 600 °C. This finding, along with the strength measurement of Zr2.5Ta at 600 °C shown in Figure 4-51(c), suggests that alloys of the ZrTa system retain higher strength at fusion breeder blanket temperatures (approximately 600 °C) than ZrNb alloys.

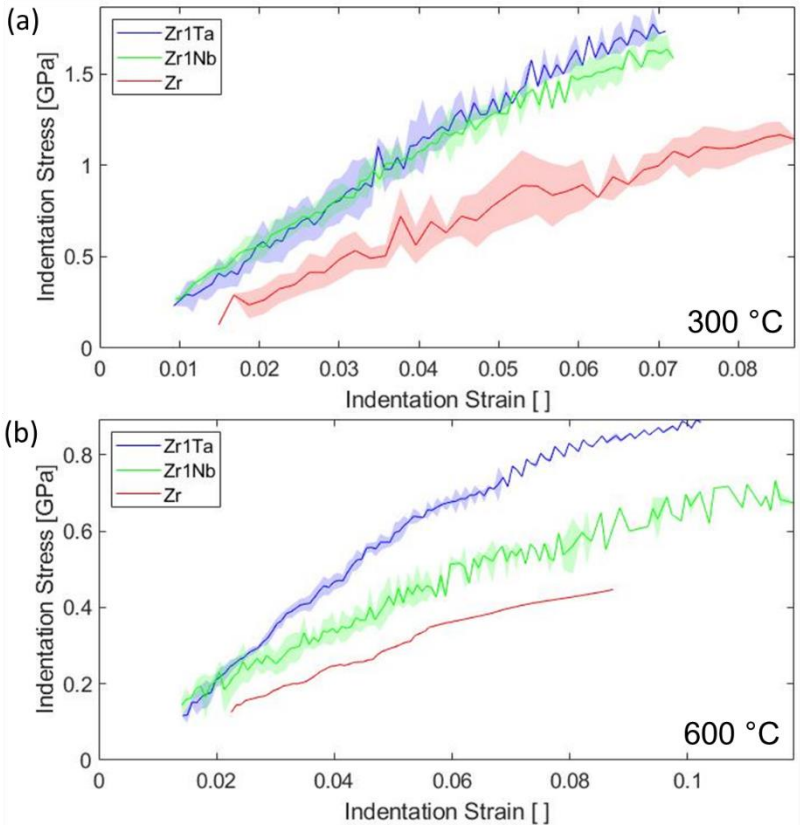


Figure 4-52: Averaged indentation flow curve comparisons between zirconium, Zr1Ta and Zr1Nb at (a) 300 °C and (b) 600 °C.

In addition to comparison of the strength between each of the zirconium alloys produced for this study, it is useful to compare the strengths of these materials to other materials selection candidates for the fusion breeder blanket. Eurofer is the RAFM of choice within Europe as a structural material for fusion [317] and is the choice for the ITER tritium blanket modules [318]–[320]. A sample of Eurofer was obtained for testing

and comparison in this study from a batch produced by Bohler Edelstahl GmbH in Austria, this was normalised at 980 °C for 0.5 hours and tempered at 760 °C for 1.5 hours followed by air cooling to produce the ferritic/martensitic microstructure necessary for the material. The nominal composition of the material is approximately Fe-8.89Cr-1.11W-0.44Mn-0.19V-0.14Ta-0.06Si-0.12C-0.01N in weight percent.

Alloys displaying the highest strengths are compared with Eurofer in Figure 4-53, in which relatively comparable strengths are indicated at room temperature. Although more significant differences are observed at 600 °C, the strength of the Zr5Al is comparable to Eurofer, as is the Zr2.5Ta alloy at lower strain values.

Overall, this comparison indicates that these zirconium alloys, which have received rather limited microstructural optimisation, have the possibility of achieving at least comparable strengths as one of the steels being considered for application in breeder blanket components.

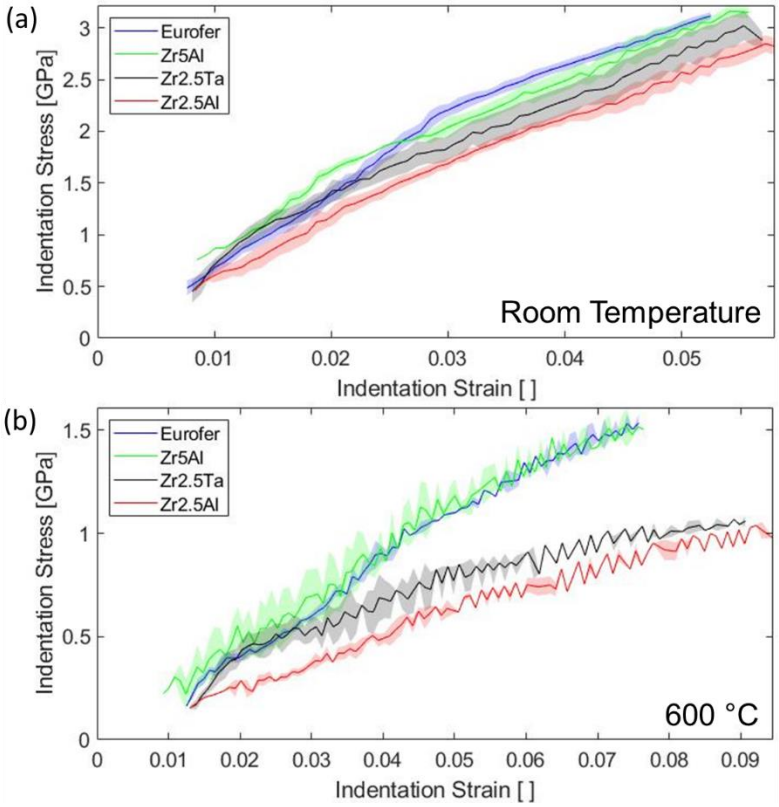


Figure 4-53: Averaged indentation flow curve comparisons between Eurofer, Zr5Al, Zr2.5Ta, and Zr2.5Al at (a) room temperature and (b) 600 °C.

4.6.3 Creep

It has been identified that creep may be a life-limiting factor for zirconium alloys in fusion applications [80], and that further investigation is required in to the creep resistance of zirconium alloys at temperatures expected for a fusion breeder blanket [84].

Due to the relatively small quantities of material available in this study, small punch creep testing is an attractive method to evaluate creep performance due to the relative ease of high-temperature testing and use of small specimen geometries [321], [322]. Whilst the complex stress state induced by this testing method [323] makes it difficult to compare data to tests performed on more conventional sample geometries, benchmark materials which have been well characterised and tested conventionally may

be tested under the same conditions so that the performance of novel alloys may be compared. In this study, Eurofer [318], [324] was obtained for this purpose.

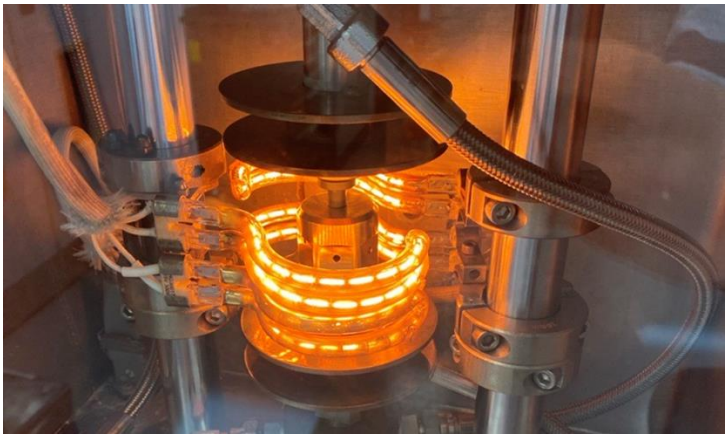


Figure 4-54: Small Punch testing rig used for this study with heating elements surrounding the central die containing the sample disc, all contained within an argon-filled environmental chamber.

For the purposes of this study, a Phoenix small punch testing rig was kindly made available for use by Dr Mark Richardson and the UK Atomic Energy Authority. The system under operation is shown in Figure 4-54. This equipment has been previously used to evaluate the creep performance of 8 mm samples, and the same method was followed in this study with the exception of the use of the smaller 3 mm diameter samples due to material availability [111], [325]. Having rectified a number of issues with the testing set-up and prepared 3 mm diameter samples to the prescribed dimensions and tolerances [326]–[328], time independent deformation measurements were taken to ensure that creep experiments were performed within the load range for which elastic deformation of the sample was dominant. Following this, a fixed load of 70 N was applied to the Eurofer specimen at 600 °C and the deflection of the sample was measured with a linear variable differential transformer (LVDT). It can be seen from the data collected in Figure 4-55 that an approximately constant rate of creep deformation was achieved in this test following a primary region of decreasing creep rate.

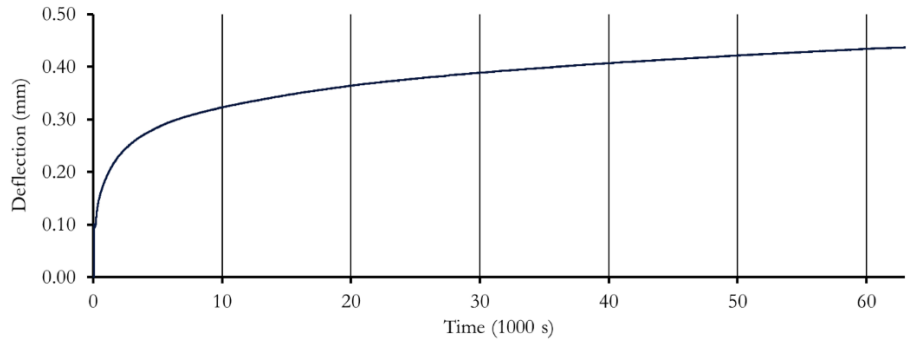


Figure 4-55: Deflection-time curve collected to evaluate the creep resistance of a 3 mm disc of Eurofer in the small punch testing geometry under a load of 70 N at 600 °C.

It was intended to collect comparable data from samples of the novel zirconium alloys created for this study in order to compare their creep performance to the benchmark Eurofer material. However, a failure of the load cell of the testing machine meant that it was incapable of applying a constant load to the samples and no other equivalent apparatus was available. Therefore, evaluation of the creep resistance of these alloys remains an area which requires further investigation.

4.7 Discussion of the microstructural and mechanical analysis of the new alloys

4.7.1 Microstructures

The results presented in this section indicate the success of the processing methods in producing materials for testing which exhibit microstructures similar to those found in current engineering alloys. This includes the production of fine and relatively equiaxed grain structures.

The length scale of the grain structures of the alloys may be compared between the microstructures shown after the hot rolling treatment in section 4.2.5.4 and after the subsequent annealing treatment shown throughout section 4.5 and there is no noticeable alteration of the microstructure as a result of the annealing treatment. This is a positive result as the intended effect of the annealing treatment is to relieve internal stresses and reduce dislocation density, but not result in any other changes in microstructure.

Quantitative measurement of the grain structures from EBSD analysis in Figure 4-27, Figure 4-32, and Figure 4-38 indicates that all three of the novel alloys with 2.5 at% solute composition exhibit a grain size between 1-10 μm, with Zr2.5V showing the smallest grain size, and Zr2.5Al the largest. The grain sizes of all the alloys are noticeably smaller than in the pure zirconium sample shown in Figure 4-20, indicating that all of the alloying elements act to refine the grain structure and increase the alloy strengthening due to the Hall-Petch effect. The results suggest that the ZrV_2 Laves phase precipitates in the Zr2.5V alloy refine the grain structure to the greatest extent.

Alloys of the Zr-V and Zr-Al systems were processed using hot rolling at a temperature below the first transformation temperature in the respective binary phase diagrams, this was selected to mirror the processing route taken for commercial alloys such as Zircaloy-4 as discussed in section 2.6.1. The aim of this processing route is to achieve a good dispersion of intermetallic precipitates to achieve precipitate strengthening of the alloy as is achieved in Zircaloy-4 [329]. A good distribution of intermetallic precipitates also appears to have been achieved for both ZrV_2 precipitates in Zr2.5V (as shown in Figure 4-29 and Figure 4-30), and for Zr_3Al precipitates in Zr2.5Al (as shown in Figure 4-24 and Figure 4-26). The mechanical testing results shown in Table 4-4, Figure

4-49 and Figure 4-50 indicate that these precipitates have contributed to the increased strength of these alloys above that of the pure zirconium benchmark sample which was processed similarly. It is also anticipated that these precipitates will effectively pin the grain boundaries and prevent significant coarsening of the microstructure at elevated temperatures in-service, and this will be examined later in this study.

The secondary phases occurring at grain boundaries in the Zr2.5Nb and Zr2.5Ta alloy microstructures would also be expected to prevent significant coarsening of the grain structure. Zr-Nb and Zr-Ta alloys are discussed concurrently and compared due to the similarity of their monotectoid-type binary phase diagrams. The processing route selected for these alloys is discussed in section 2.6.1, to mirror that of commercial Zr-Nb-based alloys. The phases and microstructure identified of the Zr2.5Nb alloy in section 4.5.5, mirrors the results shown for characterisation of commercial alloys in the literature [180], [330]–[334] which confirms the success of the chosen processing route in this study and the methods used.

The formation of a bimodal microstructure is caused by the formation of grains of both α-Zr and β-Zr phase at the hot rolling temperature, where the solute element, niobium, has a significant solubility in the β phase but not in the α phase. Enrichment of niobium at the grain boundaries is caused by the segregation of niobium to these regions from the α-Zr grains, resulting in the formation of the Nb-rich β-phase at grain boundaries in the final microstructure. Secondly, as the alloy cools from its processing temperature, the β-Zr grains undergo a phase transformation to the α-phase in which the solubility of the dissolved niobium is greatly reduced. Therefore, partitioning of the excess

niobium occurs to bands of β-Nb in an α-Zr matrix in these prior β-Zr grains during cooling. This explains the formation of the bimodal microstructure observed.

There are significant similarities as well as some differences between the Zr2.5Nb alloy and Zr2.5Ta alloy microstructures. Initially, the bimodal-type microstructure seen in the Zr2.5Nb alloy is broadly repeated in the Zr2.5Ta alloy and its formation may be described in the same way as above. This shows that the hot rolling treatment in two-phase region of the binary phase diagram has been successful, even though it was challenging given the relatively narrow temperature window, and justifies the method of calculating the necessary temperatures as detailed in section 4.2.5.1. One significant difference observed between the two alloys is that the composition of the BCC β-phase identified in the Zr2.5Ta alloy is dominated by tantalum as shown by XRD and APT analysis in Figure 4-37 and Figure 4-36 (which indicates >75 at% tantalum in the precipitate) respectively, as expected from phase prediction from the binary phase diagram shown in Figure 2-14. This contrasts with the composition of the BCC β-phase in the Zr2.5Nb alloys which is shown to have a significant level of zirconium in Figure 4-40 and Figure 4-41 showing <30 at% niobium in the second phase, in agreement with prior evaluations of this phase observed in commercial alloys in the literature [333], which is thought to be caused by the sluggish diffusion of niobium in α-Zr [174]. Another microstructural difference observed is that the Ta-rich phase in Zr2.5Ta occurs as discrete precipitates in contrast with the more continuous Nb-rich phase seen in the Zr2.5Nb alloy. Whilst it is not known whether the identified difference in composition of the solute-rich β-phases in the two alloys is likely to have a significant effect on the alloy mechanical properties, it is predicted that the discrete β-phase morphology in Zr2.5Ta may result in an increased creep resistance compared with a more continuous β-phase

morphology since grain boundary sliding may be inhibited and the precipitates may act as barriers to the fast diffusion path along grain boundaries, thus inhibiting these mechanisms which lead to creep deformation in alloys. As has been previously acknowledged, this should be confirmed experimentally.

Laves phase precipitates are commonly reported in commercial Zr-Nb alloys containing elements such as iron and chromium [335], and therefore may also be expected within alloys of the Zr-Ta system. Whilst these elements have also been identified as present in the alloys of this study, as shown in Table 4-1, the characterisation results shown in sections 4.5.4 and 4.5.5 have not identified the presence of any Laves phase precipitates, but their potential inclusion in the microstructure should not be ruled out.

The presence of the γ-ZrH hydride phase is identified in the XRD results of all the alloys analysed and the volume fraction appears to be relatively consistent throughout the alloys, based on the relative peak integral observed in XRD data. Whilst this was not a desirable phase within the microstructure, it is not unexpected due to the high hydrogen affinity of zirconium alloys and their propensity to produce hydrides as discussed in section 4.2.5.4. Given the similarity of the fractions of γ-ZrH phase within all of the produced alloys, it remains possible to provide a fair comparison between their properties.

4.7.2 Mechanical properties

Reasonable agreement between the mechanical properties of the Zircaloy-4 measured by ETMT in this study and values reported in literature [336], [337] gives confidence in the precision offered by this testing technique. Confidence in the strengths

measured by nanoindentation is supported by similar trends of alloy strength being observed when measured by ETMT, as discussed in section 4.6.2.

Combining the results of all the mechanical testing indicates that the Zr2.5Ta alloy has the greatest strength of the 2.5 at% alloys tested, as shown in Figure 4-47 and Table 4-4. This suggests that the bimodal microstructure of Zr2.5Ta, arising from the monotectic reaction in the phase diagram, is more effective at strengthening the material than the microstructures of Zr2.5V and Zr2.5Al in which intermetallic precipitates are observed, although these alloys still demonstrate good comparative strength to Zircaloy-4.

Given the similarity of the precipitates within the Zr2.5V and Zr2.5Al alloys, the increased strength of the Zr2.5Al alloy may be explained by the increased effect of solid solution strengthening by aluminium, due to its greater solubility in zirconium as shown by the phase diagrams in Figure 2-13 and Figure 2-15 [338].

Although Zr2.5Ta shows the greatest strength compared with all the alloys with 2.5 at% solute, the Zr5Al alloy displays even greater strength, as shown in Figure 4-53. Also notable is the large increase in strength shown between the 2.5 and 5 at% aluminium alloys in Figure 4-49(a). This may be explained by the significantly increased extent of precipitate strengthening between Zr2.5Al and Zr5Al alloys due to the solubility of aluminium in zirconium at 600 °C as shown in Figure 2-13.

Further consideration of the effective strengthening attributed to alloying with aluminium and tantalum should be taken in relation to the effects of these two elements on the neutron absorption of a zirconium alloy, given that the low thermal neutron absorption property of zirconium is an important factor for its consideration as a fusion

breeder blanket structural material. Whilst an addition of 2.5 at% tantalum may decrease the neutron transparency of zirconium more than is deemed acceptable to achieve the desired tritium breeding ratio [3], the Zr1Ta alloy also displays promising mechanical properties so lower Ta compositions might be considered to improve strength whilst still improving neutron efficiency compared with steels. In contrast, aluminium would have a much lesser effect on the neutron transparency of the alloy, so an alloy composition such as Zr5Al, and the good strength associated with this alloy, could be appropriate [3].

Comparison of the novel alloys displaying the greatest strength with Eurofer, a leading candidate structural material for the fusion breeder blanket [317], shown in Figure 4-53, is promising for the potential application of these alloys. This is compounded by the indication of comparable strength of the novel alloys at 600 °C and Zircaloy-4 at approximately its operational temperature of 300 °C in Figure 4-43 and Figure 4-44. The promise of these results should also be interpreted in the context that the novel alloys tested are comparatively simplistic binary compositions and the limited microstructural optimisation which has been carried out. This is in contrast to the extensive development which has occurred for structural steels, and zirconium alloys in nuclear fission applications.

4.8 Conclusions from the microstructures and mechanical properties of novel alloys

Targeted microstructures representative of engineering alloys were achieved and characterised for each of the alloy systems. Alloys of the Zr-Ta and Zr-Al systems are identified as the most promising to achieve good strength properties at the expected

service temperature of a fusion breeder blanket. In particular, the Zr5Al and Zr2.5Ta alloys tested are identified to have high strengths, and encouraging comparisons have been made between these and the strengths of commercial alloys used in both the fusion and fission industries. These results give confidence that sufficient properties could be achieved for zirconium alloys with further alloy development, along with the potential of zirconium alloys to provide greater neutron efficiency in comparison with steels to improve the achievable tritium breeding ratio in the blanket.

The creep resistance properties of these alloys remain unevaluated due to testing equipment unavailability. This should be measured and considered before undertaking further development of high temperature zirconium-based alloys. Initial experiments examining the creep resistance of zirconium alloys designed for high-temperature operation and including aluminium as a major alloying element compared with other candidate materials such as Eurofer, is ongoing by researchers at the University of Birmingham and encouraging initial results have been achieved. In addition, there should be consideration of the microstructural stability and corrosion resistance with respect to the breeder/coolant fluid in the breeder blanket of the new alloys, and this will be explored in sections 5 and 6.

4.9 Estimations of the contribution of microstructural effects to alloy strengthening

For further development of more optimised alloy compositions and microstructures, estimations of the extent of strengthening provided by mechanisms such

as solid solution strengthening, and strengthening due to Orowan bowing of dislocations around incoherent precipitates in the microstructure.

4.9.1 Solid solution strengthening in the alloys

For the purposes of the estimations in this section, assumptions will be made that the strengthening by substitutional solute atoms is dominated by the misfit strain associated with their inclusion in the lattice, and that the extent of strengthening provided scales linearly with the misfit of the solute and the solute atomic concentration in the microstructure.

It has been shown in the literature that additions of niobium in solid solution to zirconium (up to 0.2 at%) lead to an increase in yield stress of 100 $MPa.at\%^{-1}$ [339]. The calculation of the contribution of solid solution strengthening in the alloys of this study will be calculated relative to this value.

4.9.1.1 Calculations of the extent of solute solubility

In order to calculate the strengthening provided by solid solution misfit, the concentration of solute atoms must be determined. As it is deemed that the phase diagrams shown in section 2.4.2 are unlikely to provide a reasonable estimate at this value, it should be determined from the results of experimental study. These results may also be used to inform the refinement of the phase diagrams for these alloy systems with the knowledge that the samples studied were heat treated at 700 °C before air cooling.

For the Zr2.5Al alloy, the solid solubility concentration is determined from APT data shown in Figure 4-28, in agreement with results shown later in the thesis in Figure

5-30 and Figure 5-33. These results indicate a solid solution aluminium concentration of approximately 2 at%.

For the Zr2.5Ta alloy, data is similarly taken from APT data as shown in Figure 4-36. In this case the data indicates a solid solution tantalum concentration of approximately 0.4 at%.

In the case of the Zr2.5V alloy, the lack of APT data availability for this alloy leads to a requirement for the calculation of the solid solubility concentration via alternative methods. In this case it was chosen to calculate the concentration of precipitates in the microstructure, and therefore the at% of vanadium which is contained within them. This was achieved by using contrast thresholding in ImageJ software of the micrograph shown in Figure 4-29(b). This led to the finding that 4% of the area in the figure was identified as precipitates. An assumption is made that this area is representative and therefore the percentage calculated is equal to the proportion of the material volume occupied by precipitates.

It is then necessary to convert the precipitate volume percentage to a weight percentage using the densities of the two phases. The density of both the pure Zr and Zr2.5V samples was measured using the Archimedes buoyancy method which gave a value of 6.500 $g.cm^{-3}$ for both samples. This is further verified by the reported density of the ZrV_2 compound as 6.50 $g.cm^{-3}$ [340]. As these densities are consistent, it follows that the weight percent of precipitates is equal to their volume percentage. Following this, the molar percentage of ZrV_2 in the microstructure is calculated using the molar masses of both zirconium and the ZrV_2 compound. This yields a ZrV_2 concentration of 1.93 mol%.

Given this concentration of precipitates, and the known overall concentration of vanadium in the material as shown in Table 4-1 (2.43 at%), it is possible to calculate the concentration of vanadium solute in solution in the zirconium matrix. This gives a concentration of vanadium in solution of approximately 1.2 at%.

If this calculation of the solubility of vanadium in zirconium were correct, there would be no precipitation of ZrV_2 in the Zr1V alloy as the total concentration of vanadium in the alloy would be less than the maximum amount of solid solubility. However, it can be seen in the micrograph shown in Figure 5-6(c) that this is not the case and that the precipitates do form in this alloy, therefore indicating that the substitutional solid solubility of vanadium in aluminium is less than 1 at%.

Given these two conflicting pieces of information it may be concluded that the substitutional solid solubility of vanadium in aluminium is not much less than 1 at%. It is thought that the error in the calculations of this value detailed above may arise from the possibility that smaller vanadium-rich precipitates exist in the microstructure of Zr2.5V which are not visible in Figure 4-29(b), or that the region examined in this micrograph may not be completely representative of the entire sample.

4.9.1.2 Calculating the atomic misfits of the solutes

In addition to the extent of solid solubility, the misfit (δ) of the substitutional solutes must be calculated for an estimation of the strengthening imparted by this mechanism. The misfit is calculated using the relationship between the metallic radii (r) of the constituent elements and the misfit (δ) as shown below in Equation 4-1.

Equation 4-1

$$1 + \delta = {}^{r_{solute}}/_{r_{solvent}}$$

The metallic radii were identified from [341] leading to misfit values of -0.106, -0.088, -0.088 and -0.163 for aluminium, niobium, tantalum and vanadium respectively in zirconium.

As a result of these calculations, the increase in yield strength as a function of solute concentration in solid solution measured as 100 MPa.at%$^{-1}$ [339] is scaled to 120 MPa.at%$^{-1}$, 100 MPa.at%$^{-1}$ and 185 MPa.at%$^{-1}$ for solutes aluminium, tantalum and vanadium respectively.

4.9.2 Precipitation strengthening in the alloys

The increase in yield strength due to the Orowan bowing mechanism of dislocations around precipitates may be estimated using the relationship between the increase in critical resolved shear stress due to the mechanism ($\Delta\tau$), the Young's modulus of the material (E), the material Poisson ration (ν), the Burgers vector (**b**), and the spacing between precipitates (Λ) shown in Equation 4-2 [342].

Equation 4-2

$$\Delta\tau = {}^{E \cdot |\boldsymbol{b}|}/_{2 \cdot (1+\nu) \cdot \Lambda}$$

The expected increase in yield stress ($\Delta\sigma_y$), therefore, may be calculated by dividing the increase in critical resolved shear stress ($\Delta\tau$) by the maximum Schmid factor, 0.5, according to Schmid's law.

To calculate the expected increase in yield stress for each alloy due to precipitation strengthening by Orowan bowing, the Young's modulus is taken from the tensile testing

data shown in Table 4-4. The Burgers vector magnitude is calculated from the lattice parameter (a) which is shown as 3.235 Å by the XRD data in Figure 4-21, and the Burgers vector for prismatic slip in hcp, <-1,2,-1,0>, which has a magnitude of: $a \cdot \sqrt{5}$, where a is the lattice parameter. This gives a Burgers vector magnitude of 7.23 Å. The Poisson ratio is taken as 0.34 [343]. Estimation of the precipitate spacing in the alloys is discussed in the following section.

4.9.2.1 Calculating the precipitate spacing

The precipitation spacing in the Zr2.5V alloy is calculated from the ImageJ micrograph analysis discussed in 4.9.1.1. The results of this analysis were a precipitate volume fraction of 4%, and an average precipitate area of 0.01 μm^2. By assuming that the precipitates are spherical, this average precipitate area may be converted to an average precipitate radius (r_p) of 0.089 μm – accounting for the fact that precipitates will be randomly sectioned away from their equatorial plane with a geometrical factor of $\pi \cdot ½$. This precipitate radius, along with the volume percentage of precipitates (4%), may be used to calculate the precipitate spacing (Λ) by assuming that each precipitate is contained within a cube of side length $\Lambda+2r_p$, where the precipitate occupies 4% of the volume of this cube, leading to a precipitate spacing (Λ) of 0.24 μm.

Using the same method as for the Zr2.5V alloy, the precipitate spacing is calculated within the prior-β-Zr grain shown in Figure 4-34(b) of Zr2.5Ta. As this precipitate-dense grain has been selected, it is expected that the extent of precipitate strengthening will be significantly over-estimated, however it is thought this area selection is necessary to accurately estimate the precipitate spacing. Image thresholding analysis in the ImageJ software gave an average precipitate radius of 0.028 μm and a precipitate

volume percentage of 4.9%. This leads to a calculation of the precipitate spacing (Λ) as approximately 0.07 μm.

For the Zr2.5Al alloy, it is thought that the precipitate spacing shown in Figure 4-24 and Figure 4-26 is sufficiently inconsistent that a calculation of average precipitate spacing would yield an accurate calculation of strengthening. Additionally, the significantly greater spacing of precipitates shown in the Zr2.5Al alloy compared with the other two alloys discussed above would lead to a substantially lower strengthening effect.

4.9.3 Zr-Al alloy predicted strengthening mechanisms

The increase in yield strength from the pure Zr sample to the Zr2.5Al alloy, as measured by ETMT and discussed in 4.6.1, is +181.0 MPa, as shown in Table 4-4.

It was shown that the solid solution strengthening contribution to increase in yield strength was approximated as +120 MPa.at%$^{-1}$ in section 4.9.1.2, with the extent of solid solubility taken as 2 at% as discussed in section 4.9.1.1. This would lead to a prediction of the increase in yield strength of approximately +240 MPa, which is greater than the +181 MPa observed. One factor in this discrepancy may be the fact that the effect of modulus alterations by the solute has not been considered. It is therefore concluded that solid solution strengthening is the dominant strengthening mechanism in the Zr2.5Al alloy.

4.9.4 Zr-Ta alloy predicted strengthening mechanisms

The increase in yield strength from the pure Zr sample to the Zr2.5Ta alloy, as measured by ETMT and discussed in 4.6.1, is +266.2 MPa, as shown in Table 4-4.

It was shown that the solid solution strengthening contribution to increase in yield strength was approximated as +100 MPa.at%$^{-1}$ in section 4.9.1.2, with the extent of solid solubility taken as 0.4 at% as discussed in section 4.9.1.1. This would lead to a prediction of the increase in yield strength of approximately +40 MPa.

Using the method discussed and parameters calculated in section 4.9.2, the contribution of precipitation strengthening to the increase in yield stress in the prior-β-Zr grain is +670 MPa. This is far greater than the strengthening observed in this alloy, which may be attributed to the fact that the α-Zr grains in the microstructure are strengthened significantly less.

It is therefore concluded that the strengthening observed in this alloy is dominated by the effects of precipitation strengthening above the effects of solid solution strengthening.

4.9.5 Zr-V alloy predicted strengthening mechanisms

The increase in yield strength from the pure Zr sample to the Zr2.5V alloy, as measured by ETMT and discussed in 4.6.1, is +159.6 MPa, as shown in Table 4-4.

It was shown that the solid solution strengthening contribution to increase in yield strength was approximated as +185 MPa.at%$^{-1}$ in section 4.9.1.2, with the extent of solid solubility taken as <1 at% as discussed in section 4.9.1.1. This would lead to a prediction of the increase in yield strength of approximately +165 MPa if the solid solubility were taken as approximately 0.9 at%.

Using the method discussed and parameters calculated in section 4.9.2, the contribution of precipitation strengthening to the increase in yield stress of the Zr2.5V sample is +180 MPa. This, in combination with the solid solution strengthening effect calculated above, is greater than the strengthening observed in this alloy. The reason for this is thought to be the fact that a significant proportion of the precipitates observed in the alloy are at the grain boundaries, as shown in Figure 4-29. Precipitates located at the grain boundaries are likely to have little effect on strengthening – beyond grain refinement – as they do not contribute a substantial further barrier to dislocation motion than the existing boundary. As a result, it is likely that the prediction of additional yield strength resulting from precipitation strengthening here is an over-estimation.

It is therefore concluded that the strengthening observed in this alloy is mostly as a result of solid solution strengthening because the increase in yield stress observed is very similar to the increase in yield stress predicted due to solid solution strengthening.

4.9.6 Considerations for creep deformation resistance

Due to the failure of the creep testing measurements, it is difficult to determine the microstructural contributions to creep deformation resistance in these alloys. Further difficulties result due to the unknown stress and temperature state expected in-service due to immature engineering designs of fusion power plants. However, it is expected that a diffusion-based creep mechanism is likely to dominate at the temperatures and stresses anticipated in-service. Therefore, the presence of fast diffusion pathways, such as grain boundaries and dislocation lines, would likely enhance creep deformation, meaning that strengthening by Hall-Petch and work hardening mechanisms is less desirable. This would lead to a desire for a more coarse grain structure, and the strengthening contribution

would therefore be more reliant on the solid solution and precipitate mechanisms. The presence of precipitates at grain boundaries may also be desirable to inhibit deformation at the boundaries.

5 Analysis of Thermal Treatments of Novel Zirconium Alloys

5.1 Aim

For a material to be applicable for operation in the high temperature environment of a fusion breeder blanket, it must display stability of its microstructure and mechanical properties during operation to ensure that unexpected changes in component performance do not occur in-service. This section of the study will look to simulate in-service conditions, and then to characterise and test the resultant material to draw conclusions about its thermal stability. Therefore, conclusions on the potential suitability of these materials for application in a fusion breeder blanket may be drawn.

5.2 Thermal conditions and simulation method

5.2.1 Isothermal ageing

As has previously been identified, the expected steady-state operating temperature of the structural material for the fusion breeder blanket is not precisely defined due to the current lack of maturity of reactor designs. However, a temperature of approximately 500-600 °C is expected in steady-state operations [80]. This expected operation temperature is within the α-Zr phase region of the binary phase diagrams shown in section

2.4.2. The period of time for which the material is expected to be exposed to this temperature is expected to be multiple years in an operating fusion power plant, which would be unrealistic to replicate in this study.

In order to achieve significant ageing of the material within more reasonable time periods to assess the microstructural stability of the tested materials, a more elevated temperature may be applied to accelerate the effects. However, it is important that the temperature is not increased so much that the treatment is no longer representative of the conditions which are likely to be experienced in-service. Therefore, the increased temperature used in this study should remain within the same phase regime of the relevant binary phase diagrams shown in section 2.4.2. To fulfil this, a temperature of 700 °C was chosen for this study to compare the microstructural stability of the alloys under isothermal conditions and the effects of this on the materials properties.

As discussed in section 4.2.6, severe oxidation of zirconium should be avoided during the exposure of the material samples to such elevated temperatures as this would not resemble the expected fusion environment. Therefore, the samples were encased within a silica tube which was evacuated to approximately 10^{-6} mbar and backfilled with argon to improve the conduction of heat within the tube. The samples in the silica tube were introduced to a preheated furnace for the durations specified below, before being removed from the furnace and allowed to cool to ambient temperature and prepared for examination as detailed in section 3.1.

5.2.2 Transient heating

Along with the steady-state elevated operating temperature, transient occurrences of increased temperature of the structural material are expected. This is caused by the occurrence of plasma disturbances such as edge-localised modes (ELMs) which will deposit large heat loads on the plasma facing material [344], [345]. Although these disruptions may be mitigated by control methods such as resonant magnetic perturbation fields [346], thousands of such disruptions are expected to occur over the lifetime of a fusion reactor [61], [347], [348]. The materials which are the subject of this study are not proposed as plasma-facing materials but they will be nonetheless impacted by the high thermal load deposition resulting from plasma disruptions due to the conduction of heat from the plasma-facing material through the breeder blanket structural material and into the coolant fluid of the breeder blanket.

Whilst the literature relating to the effect of disruptions on the plasma facing material is extensive [60], [349]–[353], investigations in to the effects of these events on the local structural components is scarce. This has been addressed by researchers at the University of Bristol who have used details of the WCLL breeding module of the DEMO reactor to predict the temperature profile experienced by the structural material from a given heat load on the plasma facing material caused by a mitigated plasma disruption [61]. These findings show a maximum temperature of the structural material of approximately 850 °C, returning to the steady-state temperature within a few seconds.

Further to this modelling study, a method has been developed to simulate these conditions and observe their effects on the microstructures of materials. This makes use of a laser heating apparatus to rapidly heat the material sample in a controlled manner

described in more detail in [61], [348], [354]. Using this method, the sample is held in vacuum to avoid oxidation, with its temperature measured by an infrared spot pyrometer with a maximum uncertainty of 2 °C. The rate of heating and cooling of the sample achieved by this method is significantly less than expected in-service as a heating and cooling cycle takes approximately 80 seconds, as opposed to approximately 8 seconds in the modelled scenario [61].

Using this technique, the microstructural stability of Eurofer has been examined under conditions designed to be representative of the conditions expected in-service based on the modelling from [61]. Examination of the microstructure reveals that a single thermal transient with a peak temperature of 700 °C (150 °C below the predicted value) is sufficient to transform the phase structure of this martensitic steel to equiaxed ferrite grains and carbide precipitates [355], as shown in Figure 5-1 which is reproduced from [355]. Further transient treatments up to 1500 cycles with a maximum temperature of 850 °C are found to significantly coarsen the size of both the precipitates and the grains [348], [355], and this has a serious effect on the mechanical properties of Eurofer [348].

Results from equivalent testing with zirconium alloy samples will be presented in section 5.3.2.1, showing their resistance to microstructural alterations under transient heating conditions and the effects of this on mechanical properties.

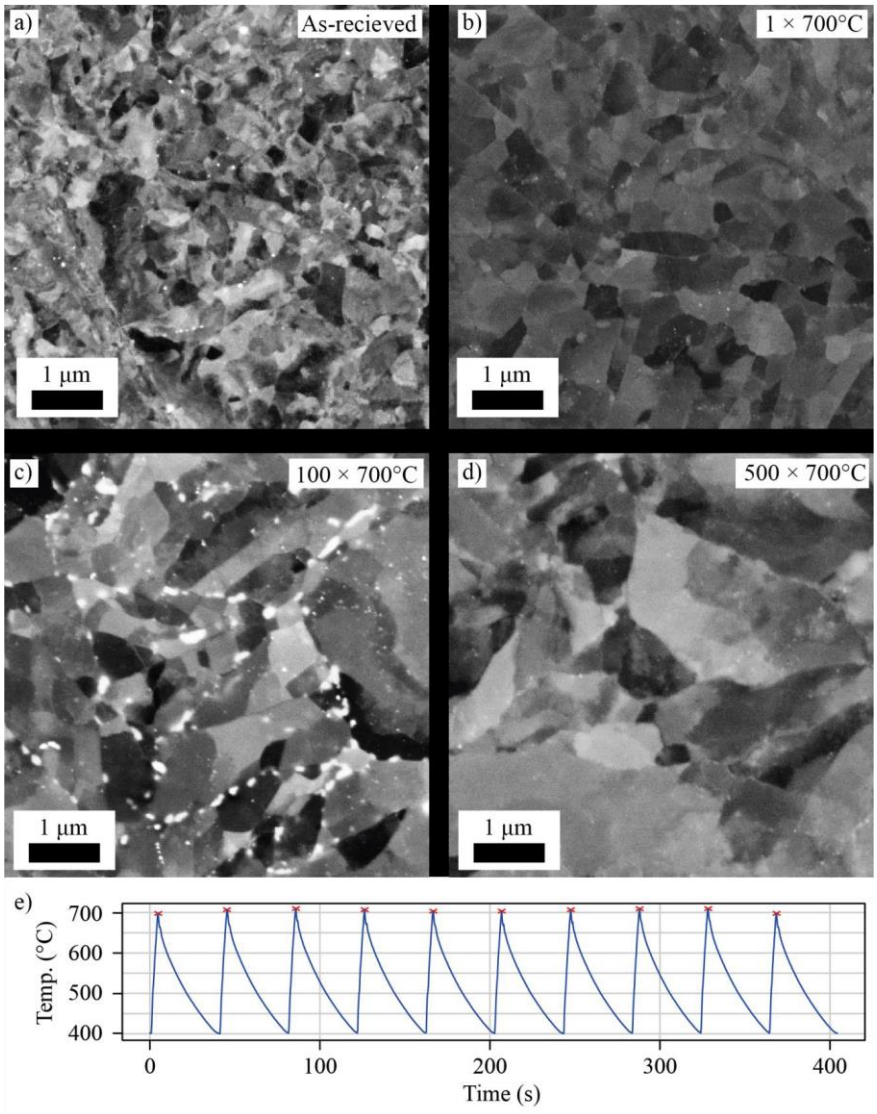


Figure 5-1: Backscattered electron micrographs of Eurofer 97 in the as-received condition (a) and exposed to 1 (b), 100 (c), and 500 (d) thermal transients with peak temperatures of 700 °C. e) Pyrometer measurements of sample temperature during transient thermal exposure (a subset of 10 transients). From [355] [vi].

5.3 Results

Alloys were tested under different condition of elevated temperature, and their thermal stability was evaluated through microstructural characterisation and mechanical testing. Results of these experiments are shown in this section and evaluation of this data

allows some conclusions to be drawn about the thermal stability of these materials, and therefore their applicability as fusion breeder blanket structural materials.

5.3.1 Zirconium-vanadium

Optical microscopy of the Zr2.5V alloy following isothermal ageing at 700 °C for 200 hours is shown in Figure 5-2(c). This indicates substantial coarsening of the grain structure in comparison with the micron-scale grain structure observed in the alloy prior to ageing as shown in Figure 4-29(b), reproduced below, and calculated as 1.5 μm by EBSD in section 4.5.3. The line intercept method of grain size measurement as described in section 4.5.1 indicated grain sizes of 0.94 ±0.15 μm before ageing, compared with 243 ±129 μm after ageing. Despite this significant coarsening, a fine distribution of precipitates, identified as ZrV_2 Laves precipitates in the alloy before ageing, remains visible by BSE imaging as shown in Figure 5-2(a). The size and distribution of these precipitates may be compared with their character prior to ageing, using Figure 5-2(b) and Figure 4-29(a), reproduced below. A quantitative comparison of the size distribution of the precipitates before and after ageing was performed using image contrast thresholding and particle analysis in ImageJ software, shown in Figure 5-3. Although substantial coarsening of the precipitate size is observed following ageing of Zr2.5V, the length scale remains of the same order of magnitude, unlike the length scale of the grain sizes.

This indicates that whilst the Laves precipitates are relatively stable in the microstructure, they do not effectively pin grain boundaries to prevent the coarsening of the microstructure at 700 °C.

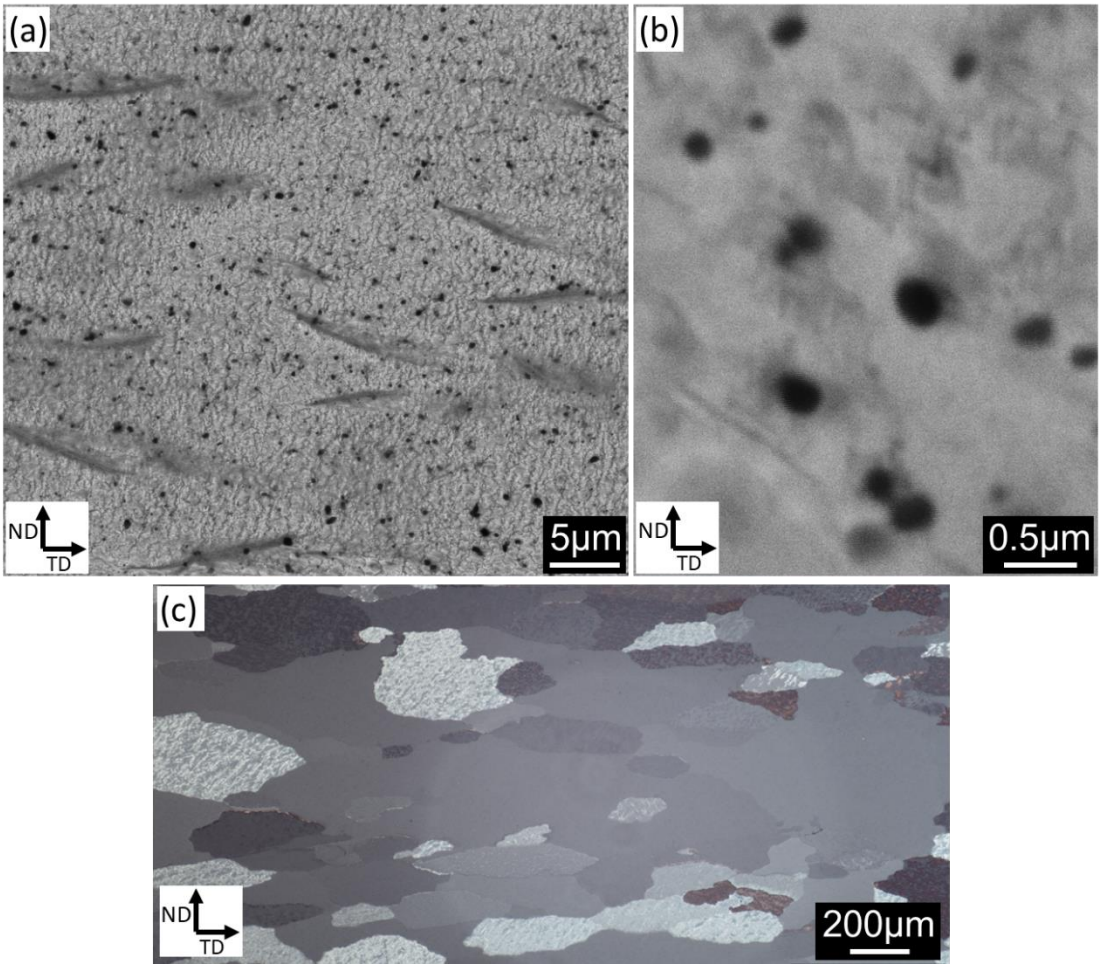


Figure 5-2: (a,b) BSE micrographs and (b) optical micrograph with crossed polarising filters of the Zr2.5V alloy after ageing at 700 °C for 200 hours. The arrows labelled ND and TD represent the normal and transverse directions respectively with respect to the rolling treatment.

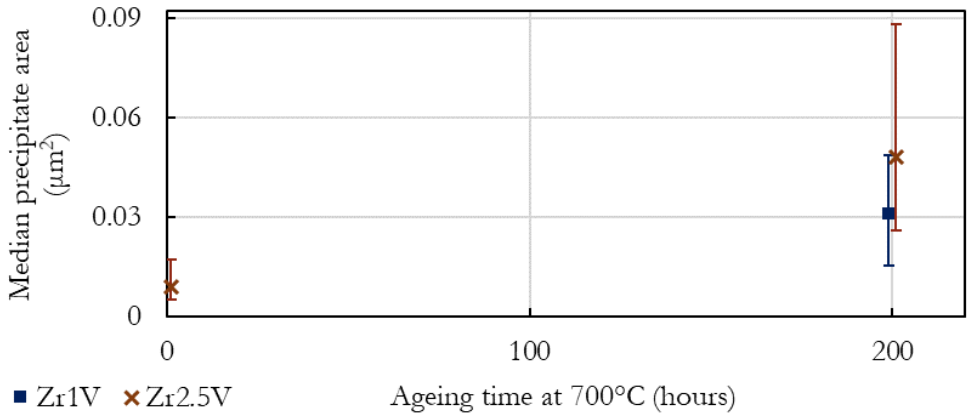


Figure 5-3: Results of ImageJ software precipitate analysis from the micrographs in Figure 5-2(a), Figure 4-29(b), and Figure 5-6(c), indicating the median precipitate area with the error indicating the interquartile range of the measured values.

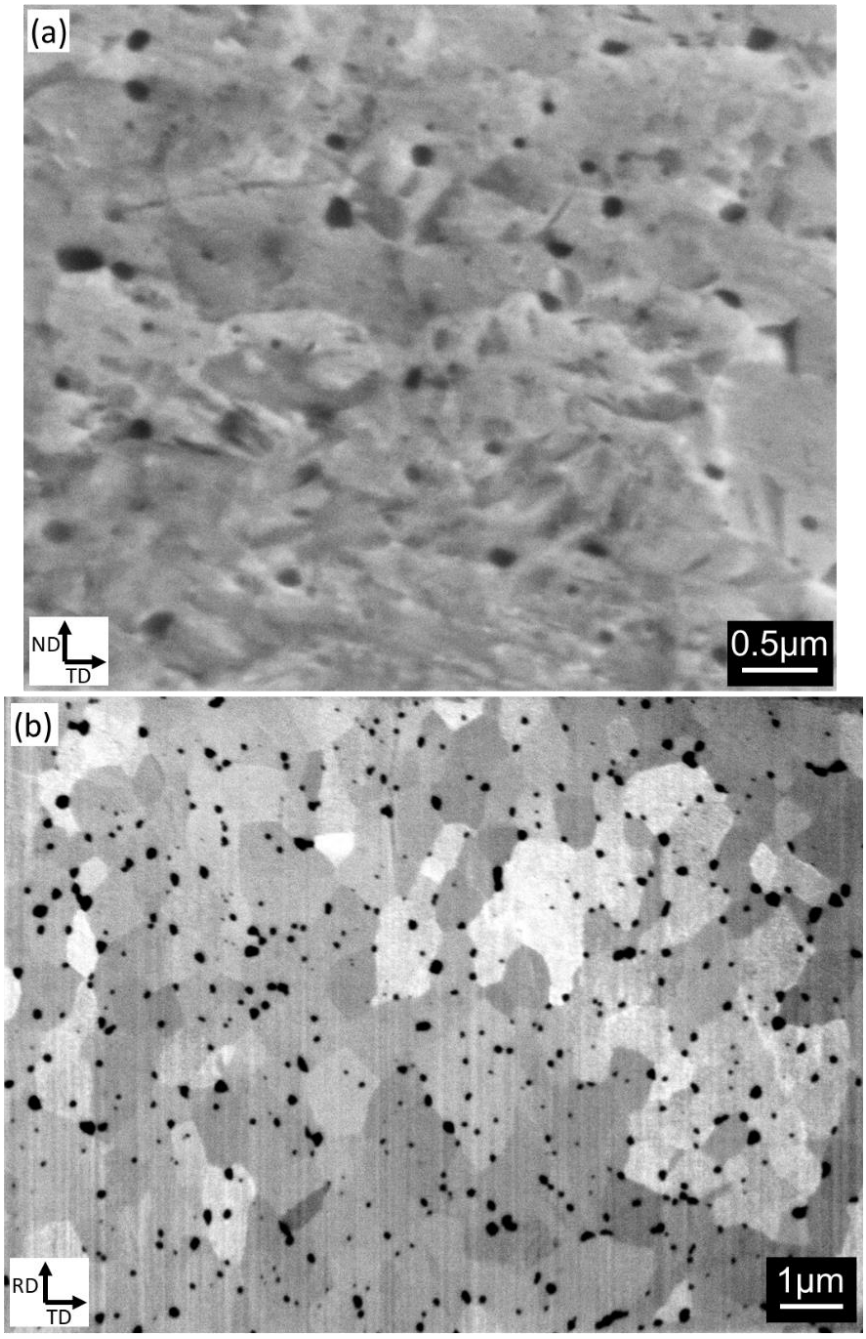


Figure 4-29 [Reproduced for comparison with Figure 5-2]: (a) surface SE micrograph and (b) SE micrograph of a thin lift-out by Dr Junliang Liu of the Zr2.5V alloy following annealing. The arrows labelled ND, TD and RD represent the normal, transverse, and rolling directions respectively with respect to the rolling treatment.

As would be expected due to the reduction in Hall-Petch strengthening caused by the coarsening of the grain structure, significantly reduced strength is displayed by the aged Zr2.5V alloy, compared with the same alloy before ageing. This is shown in Figure 5-4, although the trend of reduced strength following ageing shown in the tests at room temperature and 300 °C is not continued in the data collected at 600 °C. It is thought that the need to hold the as-annealed sample (prior to the 200-hour ageing treatment) at elevated temperature will have resulted in coarsening of the grain structure due to the lack of stability shown in Figure 5-2(c) and discussed above. Therefore, the effect of softening due to grain coarsening is likely to be less of an effect following ageing, and the difference in strength shown in Figure 5-4(c) may be attributed to the variation in hardness of different crystallographic orientations of the material. Due to the coarsening of the grain structure described above and the indentation stress field volume identified in section 3.3, the data collected by nanoindentation in these two samples is more likely to be dependent on a single measured grain, rather than the indentation response being more representative of the overall material as is the case with finer grained materials. The effect of grain coarsening during the testing procedure at 600 °C also contributes an explanation for the reduction in strength displayed by Zr2.5V at 600 °C in nanoindentation testing (Figure 4-46(c)) compared with ETMT (Figure 4-43 and Figure 4-44), relative to the other annealed materials tested. This is due to the fact that samples are not held at the elevated temperature for a significant period of time in the ETMT testing procedure. Therefore, in materials which may be expected to display significant softening due to ageing, the strength of the annealed material demonstrated by nanoindentation testing at elevated temperatures may be reduced compared with the strength measured at the same temperature by ETMT.

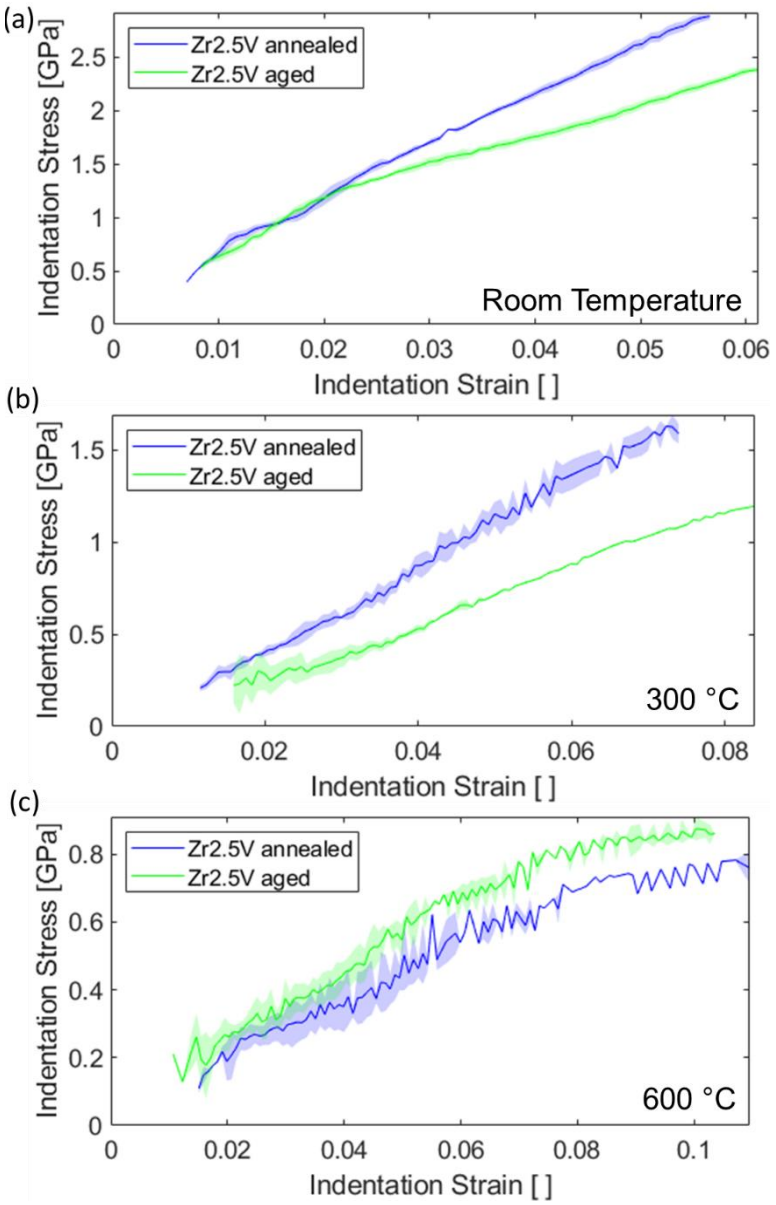


Figure 5-4: Nanoindentation flow curves of the Zr2.5V alloy before (blue) and after (green) ageing at 700 °C for 200 hours, and testing at (a) room temperature, (b) 300 °C, and (c) 600 °C.

In contrast with the significant grain coarsening observed in Zr2.5V after ageing at 700 °C for 200 hours, a much greater stability of the grain structure is observed following ageing of the Zr1V alloy at the same temperature for both 200 and 1343 hours in Figure 5-6(a,b,d), despite its lower solute percentage. Although a slight coarsening of the Zr1V grain structure may be observed, it is significantly less than the severe grain coarsening observed in the Zr2.5V alloy in Figure 5-2. The relatively consistent grain size

in the Zr1V alloy following ageing treatments is shown by the comparison of grain sizes measured by the line intercept method (as described in section 4.5.1) in Figure 5-5.

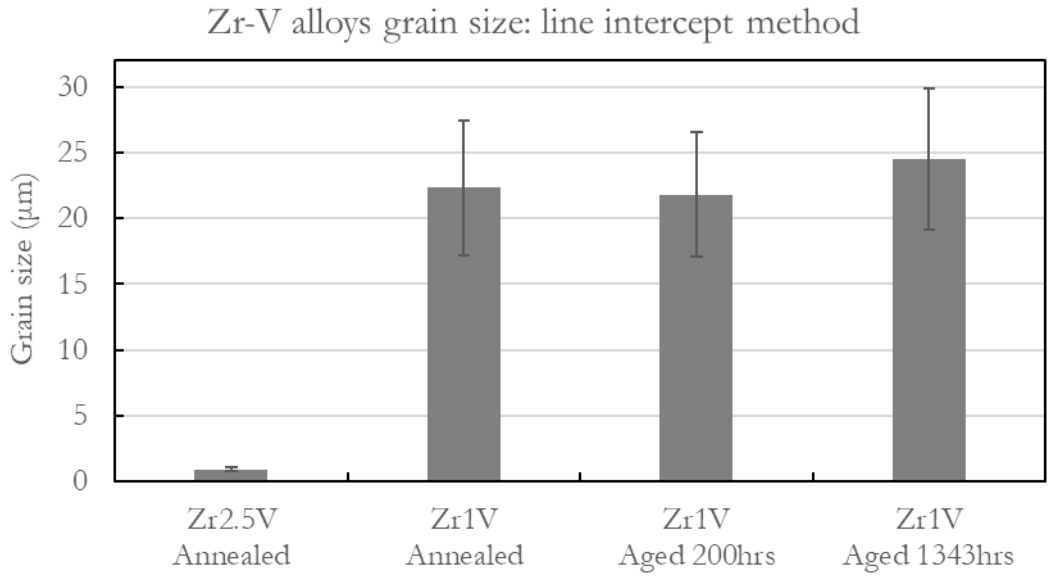


Figure 5-5: Comparison of the approximate grain sizes of Zr-V alloys of different compositions and ageing treatments, as measured by the line intercept method described in section 4.5.1 from the micrographs in Figure 4-29(b) and Figure 5-6.

In addition, the retention of fine, dispersed precipitates in the microstructure of Zr1V following ageing is observed in Figure 5-6(c) with examples indicated by the red arrows on the micrograph, similar to that observed for the Zr2.5V alloy in Figure 5-2(a). The similarity in size distribution of precipitates between the two compositions is shown quantitatively in Figure 5-3.

The observation of limited grain coarsening in Zr1V following ageing is consistent with the relatively small reduction in strength generally observed when comparing the alloy before and after the 200-hour ageing treatment in Figure 5-7. Although noticeable, the difference in strengths observed is generally less severe than is observed for the

Zr2.5V alloy in Figure 5-4, as would be expected given the lesser extent of coarsening seen.

A comparison may also be made between the grain sizes observed for the annealed Zr1V and Zr2.5V alloys prior to ageing, shown in Figure 5-6(a) and Figure 4-29(b) (reproduced above) respectively, indicating that the increased solute percentage of Zr2.5V has resulted in a much finer grain structure than is seen in Zr1V. The significant difference between the grain size of these two alloys following annealing is shown in Figure 5-5. Although the observation of more significant coarsening in an alloy with higher solute percentage may be surprising, this may be explained by the much finer initial grain size in the Zr2.5V alloy leading to a much greater driving force for grain coarsening.

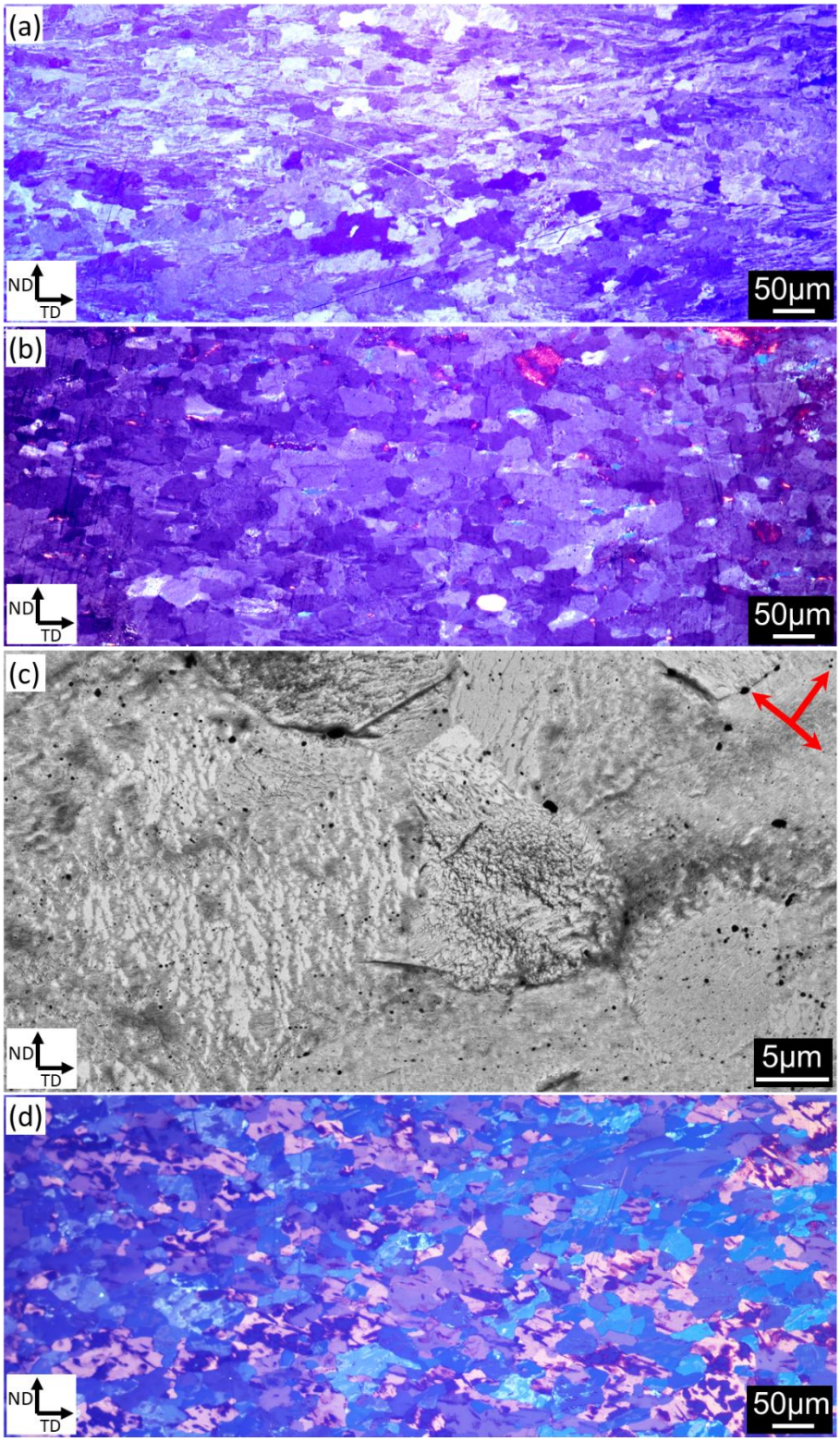


Figure 5-6: (a,b,d) Optical micrographs with crossed polarising filters and (c) BSE micrograph of the Zr1V alloy (a) before and after ageing at 700 °C for (b,c) 200 hours and (d) 1343 hours. The arrows labelled ND and TD represent the normal and transverse directions respectively with respect to the rolling treatment. The red arrows in (c) indicate precipitates in the microstructure.

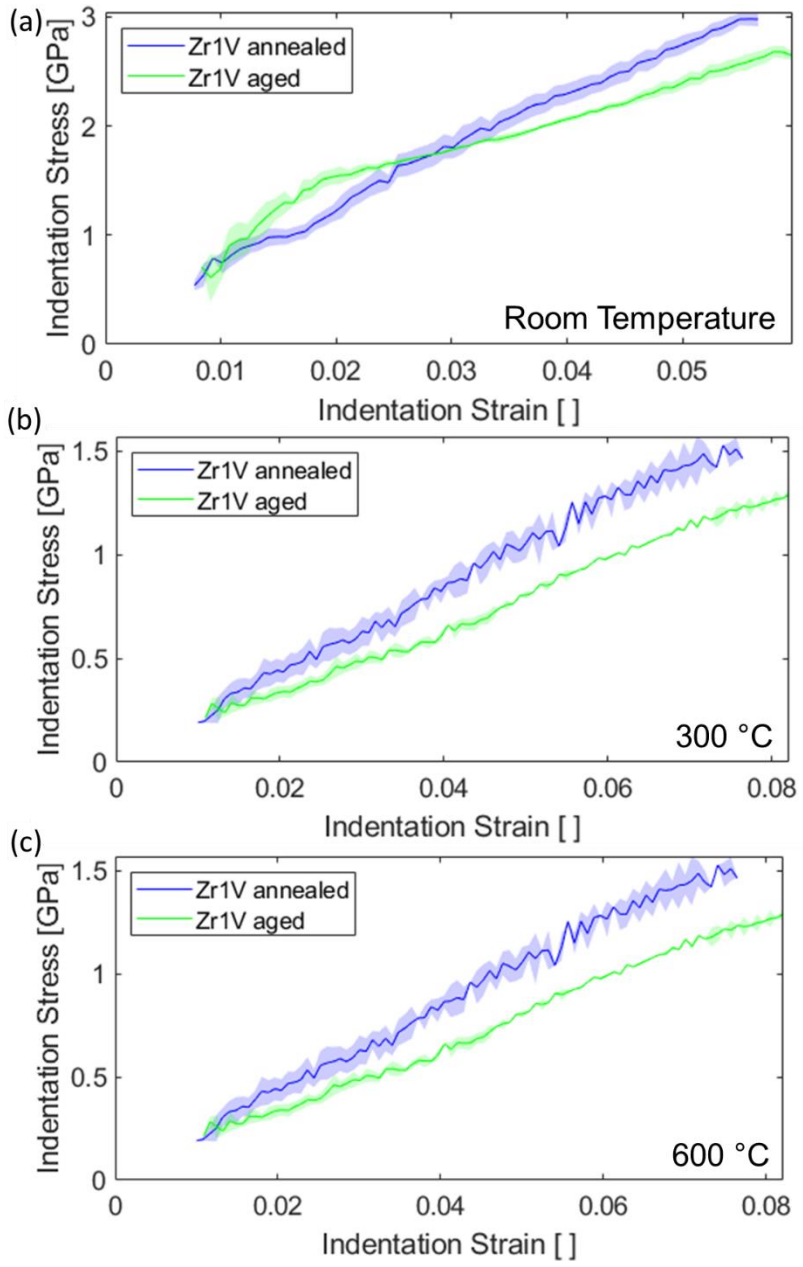


Figure 5-7: Nanoindentation flow curves of the Zr1V alloy before (blue) and after (green) ageing at 700 °C for 200 hours, and testing at (a) room temperature, (b) 300 °C, and (c) 600 °C.

5.3.2 Zirconium-tantalum

Microstructural analysis of the Zr2.5Ta alloy by optical microscopy following isothermal ageing at 700 °C under argon is shown in Figure 5-10(b,c). This may be compared with the grain structure before ageing, shown in Figure 5-10(a), indicating that the length scale and morphology of the overall grain structure is relatively unchanged as

a result of the ageing treatments. This is confirmed by the EBSD analysis shown in Figure 5-8 for which a grain size of 4.1 μm was measured in comparison with 3.4 μm prior to ageing, this comparison is shown in Figure 5-9. Both of these measurements were made using the method outlined in section 3.5.2 with a misorientation threshold of 3° and a minimum pixel threshold of 8. EBSD analysis does indicate a reduction in the crystallographic texture following ageing with Kearns factors for the aged sample calculated as f_{ND}=0.33, f_{TD}=0.31, f_{RD}=0.36 (compared with f_{ND}=0.31, f_{TD}=0.19, f_{RD}=0.50 prior to ageing).

The same approximate length scale and morphology of the grain structure can also be seen in the Zr1Ta alloy in Figure 5-11, both before and after ageing for 200 hours, despite the lower solute percentage. Comparison of the grain sizes – showing similar grain sizes in the annealed samples of Zr1Ta and Zr2.5Ta – by the line intercept method described in section 4.5.1 is shown in Figure 5-9. However, after ageing for 1343 hours, extensive coarsening of the grain structure is observed in the Zr1Ta alloy in Figure 5-11(c), indicating that 1 at% of tantalum in the alloy is unlikely to be sufficient to maintain a refined grain structure in-service.

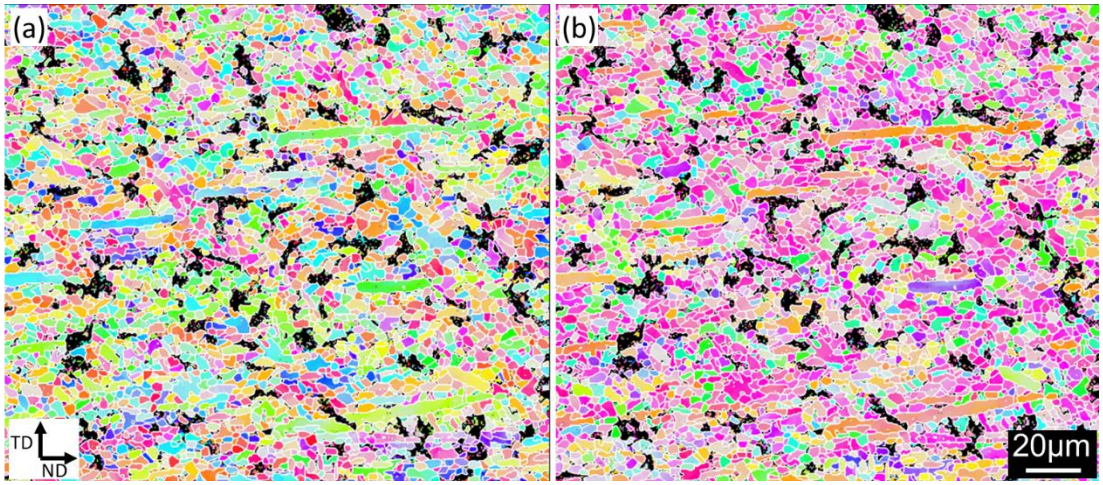


Figure 5-8: EBSD data of the Zr2.5Ta sample following ageing at 700 °C for 1343 hours showing the crystallographic alignment of measured pixels with (a) the normal direction and (b) the rolling direction with reference to the colour scale shown in Figure 3-7 with calculated grain boundaries overlaid in white.

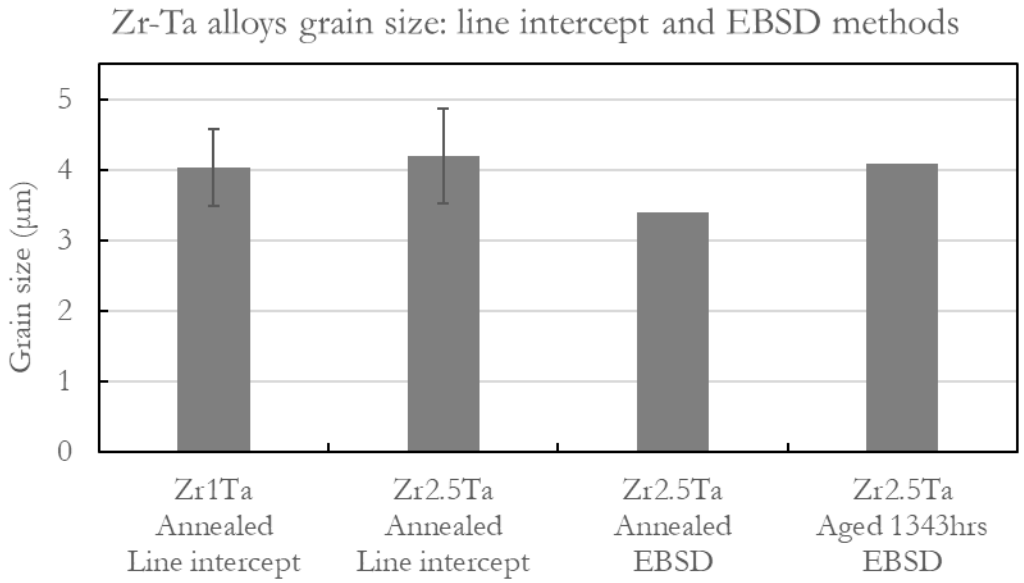


Figure 5-9: Comparison of the approximate grain sizes of Zr-Ta alloys of different compositions and ageing treatments, as measured by the line intercept method described in section 4.5.1 from the micrographs in Figure 5-10(a) and Figure 5-11(a) and from EBSD data shown in Figure 4-38 and Figure 5-8.

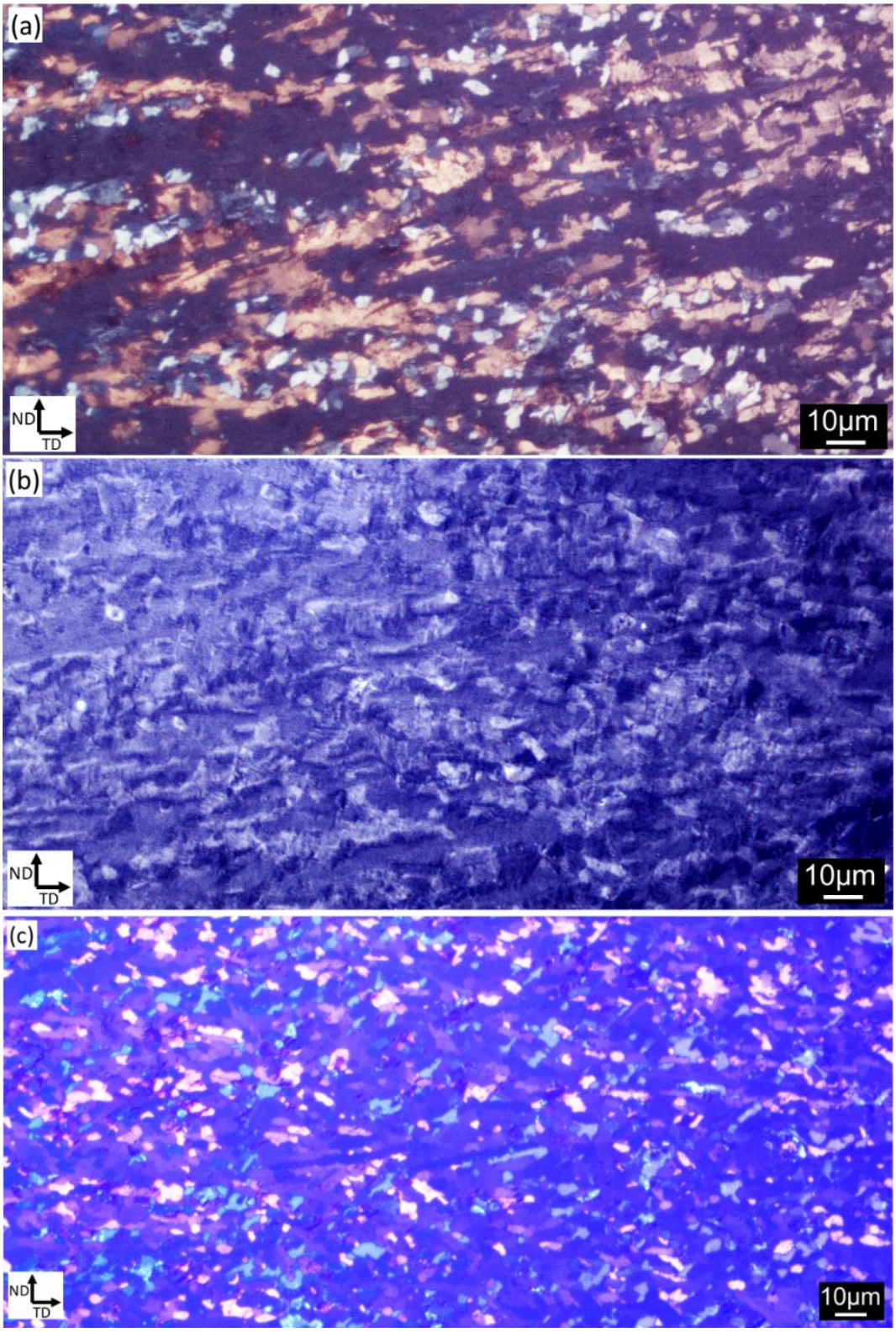


Figure 5-10: Optical micrograph with crossed polarising filters of the Zr2.5Ta alloy after ageing at 700 °C for (a) 200 hours and (b) 1343 hours. The arrows labelled ND and TD represent the normal and transverse directions respectively with respect to the rolling treatment.

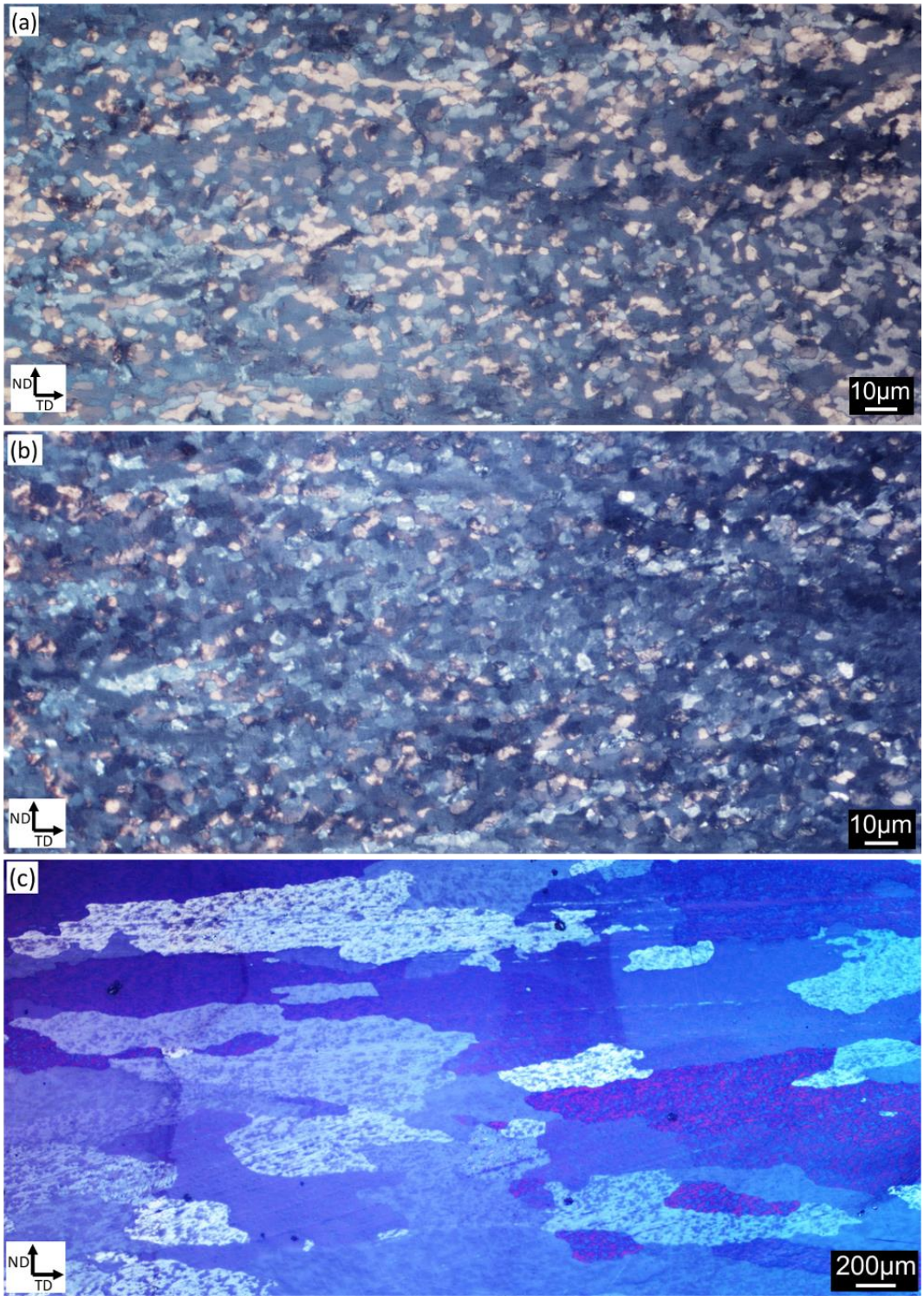


Figure 5-11: Optical micrographs with crossed polarising filters of the Zr1Ta alloy (a) before and (b,c) after ageing at 700 °C for (b) 200 hours and (c) 1343 hours. The arrows labelled ND and TD represent the normal and transverse directions respectively with respect to the rolling treatment.

SEM analysis of the Zr2.5Ta microstructure following isothermal ageing in Figure 5-12 confirms the grain structure observed in Figure 5-10. This analysis also indicates that the bimodal microstructure has remained, including α-Zr grains, prior-β-Zr grains with banded intragranular precipitates, and intergranular precipitates as discussed in sections 4.5.4 and 4.7.1. Although the overall structure appears unchanged, some coarsening of the intergranular precipitates can be seen following isothermal ageing when comparing the different thermal treatments shown in Figure 5-12. Quantitative analysis of the intergranular precipitates was performed to confirm the observed coarsening using image contrast thresholding and particle analysis in ImageJ software, shown in Figure 5-13. This is consistent with the increased diffusivity of the tantalum due to the elevated temperature and the relatively fast diffusion paths offered by grain boundaries as a result of the increased free volume in these regions.

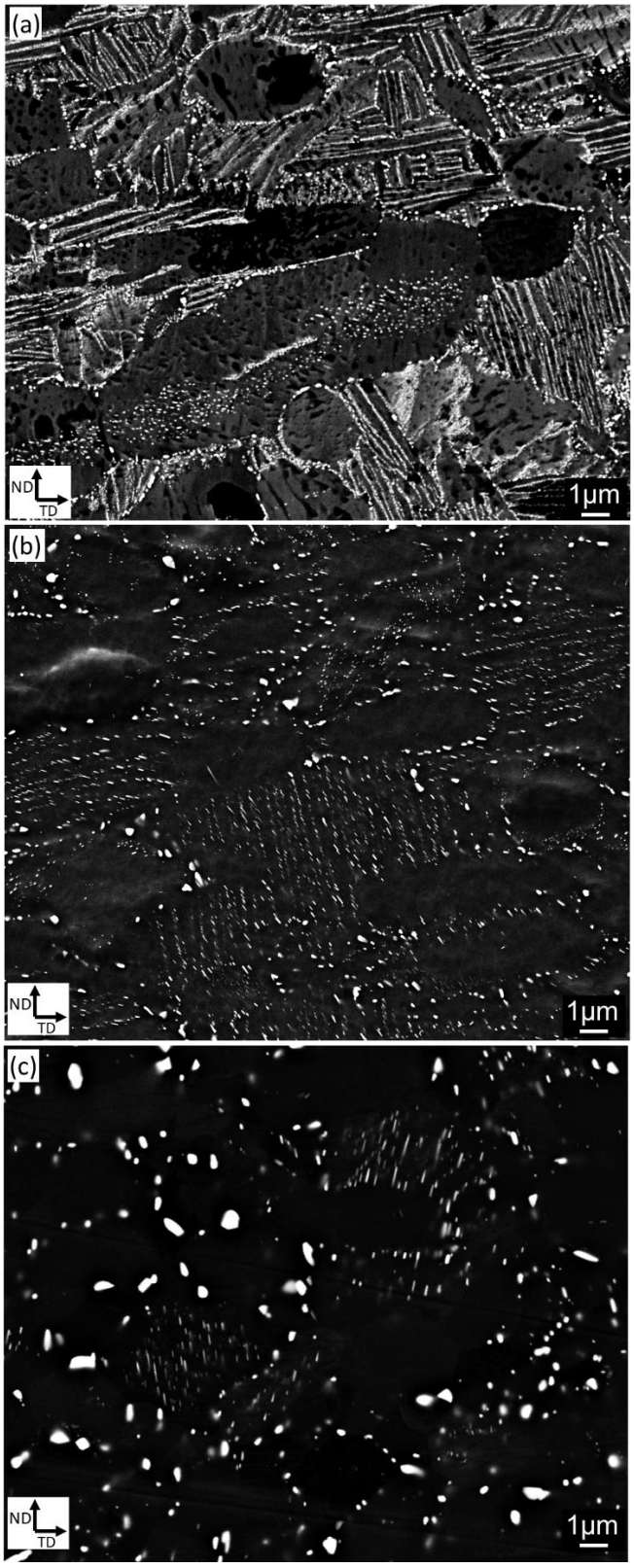


Figure 5-12: BSE micrographs of (a) the annealed Zr2.5Ta alloy following ageing (b,c) at 700 °C for (b) 200 hours and (c) 1343 hours. The arrows labelled ND and TD represent the normal and transverse directions respectively with respect to the rolling treatment.

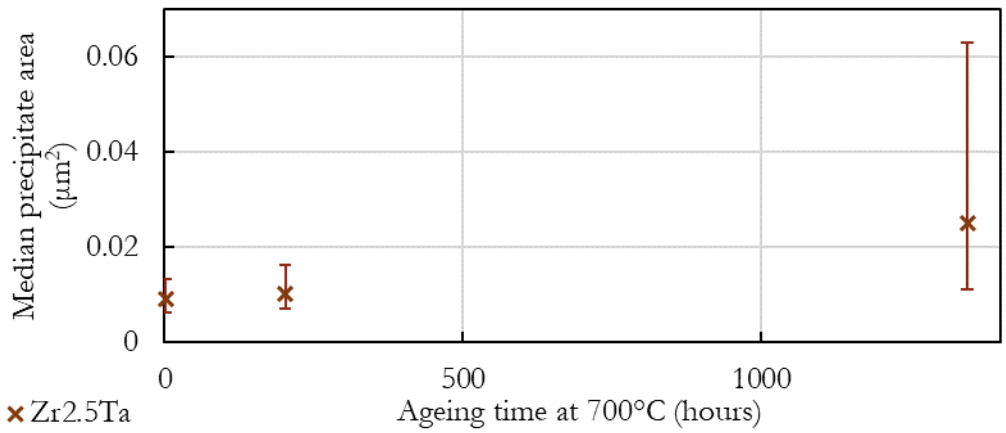


Figure 5-13: Results of ImageJ software precipitate analysis from the micrographs in Figure 5-12, indicating the median intergranular precipitate area with the error indicating the interquartile range of the measured values.

Flow curves were obtained from the Zr-Ta alloys at room temperature, 300 °C and 600 °C using the MicroMaterials NanoTest Extreme machine and the method outlined in section 3.3 to compare the strength displayed by the material before and after ageing at 700 °C for 200 hours. The results are shown in Figure 5-14 and Figure 5-15 which can be seen to show relatively consistent strengths of the alloy following the ageing treatment. A slight softening following ageing is observed for both the alloys, which may be attributed to a reduction in microstructural defect density. However, this softening is not significant in comparison with that observed in the Zr-V alloys in Figure 5-4 and Figure 5-7. In addition, the softening effects appear remain minimal at 600 °C, the test most representative of the anticipated in-service conditions.

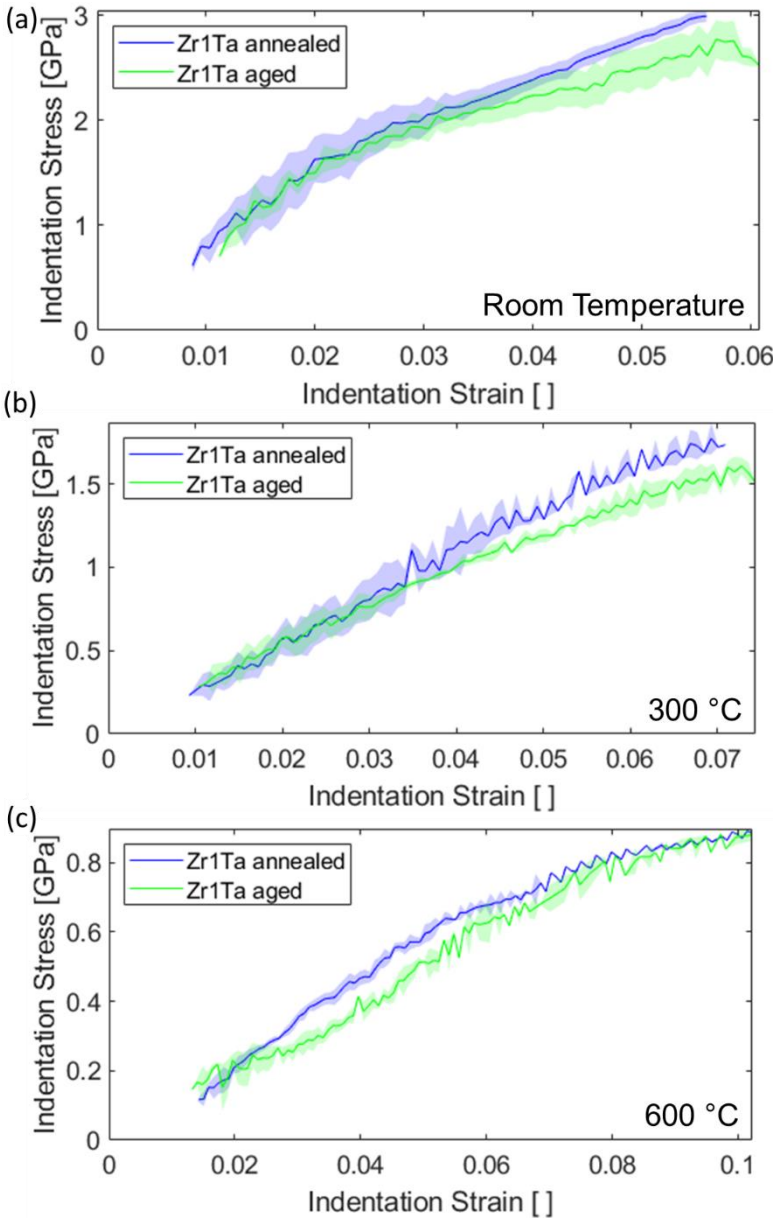


Figure 5-14: Nanoindentation flow curves of the Zr1Ta alloy before (blue) and after (green) ageing at 700 °C for 200 hours, and tested at (a) room temperature, (b) 300 °C, and (c) 600 °C.

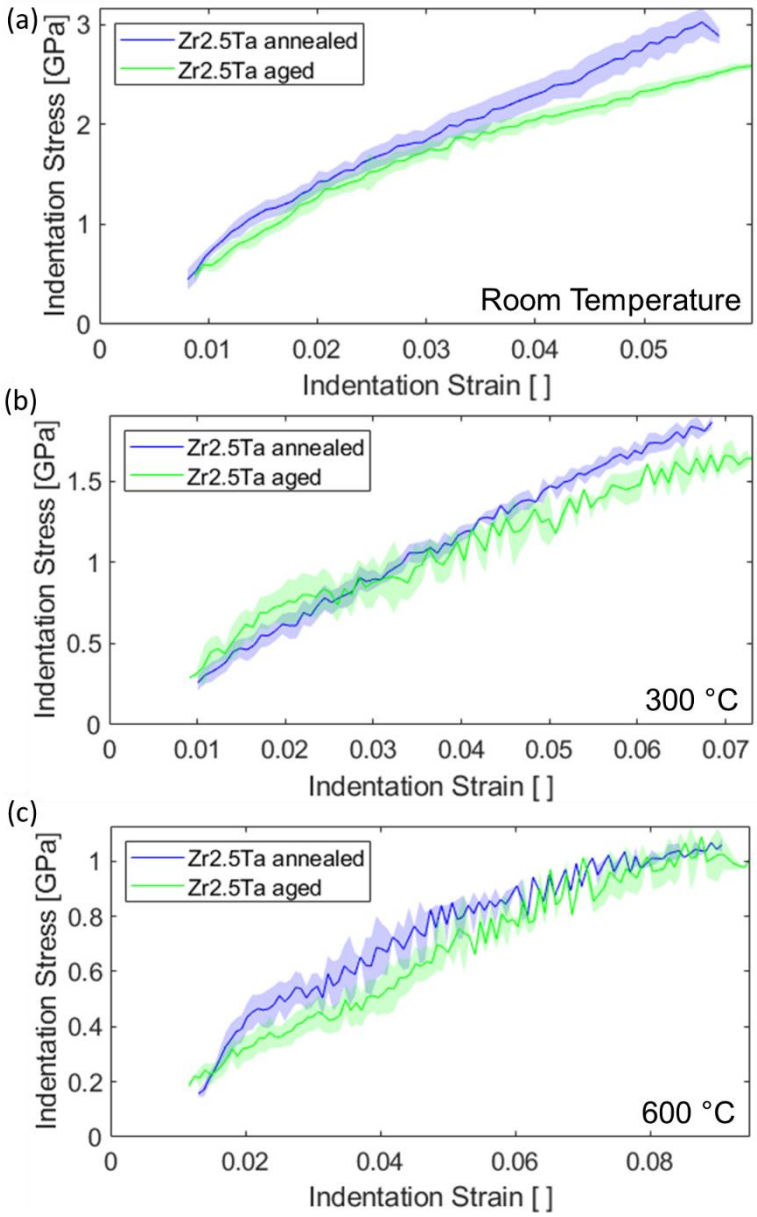


Figure 5-15: Nanoindentation flow curves of the Zr2.5Ta alloy before (blue) and after (green) ageing at 700 °C for 200 hours, and tested at (a) room temperature, (b) 300 °C, and (c) 600 °C.

Due to the encouraging results indicating the good thermal stability of Zr-Ta alloys following isothermal ageing, this alloy system was selected for thermal stability testing under transient heating conditions.

5.3.2.1 Transient heating testing

Samples of the Zr2.5Ta alloy with appropriate dimensions (0.5 mm thickness) were prepared using a diamond wire saw and sent to Hannah Tipping at the University of Bristol for exposure to transient thermal conditions. This was performed with an upper temperature of 850 °C, using the same equipment and method which was described in section 5.2.2 to simulate the effects of plasma disruptions on the breeder blanket structural material [61]. The context of this temperature in terms of the phase transition temperatures may be seen in Table 4-2, and it is expected that the alloy will be in the two-phase α-Zr+β-Zr,Ta at this temperature. Three samples were returned from this treatment, each having been exposed to a different number of thermal transients: 1, 100, and 1000 cycles. The heating and cooling cycle for these tests lasted approximately 80 seconds, equivalent to those used in the testing of Eurofer reported in [61]. The samples were then prepared for microscopy and indentation measurements by polishing as described in section 3.1.

The microstructural analysis shown in Figure 5-16 indicates that there is no observable effect on the microstructure from one transient heating cycle to 850 °C in Figure 5-16(b), as intergranular and banded intragranular precipitates remain with no apparent change in grain size. This may be compared to the microstructure before the heating treatment shown in Figure 5-16(a). These observations remain consistent following 100 transient heating cycles as shown in Figure 5-16(c), although a small amount of coarsening of the intergranular precipitates may be observed in this sample. The extent of precipitate coarsening was analysed quantitatively using image contrast thresholding and particle analysis in ImageJ software, shown in Figure 5-17. This alteration of the microstructure is similar to that observed following isothermal ageing at 700 °C for

200 hours, as is shown in Figure 5-12. These results indicate that Zr2.5Ta displays good resistance to microstructural alteration when exposed to up to 100 transient heating cycles designed to be representative of those which may be expected in-service.

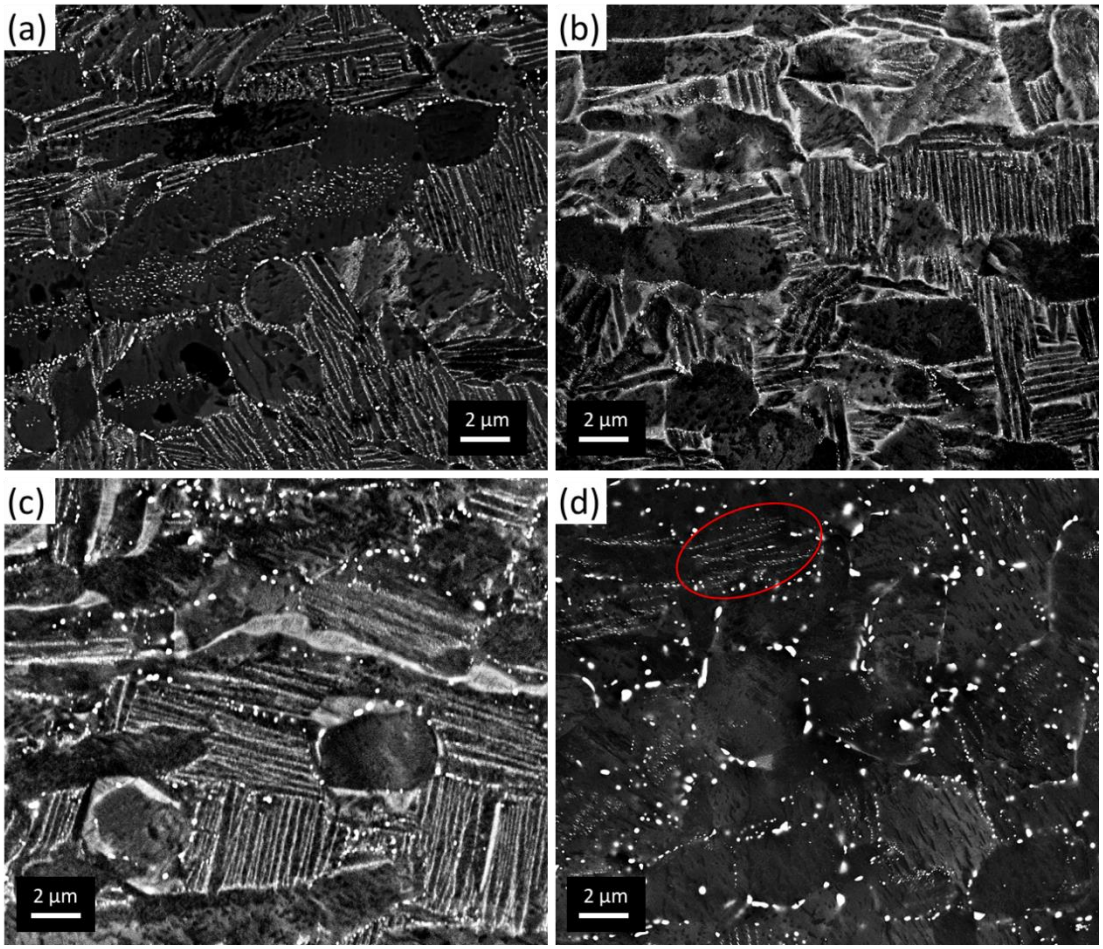


Figure 5-16: SE micrographs of Zr2.5Ta showing the microstructure (a) after annealing and no further thermal treatments, (b) after 1 transient heating cycle, (c) after 100 transient heating cycles, and (d) after 1000 transient heating cycles with the circled region indicating the area with banded intragranular precipitates remaining.

Following 1000 transient heating cycles, more significant microstructural changes to the Zr2.5Ta alloy may be observed in Figure 5-16(d). The approximate grain size shown in this micrograph does not appear significantly altered compared to any of the other samples in Figure 5-16. The size of the intergranular precipitates does not appear to have

coarsened substantially when compared with those observed following 100 thermal transient cycles shown in Figure 5-16(c), although some increase in size may be seen from the quantitative analysis shown in Figure 5-17. However, the prevalence of banded intragranular precipitates appears to be significantly reduced in the sample following 1000 heating cycles compared with the other samples shown, as this structure is now only visible in a small number of grains in Figure 5-16(d), with the clearest indicated by the red circle. This indicates that the microstructural stability which is shown by the material up to 100 cycles, is not maintained following 1000 cycles. This is likely caused by the diffusion of tantalum to the grain boundaries, enabled by extended period at the high temperature, to coarsen precipitates in those areas with greater free volume.

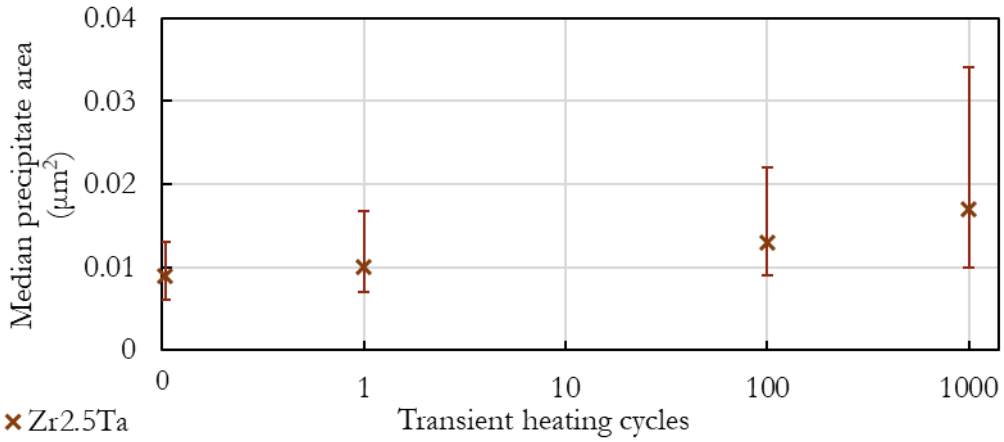


Figure 5-17: Results of ImageJ software precipitate analysis from the micrographs in Figure 5-16, indicating the median intergranular precipitate area with the error indicating the interquartile range of the measured values.

Although a significant microstructural change has been observed as a result of 1000 thermal transient cycles, mechanical testing of the alloy following this treatment should be used to evaluate the effect of this microstructural alteration on the properties of the material.

Therefore, nanoindentation testing using the MTS XP machine and the method described in section 3.3 were used to produce flow curves so that the strength of the material following different thermal treatments may be compared. The results of this analysis are shown in Figure 5-18.

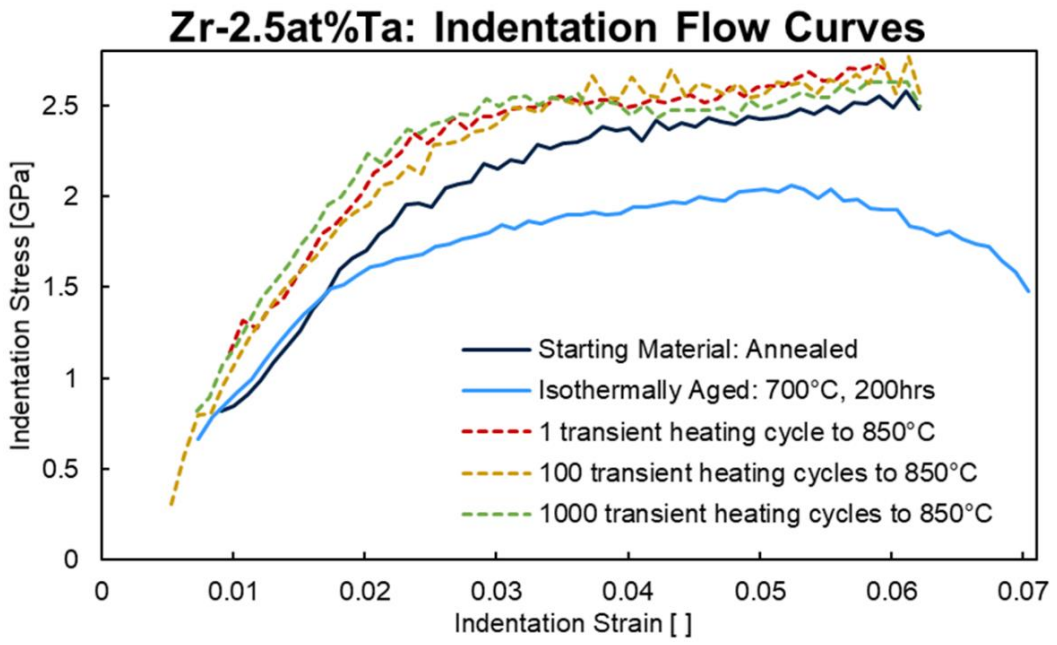


Figure 5-18: Averaged nanoindentation flow curves of the annealed Zr2.5Ta alloy at room temperature following different thermal ageing procedures including none, isothermal ageing, and transient heating cycles.

Despite the apparent alterations to the microstructure caused by a large number of transient heating cycles shown in Figure 5-16, the measurement of flow curves by nanoindentation shown in Figure 5-18 does not indicate a significant change of mechanical properties following the transient heating exposure. This is further evidenced when considering the experimental error associated with the calculation of the averaged flow curves shown in Figure 5-19. Taking this in to account, the mechanical response displayed by the three samples following transient heating appears essentially the same as the annealed Zr2.5Ta alloy. This is further supported by the calculation of indentation

yield stress and proof stress values, which also do not display a clear trend with increasing number of transient heating cycles, as shown in Figure 5-20.

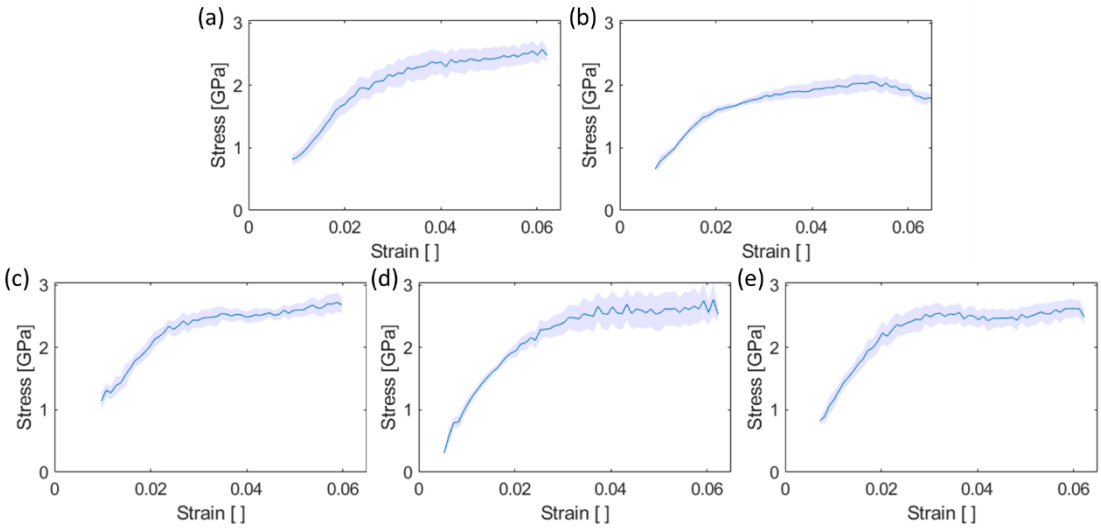


Figure 5-19: Averaged nanoindentation flow curves of the annealed Zr2.5Ta alloy at room temperature following different thermal ageing procedures including (a) none, (b) isothermal ageing at 700 °C for 200 hours, and (c) one, (d) 100, (e) 1000 thermal transient heating cycles to 850 °C. The averaged curves, using the method described in section 3.3.4, are shown as blue lines, with shaded regions around them indicating the associated standard deviation.

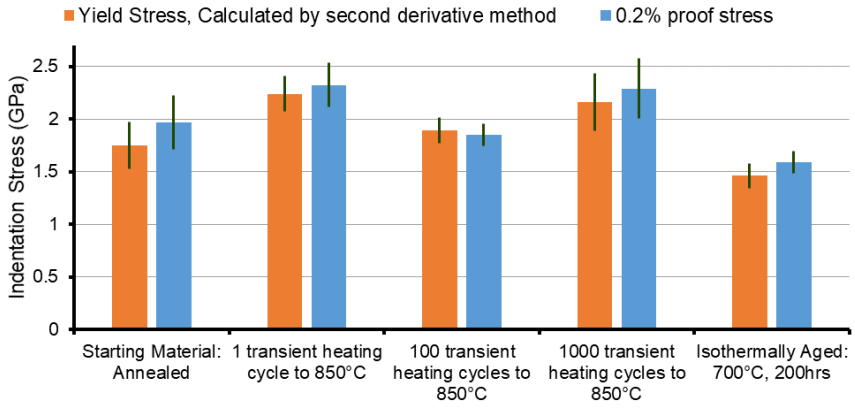


Figure 5-20: Calculated values of the yield stress of the annealed Zr2.5Ta alloy at room temperature following different thermal ageing procedures including none, isothermal ageing, and transient heating cycles, using the averaged nanoindentation flow curves shown above and the analysis methods described in 4.6.1. The indicated error results are from the standard deviation at the calculated point of the graph as shown in Figure 5-19.

It is not expected that the experimental method of thermal heating cycles by laser impingement will result in microstructural damage to the surface of the material, which would cause an artificially increased measurement of strength by a method such as nanoindentation that only measures surface properties. Any strengthening microstructural damage which had occurred at the surface during testing would be removed by the sample preparation and polishing necessary for indentation and microscopy.

The lack of material softening observable from Zr2.5Ta following transient heating shown in this section is surprising, given the removal of microstructural features which would be expected to strengthen the material, such as the removal of intragranular precipitates seen especially in Figure 5-16(d). This may indicate that features such as the intragranular precipitates do not contribute significantly to the material strength compared with other microstructural effects such as Hall-Petch and solid solution strengthening. Significant solid solution strengthening may be inferred from the approximately 0.4 at% composition of Ta in the Zr matrix indicated by the APT analysis shown in Figure 4-36. Further examination of the microstructures observed following transient heating is warranted to explore the possibilities of strengthening mechanisms such as increased dislocation density or matrix solute solubility, which cannot be observed by the characterisation shown in Figure 5-16.

The mechanical results comparing the strength of annealed Zr2.5Ta before and after isothermal ageing in Figure 5-15 and Figure 5-18 appear relatively consistent, despite the slightly different experimental methods used, as discussed in section 3.3, due to machine capability. The reduced strength following isothermal ageing is discussed in

section 5.3.2, and is further confirmed by the indentation yield stress and proof stress calculations shown in Figure 5-20.

5.3.3 Zirconium-aluminium

Optical microscopy of Zr2.5Al following isothermal ageing at 700 °C is shown in Figure 5-21(b,c). These micrographs indicate that the length scale of the grain structure of the alloy has not been significantly altered as a result of the isothermal ageing by comparison with the microstructure of the annealed Zr2.5Al material shown in Figure 5-21(a).

This is further confirmed by the results of EBSD analysis following the 200-hour ageing treatment, shown in Figure 5-22, and may be compared with the equivalent results prior to ageing shown in Figure 4-27. Equivalent analysis parameters as used previously (a misorientation threshold of 3° and a minimum pixel threshold of 8, using the method described in section 3.5.2), result in a median grain diameter calculation of 7.4 μm from the data in Figure 5-22, compared with 6.5 μm before ageing. This represents an insignificant change in grain size following the isothermal ageing treatment, as was suggested by the optical microscopy in Figure 5-21. Increased indexing success is seen in Figure 5-22 compared with Figure 4-27 and this might be due to the reduction in microstructural defects during ageing, and may also contribute the small increase in calculated grain size between the samples.

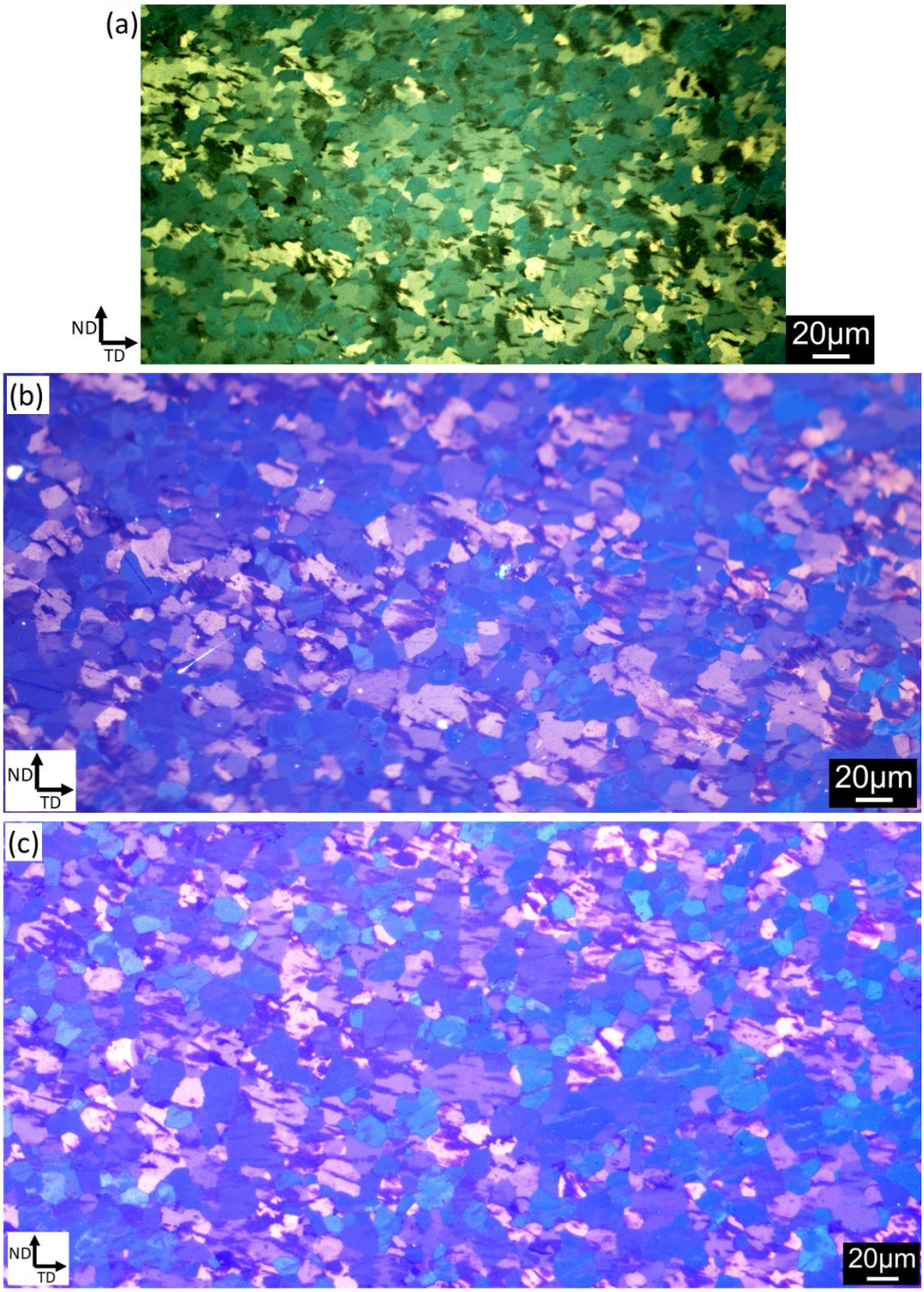


Figure 5-21: Optical micrographs with crossed polarising filters of the Zr2.5Al alloy (a) before and (b,c) after ageing at 700 °C for (b) 200 hours and (c) 1343 hours. The arrows labelled ND and TD represent the normal and transverse directions respectively with respect to the rolling treatment.

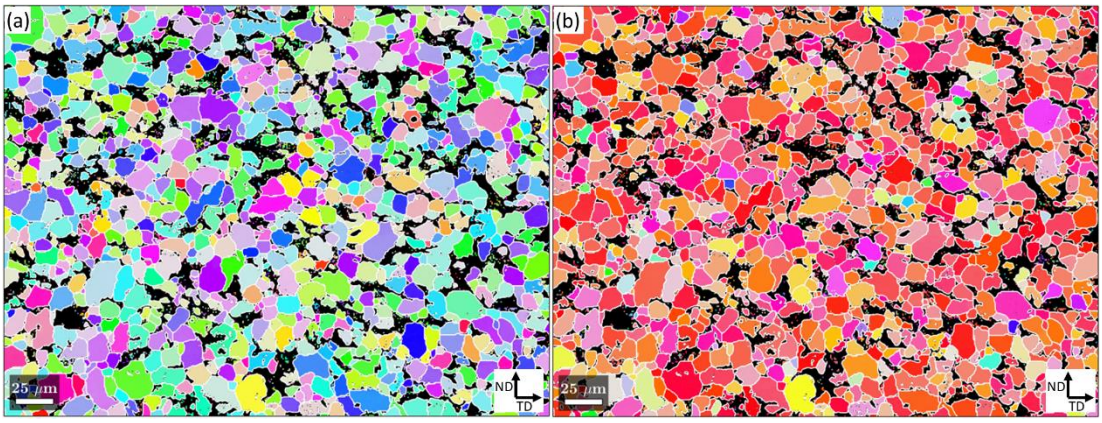


Figure 5-22: EBSD data of the annealed Zr2.5Al sample following ageing at 700 °C for 200 hours showing the crystallographic alignment of measured pixels with (a) the rolling direction and (b) the normal direction with reference to the colour scale shown in Figure 3-7 with calculated grain boundaries overlaid in white.

BSE micrographs of the isothermally aged Zr2.5Al alloy are shown in Figure 5-23 and Figure 5-24 to demonstrate the size and distribution of the precipitates in the microstructure, which are shown as small black dots. These may be compared with the precipitate size and distribution prior to ageing shown in Figure 4-24 (reproduced below), and quantitative comparison of the size distribution of the precipitates was performed using image contrast thresholding and particle analysis in ImageJ software, shown in Figure 5-25. Comparison of the micrographs and analysis indicates that there has been no significant coarsening of these micro-scale precipitates, as may be expected due to the sluggish diffusion rate of aluminium in zirconium [174]. Electron channelling contrast shown in Figure 5-23 also confirms the grain structure seen in Figure 5-21 and Figure 5-22.

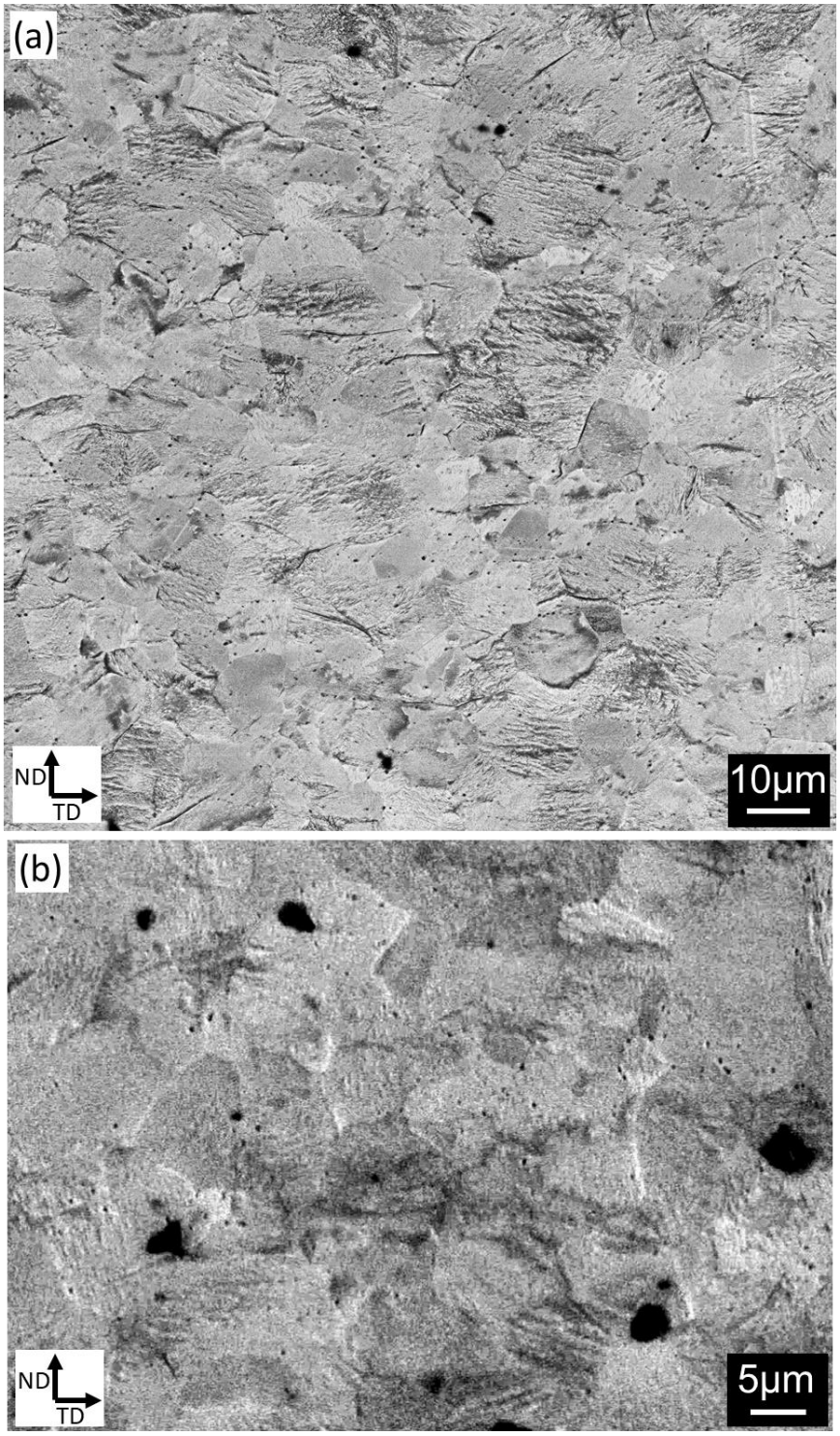


Figure 4-24 [Reproduced for comparison with Figure 5-23 and Figure 5-24]: BSE micrographs of the annealed Zr2.5Al alloy with dark spots indicating the presence of precipitates within the microstructure. The arrows labelled ND and TD represent the normal and transverse directions respectively with respect to the rolling treatment.

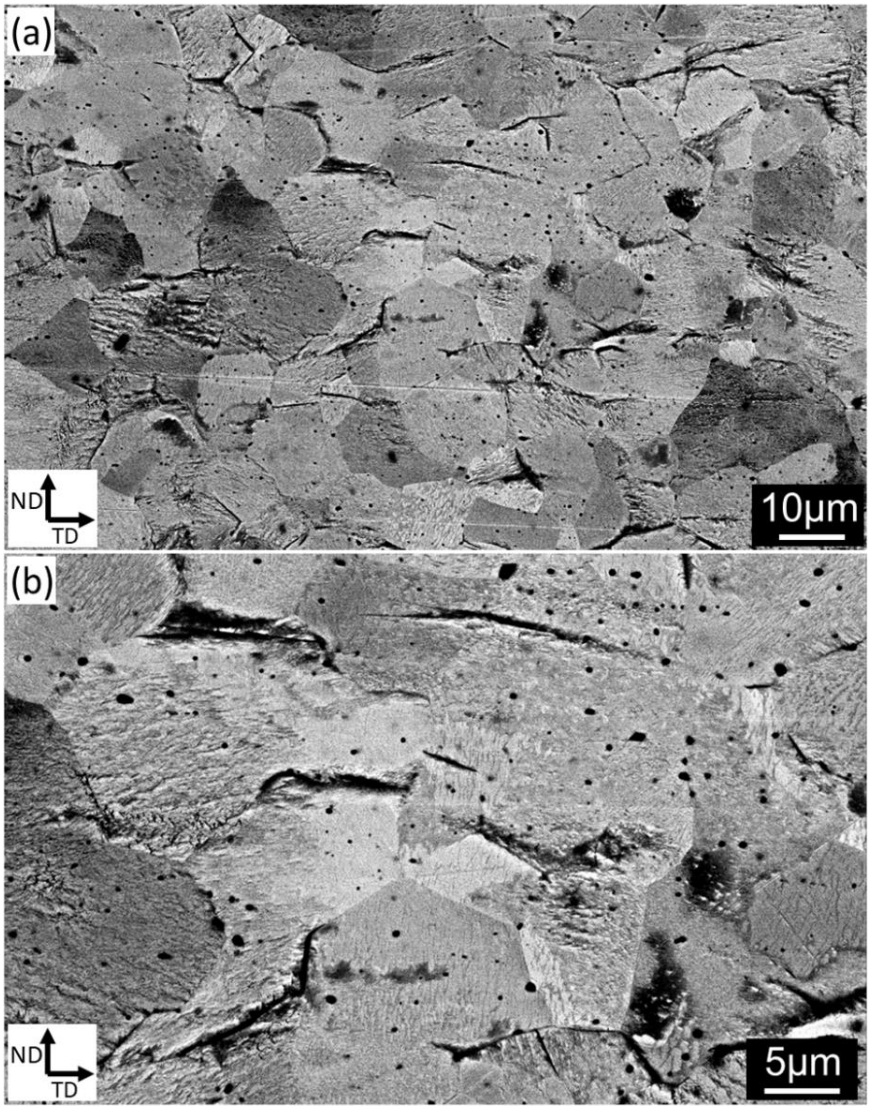


Figure 5-23: BSE micrographs of Zr2.5Al following ageing at 700 °C for 200 hours with dark spots indicating the presence of precipitates within the microstructure. The arrows labelled ND and TD represent the normal and transverse directions respectively with respect to the rolling treatment.

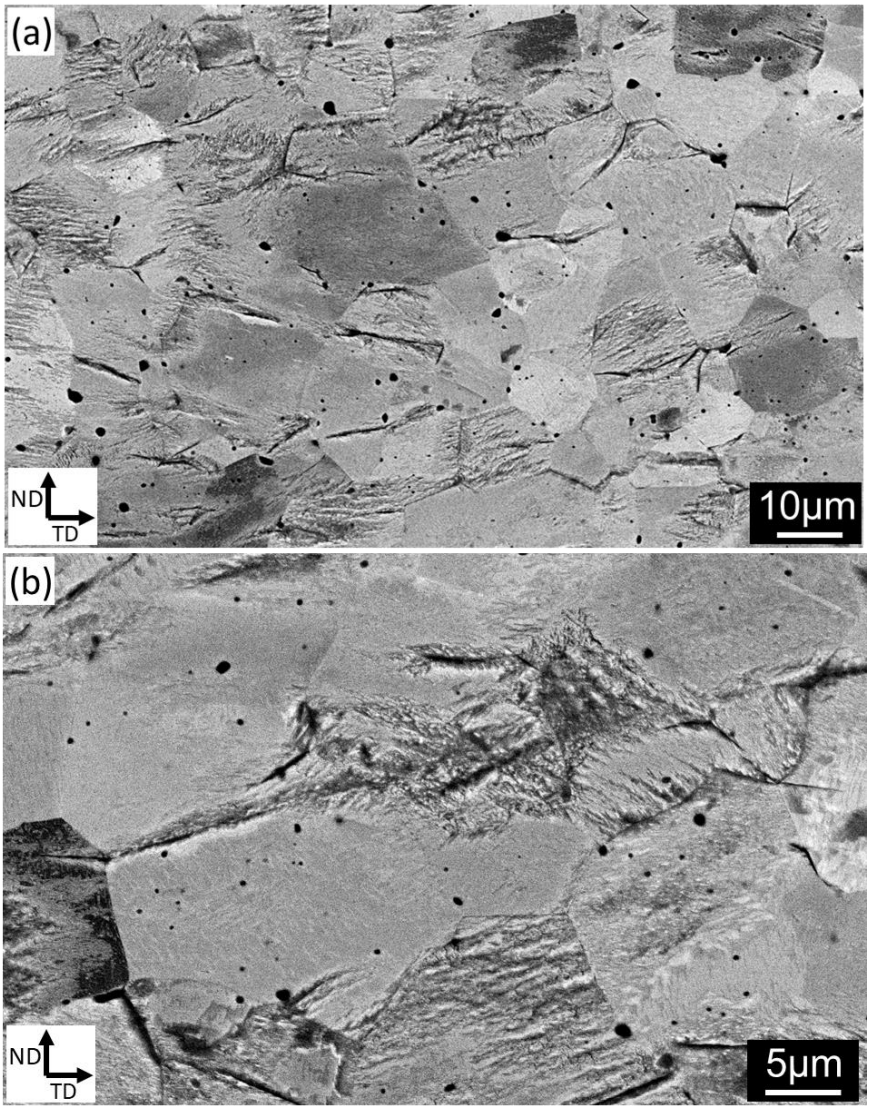


Figure 5-24: BSE micrographs of Zr2.5Al following ageing at 700 °C for 1343 hours with dark spots indicating the presence of precipitates within the microstructure. The arrows labelled ND and TD represent the normal and transverse directions respectively with respect to the rolling treatment.

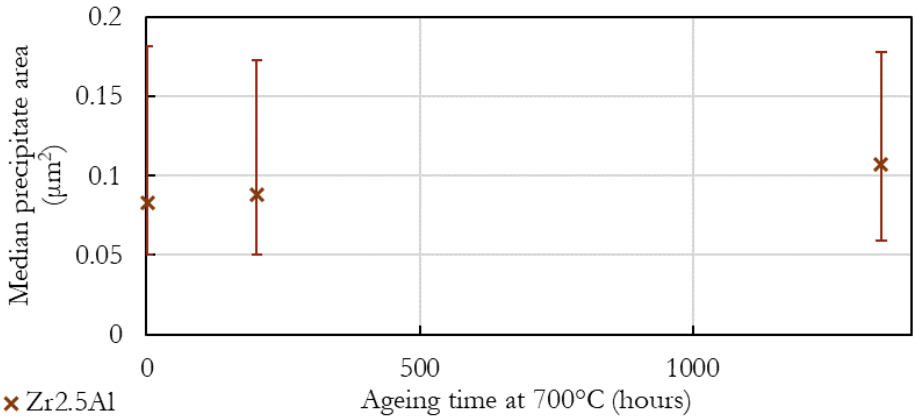


Figure 5-25: Results of ImageJ software precipitate analysis from the micrographs in Figure 4-24, Figure 5-23, and Figure 5-24, indicating the median precipitate area with the error indicating the interquartile range of the measured values.

The grain structure of the Zr5Al alloy is shown by optical microscopy, both before and after isothermal ageing, in Figure 5-26. It can be seen that the grain structure of Zr5Al shown in Figure 5-26, is comparable to that displayed for Zr2.5Al in Figure 5-21. Figure 5-26 also shows that the grain structure of Zr5Al is relatively consistent following isothermal ageing treatments, as would be expected due to the similar results shown previously for the Zr2.5Al alloy. Similarity with Zr2.5Al is also seen in terms of the precipitate distribution of the annealed Zr5Al microstructure prior to isothermal ageing, as shown by the BSE micrograph in Figure 5-27(a), which may be compared with Figure 4-24 (reproduced above) of Zr2.5Al. Quantitative analysis of this comparison was performed using image analysis software, as shown previously, and the consistency of precipitate size distribution between the two alloys is shown in Figure 5-28.

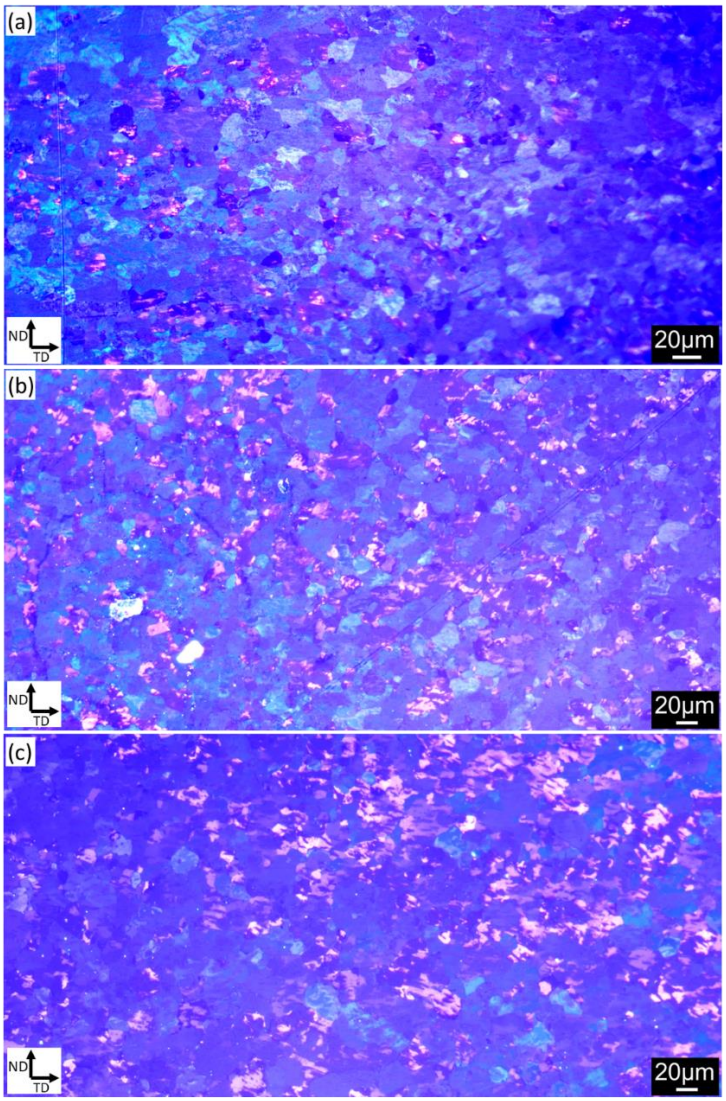


Figure 5-26: Optical micrographs with crossed polarising filters of the Zr5Al alloy (a) before and (b,c) after ageing at 700 °C for (b) 200 hours and (c) 1343 hours. The arrows labelled ND and TD represent the normal and transverse directions respectively with respect to the rolling treatment.

Despite the similarities observed between the microstructures of Zr2.5Al and Zr5Al, a significant difference can be seen in the evolution of the micro-scale precipitates in Zr5Al. Figure 5-27(b) shows a significant coarsening of the precipitates following the 200-hour ageing treatment, which is not observed in the case of the Zr2.5Al alloy in Figure 5-23. Despite this significant coarsening following the initial ageing treatment, Figure 5-27(c) shows that a relatively small amount of further coarsening is observed following 1143 hours of further ageing, indicating that the overall microstructure is relatively stable

to the thermal ageing. Confirmation of this trend of significant coarsening during the first ageing period, followed by a consistent precipitate size observed upon further ageing, is confirmed by the results of quantitative image analysis shown in Figure 5-29.

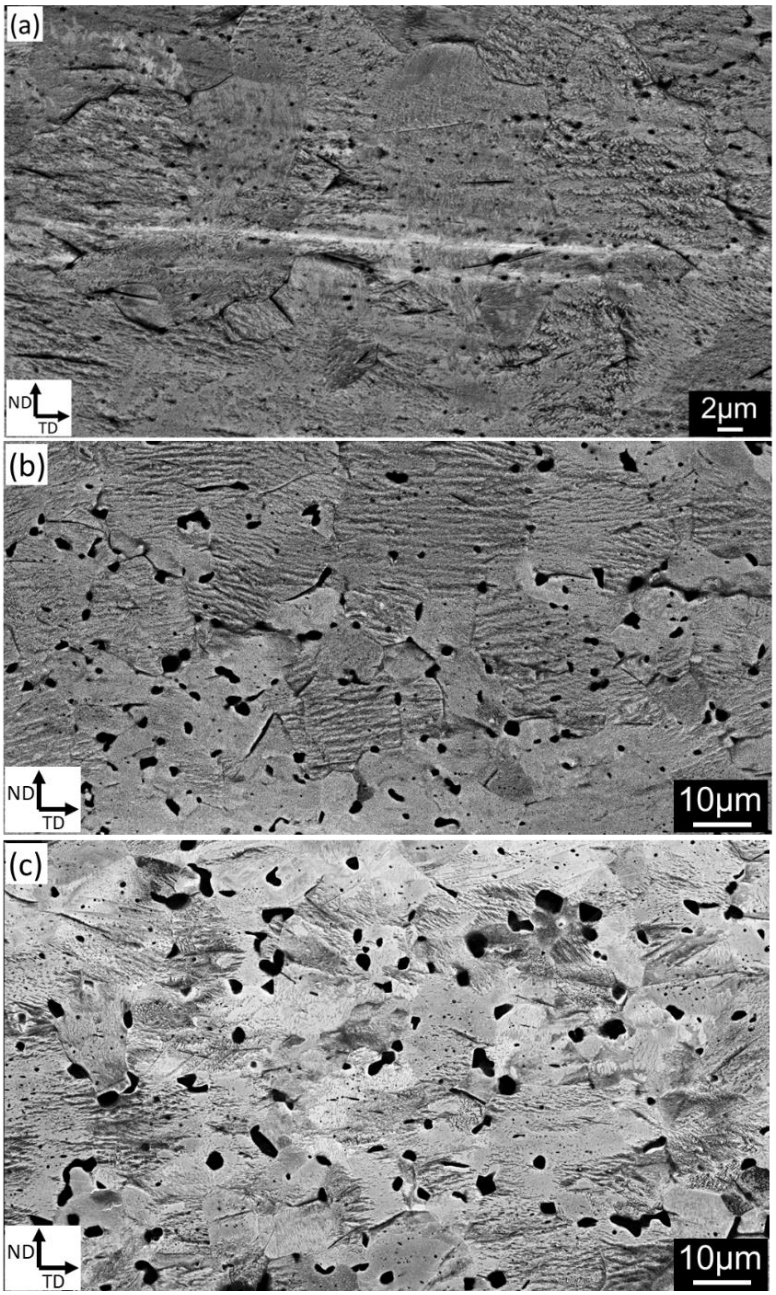


Figure 5-27: BSE micrographs of (a) the annealed Zr5Al alloy following ageing (b,c) at 700 °C for (b) 200 hours and (c) 1343 hours. With dark spots and regions indicating precipitates within the microstructure. The arrows labelled ND and TD represent the normal and transverse directions respectively with respect to the rolling treatment.

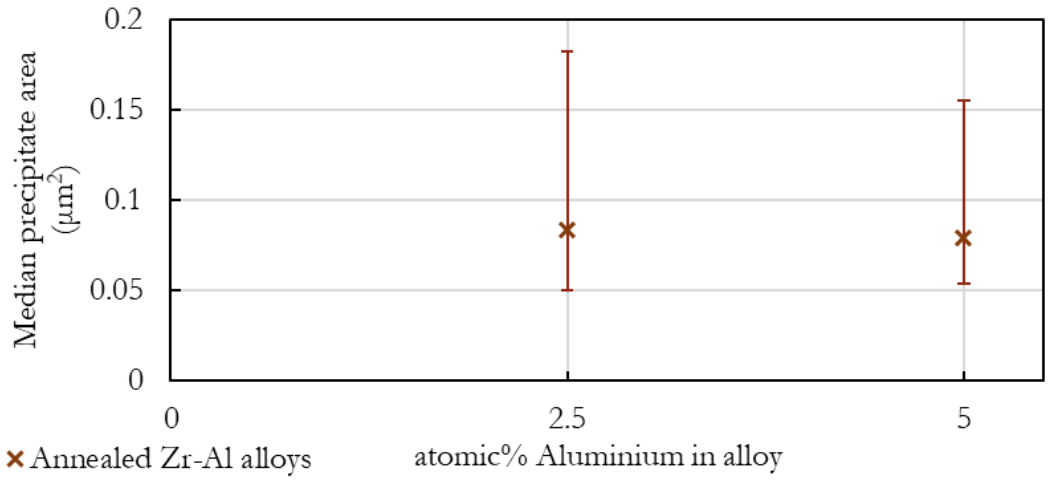


Figure 5-28: Results of ImageJ software precipitate analysis from the micrographs in Figure 4-24 and Figure 5-27(a), indicating the median precipitate area with the error indicating the interquartile range of the measured values.

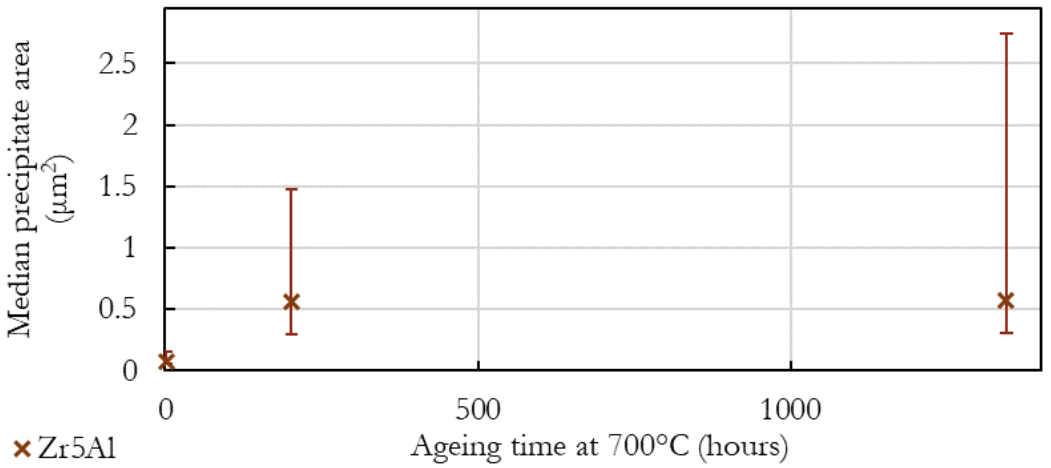


Figure 5-29: Results of ImageJ software precipitate analysis from the micrographs in Figure 5-27, indicating the median precipitate area with the error indicating the interquartile range of the measured values.

5.3.3.1 Analysis of nano-scale precipitates

It has been previously shown that Ti-Al alloys exhibit nano-scale precipitates of Ti_3Al in the microstructure following ageing treatments [308]. Titanium and zirconium may be thought of as analogous metals due to their common crystal structure and similar atomic size, therefore similarities may be expected between Ti-Al alloys and Zr-Al alloys. APT datasets were taken by Wenyu Zhang from samples of both Zr2.5Al and Zr5Al following isothermal ageing treatments to investigate the possibility that nano-scale precipitates may occur in these alloys; the results are shown in Figure 5-30.

Whereas no inhomogeneity in the distribution of aluminium could be seen in the Zr2.5Al sample before isothermal ageing in Figure 4-28, the results shown in Figure 5-30 clearly demonstrate an inhomogeneous distribution of aluminium. This may be more clearly observed with the addition of isoconcentration surfaces to the APT datasets, as shown in Figure 5-31. This visualisation allows for the observation of discrete regions of aluminium enrichment, which are therefore identified as nanoscale Al-rich precipitates, in these alloys following the ageing treatments.

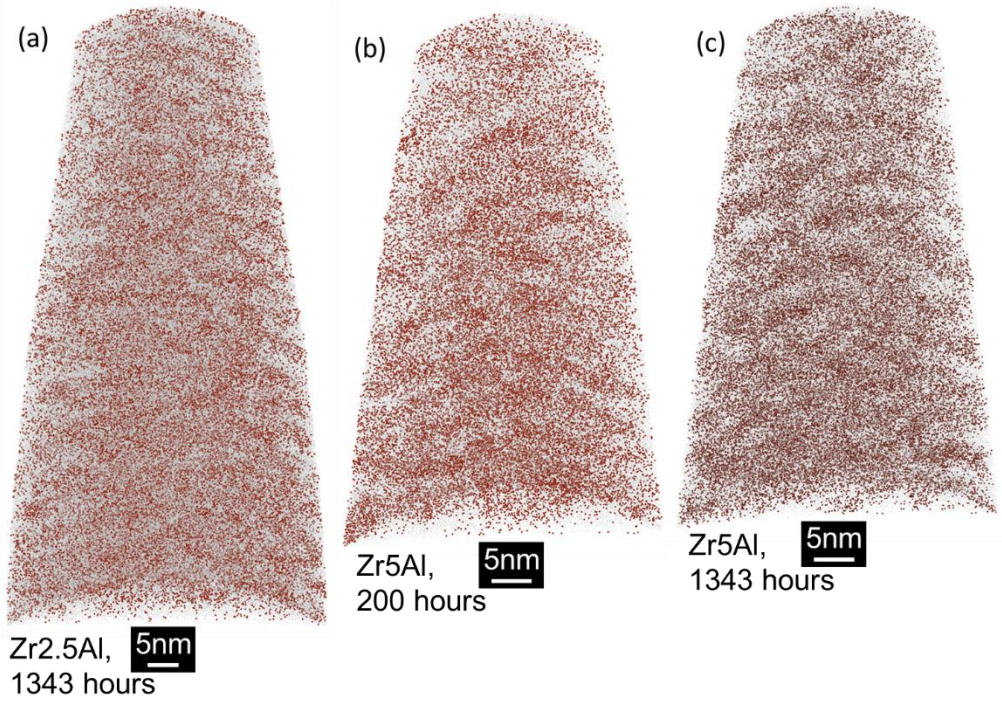


Figure 5-30: Examples of APT datasets by Wenyu Zhang of (a) Zr2.5Al and (b,c) Zr5Al aged at 700 °C for (b) 200 hours and (a,c) 1343 hours, showing Al ions as red dots and Zr ions as grey, indicating a non-homogenous distribution of aluminium within the sample volume.

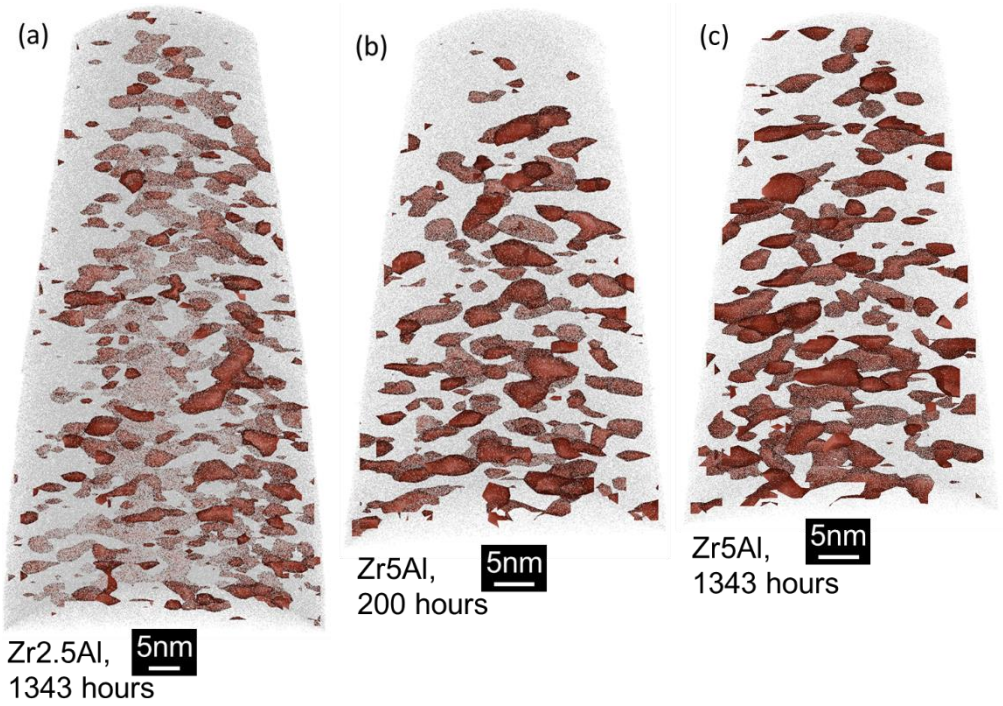


Figure 5-31: APT datasets by Wenyu Zhang of (a) Zr2.5Al and (b,c) Zr5Al aged at 700 °C for (b) 200 hours and (a,c) 1343 hours, showing Zr ions in grey dots and Al isoconcentration surfaces in red at compositions of (a) 3.5 at%, (b) 5.5 at%, (c) 6.5 at%.

To further explore the character of the precipitates after different heating treatments, isoconcentration surfaces of equal value (5.5 at%) were used to define the location of precipitates in the three APT datasets, Figure 5-32, with the corresponding proxigrams in Figure 5-33 showing the average aluminium composition as a function of distance from the isoconcentration surfaces at the edge of the precipitates. Visual comparison of the isosurfaces shown in Figure 5-32 indicate that, although there appears to be some evolution of the precipitates in Zr5Al with increased ageing time, the approximate size and distribution of the precipitates does not change drastically. More quantitative evaluation is performed in the following figures.

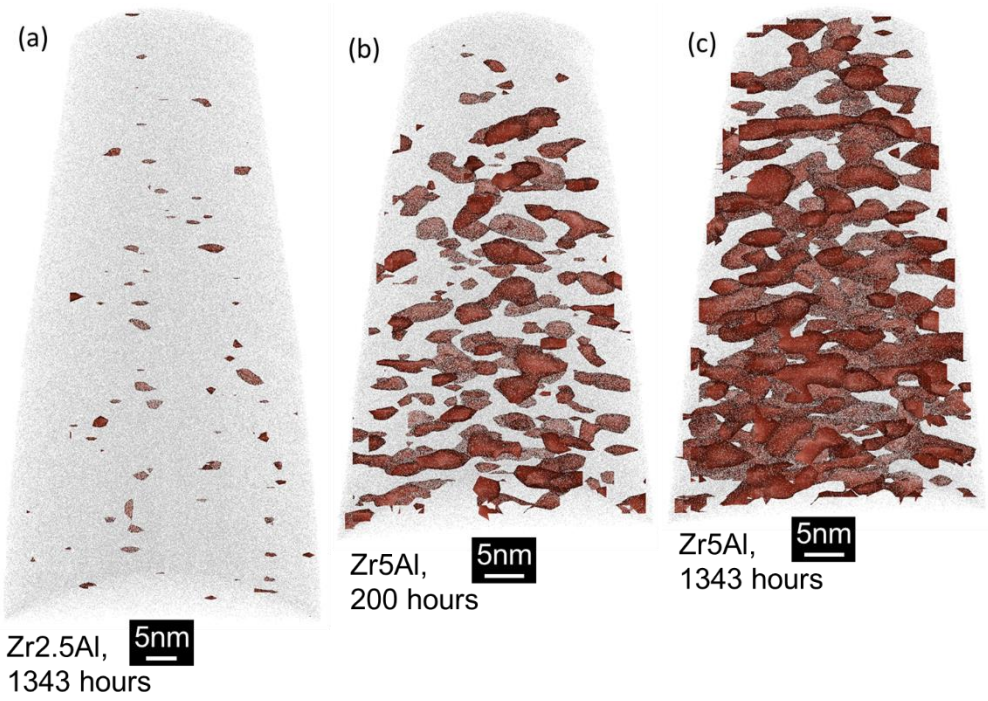


Figure 5-32: APT datasets by Wenyu Zhang of (a) Zr2.5Al and (b,c) Zr5Al aged at 700 °C for (b) 200 hours and (a,c) 1343 hours, showing Zr ions in grey dots and 5.5 at% Al isoconcentration surfaces in red.

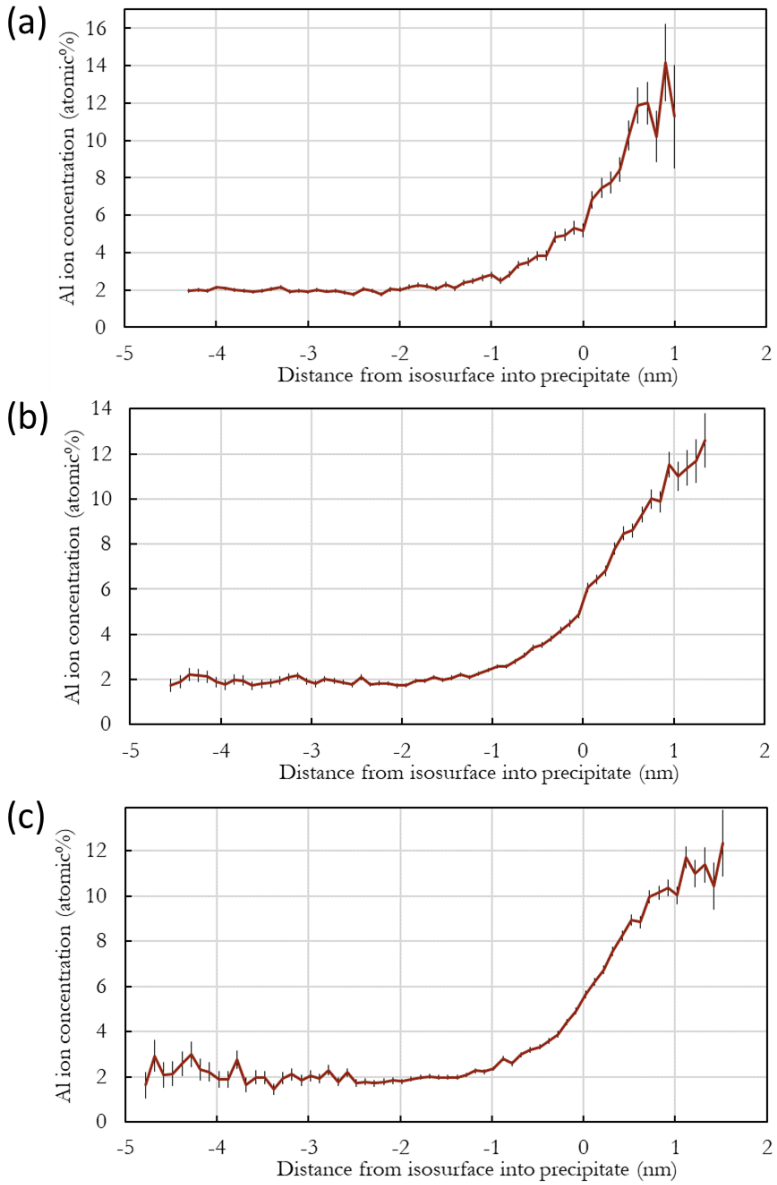


Figure 5-33: Examples of proxigram composition profiles using the 5.5 at% Al composition isosurfaces shown in Figure 5-32 for (a) Zr2.5Al and (b,c) Zr5Al aged at 700 °C for (b) 200 hours and (a,c) 1343 hours. The horizontal axis represents the distance away from the calculated isosurface either into (positive) or away from (negative) the precipitate.

Examination of the proxigrams shown in Figure 5-33 show that the aluminium concentration reached in the matrix (outside the precipitates), and in the centre of the precipitates is approximately equal for all samples. Additionally, the extended plateau region of aluminium composition in the matrix supports a nucleation and growth mechanism of precipitation formation as opposed to spinodal decomposition, in

agreement with observations of Ti-Al nano-scale precipitates [308]. This is shown in Figure 5-34 where the matrix composition is calculated using the average composition of datapoints in the proxigram more than 2 nm away from the isosurface position, and the precipitate composition is taken by visually assessing the plateau value on the right-hand side of the proxigram. The analysis shown in Figure 5-34 shows no significant change in the composition of the precipitates nor the matrix between the different alloys and ageing treatments, indicating the stability of these precipitates in the microstructure. Although a composition of approximately 25 at% aluminium would be expected for a Zr_3Al precipitate, the lower composition indicated in Figure 5-34(b) may be explained by their small size.

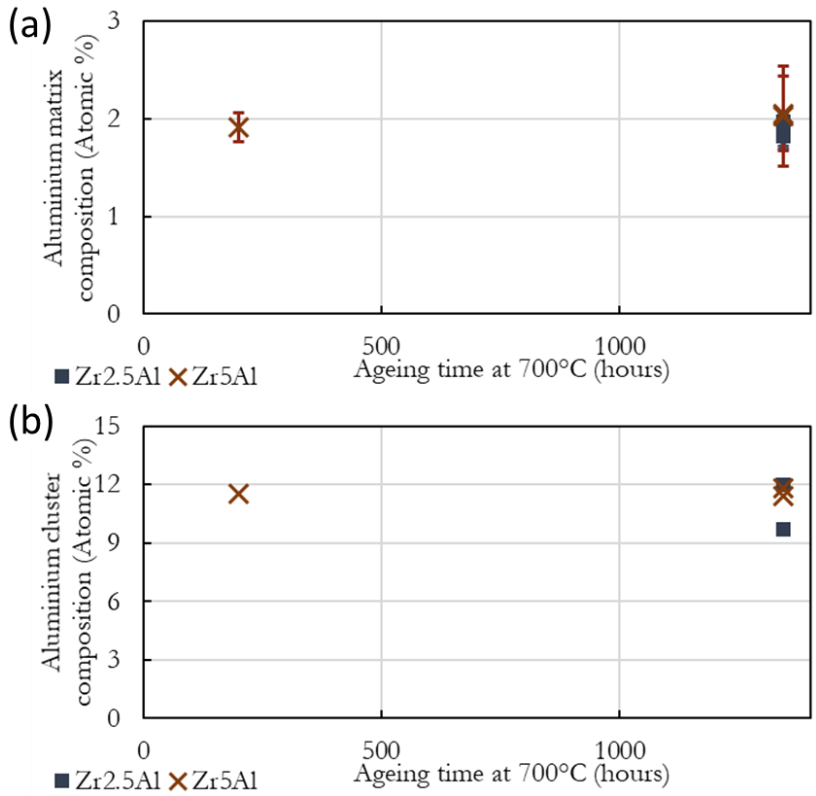


Figure 5-34: Analysis of the approximate compositions of (a) the matrix and (b) the precipitates from proxigrams of APT datasets of Zr-Al alloys as shown in Figure 5-33 with the error in (a) indicating the standard deviation of composition data points more than 2 nm from the isosurface.

Cluster analysis using the AP Suite software was used to provide estimates of the size and number density of precipitates in the microstructures, as shown in Figure 5-35, using the parameters shown in Table 5-1.

The estimate of cluster size shown in Figure 5-35(b) indicates limited variation between the samples tested, therefore showing that the precipitates do not appear to coarsen significantly in the Zr5Al alloy with increased ageing time. This further indicates the stability of these precipitates in the microstructure.

In contrast, the apparent reduction in number density of the precipitates in Zr5Al shown in Figure 5-35(a) would suggest that coarsening of the nano-scale precipitates does occur. This contradicts the consistent size and composition values shown in Figure 5-35(b) and Figure 5-34(b) respectively. This apparent reduction in number density of these nano-scale precipitates in the Zr5Al alloy with increased ageing time may be caused by the segregation of aluminium to the micron-scale precipitates which are seen to coarsen in Figure 5-27(a,b) and Figure 5-29, rather than being caused by the coarsening of nano-precipitates themselves as this is not supported by either a change in their composition or size.

The number density of precipitates in the Zr5Al alloy appears notably larger than in the Zr2.5Al alloy following the same thermal treatment in Figure 5-35(a), this is consistent with the similar size and composition of the precipitates in the two alloys and the increased proportion of solute.

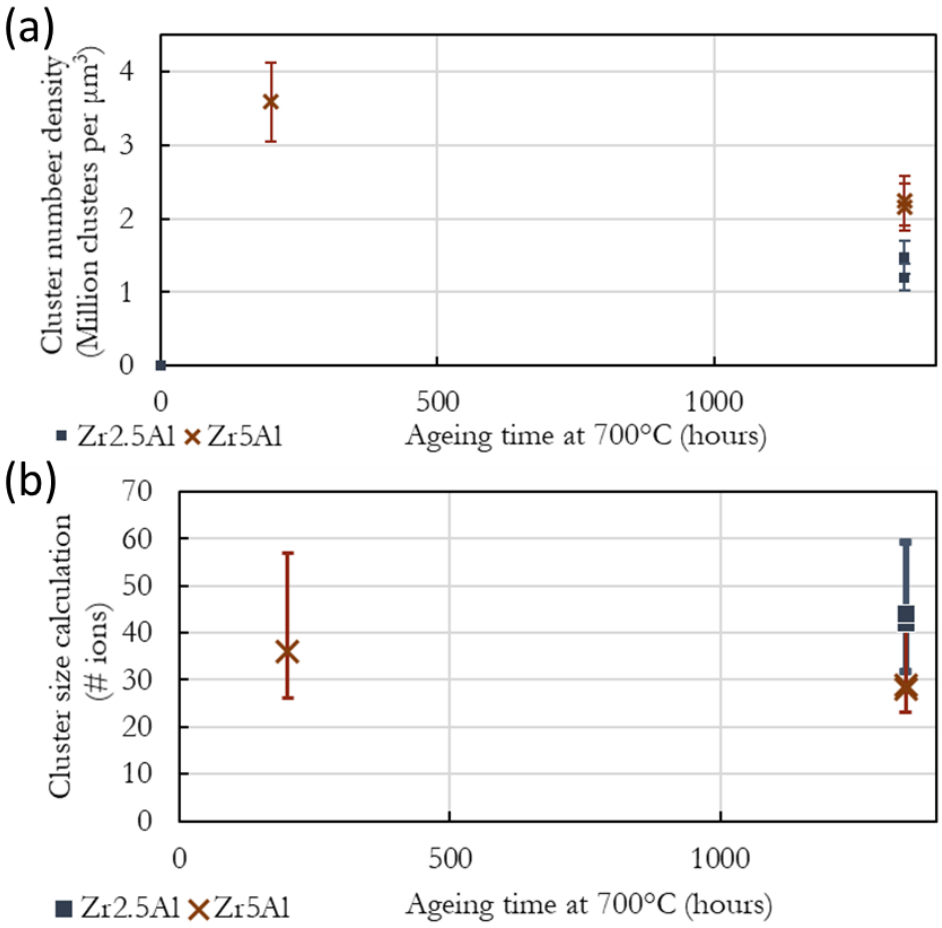


Figure 5-35: Results of AP Suite software cluster analysis from APT datasets with the parameters shown in Table 5-1, indicating (a) the number of identified clusters in the calculated tip analysis volume with an error estimate based on the accuracy of the tip volume calculation, and (b) the median number of ions counted in an identified cluster with the error indicating the interquartile range of the dataset.

Table 5-1: Parameters used for cluster analysis in AP Suite software, determined using methods of best practice for data analysis.

Alloy	**Ageing time (hours)**	**d_{max} (nm)**	**N_{min} ( )**	**Order ( )**
Zr2.5Al	1343	0.9	16	6
Zr5Al	200	0.76	12	6
Zr5Al	1343	0.6	11	6

To further characterise the precipitates, Transmission Electron Microscopy (TEM) of the Zr5Al sample following isothermal ageing at 700 °C for 1343 hours was performed by Rajat Nama. The TEM micrograph in Figure 5-36(a) shows precipitate size and distribution similar to that shown by APT analysis, thereby confirming the presence of nano-scale precipitates in the alloy microstructure. Figure 5-36(b) shows a diffraction pattern with spots which match well to the predicted positions of the α-Zr phase (Figure 5-36(c)), as well as extra spots which are attributed to the precipitate phase.

Based on knowledge of the phase diagram shown in Figure 2-13, and analysis of the micro-scale precipitates as shown in section 4.5.2, Zr_3Al precipitates would be expected. The $L1_2$ structure is the equilibrium crystal structure of this phase, and is also the crystal structure identified in the micron-scale precipitates by XRD analysis in Figure 4-25, and therefore may be expected to be the phase of these much smaller precipitates. However, $D0_{19}$ crystals of the same stoichiometry have been previously observed as the structure of nano-scale precipitates in analogous Ti-Al alloys [356]. The database pattern of the $L1_2$ phase is shown to fit the extra diffraction spots well in Figure 5-36(c), and it is therefore concluded that this is the crystal structure of these nano-scale precipitates. Whilst the extra spots observed in the diffraction pattern may also be accounted for by the $D0_{19}$ structure, if this structure were present, extra spots would be expected close to the central (0 0 0) spot, as shown in Figure 5-36(d), which are not present in the experimental diffraction pattern.

If the precipitates were randomly oriented within the matrix from which the diffraction pattern was collected, this would lead to continuous rings in the diffraction pattern shown in Figure 5-36(b). However, this is not the case in Figure 5-36, and more

discrete points of diffraction intensity corresponding to the precipitates are observed instead. This observation indicates that the precipitates are not randomly oriented within the matrix, and instead have a fixed orientation relationship to the matrix. This result suggests a coherency across the precipitate-matrix interface, indicating the strengthening mechanisms which are likely. These include the introduction of coherency strains to the crystal lattice and the necessity for precipitate shearing for dislocation motion, both of which act to impede dislocation motion.

Overall, nano-scale analysis of the microstructure observed in the isothermally aged Zr-Al alloys with TEM and APT indicates the presence of coherent, nano-scale Zr_3Al precipitates with the $L1_2$ structure, and that the size, distribution, and composition of these precipitates are relatively stable in the microstructure. However, due to the small volume of materials analysed with the techniques in this section, further analysis should be carried out to draw definitive conclusions about the characteristics of these nano-scale precipitates.

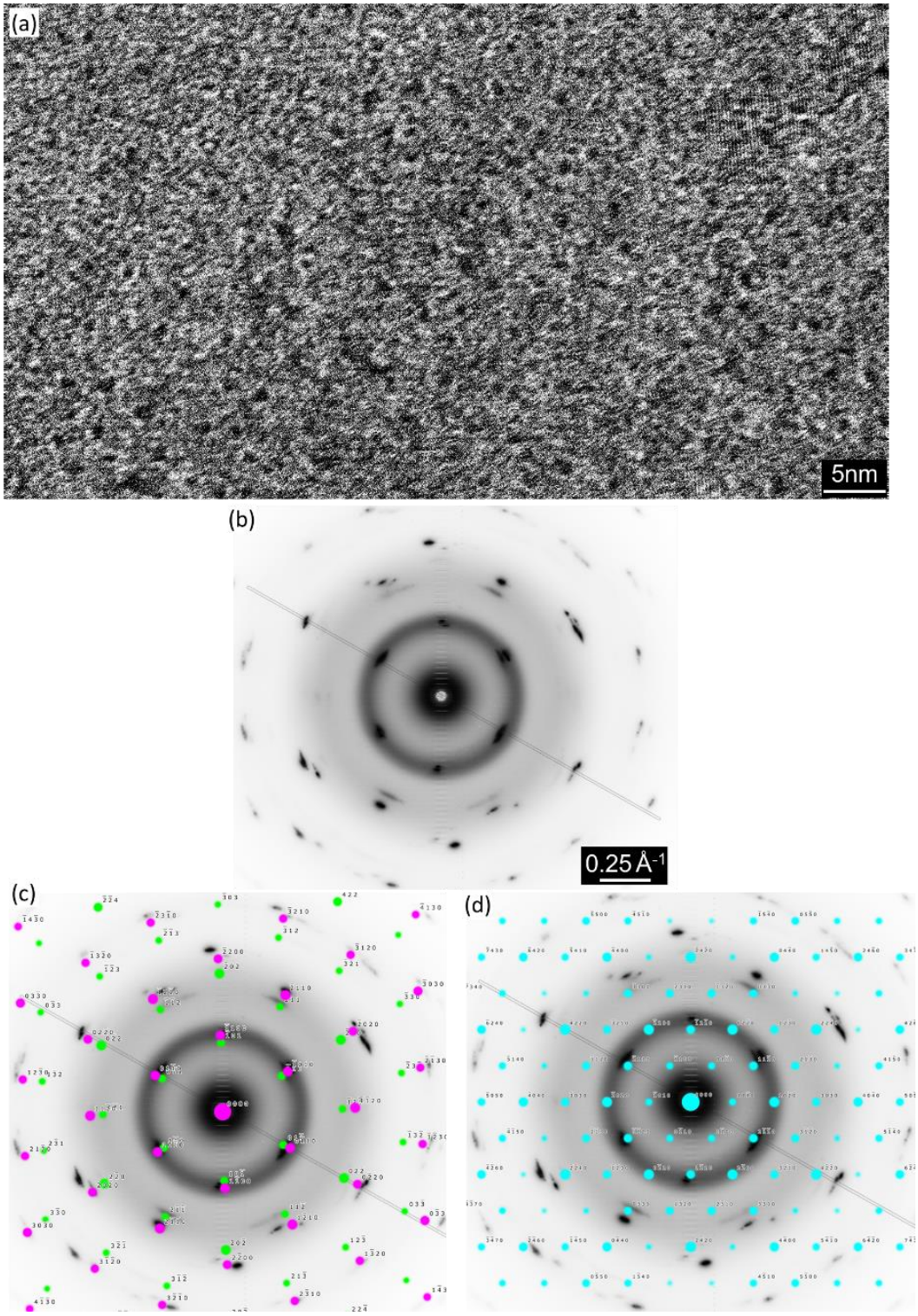


Figure 5-36: TEM analysis of data taken by Rajat Nama from Zr5Al following isothermal ageing at 700 °C for 1343 hours. (a) Defocussed bright field micrograph showing the size and distribution of precipitates, indicated as dark circular regions. (b) Diffraction pattern obtained from the region shown in (a), analysed in (c) and (d) with overlaid database diffraction patterns for α-Zr (pink), $L1_2$ structure Zr_3Al (green), and $D0_{19}$ structure Zr_3Al (blue).

5.3.3.2 Nanoindentation analysis

As has been shown for alloy systems discussed previously, nanoindentation measurements of the alloys discussed in this section were taken to compare the relative strength of the alloys before and after isothermal ageing. The results in Figure 5-37 show that an increased strength is displayed at all three testing temperatures by Zr2.5Al following the isothermal ageing treatment, and most notably at the highest temperature of 600 °C. It has been seen in the previous section that nano-scale precipitates are formed following isothermal ageing of the Zr-Al alloys, and this is likely to explain the strengthening seen in this alloy following the ageing treatment. Similar strengthening effects have been observed in Ti-Al alloys following ageing, also attributed to the formation of strengthening nano-precipitates [309].

Conversely, in Figure 5-38, equivalent strengthening is not seen in Zr5Al following ageing. Instead, a relatively consistent strength is seen when comparing the samples before and after the 200-hour ageing treatment. One possible explanation for the difference between this result and that shown for the Zr2.5Al is that nano-scale precipitates may have been present in the more supersaturated Zr5Al microstructure prior to ageing, and therefore an increase in strength due to their formation is not seen following ageing. However, it is thought that this is unlikely as it has been seen in the Zr2.5Al alloy, and shown in literature for the comparable Ti-Al system [308], that nano-scale precipitates are only observed following ageing treatments. Instead, it is thought that the strengthening effects imparted by the formation of nano-scale precipitates within the microstructure, may be offset by a softening effect as a result of the coarsening of the micro-scale precipitates during the ageing treatment as shown in Figure 5-27(a,b) and Figure 5-29.

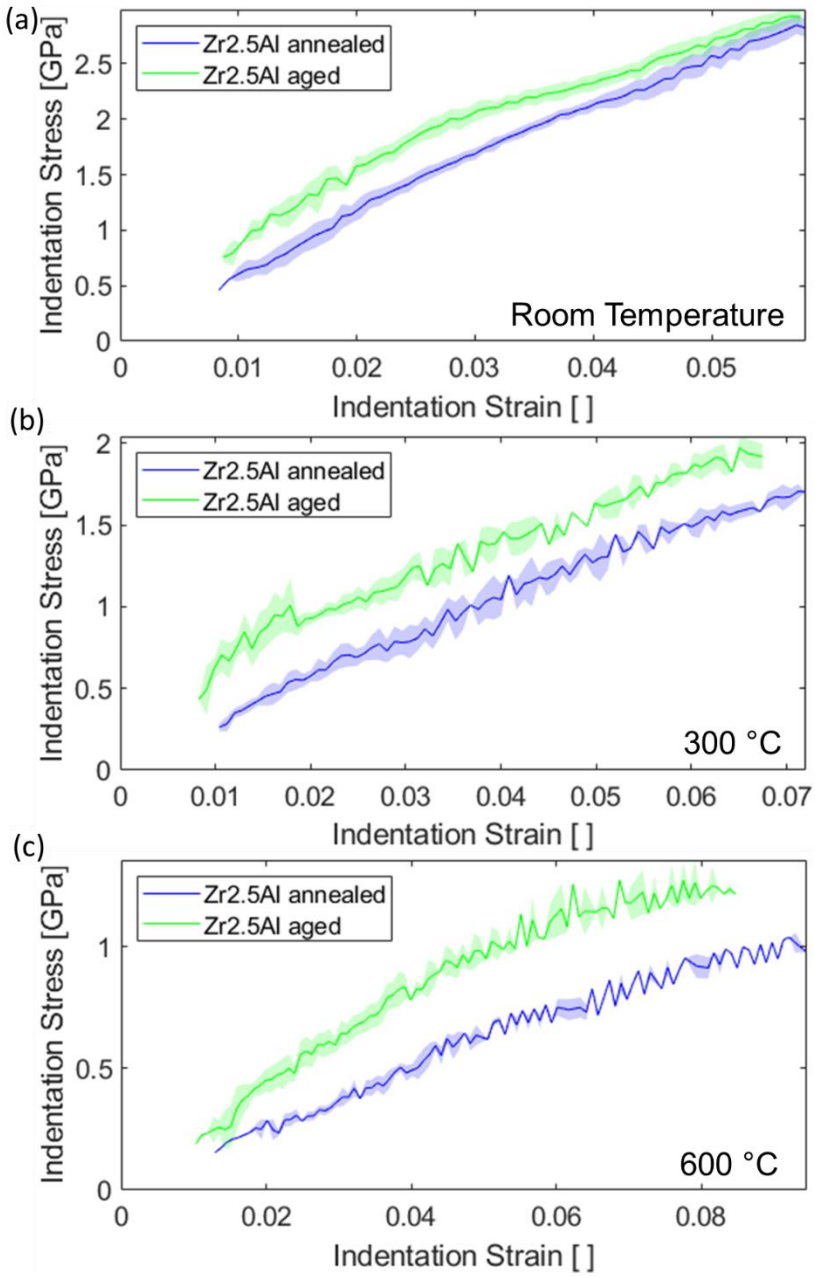


Figure 5-37: Nanoindentation flow curves of the Zr2.5Al alloy before (blue) and after (green) ageing at 700 °C for 200 hours, and tested at (a) room temperature, (b) 300 °C, and (c) 600 °C.

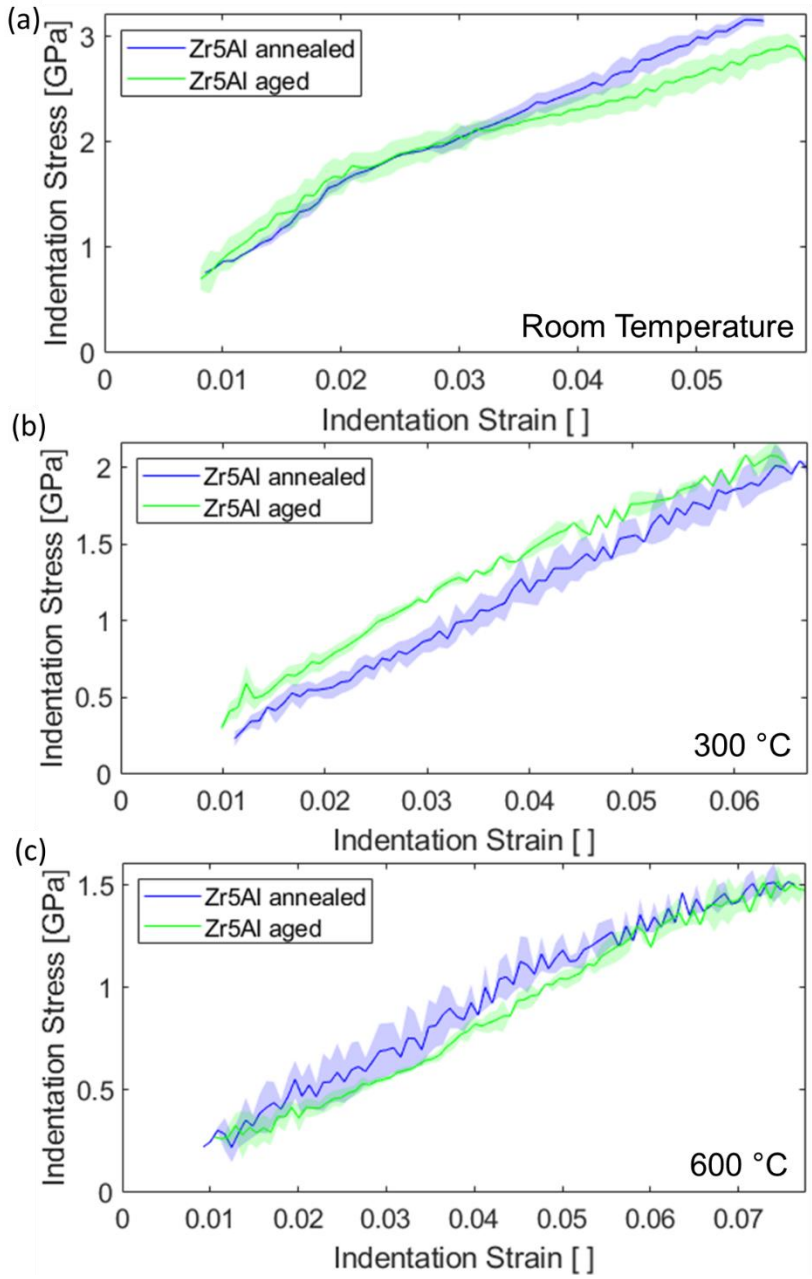


Figure 5-38: Nanoindentation flow curves of the Zr5Al alloy before (blue) and after (green) ageing at 700 °C for 200 hours, and tested at (a) room temperature, (b) 300 °C, and (c) 600 °C.

5.4 Conclusions

Although the presence of ZrV_2 Laves phase precipitates in the alloys of the Zr-V system has been shown to refine the grain structure of the alloys in their annealed form, the observation of severe grain coarsening during ageing of the alloys indicates that these precipitates do not sufficiently pin the grain boundaries to prevent coarsening in-service. Therefore, it is suggested that if vanadium is to be used as an alloying addition for zirconium, that other precipitates should be included in the microstructure for the purpose of maintaining microstructural stability.

The results shown in 5.3.2 indicate that alloys of the Zr-Ta system display promising thermal stability under both isothermal and transient conditions. Whilst further microstructural analysis is warranted to fully explain the observed variations in strength of the Zr2.5Ta alloy following various thermal ageing conditions, it is reasonable to conclude that the thermal stability displayed far exceeds that of Eurofer. Eurofer has been shown to undergo catastrophic microstructural alteration following transient heating exposure in [61], [348], [355], which is significant as it is a leading structural material candidate for the fusion breeder blanket. The improvement offered by zirconium alloys in this respect gives strong weight to their continued investigation for this application.

The microstructural stability of Zr-Al alloys with isothermal ageing at 700 °C is examined in section 5.3.3. Overall, the microstructural features observed in these alloys are shown to be relatively stable, despite the exposure to elevated temperatures for extended periods. This is especially demonstrated by the grain structure of the alloys shown which appears to undergo no significant alterations as a result of the ageing

treatments performed. Although there is some coarsening of micro-scale precipitates, and development of nano-scale precipitates in the microstructure, analysis of these indicates that they are also stable following further, extended thermal treatments. Similarities are drawn with previously researched Ti-Al alloys with respect to the development of nano-scale Al-rich precipitates in the microstructure, observed following ageing treatments [356]. However, a difference in the crystal structure of these precipitates between the two systems is identified, with an $L1_2$ structure reported in the Ti-Al system [356], and a $D0_{19}$ structure suggested as a result of TEM analysis in this study.

5.5 Further work

Isothermal testing of alloys in this study was performed at temperatures above the expected steady-state temperature of the fusion breeder blanket structure, as detailed and justified in section 5.2.1. Therefore, once an expected steady-state operating temperature is identified for the component, sample evaluation following isothermal ageing at this temperature should be used to verify the applicability of the thermal stability results produced in this study. This evaluation may also allow for quantification of the acceleration of changes to the microstructures due to the higher temperature used in this study.

The results of transient heating of Zr2.5Ta presented in section 5.3.2.1 indicate promising resistance of zirconium alloys to this likely in-service condition. Limitations of the testing equipment used mean that the heating and cooling rates are significantly slower than those which may be expected in-service [61]. Therefore, improvements to the testing method, such as increased heating power and an actively cooled stage, should be sought

to increase the applicability of the results to the anticipated conditions in-service. The use of the current equipment was kindly offered by collaborators at the University of Bristol to obtain results for the Zr2.5Ta alloy. Similar testing of a Zr-Al system alloy would be valuable due to their promising mechanical properties and stability during isothermal ageing. Encouraging results would also be expected for Zr-Al alloys under transient heating conditions due to the elevated transus temperature in the phase diagram shown in Figure 2-13, and the sluggish diffusion of aluminium in α-Zr [174], but should be demonstrated experimentally.

6 Liquid Lithium Corrosion

6.1 Aim

The overall aim of this project is to provide data for novel zirconium alloys to contribute to the materials selection discussion with respect to their potential application as a fusion breeder blanket structural material. As discussed in section 2.5.3, the literature relating to non-aqueous corrosion of zirconium is scarce, and further work in this area is required [3]. In this chapter, results of corrosion experiments on my alloys in liquid lithium, an attractive choice of breeder/coolant fluid [68], [357], at fusion breeder relevant temperatures are reported, and compared to the performance of other candidate materials. The compatibility of zirconium or its alloys with liquid lithium was previously unknown [84] and it was thought that this could be a life-limiting factor in the materials' application as a breeder blanket structural material [80].

6.2 Method

There is no widely accepted technique for exposure of samples to fusion blanket-relevant liquid lithium conditions, and therefore a method had to be developed for this study in order to reliably and repeatably expose material samples to these conditions (within the capabilities available) so that the effects of corrosion could be observed. It was not feasible within the project to produce a flow loop (such as the Lifus6 loop in Italy [358]) in which the samples could be exposed to liquid lithium at the necessary temperature to emulate the in-service condition. Instead, a method was developed to suspend the samples in a static pool of liquid lithium so that they were partly submerged

and not in contact with the sides or bottom of the liquid container. The method developed is shown schematically in Figure 6-1 and will be described in detail below.

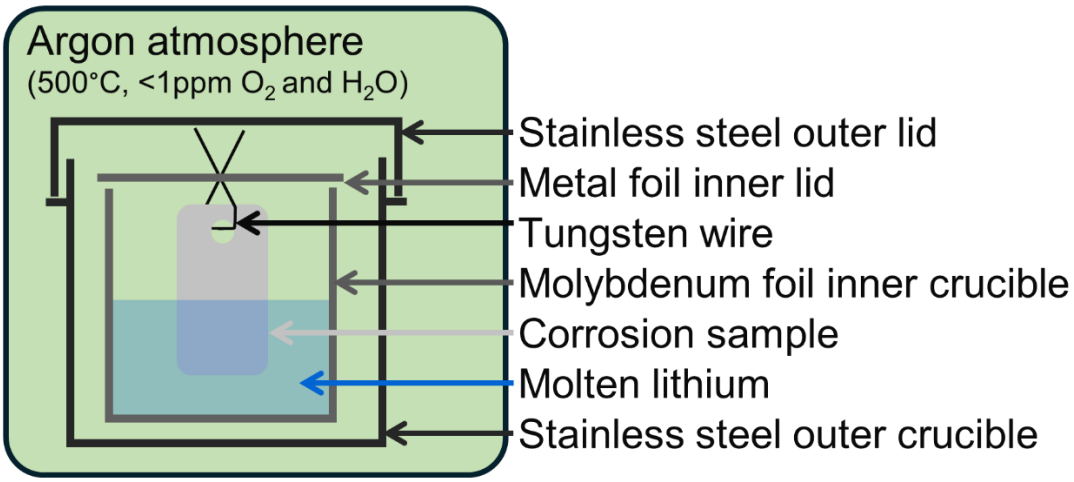


Figure 6-1: Schematic of the method developed for exposure of samples to a high-temperature, static liquid lithium corrosive environment.

Samples of material to be studied were produced with approximate dimensions of 14 x 10 x 1 mm, and a small hole was drilled near one of the short edges to facilitate suspension in a pool of molten lithium. The faces of the samples were polished prior to exposure to ensure a consistent flat surface morphology and to help subsequent analysis. All samples had a final polishing stage of colloidal silica suspension, with the exception of the Eurofer steel sample for which a final stage of 1 μm diamond polishing suspension was used to obtain a polished surface. The samples were hung using 0.3 mm tungsten wire from the centre of a piece of molybdenum foil resting on top of the crucibles containing the lithium.

For each individual sample, approximately 1.5 g of 99.9% purity lithium was contained within a crucible formed of molybdenum foil. The lithium was obtained in ribbon format from Sigma-Aldrich. The choice of molybdenum was due to the fact that

it was expected to be relatively resistant to lithium corrosion [97], [138] and therefore reduce the addition of unwanted elements to the liquid lithium which could affect the interaction with the samples being corroded. Molybdenum is also a relatively uncommon element in the materials being tested and therefore any observation of molybdenum particles on the samples could be attributed to the crucible with confidence; however, this was never observed. The foil format of the material was selected so that the crucibles used could be treated as disposable due to the difficulty of removing lithium following the test. Another advantage of this approach is that there was no opportunity for the test environment to have been contaminated by impurities in the lithium arising from previous tests. These molybdenum foil crucibles were hand-folded and therefore not particularly stable and there was a risk that small holes could occur at the corners. As a result, for practicality and safety purposes, foil crucibles were contained within a larger and thicker stainless-steel crucible for ease of use. The foil crucibles were checked for holes prior to testing using a torch, and no lithium was observed outside of the molybdenum crucibles after the corrosion test indicating that it is unlikely any significant leaks occurred. The stainless-steel crucible material was thus not in contact with the corrosive environment, and therefore did not have an opportunity to contaminate the lithium, which might affect the corrosion process.

It is known that the presence and concentration of elements such as oxygen and nitrogen within the corrosion environment can have a significant impact on the corrosion rates and mechanisms observed. Materials with increased levels of these elements show more serious corrosion [228]. With the testing method used for this study, there was no opportunity for the control nor measurement of the concentrations of these elements present directly in the liquid. Whilst this is clearly a limitation of the work reported here,

the results should remain relevant for a number of reasons. Firstly, the concentrations of these elements were likely at or close to the saturation levels of their solubility in lithium due to the scale that could be observed on the surface of the molten lithium as samples were being introduced to and removed from the liquid. Therefore, the observations here likely present a worst-case scenario which is useful when considering engineering applications where safety is critical. In addition, whilst some liquid lithium purification systems have been employed in loops at lower temperatures [235], it is not clear to what extent elements such as nitrogen and oxygen could be effectively removed in a full-scale fusion power plant with lithium flowing through the breeder blanket at temperatures in excess of 450 °C. It should be considered that impurity elements may originate from the structural materials being used as well as being present in the lithium used, and therefore any benefits of purification may be short lived as the lithium fluid flows around the loop. As a result, the use of nominally pure lithium within a controlled inert environment, as described below, is thought to be practically relevant to the likely conditions that will occur in-service.

The crucible system containing the lithium was introduced to a pre-heated furnace at the desired test temperature of 500 °C, before the samples were introduced, to melt the lithium and homogenise the system at this temperature. This process took approximately 1 hour. The furnace was contained within an argon inert gas atmosphere of an MBraun MB200B glovebox with control and monitoring of the oxygen and moisture levels. After melting and homogenisation, the stainless-steel crucible was removed from the furnace and the small metal foil lids with the samples hanging from each were placed on top of the foil crucibles so that the samples were suspended within the molten lithium and the

crucible assembly returned to the furnace. It is estimated that the period over which the crucibles were outside the furnace was less than two minutes.

At the end of the exposure period of 24 hours, the crucibles were removed from the furnace, and the samples immediately lifted out of the liquid lithium using the metal foil lids and tungsten wire that they were attached to. The samples were suspended in the room temperature glovebox atmosphere to cool so that the freezing of the layer of adhered lithium on their surface did not cause the samples to adhere to other surfaces.

A substantial stainless-steel lid was used to cover the stainless-steel crucible and to enclose the individual molybdenum foil crucibles during pre-melting and during the corrosion test so that the atmospheric environment within the crucibles could be maintained. This was necessary due to the potential for evaporation of the liquid lithium over the test. The lid ensured that a vapour pressure equilibrium could be reached and prevent significant further evaporation, whilst not being clamped down so over pressurisation of the system could not occur.

During the exposure period, the high temperature molten lithium presented a significant risk of fire in the event that the inert atmosphere was not maintained. Therefore, the system was carefully monitored, and checks at regular intervals (at least every 4 hours) were carried out. The monitoring allowed for confirmation that the glovebox atmosphere was maintained below 1 ppm O_2 and H_2O throughout the tests, and the temperature remained at 500 °C within a margin of ±0.5 °C.

In order to analyse the corroded surface of the materials, the layer of lithium that was adhered to the sample following removal from the crucible had to be removed. This

could not be done mechanically without damaging the corroded surface of the material that was to be analysed, and therefore a chemical approach was developed and adopted. It is well known that water reacts vigorously with lithium and it is thought unlikely that the presence of water would have any significant impact on the surface of the corroded metal samples used and therefore submerging the sample in water would allow the corroded sample surface to be revealed and analysed. However, the exothermic nature of this reaction and the rapid evolution of hydrogen leads to laboratory safety concerns and the potential for localised heating of the sample which could alter surface chemistry and morphology. As a result, it was decided to use a solution of 95% ethanol, 5% water by volume to suppress the kinetics of the lithium reaction [359] and no noticeable increase in the temperature of the solution was observed during the reaction. It is believed that the use of this relatively mild solution will not have altered the underlying morphology of the corroded surface other than removing the adhered lithium layer [222]. Multiple solution mixtures (approximately three) of approximately 200 mL were used for each sample. As each solution became saturated, the sample was placed in a new volume of solution until no more hydrogen evolution could be observed and the adhered lithium had been completely removed. The presence of water prevents this reaction being conducted within the glovebox so the samples were transferred out of the glovebox using an airtight container meaning the samples had minimal exposure to air before being introduced to the cleaning solution. The reaction was performed within a fume hood so that the evolved hydrogen would be extracted, and a reservoir of cold water was available which the beakers containing the samples and ethanol/water solution could be placed in to in the event that their temperature began to rise significantly. A powder fire extinguisher was available nearby in the lab for appropriate use in the event that the reaction with lithium metal resulted in a fire.

Mass measurements of samples corroded as part of this study were taken before corrosion and following the chemical removal of lithium adhered to the sample surface after corrosion as described above. These used a Sartorius Cubis® Ultra-Micro Balance with a sensitivity of 0.001 mg. Each mass measurement was repeated at least three times, with strong agreement between the results such that masses may be reported to the nearest 0.01 mg with confidence. Residual colour changes are left on the partially submerged samples after cleaning which allows identification and measurement of the submerged surface area using a ruler. Density measurements of the zirconium samples were taken using the Archimedes buoyancy method and an Adam Equipment Luna LPB423i balance with a sensitivity of 0.001 g and a repeatability of 0.002 g. The density of the steel samples was not measured, and instead a value of 7.47 $g.cm^{-3}$ as the density of iron [360] was used as an estimate for these samples. In the presentation of these results, it has been assumed that no significant mass change occurs in the unsubmerged portion of the sample, and that the mass change measured is due completely to effects within the submerged portion of the sample. The relevance and utility of these mass change measurements is discussed below in section 6.3.

Using this method, it is not possible to monitor the relevant properties of the sample material in-situ in the corrosive environment and it is known that liquid metal embrittlement phenomena cannot be reliably evaluated after removal from the corroding environment [361]. Therefore, the way to extract the most information from these samples as to their susceptibility or resistance to liquid lithium corrosion at blanket-relevant temperatures is to perform detailed microstructural characterisation and draw conclusions from this about the level of damage to the material microstructure that can be observed, and then comment on the extent and likely effects of these. Although

some research has been performed in this field in the past, the introduction of multiple materials to the same environment in studies [238], [362] has likely significantly affected their results to the extent that they may not be used as direct comparisons to the novel alloys produced for this study. Other studies cannot be directly compared due to alternative variables used – such as the study time or temperature [235], [239] – or the lack of advanced characterisation [221], [228]. Therefore, in order to provide insight as to the corrosion resistance of the novel alloys produced in this work, other candidate materials for application as breeder blanket structure were evaluated under the same conditions in order that the results might be compared.

6.3 Discussion of the relevance of mass change in liquid lithium corrosion

Measurements of mass change due to corrosion are commonly reported in the literature for samples of other materials [97], [236], [238], [363], [364], and might be expected to produce a useful headline figure for assessing relative corrosion performance in liquid lithium. Measurements of mass loss are often normalised when reported to give a value of mass loss per surface area of the material exposed [97], [363], [364], and this is sometimes converted to a volume loss measurement by use of the material density, or a thickness of lost material [238]. These interpretations are somewhat flawed and this will be critically discussed below.

The measured mass change per surface area exposed, measured density, and calculated volume change per surface area exposed for each of the samples in this study are shown in Table 6-1, using the method detailed in section 6.2. Details of the steel

samples (Eurofer, CNA and YWT), which were corroded and included in this study for the purposes of a benchmark against which to compare the zirconium alloys, are laid out in section 6.4 where more detailed analysis of the microstructural effects of the corrosion on each of the samples is analysed. Additionally, the selection methodology of zirconium alloys for corrosion testing in this study is detailed in section 6.6.1.

Table 6-1: Quantitative results of sample mass change due to corrosion at 500 °C for 24 hours following chemical removal of lithium adhered to the surface of the corroded sample. Measured or estimated densities are used to convert mass change to volume change. Volume change per surface area may be interpreted as thickness change with the assumption of uniform surface removal of material.

Material	**Measured mass change per surface area exposed ($mg.cm^{-2}$)**	**Measured (or estimated) density ($g.cm^{-3}$)**	**Calculated volume change per surface area exposed ($\mu m^3.\mu m^{-2}$)**
Eurofer	-0.06	(7.87)	-0.08
CNA	-30.5	(7.87)	-3.9
14YWT	+0.01	(7.87)	+0.01
Pure Zr	-0.047	6.50	-0.072
Zr1V	-0.036	6.52	-0.055
Zr2.5Al	-0.006	6.45	-0.009
Zr2.5Ta	-0.022	6.71	-0.033

An upper-limit for an allowable thickness loss for hands-on maintenance to be viable from experience on fission reactors is likely 0.5 μm per year [218] which would correspond to 0.0014 μm per 24 hours. Smith and Morgan state that a limit of 5 μm per year (equivalent to 0.014 μm per 24 hours) would avoid excessive deposition of corrosion product in localised regions as a result of mass transfer and a more liberal limit of 20 μm per year (equivalent to 0.055 μm per 24 hours) may be used due to the uncertainties related to the specific design dependency associated with fusion reactors [218]. It can be seen that the data provided in Table 6-1 indicates approximate compliance with these

higher limits for the materials as tested in static lithium with the exception of CNA. In addition, the results presented in Table 6-1 show approximate agreement in magnitude with measurements reported in the literature for steel samples tested for much longer exposure times (100-1320 hours) [97], [239]. This would suggest that a process such as saturation of the liquid lithium causes corrosion effects to be concentrated within the early stages of these corrosion tests with longer exposure times. The extreme variability of this data when repeat measurements are taken is shown by Kondo et al. to span more than half an order of magnitude [239] hinting at its inapplicability for accurate determination of a material's corrosion resistance.

Further undermining the use of this method is the observation of mechanisms of mass gain, due to the addition of corrosion product particles to the material surface as discussed in the previous sections as well as by others [240], [362]. This will lead to serious underestimation of the quantity of material removed by corrosion. This is evidenced especially by the result for mass change of the 14YWT material in Table 6-1 being positive, which is likely caused by the extensive surface corrosion product addition to the sample surface seen in Figure 6-5.

Overall, it is not thought that this method provides a representative nor useful metric of corrosion damage to a material. Microstructural characterisation of the corrosion effects should be used, as it has been in this study with results presented and discussed in the following sections, to provide insights in to the corrosion resistance or susceptibility of a material, and a more sophisticated method is necessary to estimate the quantity of elements which have been removed from the sample which can contribute to active mass transport. A method examining the change in elemental levels within the

liquid lithium such as mass spectrometry [365] is recommended for this but care should be taken that the sample of lithium analysed is representative due to the fact that elemental impurities from the sample may be dissolved or suspended in the liquid, or form precipitates which may sink to the bottom or float to the top of the pool.

6.4 Results of post-corrosion analysis of candidate structural steels

Steels have widely been considered as the primary choice of structural material for breeder blankets in fusion due to the relatively extensive knowledge of their properties under the temperature and irradiation environment, and the wide experience of construction using them [109], [110], [366]. Specific reduced-activation ferritic-martensitic (RAFM) fusion-grade steels, such as Eurofer, Oxide Dispersion Strengthened (ODS) steels, and Castable Nanostructured Alloys (CNA) have been designed specifically for fusion components, such as breeder blankets [109], [318], [367]. Samples of these three types of steel were procured for corrosion and analysis as comparisons to my novel zirconium alloys as part of a research project led by Oxford Sigma Ltd., funded as part of UKAEA's "Small Business Research Initiative (SBRI): Fusion Industry Challenges" programme, and included the experimental input of Dr Junliang Liu and myself at Oxford University.

6.4.1 Results from Eurofer steel sample

Eurofer is the RAFM of choice within Europe as a structural material for fusion [317] and a sample was obtained for testing as described in section 4.6.2. A sample from

this batch of material has been characterised and tested in detail by Jones [368]. Some key details of this material were identified previously in section 4.6.2.

Figure 6-2 was taken by Dr Junliang Liu, and shows the surface morphology of a sample initially polished to a mirror finish, following exposure to static liquid lithium for 24 hours at 500 °C. Two distinct areas of different surface morphology can be seen in Figure 6-2(a), with a smoother surface morphology visible in globular-shaped regions and a more porous structure visible in more severely affected regions between these. Facetted particles which appear to be on top of the surface of the sample are also visible in this image. Figure 6-2(b) shows a higher magnification image of the more porous region, where a dendritic-like structure can be seen more clearly and distinct dark holes are visible within the structure. This would indicate that corrosion may be enhanced at and around sites of microstructural features which are more susceptible to liquid lithium corrosion.

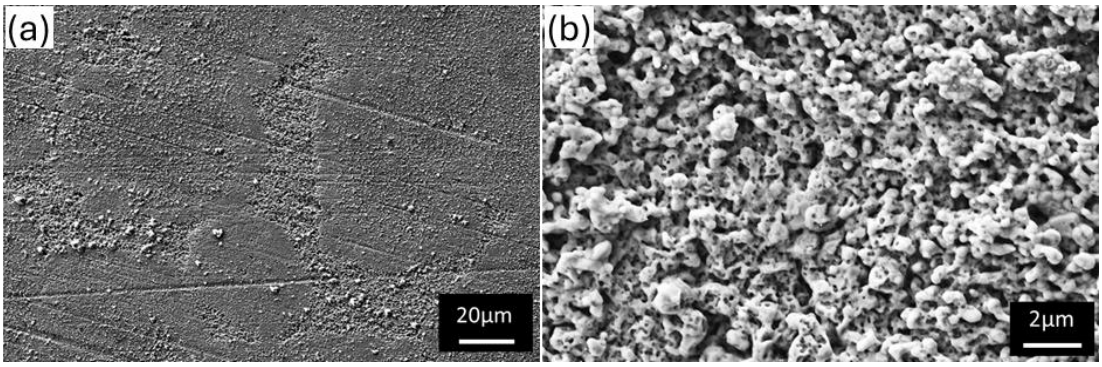


Figure 6-2: Secondary electron (SE) micrographs by Dr Junliang Liu, (a) and (b) showing the polished surface of a Eurofer sample following submersion in molten lithium at 500 °C for 24 hours and the subsequent removal of residual lithium adhered to the surface.

6.4.2 Results from Castable Nanostructured Alloy steel sample

Castable Nanostructured Alloys (CNA) are steels developed and produced by Oak Ridge National Laboratory (ORNL)[1] designed for superior resistance to creep and irradiation damage under fusion breeder blanket conditions. A sample was kindly supplied by ORNL for this study from heat number FTT1 of the GAMOW heat, and was supplied with a report of X-ray Fluorescence analysis showing its composition to be Fe-8.77Cr-0.57Mn-1.46W-0.1Si-0.13Ti-0.08V-0.05Ta-0.09C (in weight percent). Following the melt, the processing of this material involved homogenisation at 1170 °C for 2 hours followed by a ~70% thickness reduction by hot rolling at 1150 °C; it was then normalised between 1150-1170 °C for 0.5 hours, water quenched, and tempered at 750 °C for 1 hour followed by air cooling to produce the nano-precipitated ferritic/martensitic microstructure desired. The radiation resistance, microstructure, and mechanical properties of this material have been analysed in previous studies [367], [369].

Micrographs shown in Figure 6-3 were taken by Dr Junliang Liu. Figure 6-3 (a) and (b) shows micrographs of the same region of the CNA sample before (a) and after (b) exposure to the liquid lithium. These images reveal the surface topology in which some grain structure can be seen in Figure 6-3(a) due to the surface relief caused by colloidal silica polishing. The grain structure is more clearly visible following corrosion in Figure

[1] CNA material for this work was provided by ORNL and produced by the United States Department of Energy, Office of Fusion Energy Sciences, under contract DE-AC05- 00OR22725 with UT-Battelle, LLC

6-3(b) as the grain boundaries appear etched. The etched appearance of grain boundaries is more clearly visible in Figure 6-3(c), which shows a higher magnification micrograph after corrosion. Also visible in Figure 6-3(c) is some terracing of the surface in a number of grains but, most clearly within the large grain at the bottom-left corner of the image. The notable observation from this image is the prevalence of small, intragranular black circles everywhere which are identified as small holes in the corroded surface.

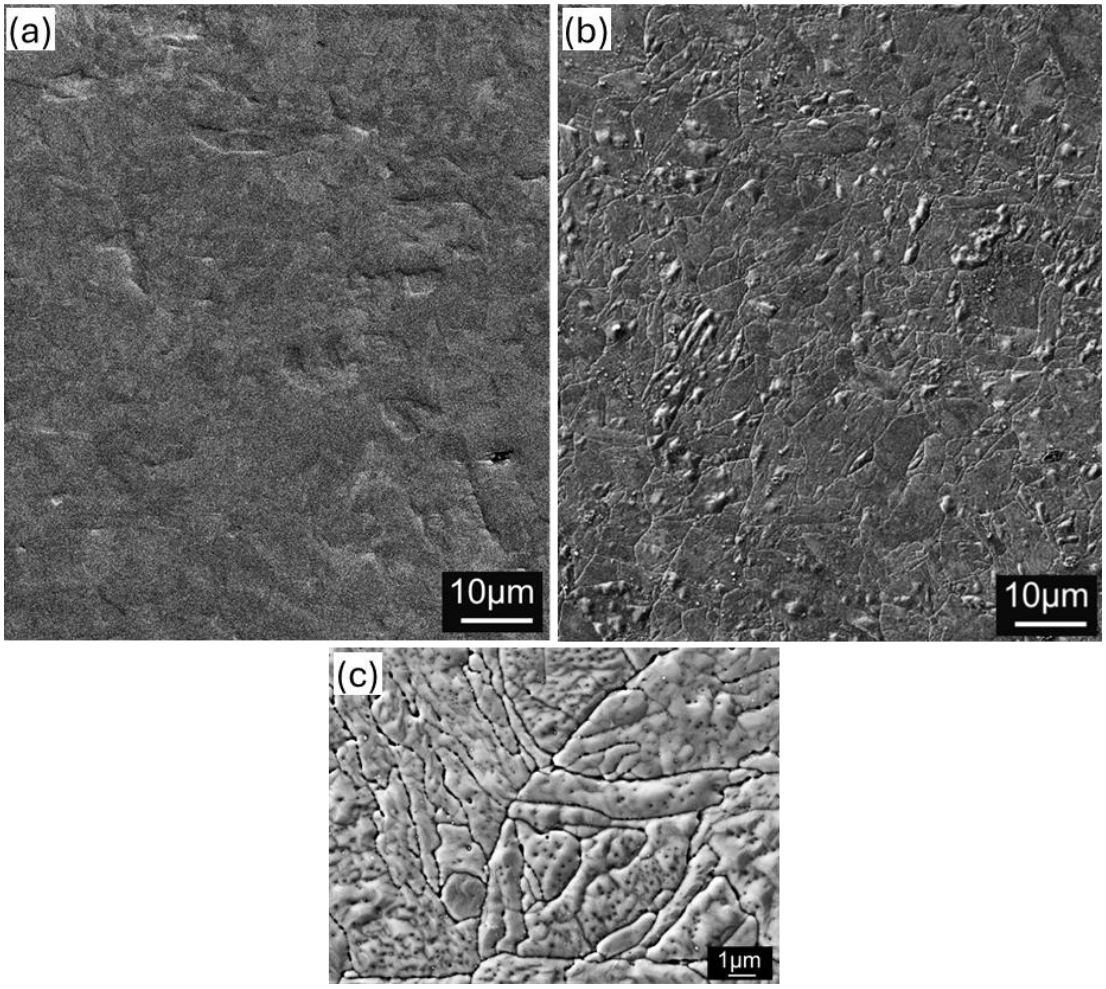


Figure 6-3: SE micrographs by Dr Junliang Liu showing the exposed surface of the CNA sample before (a) and after (b,c) submersion in molten lithium at 500 °C for 24 hours and the subsequent removal of residual lithium adhered to the surface.

In order to be able to observe the relative concentration of nano-scale microstructural features within the uncorroded and corroded CNA material, a sample of each was prepared for Small-Angle Neutron Scattering (SANS) at the ISIS neutron source by thinning a slice to approximately 0.6 mm to allow sufficient neutron transparency. As a result, only one of the two faces of the corroded sample used for this analysis was directly exposed to lithium. For normalisation of the results, the thickness of each sample was measured using an average of at least eight results, each taken to an accuracy of 0.01 mm, leading to a maximum of 4% error in the measured thickness. The results of SANS analysis of the CNA samples are shown as a comparison between the two datasets in Figure 6-4. The wavelength of incident neutrons was restricted to 11 Å to minimise the effect of neutrons which may be scattered multiple times, and the detector was placed 4 metres from the sample. The range of scattering vectors between 0.2-0.6 $Å^{-1}$ is highlighted in the graphs, and the relevance of this is discussed in Section 6.5. In Figure 6-4(a), within the highlighted region, a positive deviation in normalised scattering intensity from the smooth curve can be seen for the uncorroded sample shown by the purple line. For the data taken from the corroded sample, represented by the green line in Figure 6-4(a), the curve within this highlighted region appears flatter. This observation is supported by the calculation of the value of the ratio between the two datasets as shown in Figure 6-4(b) where there is a noticeable increase in the ratio within the highlighted region which indicates the same neutron scattering vector range.

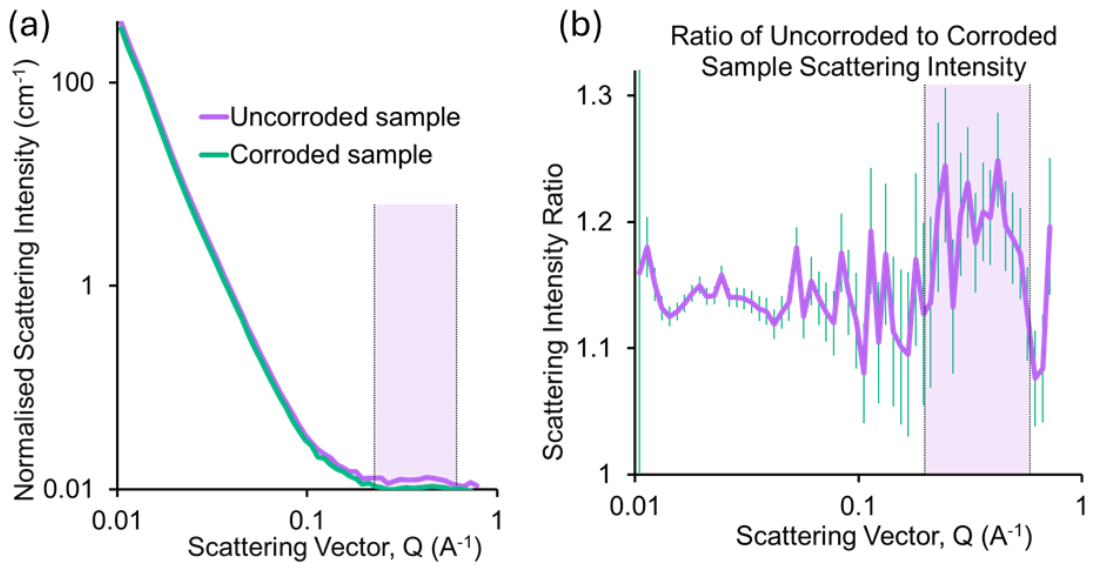


Figure 6-4: Results of SANS analysis of both corroded and uncorroded samples of the CNA material where the corroded sample was exposed to static lithium at 500 °C for 24 hours and residual lithium was chemically removed from the surface. (a) shows scattering intensity normalised for sample thickness plotted against the neutron scattering vector for both samples and (b) shows how the ratio between the normalised scattering intensities varies with the neutron scattering vector. The highlighted regions in (a) and (b) indicate the 0.2-0.6 Å^{-1} scattering vector range.

6.4.3 Results from 14YWT ODS steel sample

Finally, for these steels, a sample of ODS steel was chosen. This was from a batch of 14YWT material manufactured at the University of Oxford using hot isostatic pressing (HIP) consolidation following mechanical milling of pre-alloyed powders as detailed by Gorley [370], and has been extensively characterised (including measurement of exact composition) by others [368], [371], [372]. This material includes Y-Ti-O compounds as nano-scale oxides, and has an overall nominal composition of Fe-14Cr-3W-0.2Ti-0.25Y_2O_3 in weight percent. Figure 6-5 shows two micrographs of the surface of the 14YWT material sample following corrosion. Grain boundary etching is apparent in this sample to a slightly reduced degree in comparison with the corroded CNA shown in Figure 6-3(c). Bright, facetted particles which are raised from the surface are

also clearly visible on the 14YWT in Figure 6-5, which are similar to the structure of particles seen on Eurofer in Figure 6-2(a).

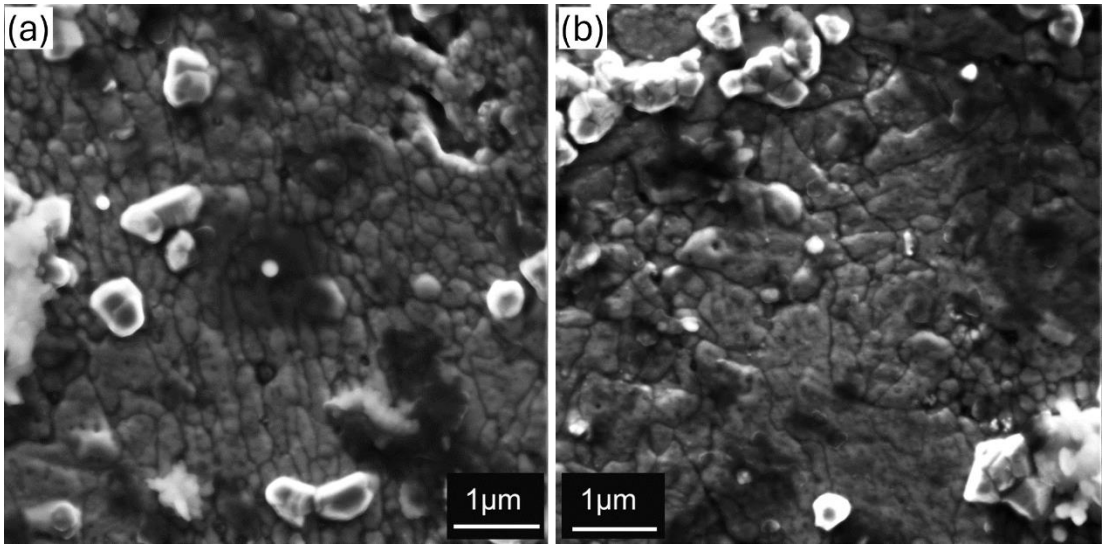


Figure 6-5: SE micrographs of the corroded surface of 14YWT ODS steel material which was polished prior to exposure in lithium at 500 °C for 24 hours followed by the removal of residual lithium adhered to the surface.

The SANS method was used to interrogate the relative concentration of nano-scale microstructural features within the uncorroded and corroded 14YWT material as for the CNA material in Figure 6-4. Samples were prepared and analysed in the same way and the results are shown in Figure 6-6. The highlighted range represents the 0.21-0.5 $Å^{-1}$ range of scattering vectors within which the ratio between the intensity of the data for the corroded sample and the uncorroded sample can be seen to be approximately 1 in Figure 6-6(b). It can also be seen in this graph that the ratio drops significantly below 1 between scattering vectors of 0.0024-0.12 $Å^{-1}$. The relevance of this will be discussed in Section 6.5.

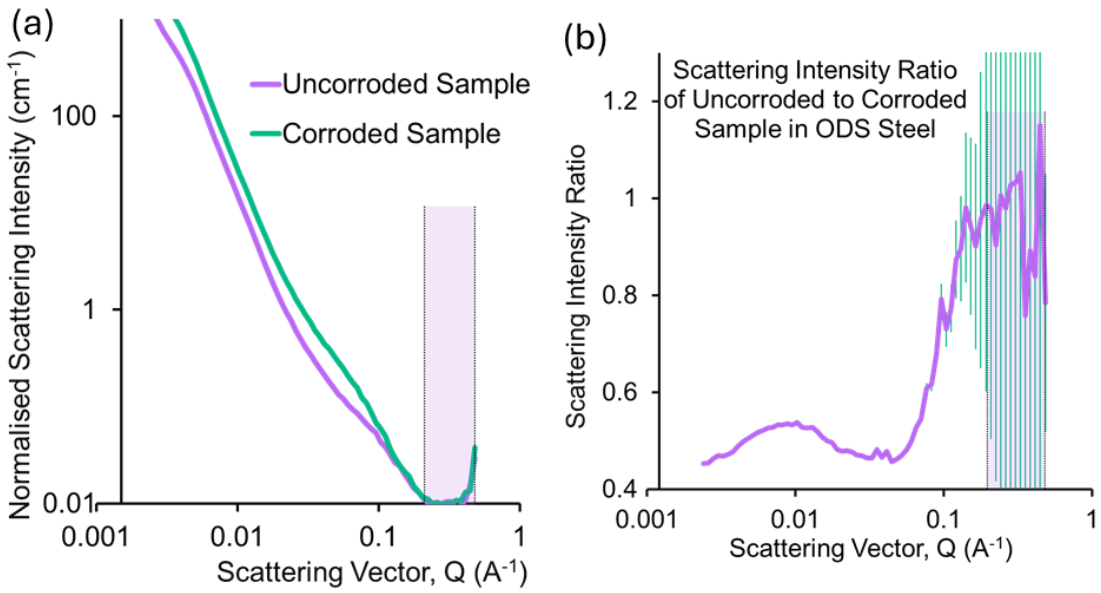


Figure 6-6: Results of SANS analysis of both corroded and uncorroded samples of the 14YWT material where the corroded sample was exposed to static lithium at 500 °C for 24 hours and residual lithium was chemically removed from the surface. (a) shows scattering intensity normalised for sample thickness plotted against the neutron scattering vector for both samples and (b) shows how the ratio between the normalised scattering intensities varies with the neutron scattering vector. The highlighted regions in (a) and (b) indicate the 0.21-0.5 Å^{-1} scattering vector range.

The common features observed in this analysis of the corroded surface of candidate steels for fusion breeder structures will now be discussed along with likely causes and the potential ramifications of these observations.

6.5 Discussion of the corrosion analysis results for steel samples

6.5.1 The effect of corrosion on precipitates

Previous literature has identified that carbide precipitates within steels can be particularly vulnerable to removal by liquid lithium corrosion due to thermodynamically

favourable reactions involving lithium and interstitial elements (including carbon, nitrogen, and oxygen) [138], [222]–[224]. This phenomenon provides an explanation for the observation of holes within the microstructures observed for the Eurofer and CNA materials shown in Figure 6-2(b) and Figure 6-3(c) respectively. Eurofer is known to contain tantalum and vanadium enriched MX-type carbide precipitates with a size range of approximately 8-40 nm, and chromium enriched $M_{23}C_6$-type carbides with a size range of approximately 25-200 nm [373]. The removal of these precipitates from the microstructure explains the holes observed in Figure 6-2(b) which are approximately consistent with the size expected for these precipitates.

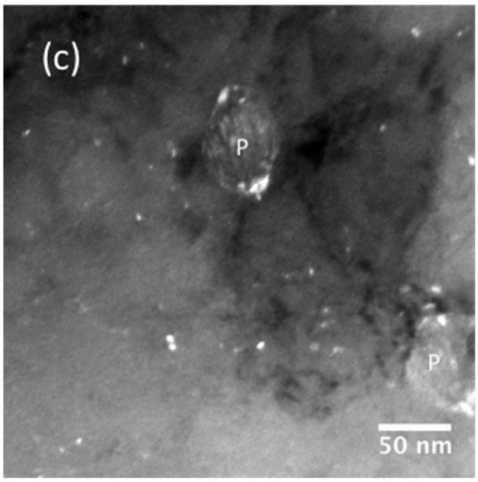


Figure 6-7: Dark-field TEM micrograph of CNA material from [367] [vii] *showing MX-type precipitates as bright white spots and $M_{23}C_6$-type precipitates labelled 'P'.*

Following this, it is thought that the intragranular holes observed in the CNA sample in Figure 6-3(c) are likely to also have been caused by the removal of carbides from the microstructure. However, the hole sizes observed in the corroded sample are somewhat larger that the intragranular precipitate sizes observed in the literature for this material, approximately 30 nm for the $M_{23}C_6$-type precipitates, and MX-type precipitates with sizes <5 nm, as shown in Figure 6-7 from [367]. An explanation for this is that the

initial removal of the carbide precipitate is followed by further corrosion at the site due to the increased surface area locally, which enlarges the hole that is left behind. In order to confirm the removal of the carbides, a technique which was capable of observing the change in the presence of the nano-scale precipitates was necessary. SANS is a suitable technique for that as the neutron scattering vector, Q, is inversely proportional to the characteristic length scale of the microstructural feature which has caused the scattering, as shown in Equation 6-1 [374]. Therefore, the scattering intensity shown in Figure 6-4 and Figure 6-6 indicates the concentration of microstructural features of different length scales.

Equation 6-1 $$d = {}^{2\pi}/_{Q}$$

Equation 6-2 $$Q = {}^{4\pi}/_{\lambda} . {}^{sin(\psi)}/_{2}$$

where d represents the characteristic length scale of the scattering feature and Q is the neutron scattering vector as defined in Equation 6-2 by the neutron wavelength (λ) and the scattering angle (ψ).

The highlighted region in Figure 6-4 corresponds to a range of characteristic length scales between 1-3 nm, and the positive deviation in the purple line of Figure 6-4(a) identified previously is thought to confirm the presence of a significant density of MX-type precipitates at this length scale. The flattening of this region in the green line of Figure 6-4(a) and the increased ratio shown in Figure 6-4(b) is interpreted as an indication that these MX-type precipitates are preferentially removed from the microstructure during the corrosion. A ratio between the data of the uncorroded and corroded CNA sample data greater than 1 is observed in the remainder of the graph in Figure 6-4(b)

which corresponds to length scales between 3-63 nm indicating that larger microstructural features such as the $M_{23}C_6$-type carbides are also likely removed from the microstructure during corrosion. This behaviour is as expected due to previous observations of the instability of carbide precipitates in steel microstructures during lithium corrosion.

By contrast, in the SANS data for the 14YWT material shown in Figure 6-6 a ratio of approximately 1 is seen in the microstructural length scale of 1.2-3 nm indicated by the highlighted region. This is the range of length scales over which nano-oxides occur in this material [110], and therefore this suggests that these nano-oxides are more resistant to the lithium corrosion environment than the carbides in the other steel samples. This interpretation is supported by the lack of observation of intragranular holes within the microstructure in Figure 6-5. The relative thermodynamic stability of various oxide compounds may be measured by their Gibbs free energy of formation which is can be plotted on an Ellingham diagram with a lower position representing greater thermodynamic stability. The Ellingham diagrams shown in Figure 6-8 from [375], [376] show how the Gibbs free energy of the oxides of lithium, titanium and yttrium compare. This is supported by the relative stabilities of the compounds shown by [377]. Whilst the specific reaction mechanisms involved with the corrosion of the Y-Ti-O oxides in the microstructure by lithium are unknown, and are likely to be relatively complex, the comparison of the thermodynamic stability of the oxides of these elements suggests that there is likely to be relatively little thermodynamic driving force for the decomposition of these important strengthening and defect-trapping precipitates.

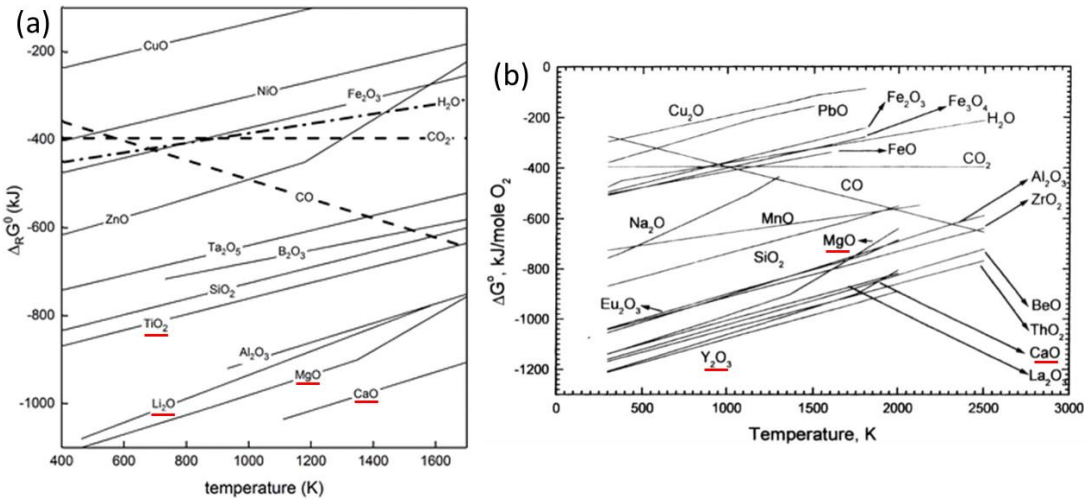


Figure 6-8: Ellingham diagrams from (a) [375] *(Reproduced with permission from Springer Nature, modified) and (b)* [376] [viii] *indicating the relative Gibbs free energy of relevant oxides: Li_2O, Y_2O_3, and TiO_2. Their positions may be compared between the two graphs using the lines for MgO and CaO which appear on both.*

The identification of a ratio significantly less than 1 between neutron scattering vectors 0.0024-0.12 $Å^{-1}$ in Figure 6-6 from the 14YWT material indicates an increase in the concentration of precipitates in the 5-263 nm length scale range following the corrosion. The most likely explanation for this observation is the nucleation and coarsening of precipitates including carbides and nitrides within the microstructure due to the heat treatment associated with the corrosion due to the lack of an optimised tempering process being performed on this material prior to testing, as described by [370], and therefore this observation is not thought to be caused directly by the corrosion of the material.

6.5.2 The effect of corrosion on grain boundaries

The comparison of the micrographs in Figure 6-3(a,b) of the same area of the CNA sample before and after the corrosion gives strong evidence that preferential attack of the material at the grain boundaries is leading to crevassing which can be clearly seen

in Figure 6-3(c), and can also be seen to a slightly lesser extent in the 14YWT sample in Figure 6-5. This phenomenon has been investigated previously as a liquid lithium corrosion mechanism [239], and a mechanism in liquid metal corrosion more widely [378], [379], and is likely to have a significant impact on components subjected to a load as the crevassing could cause stress concentrations within the component leading to failure. Continued grain boundary penetration may also lead to through-cracks in the component due to the interconnected nature of grain boundaries, resulting in a leak of the contained fluid.

Whilst this effect is seen in the CNA and 14YWT samples, it does not appear to be the case for the Eurofer sample. In fact the observed surface morphology after corrosion shown in Figure 6-2(a) appears to show little resemblance to the grain structure of this material shown by EBSD analysis by [368], reproduced in Figure 6-9. This suggests that the grain boundary corrosion mechanism is not as severe for this material, rather the corrosion appears to be more dominated by a mechanism related to the preferential removal of precipitates.

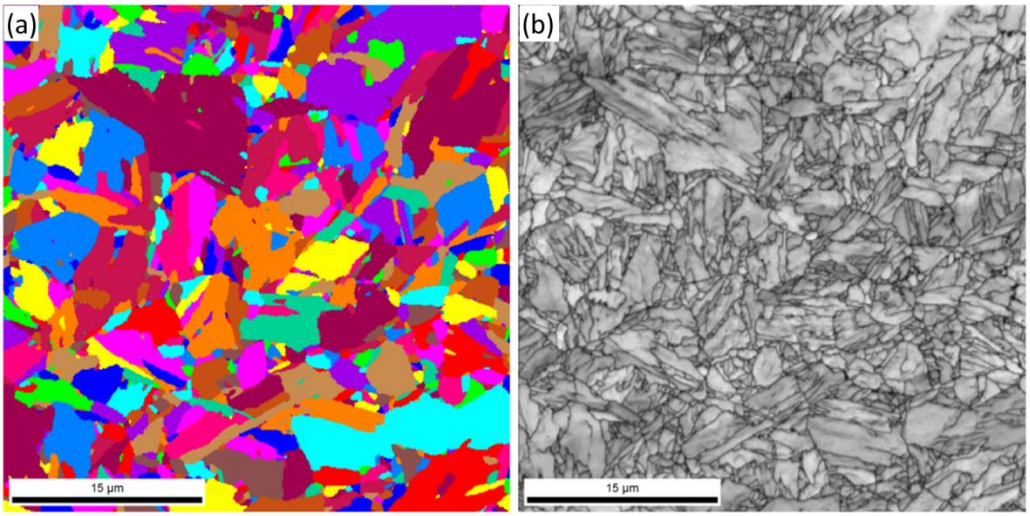


Figure 6-9: EBSD map of Eurofer showing (a) the unique grains identified (encircled by a grain boundary of misorientation angle >15°) and (b) diffraction pattern quality map, from [368]. *The IPF key is not included with the EBSD data presented in the source.*

6.5.3 The appearance of surface particles on the corroded samples

Particles which are raised from the surface of the sample show up brightly in SE imaging, and are clearly visible in Figure 6-5 from the 14YWT material, and can also be seen in Figure 6-2(a) from the Eurofer material. These particles display surface faceting indicating significant variations in surface energy in different crystallographic orientations. It is possible that these particles result from the formation of salts such as Li-O-H compounds formed and deposited on the sample surface during the chemical removal of adhered lithium by the procedure described in section 6.2. Alternatively, they may be Li-X-O compounds, where X denotes a constituent element in the steel such as chromium, formed as products of the corrosion which have attached to the sample surface. This second theory is thought to be a more likely explanation of the origin of these particles due to the similarities observed between them and bright, facetted particles observed on the surface of steel samples after corrosion by liquid sodium which have been identified as $NaCrO_2$ and $NaFeO_4$ corrosion products [380]. Alternatively, Bell et al.

suggest that morphologically similar observations on the surface of their 12Cr-1MoVW steel following lithium corrosion are $M_{23}C_6$-type carbides of iron and chromium [240]. It has not been possible to definitively identify the surface particles seen in this study but comparison to the literature justifies their characterisation as corrosion products.

6.5.4 The appearance of crystallographic terracing on the corroded samples

Terracing of the surface of the corroded CNA sample was identified in Figure 6-3. It is believed that this observation shows that the local rate of dissolution of material from the surface of the sample has a dependence on crystallographic orientation, likely due to the variation of free energy of the surface of different crystallographic planes. This theory is supported by the fact that this effect has previously been observed in results of corrosion tests with other fluids [381]. Further work to correlate EBSD crystallographic orientation data with micrographs displaying surface terracing should be conducted to substantiate this theory.

6.6 Results of post-corrosion analysis of novel zirconium alloys

6.6.1 Selection of zirconium alloy samples for testing

Samples of zirconium alloys were selected for exposure to the static liquid lithium corrosion environment using the same conditions as for the steel samples. This allows for comparison of the performance of the zirconium alloys with each other and with steels of the kind selected for applications in fusion reactors.

Samples were chosen based on the desire to observe how corrosion effects differed due to a change in alloy composition, so one sample from each of the Zr-Al, Zr-V, and Zr-Ta systems were chosen. It was decided to use the samples following the hot rolling and annealing stages of their processing as this would indicate the proposed microstructure of the material as it would enter service. Work throughout this study has focussed on the 2.5 at% solute compositions of these alloys, so Zr2.5Al and Zr2.5Ta following annealing treatments for 2 hours at 700 °C were selected. The Zr2.5V sample was deemed to be too microstructurally unstable after annealing as shown by the extensive grain growth observed previously following ageing at 700 °C for 200 hours in section 5.3.1. This would make it difficult to compare the microstructure of the sample before and after the corrosion and confidently attribute changes to the effects of corrosion. Conversely, the annealed Zr1V sample displayed better microstructural stability following ageing at 700 °C for 200 hours so a sample of this alloy was selected for corrosion testing.

In addition to the annealed samples of Zr1V, Zr2.5Al, and Zr2.5Ta, a sample of pure Zr which had followed the same casting and processing stages as the alloys was included in the testing. By including this sample, the corrosion resistance of the base material could be characterised, and it could be observed how the alloying elements introduced caused any changes in behaviour. All samples were polished with colloidal silica suspension to a mirror finish before exposure.

6.6.2 Results from the Pure Zr sample

SEM micrographs of the pure Zr sample following exposure to the static liquid lithium are shown in Figure 6-10. Some evidence of corrosion product particles on the surface of the sample, which appear with bright contrast in the imaging, can be seen in

Figure 6-10(a,c), but these were not particularly widespread across the sample surface. Visible in Figure 6-10(a) is the grain structure due to electron channelling contrast caused by the variation in crystallographic orientation of the grains rather than due to any significant apparent etching of the grain boundaries. Figure 6-10(b) shows an area from Figure 6-10(a) which contained the most defined grain boundaries at higher magnification. There is little evidence of grain boundary etching in this image. Figure 6-10(c,d) show other areas of Figure 6-10(a) at higher magnification to more clearly reveal the presence of terraced regions of the sample surface, as previously observed for the CNA steel sample in Figure 6-3(c).

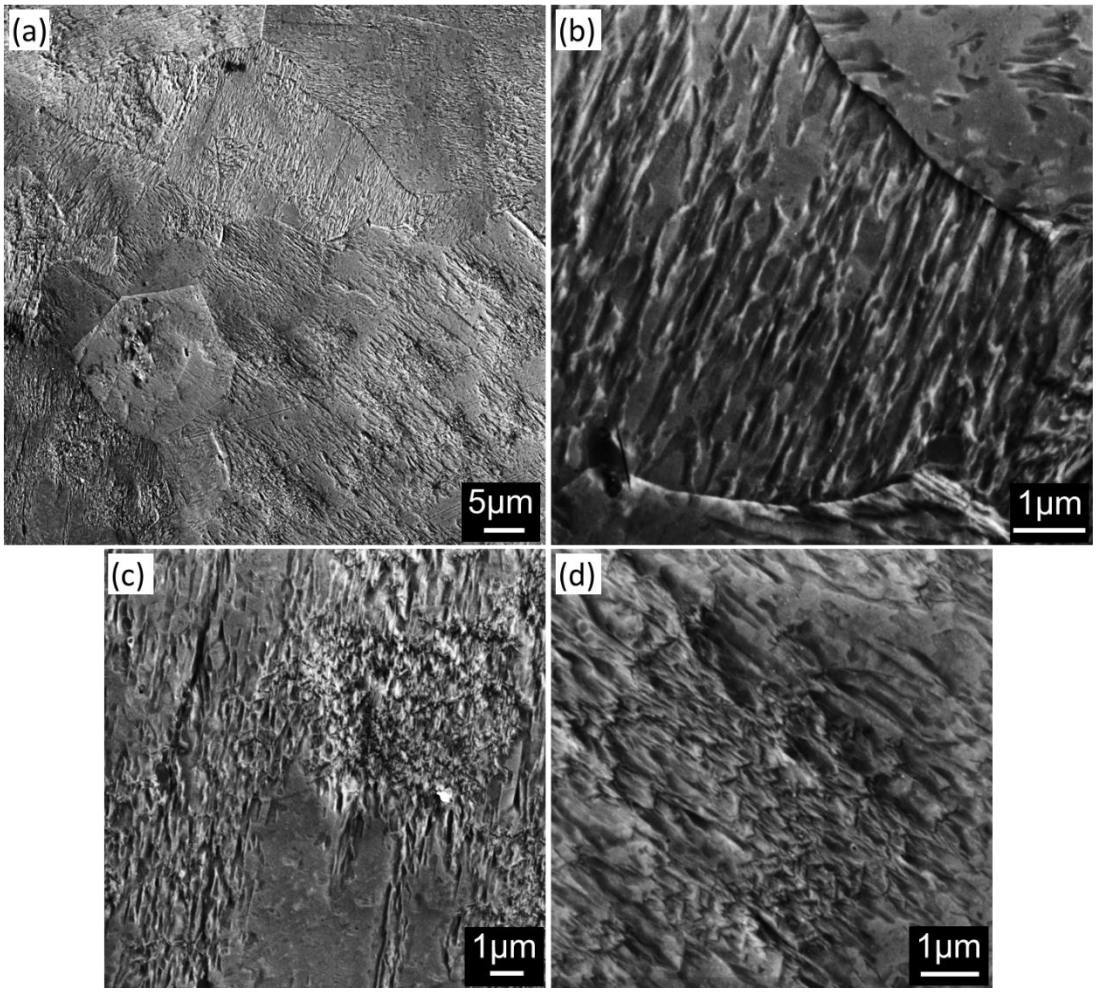


Figure 6-10: SE micrographs showing the surface of the Pure Zr sample following submersion in molten lithium at 500 °C for 24 hours and the subsequent removal of residual lithium adhered to the surface.

6.6.3 Results from the Zr1V sample

Analysis of the Zr1V sample before corrosion is shown in Figure 6-11. The BSE micrograph in Figure 6-11(a) shows a fine distribution of small black dots across the sample. The EDX analysis in Figure 6-11(b) shows that these black dots display an increased vanadium signal compared with their surroundings. This is supported by the observations of the BSE micrograph in which a darker contrast is correlated with elements of a lower atomic number, as is the case for vanadium when compared with zirconium. It is expected that these black dots represent a fine dispersion of ZrV_2 laves phase

precipitates as is predicted by the phase diagram in Figure 2-15, and similarly observed in the Zr2.5V sample as shown in section 4.5.3.

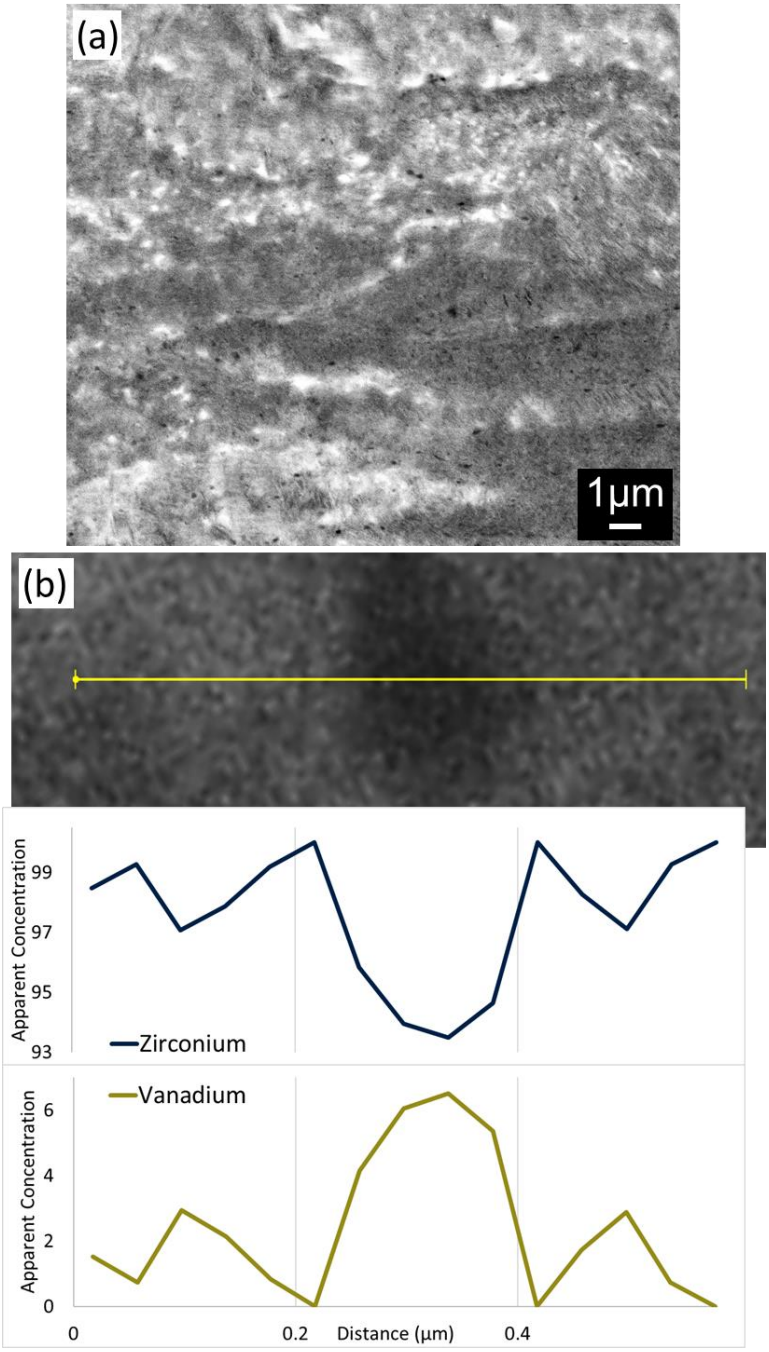


Figure 6-11: (a) BSE micrograph of the annealed Zr1V sample before corrosion and (b) EDX linescan analysis across one of the black spots seen in (a) with indications of apparent concentration variations of zirconium and vanadium.

SE micrographs are shown of the corroded surface of the Zr1V in Figure 6-12. A lower magnification micrograph is shown in Figure 6-12(a) which appears to show that the surface contains 2 different types of area, one with light contrast in this image and the other displaying darker contrast. Higher magnification micrographs were taken in each of these areas, with an example from an area of lighter contrast in Figure 6-12(b) and from an area of darker contrast in Figure 6-12(c). There appears to be little discernible difference between the surface morphologies shown for the two different areas in Figure 6-12(b,c) other than the presence of bright particles on the surface of the sample in (c) which are not present in (b). This may suggest that the presence of corrosion particles on the surface of the sample leads to darker contrast in SE imaging at lower magnifications.

Also visible in Figure 6-12(b,c) is a fine dispersion of small black regions encircled by a ring of bright, topographic contrast. These are interpreted as holes in the surface with a similar size and distribution profile as the ZrV_2 Laves phase precipitates identified in the sample before corrosion and shown in Figure 6-11(a). This suggests that the ZrV_2 Laves phase precipitates are particularly susceptible to corrosion and appear to have been removed entirely from the surface of the corroded sample.

A region of different crystallographic orientation can be observed in Figure 6-12(b) from the electron channelling contrast. However, as was the case for the pure Zr sample following corrosion, there is no significant appearance of preferential etching having occurred at the grain boundary surrounding this grain. Nor is there any evidence in either of the micrographs of Figure 6-12(b,c) showing any feature which may be observed as preferential corrosive attack of grain boundaries.

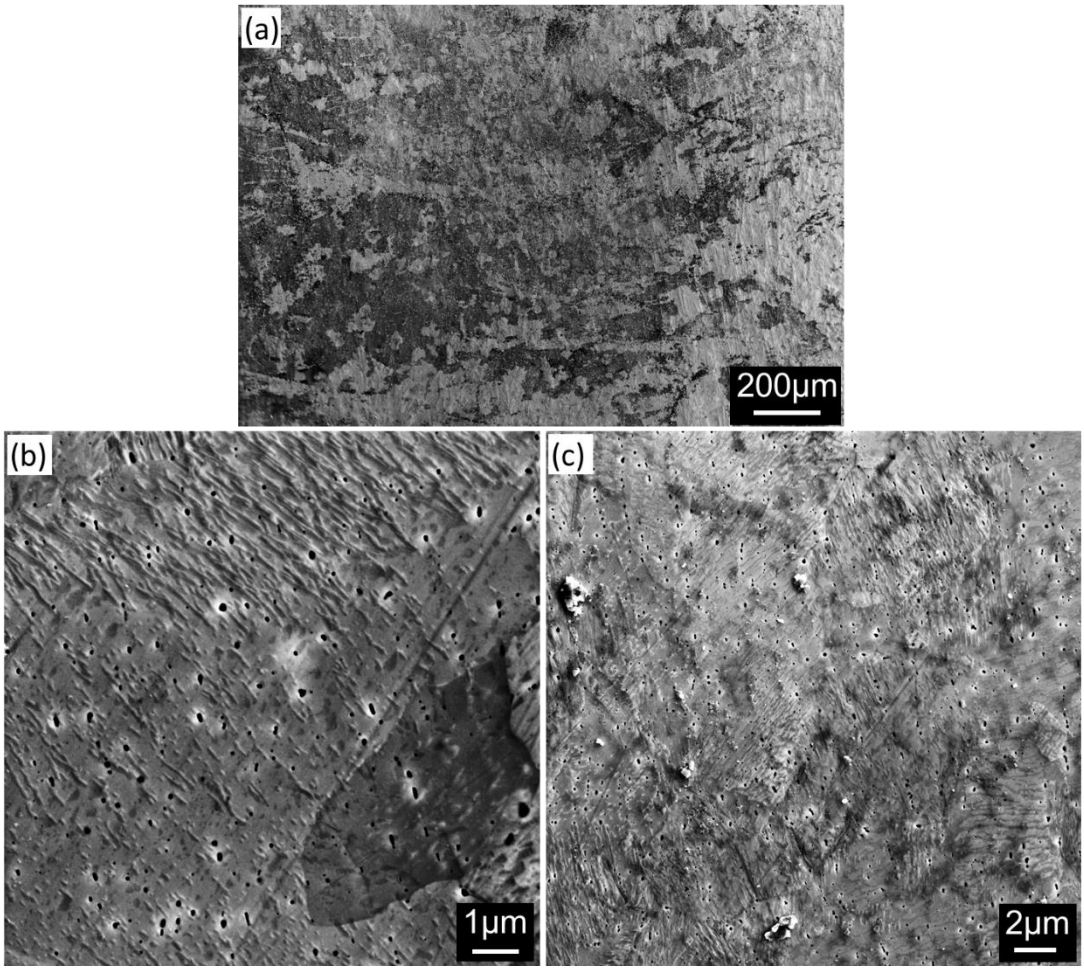


Figure 6-12: SE micrographs showing the surface of the Zr1V sample following submersion in molten lithium at 500 °C for 24 hours and the subsequent removal of residual lithium adhered to the surface. (b) and (c) show examples of the lighter (b) and darker (c) region identified in (a) at higher magnification.

Analysis of the variation of elemental concentration across one of the holes identified in Figure 6-12(c) is shown in Figure 6-13. The lack of elemental concentration variation across this region confirms the previous observation that the ZrV_2 precipitate has likely been completely removed from this area of the microstructure.

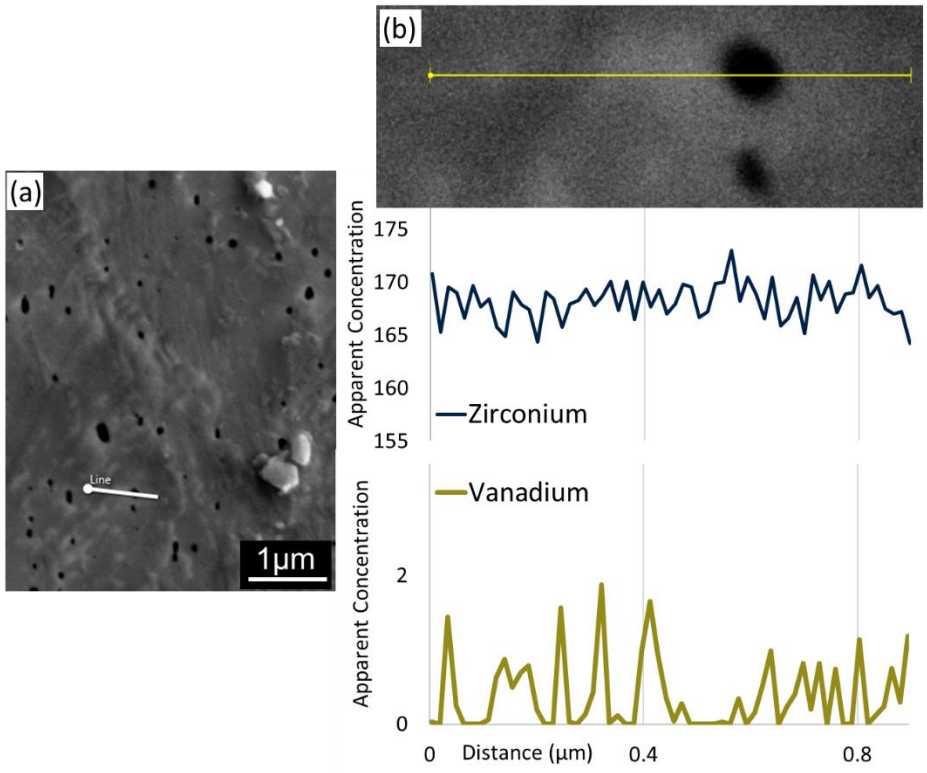


Figure 6-13: (a) SE micrograph showing a region on the surface of the Zr1V sample following corrosion and the region in this image from which EDX linescan data was taken across a circular area of dark contrast. EDX linescan data is shown in (b) with graphs displaying the relative concentrations of the two elements indicated and how these remain relatively consistent along the length of the line.

The surface particles identified in Figure 6-12(c) are more thoroughly analysed in Figure 6-14. Two of these particles are identified in Figure 6-14(a) and the composition variation across them is measured using EDX analysis along the line indicated. The compositional variation measured across the particles is shown in Figure 6-14(b) where a depletion of zirconium and an increase of oxygen concentration can be seen for both particles. This indicates that the surface particles are significantly depleted in zirconium and enriched in oxygen in comparison with the underlying material. Whilst both particles are enriched in oxygen, it can be seen that only the left-hand particle shown in Figure 6-14(b) is enriched in vanadium whilst the right-hand particle displays magnesium enrichment, indicating that not all surface particles on a sample are of the same

compound. The holes visible in Figure 6-14(a) which are interpreted as the sites where ZrV_2 Laves phase precipitates have been removed may contribute the necessary vanadium for the formation of the vanadium-rich surface particle. The origin of the magnesium in the system is unclear.

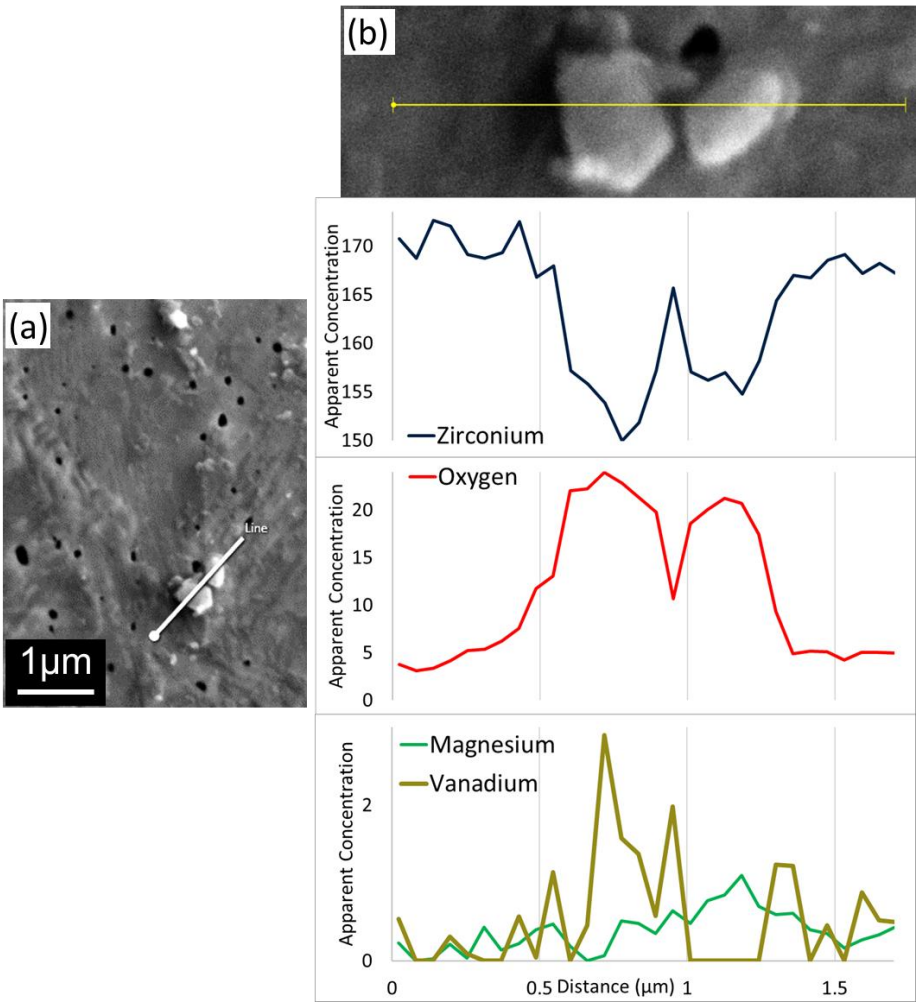


Figure 6-14: (a) SE micrograph showing a particle on the surface of the Zr1V sample following corrosion and the region in this image from which EDX linescan data was taken. EDX linescan data is shown in (b) with graphs displaying the relative concentrations of the four elements indicated and how these vary along the length of the line.

6.6.4 Results from the Zr2.5Al sample

The BSE micrograph in Figure 6-15(a) shows a fine distribution of Zr_3Al precipitates in the annealed Zr2.5Al sample at both intergranular and intragranular sites. These Al-rich phases appear as black dots of sub-micron size due to atomic number contrast. The same precipitates are also visible in the SE micrograph of the surface of the corroded sample of the same material in Figure 6-15(b). The precipitates appear as darker grey areas in Figure 6-15(b) due to the reduced effect of atomic number contrast in SE imaging compared with BSE imaging but are similarly visible at both within grains and at grain boundaries. Some of the smaller sub-micron darker contrast regions appear noticeably darker than the larger (but still sub-micron) dark grey precipitates. These may be holes at prior sites of Zr_3Al precipitates and will be more closely examined. Additionally, the darker grey precipitates which are retained within the microstructure appear slightly recessed when compared with the level of the surface around them.

Grain boundaries can be clearly seen in Figure 6-15(b) but the surface appears continuous across these lines and there is no evidence of any preferential etching effects.

Regions of darker contrast without clearly defined edges can be observed, especially towards the centre of Figure 6-15(b). These regions appear to co-locate with an increased density of particles of bright contrast which appear to be raised from the surface. An example of these particles is examined in more detail in Figure 6-18, and these are thought to be products of corrosion deposited on the surface of the sample. If this is the case, this observation of darker regions surrounding surface corrosion particles supports the observation from Figure 6-12 of the corroded Zr1V sample where regions

of darker contrast in SE imaging were seen to contain surface corrosion products at higher magnification.

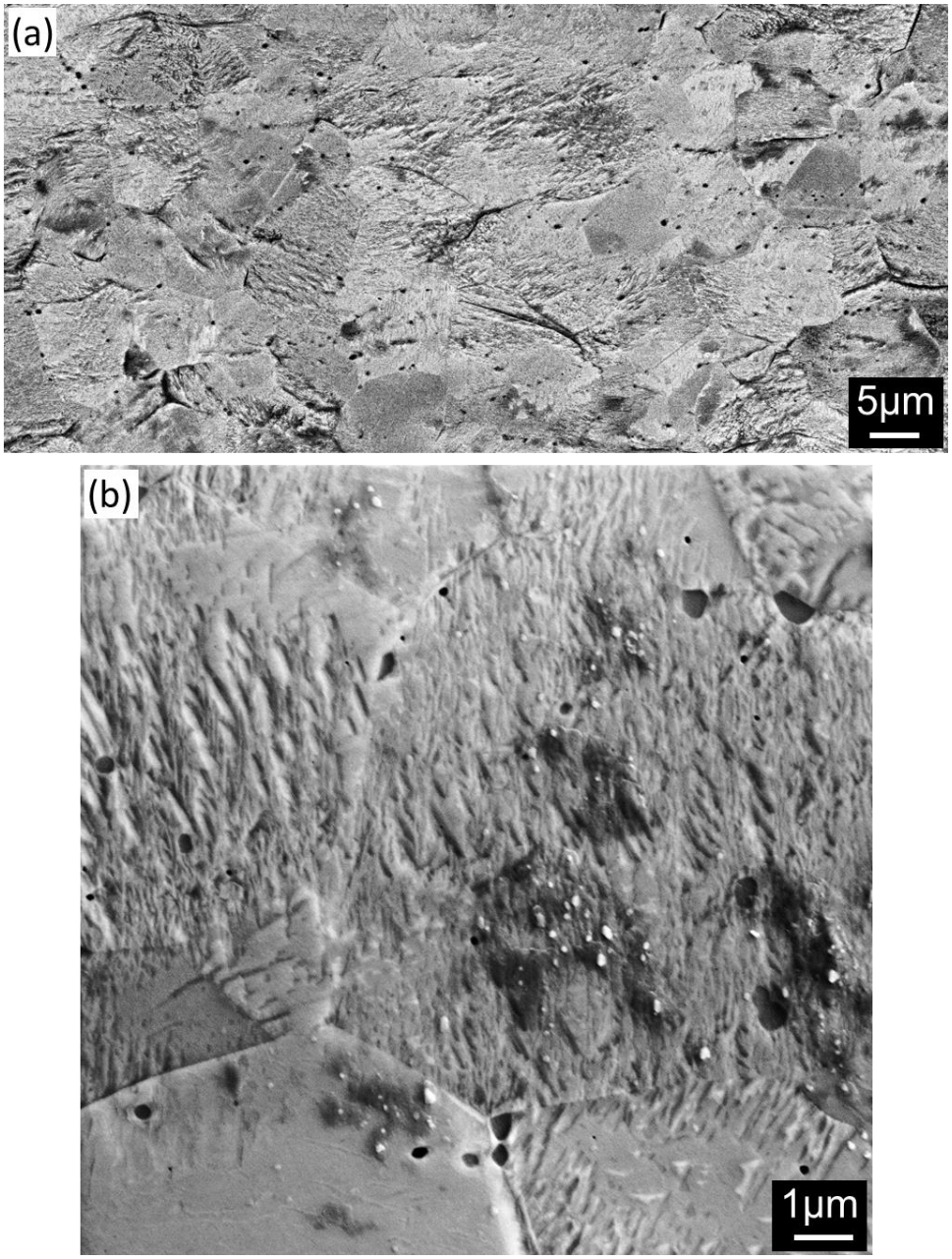


Figure 6-15: (a) BSE micrograph of the microstructure of an annealed Zr2.5Al sample before corrosion and (b) SE micrograph of a sample of the same material following exposure to liquid lithium at 500 °C for 24 hours.

Figure 6-16 and Figure 6-17 show chemical analysis using EDX of sub-micron-sized regions along grain boundaries which show darker contrast in the SE images. The bright fringe to the darker region in Figure 6-16 suggests that it is slightly recessed below the sample surface. The chemical analysis of this region indicates a noticeable enrichment in aluminium which would suggest that it is an intergranular Zr_3Al precipitate which has survived exposure to liquid lithium. Iron is a known impurity within the alloy and it appears that this element also segregates to the precipitate.

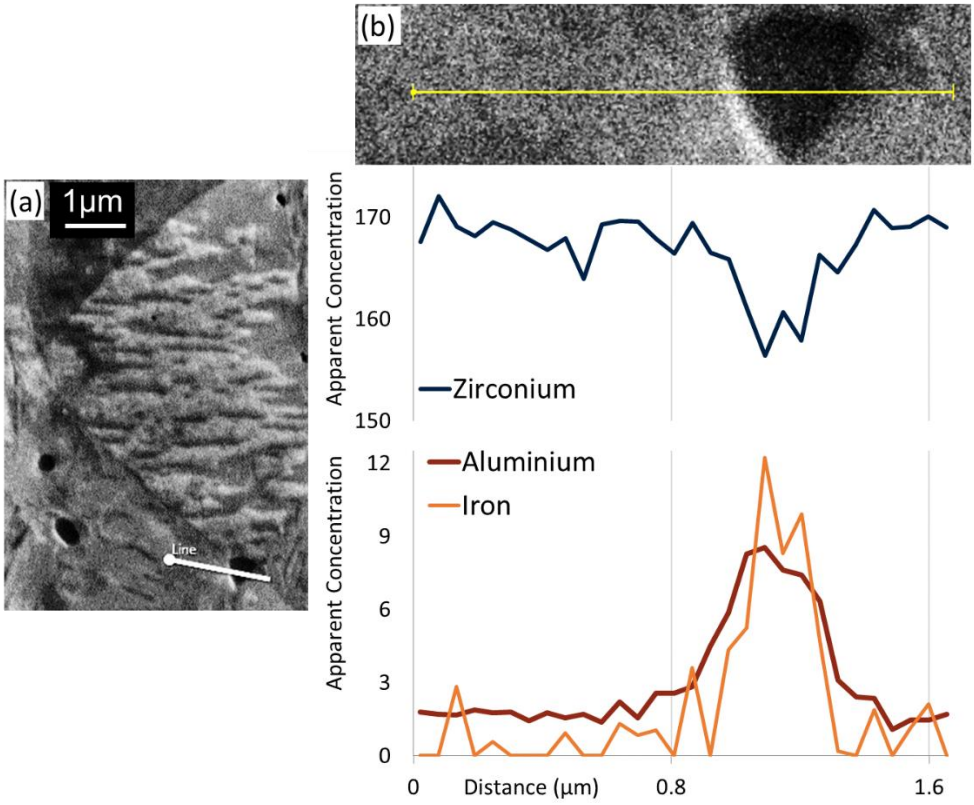


Figure 6-16: (a) SE micrograph showing a region on the surface of the Zr2.5Al sample following corrosion and the region in this image from which EDX linescan data was taken across an area of darker contrast on a grain boundary. EDX linescan data is shown in (b) with graphs displaying the relative concentrations of the three elements indicated and how these vary along the length of the line.

In contrast, the darker intragranular region shown in Figure 6-17 has no indication of aluminium enrichment with EDX analysis suggesting that there is no precipitate

present at this site. Due to the contrast of the surface surrounding this feature indicating its topology, this area is interpreted as a hole in the surface of the corroded sample, from which a precipitate may have been removed.

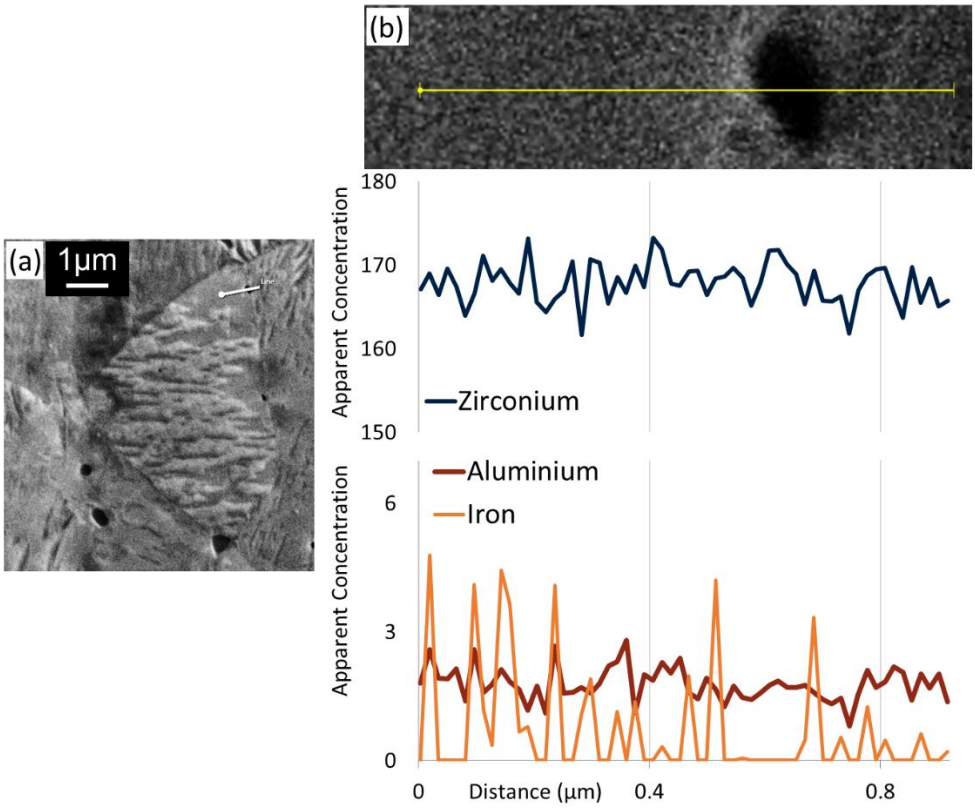


Figure 6-17: (a) SE micrograph showing a region on the surface of the Zr2.5Al sample following corrosion and the region in this image from which EDX linescan data was taken across an area of very dark contrast on a grain boundary. EDX linescan data is shown in (b) with graphs displaying the relative concentrations of the three elements indicated and how these vary along the length of the line.

Bright surface particles were identified on the surface of the corroded Zr2.5Al in Figure 6-15(b). An example of chemical analysis of one of these particles is shown in Figure 6-18, and indicates enrichment with the primary alloying element of this sample, aluminium, but a smaller than expected enrichment of oxygen when compared with the surface particles observed on the surface of Zr1V following corrosion in Figure 6-14. Nevertheless, the source of the aluminium enrichment within the surface particle is

expected to be from the Zr2.5Al material being corroded and therefore this particle is identified as a corrosion product. Whilst they do not all display noticeable aluminium content, it is likely that all of the bright surface particles observed in Figure 6-15(b) can be described as corrosion products left on the surface of the material following exposure.

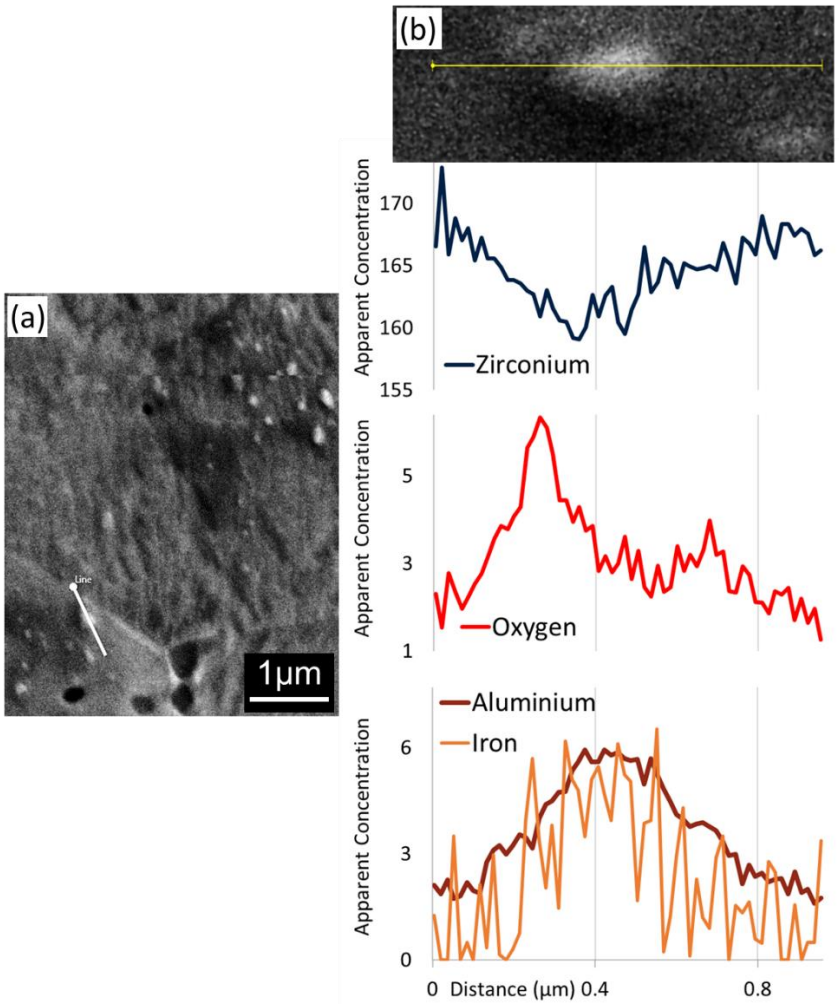


Figure 6-18: : (a) SE micrograph showing a region from Figure 6-15(b) on the surface of the Zr2.5Al sample following corrosion and the region in this image from which EDX linescan data was taken across a surface particle. EDX linescan data is shown in (b) with graphs displaying the relative concentrations of the four elements indicated and how these vary along the length of the line.

6.6.5 Results from the Zr2.5Ta sample

Inspection of the SE micrograph of the surface of the corroded Zr2.5Ta sample shown in Figure 6-19(c) reveals significant holes in the surface of size >1 μm that it is tempting to identify as evidence of local corrosion. However, these can be compared with similar shaped and sized holes in the microstructure of a sample of the same material before corrosion shown in Figure 6-19(a,b). This suggests are not caused primarily by liquid lithium corrosion, but may instead be casting defects not fully removed by the thermo-mechanical processing or due to the surface preparation of the samples.

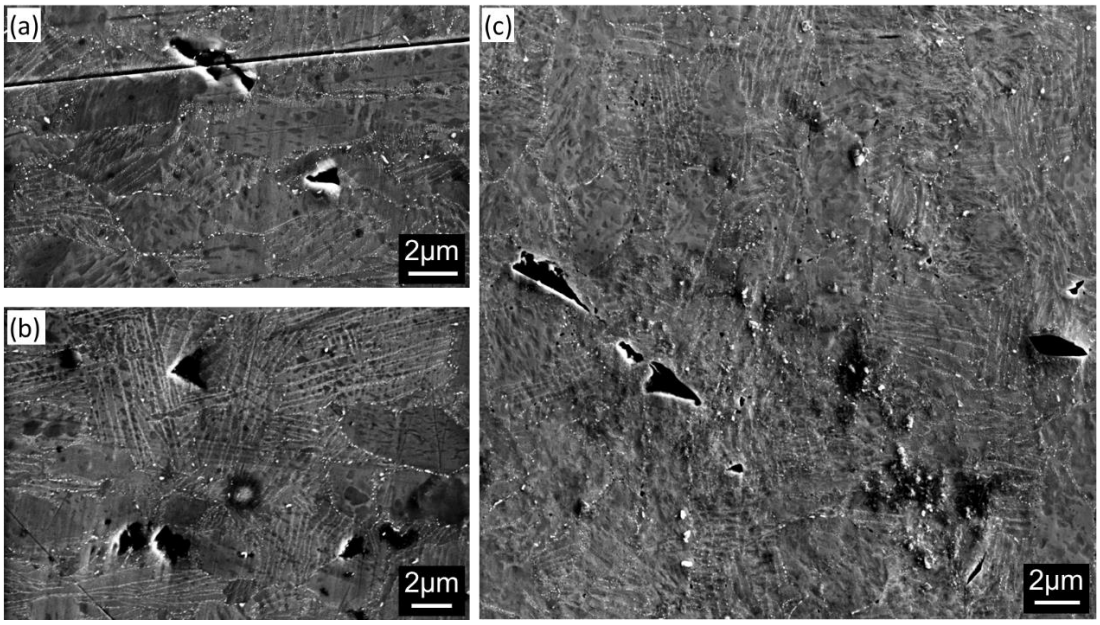


Figure 6-19: SE micrographs of the microstructure of annealed Zr2.5Ta samples before (a,b) and after (c) exposure to liquid lithium at 500 °C for 24 hours showing the presence of holes within the surface of both samples.

As has been observed above, bright particles can be seen on the surface of this sample following corrosion in Figure 6-19(c). EDX analysis on these particles is shown in Figure 6-20 revealing similar elemental segregation as was observed for the Zr1V sample in Figure 6-14. This includes the enrichment of oxygen and the depletion of

zirconium when compared with the underlying material. The primary alloying element, in this case tantalum, is also enriched in one of the two particles analysed. This indicates again that the surface particles cannot all be characterised as the same compound, but that some may be characterised as products of the corrosion process due to enrichment by the primary alloying element which must have originated from the sample. The right-hand particle analysed is expected to be a compound of Zr-O-C-N.

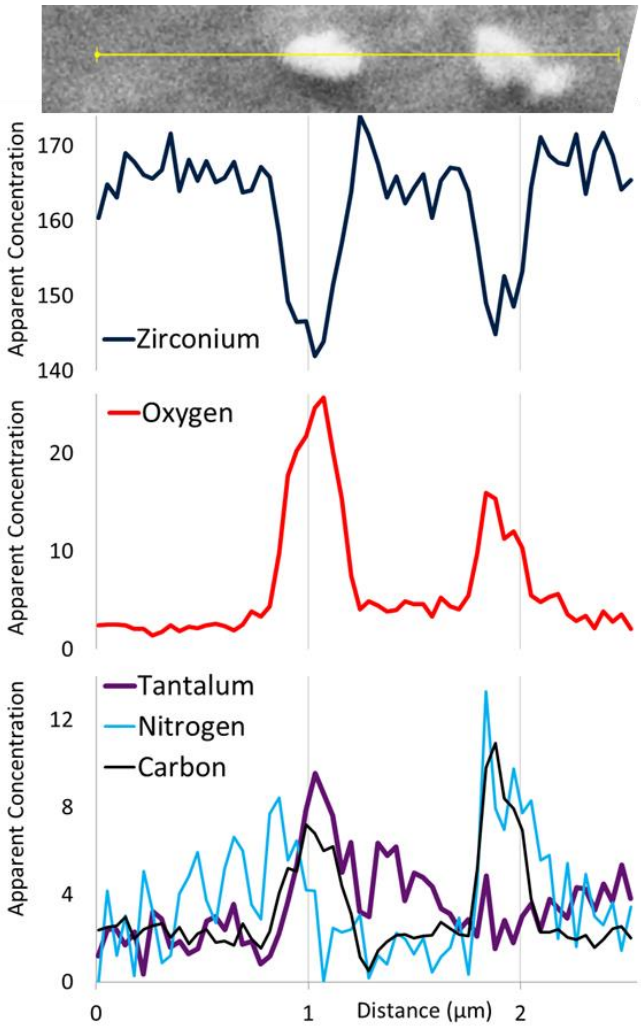


Figure 6-20: EDX linescan data from a region of the surface of the Zr2.5Ta sample shown in Figure 6-19(c) following exposure to liquid lithium at 500 °C for 24 hours with graphs displaying the relative concentrations of the seven elements indicated and how these vary along the length of the line which crosses two surface particles.

A region of this sample following corrosion displayed areas of darker contrast. Closer observation of these darker areas revealed an increased density of bright surface particles in the same area, as shown in Figure 6-21(a). EDX analysis of the bright surface particles shown in Figure 6-21(b) revealed similar elemental segregation as has been observed previously including oxygen, tantalum, and smaller amounts of other elements including carbon, suggesting an oxycarbide-type compound. This supports observations from the corroded Zr1V and Zr2.5Al samples that corrosion product particles on the surface are associated with darker regions of contrast in SE imaging.

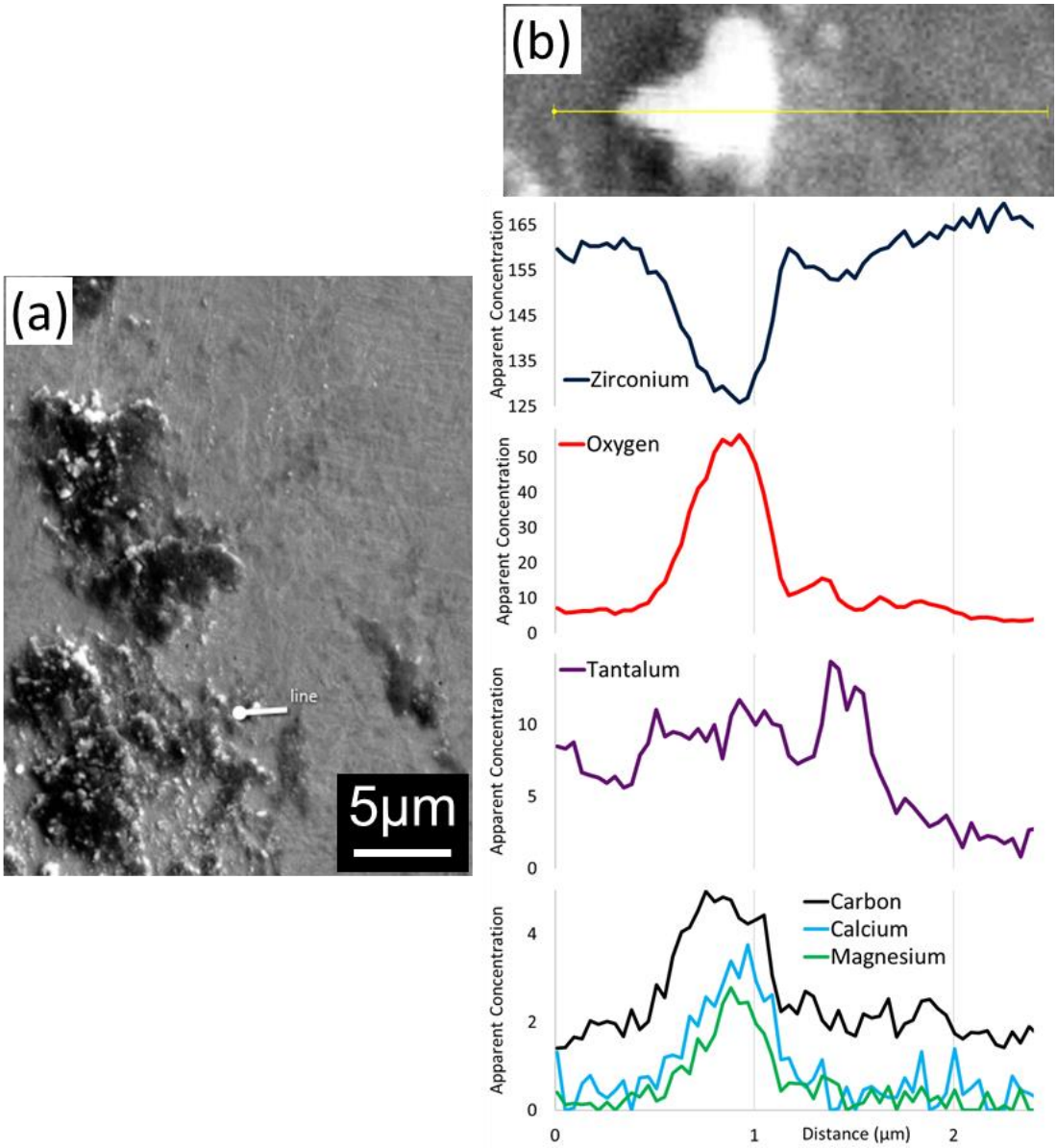


Figure 6-21: (a) SE micrograph showing a region of the surface of the Zr2.5Ta sample following corrosion and the region in this image from which EDX linescan data was taken across a surface particle. EDX linescan data is shown in (b) with graphs displaying the relative concentrations of seven elements indicated and how these vary along the length of the line.

The micrographs in Figure 6-19(c) and Figure 6-21(a) do not appear to show a fine distribution of holes like those observed for the Zr1V sample in Figure 6-12. However, increased magnification does reveal the presence of sub-micron sized holes within the microstructure following corrosion, as seen in intragranular regions towards

the left-hand side of Figure 6-22(b). Unlike the larger holes shown in Figure 6-19 which could also be seen in the microstructure before corrosion, sub-micron sized holes could not be observed in the microstructure pre-corrosion as shown by the micrograph of comparable magnification in Figure 6-22(a). The sub-micron sized holes seen in Figure 6-22(b) are intergranular and visibly of a similar size and shape as the intergranular precipitates that are observable in the microstructure both before and after corrosion in Figure 6-22.

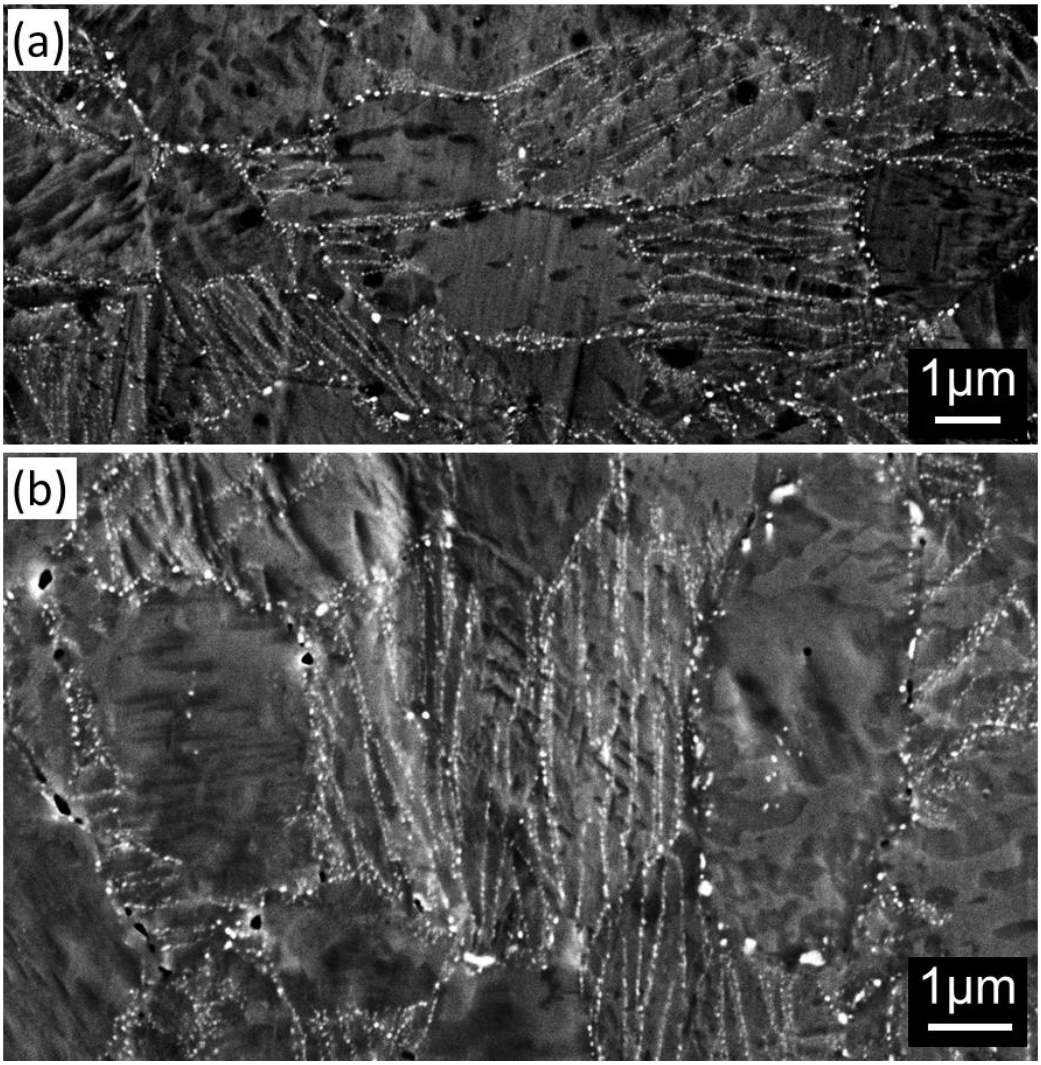


Figure 6-22: SE micrographs of the microstructure of annealed Zr2.5Ta samples before (a) and after (b) exposure to liquid lithium at 500 °C for 24 hours showing the size and distribution of precipitates in the microstructure and the presence of intergranular holes in the sample following corrosion (b) of similar size to the intergranular precipitates.

Precipitates which decorate the grain boundaries in this material appear to have been mostly retained following corrosion when comparing the micrographs in Figure 6-22. There is also no clear evidence of surface relief around grain boundary regions which could be interpreted as etching effects at the grain boundaries.

To undertake higher resolution microstructural analysis, a sample of annealed Zr2.5Ta was imaged using Scanning-Transmission Electron Microscopy (STEM) and

EDX mapping by Dr Guanze He. Analysis of this data reveals that the intragranular precipitates do not show consistent elemental segregation. Figure 6-23 shows two examples of precipitates where one displays an increased concentration of iron (as shown in Figure 6-23(b)) whereas the other (shown in Figure 6-23(c)) does not appear to contain a noticeable concentration of iron.

Similar SEM analysis was performed of the Zr2.5Ta sample following corrosion. All the remaining precipitates in this sample were measured to have a noticeable segregation of iron within the precipitate, like the example shown in Figure 6-24. No iron-free precipitates, like those found in the uncorroded sample in Figure 6-23(c), were identified after corrosion.

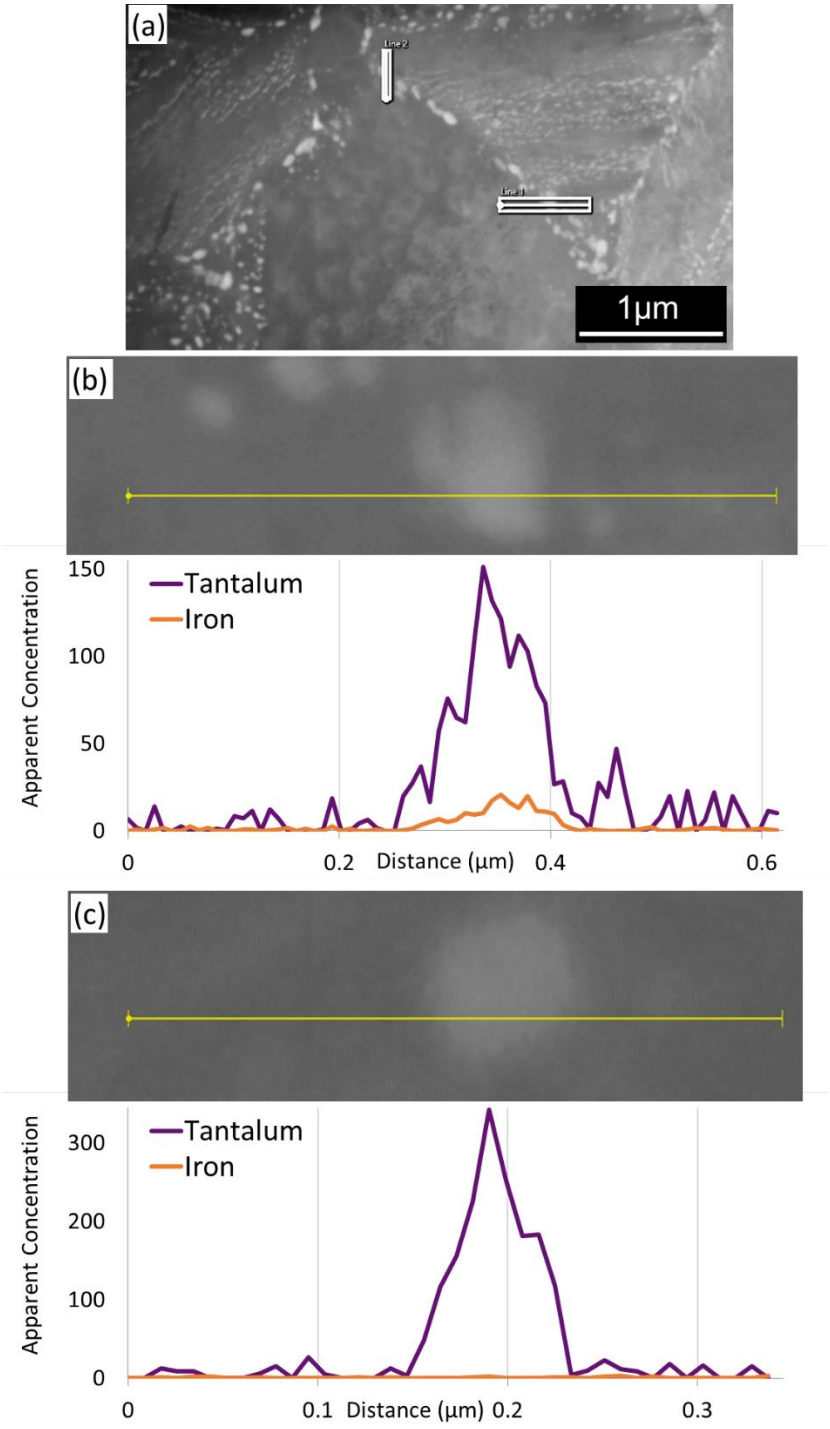


Figure 6-23: (a) STEM micrograph by Dr Guanze He showing the Zr2.5Ta sample before corrosion and the regions in this image from which EDX linescan data was taken across precipitates. EDX linescan data is shown in (b) and (c) for the horizontal and vertical regions shown in (a) respectively, with graphs displaying the relative concentrations of the tantalum and iron and how these vary along the length of the line.

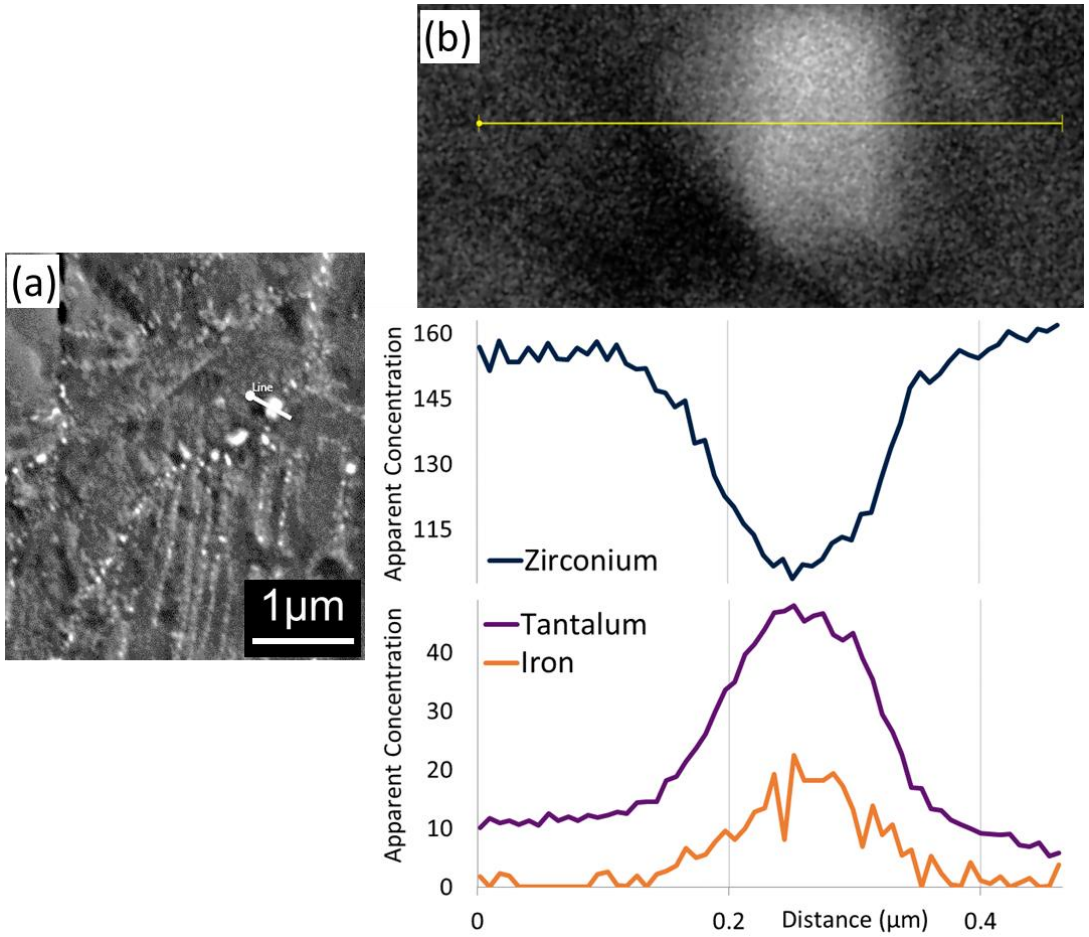


Figure 6-24: (a) SE micrograph showing the surface of the Zr2.5Ta sample following corrosion and the region in this image from which EDX linescan data was taken across a precipitate. EDX linescan data is shown in (b) with graphs displaying the relative concentrations of the zirconium, tantalum, and iron and how these vary along the length of the line.

6.7 Discussion of the corrosion analysis results for zirconium alloy samples

6.7.1 The effect of corrosion on precipitates

The distribution of fine holes across the surface of the Zr1V sample following corrosion in Figure 6-12(b,c) and Figure 6-14(a) indicate that the ZrV_2 Laves phase precipitates in the microstructure appear particularly vulnerable to corrosion by liquid

lithium. This result is comparable to the surface morphology observed due to the susceptibility of carbides to liquid lithium corrosion seen for the CNA and Eurofer steel samples in Figure 6-3(c) and Figure 6-2(b) respectively.

Figure 6-16 indicates that some Zr_3Al precipitates remain on the surface of the Zr2.5Al sample following the corrosion. Some removal of Zr_3Al precipitates is thought to have occurred in the microstructure, evidenced by the appropriately sized intergranular hole identified in Figure 6-17. Further evidence of some preferential removal of the precipitates may be shown by the observation that the ones which remain visible are slightly recessed from the surface as shown in Figure 6-15(b). Overall this indicates that the precipitates within this microstructure display some resistance to corrosion in the environment used in this study, especially when compared with the significant removal of precipitates observed in other samples. However, the Al-rich precipitates are not completely resistant to the corrosive environment.

Ta-rich precipitates are widespread in the microstructure of the Zr2.5Ta sample both along grain boundaries and within grains as shown most clearly in Figure 6-22(a) and Figure 6-23(a). These precipitates appear to be mostly resistant to removal by the liquid lithium as their distribution remains widespread in the microstructure of the corroded sample as shown in Figure 6-22(b) and Figure 6-24(a).

However, there does appear to have been limited removal of the Ta-rich precipitates due to the holes which can be observed along grain boundaries on the left-hand side of Figure 6-22(b). Upon more detailed chemical examination of precipitates in the sample before corrosion using EDX analysis it was identified that there are two populations of precipitates. one containing iron and the other not, as shown in Figure

6-23. Whilst there may be some limited solubility of iron in BCC tantalum [382], the presence of iron in the precipitates may indicate that Laves phases containing Zr, Ta, and Fe are formed as is observed in comparable commercial Zr-Nb alloys in the fission industry [335]. Following corrosion, only precipitates containing iron could be identified. This observation would suggest that the two different types of precipitates within the microstructure have differing levels of corrosion resistance in the tested environment and that the precipitates which contain iron, whether these are BCC tantalum phase, or a Laves phase, are more resistant.

The precipitates in the Zr2.5Ta alloy appear to be the most resistant to corrosion of any of the precipitates directly studied, although the Y-Ti-O nano-precipitates in the 14YWT sample may also be resistant to liquid lithium.

6.7.2 The effect of corrosion on grain boundaries

Examples of grain boundaries that have been exposed to liquid lithium in pure Zr, Zr1V, Zr2.5Al, and Zr2.5Ta samples can be seen in the SE micrographs in Figure 6-10(a,b), Figure 6-12(b), Figure 6-15(b), and Figure 6-22(b) respectively. In none of these is there any indication of significant preferential attack at any grain boundaries.

This contrasts with the observations of the steel samples in which the etching of grain boundaries appeared more severe. This may be directly compared in Figure 6-3(b) for the CNA steel sample and in Figure 6-5 for the 14YWT steel sample. This comparison leads to the conclusion that the grain boundaries in the zirconium samples are less susceptible to this mechanism of corrosion than the steel samples exposed in the same corrosion environment.

6.7.3 The appearance of surface particles on the corroded samples

Surface particles which appeared bright in SE imaging were seen for all three of the zirconium-based alloys. Chemical analysis of these particles shown in Figure 6-14, Figure 6-18, and Figure 6-21 revealed that they contain oxygen and some enrichment of the primary alloying element, suggesting that they are Li-X-O-type compounds, where X denotes a constituent element in the alloy, with essentially the same origin as those observed on the surface of the steel samples as discussed in 6.5.3. There may be several types of these compounds, also containing elements such as nitrogen and carbon as observed in Figure 6-20 and Figure 6-21 and suggested by [383] for steel samples. The presence of lithium in the particles is inferred from their similarity to observations from the literature [240], [380], as lithium cannot be directly observed using EDX. The source of the oxygen in these compounds may be from either or both of impurities in the lithium liquid and the zirconium sample.

Regions of darker contrast associated with the same areas decorated with corrosion product particles were repeatedly observed in section 6.6. This may have been caused by the shadowing of the SE detector by the corrosion product particles protruding from the surface, or by the effects of charging of insulating surface particles.

6.7.4 The appearance of crystallographic terracing on the corroded samples

The appearance of terracing on the surface of corroded samples and its cause was discussed in section 6.5.4, especially in the pure zirconium sample shown in Figure

6-10(c,d) and the Zr2.5Al sample in Figure 6-15(b), and perhaps in the Zr1V sample in the upper-left region of Figure 6-12(b).

No surface terracing has been observed on the corroded Zr2.5Ta sample shown in Figure 6-19(c) and Figure 6-22(b).

One possible explanation for this observation is that the difference in relative surface energies of different crystallographic orientations is reduced in the Zr2.5Ta alloy compared with the others, making surface terracing less energetically favourable, but perhaps this is unlikely due to the similarity between the matrix compositions of the various alloys. An alternative possible explanation relates to changes in composition of the liquid lithium. The terracing effect is thought to be associated with the simple dissolution mechanism of corrosion by liquid metals as discussed in section 6.5.4, and tantalum is expected to have a very low solubility in liquid lithium [384], [385]. The dissolution of Ta-rich precipitates discussed in section 6.7.1could lead to some level of saturation of the lithium which suppresses further corrosion by the dissolution mechanism by reducing the capacity of the liquid lithium to further dissolve other elements. If this is the case then the corrosion resistance of the Zr-Ta alloy system should be reassessed with larger volumes of liquid lithium as saturation is unlikely in-service. An additional consideration is that the texture of the Zr-Ta alloy is quite different to that of the other zirconium alloys, as shown by the measurement of the Kearns factors by EBSD in section 4.5. It is unknown whether this may explain a substantial difference in corrosion performance.

6.8 Conclusions of observations of liquid lithium corrosion

Simple experiments were conducted on a variety of samples of candidate structural materials for fusion breeder blankets to assess their resistance or susceptibility to corrosion in static liquid lithium at 500 °C for 24 hours. Particles have been observed adhered to the surface of all the samples following corrosion and these have been identified as products of the corrosion mechanisms. Surface particles present an issue when interpreting the mass change measurements of the samples due to corrosion.

Instead, comparisons of the analysis of the microstructural characterisation of the surface of the materials following exposure to the corrosive environment will be used to compare their relative susceptibility to corrosion attack.

Penetration of grain boundaries caused by preferential intragranular corrosive attack has been clearly observed for steel samples CNA and 14YWT. Grain boundary penetration has not been clearly observed for any of the zirconium alloy samples studied. Preferential corrosion at grain boundaries is particularly damaging for a material as this provides a network for lithium penetration and microstructural alteration deeper in to the material and could also cause stress concentrations at the surface. Both of these effects are potentially problematic for the structural integrity of components in-service and may lead to reduced failure stresses as the mechanical properties are degraded. These effects may also be accelerated by the stress imposed on a material in-service, in a mechanism akin to stress corrosion cracking in aqueous systems.

The reason that penetration of the effects of lithium corrosion deeper in to the material is concerning is due to its potential to remove precipitates from the microstructure. Precipitates within the microstructure are beneficial due to their strengthening effects and they may also be designed to act as sinks to reduce the effects of radiation damage [109], [367]. Therefore, removal of these precipitates is likely to be deleterious for the material properties. The results presented above suggest that carbides in steel samples are particularly susceptible to removal by lithium corrosion in the Eurofer and CNA samples. Conversely, there is some evidence from microscopy and SANS data that the nano-oxide precipitates within the 14YWT material are more resistant.

Some types of precipitates in the zirconium samples appear more resistant than others. ZrV_2 Laves phase precipitates are particularly susceptible to corrosion, whilst Zr_3Al precipitates display some resistance. Ta-rich precipitates within the Zr2.5Ta samples appear to show the greatest resistance to corrosion. However, the resistance of these precipitates to corrosion appears to be at least partially dependent on the iron concentration within them, with a noticeable iron content appearing to increase their resistance. This may indicate an alternative nature of these precipitates with a Laves structure hypothesised due to similar structures widely observed in Zr-Nb alloys in the literature [335].

Summarising these results, novel zirconium alloys display promising resistance against corrosion by static liquid lithium at 500 °C in comparison with steel samples. Some of the strengthening precipitates appear to display resistance to preferential removal and much less grain boundary penetration is observed in comparison with the steel samples.

Despite these promising results, zirconium and its alloys are not impervious to corrosion by liquid lithium, and it should be kept in mind that these results are taken after only 24 hours of exposure in static lithium whereas components would be expected to be in a flowing environment for much longer time periods. In order that the extraction of tritium for the fuel cycle may be maximised, it is likely that barrier coatings will be added to structural components to prevent the permeation of tritium [386], although the high solubility of tritium in liquid lithium may mean that this protective layer is unnecessary. Even where protective barrier coatings are applied and would provide protection from corrosion, it would remain advantageous to use a structural material which displays adequate corrosion resistance to provide confidence in the structural integrity of the breeder blanket in the event of coating failure. Coating cracking is thought to be likely due to the mismatch in coefficients of thermal expansion between the structural metal and the ceramic coating. Therefore, the use of zirconium alloys instead of steels may remain advantageous even if a suitable corrosion resistant barrier coating is identified.

6.9 Further work suggested in this area

The work presented in this study gives initial results comparing the resistance to corrosion of a variety of steel and zirconium-based samples in static liquid lithium held at 500 °C for 24 hours. This is a useful and relatively straightforward screening technique for the exclusion of materials which display poor resistance from consideration. For the materials which displayed the more promising performance, further testing should be carried out for longer times, in flowing lithium, at a wider range of temperatures, and including the effects of magnetohydrodynamics on the flow [387]. Additionally the materials should be tested whilst under mechanical stress representative of the in-service

condition, as it has been shown that this can have further corrosion effects in materials, often referred to as stress corrosion cracking in aqueous systems [388].

A temperature of 500 °C was chosen for this study as a reasonable point to collect initial data based on expected operating temperatures of fusion breeder blankets [78]. However, once component designs are sufficiently mature that upper operating temperatures and required levels of nitrogen and oxygen impurities in the lithium have been defined, testing should be tailored to these levels to maximise its applicability. Measurement of the impurity levels may be achieved ex-situ using mass spectrometry techniques [365] and levels may be controlled using methods such as cold trapping or hot trapping for different elements [235].

In addition to the fusion industry-specific steels obtained for benchmarking against the performance of the novel zirconium alloys in this study, their performance should also be directly compared to vanadium alloys. Despite issues relating to their availability and cost, vanadium alloys have become popular breeder blanket structural material candidates recently [317] due to reports of promising resistance to lithium corrosion [126].

In this study, only the sample surfaces have been directly imaged, and imaging of the sample cross-section would provide further insight as to the depth to which corrosive attack of the material has occurred. This would allow observation of the extent to which the porous structure extends within the Eurofer material as shown in Figure 6-2 and the depth to which grain boundary penetration which appears on the surface extends. This may be achieved by focussed ion beam milling of a trench within an analytical SEM, however this technique is limited by the shadowing caused by the trench geometry and is

limited to analysis of a relatively small cross-sectional area which may or may not be representative of the entire sample. Alternatively, the corroded sample may be cut to expose a cross-section and then polished for microstructural examination allowing a wider view of the material cross-section for more thorough microstructural analysis.

7 Summary, Conclusions, and Further Work

7.1 Summary and Conclusions

In this study, it was determined that novel zirconium alloys had the potential to achieve properties which would make them suitable candidates as structural materials for a fusion breeder blanket but that insufficient data was available to fully assess this possibility. Aluminium, molybdenum, tantalum and vanadium were selected as the most promising binary alloying elements to achieve the properties necessary for this application and alloy samples were therefore cast and processed to achieve a representative engineering microstructure for further testing. During this processing, it was determined that the molybdenum containing-alloy was insufficiently ductile due to the formation of the ω-Zr phase, and therefore further work on this alloy was discontinued. Fine and equiaxed microstructures with second-phase strengthening were observed for the alloys containing aluminium, tantalum, and vanadium.

Mechanical testing demonstrated that the Zr2.5Al, Zr2.5Ta and Zr2.5V alloys displayed similar strengths at 600 °C as Zircaloy-4 did at 300 °C (approximately its in-service temperature in fission reactors). Additionally, it was shown that binary Zr2.5Ta and Zr5Al alloys exhibit comparable strength at 600 °C as Eurofer, a leading candidate structural material for fusion.

An exceptionally fine grain structure was observed in the Zr2.5V alloy, but this was unstable under isothermal ageing at 700 °C, however the coarser structure obtained in Zr1V did remain stable under the 700 °C tests. The Zr2.5Ta, Zr2.5Al, and Zr5Al alloys tested all showed good stability of their microstructure and mechanical properties under the same isothermal ageing conditions. Additionally, Zr2.5Ta demonstrated exceptional microstructural and mechanical stability under the transient heating conditions tested at Bristol University, especially in comparison with Eurofer which demonstrated catastrophic microstructural changes.

The formation of nano-precipitates was observed in Zr-Al alloys following isothermal ageing which were relatively stable within the microstructure. These precipitates were compared with similar formations observed in Ti-Al alloys, and their crystal structure was identified as $L1_2$.

Finally, using an experimental apparatus developed for this study, it was demonstrated that the zirconium alloys appear to be significantly more resistant to corrosion by liquid lithium at 500 °C than steels. Although the ZrV_2 precipitates in the Zr-V alloy appeared particularly susceptible to removal during corrosion, precipitates in the Zr-Al and Zr-Ta systems showed better resistance. Also, grain boundary penetration appeared far less significant in the zirconium alloys than was observed in the steels.

Overall, encouraging properties of novel zirconium alloys have been measured which align them with the requirements set out for fusion breeder blanket structural materials in section 2.3.1 [80]. This result is in agreement with research undertaken by Jóhan Pauli Magnussen at the University of Birmingham which shows encouraging results on zirconium-based alloys with more complex compositions. Although this is

relatively preliminary research, it suggests work should be continued in this area to achieve alloys optimised for the operating conditions to become a genuine candidate breeder blanket structural material, as an alternative to RAFM steels.

7.2 Further Work

At the end of each chapter of this study, suggestions of further work in that specific area are identified and presented. Here, a more general overview of the work necessary to identify an optimal zirconium alloy composition for a fusion breeder blanket structural material is presented and discussed.

7.2.1 Further material development

This study has focussed on binary alloys to obtain fundamental understanding of the characteristics of individual alloying elements in zirconium. However, it is expected that a more complex alloy composition would offer even better properties. Exploration of ternary and quaternary dilute zirconium alloys and evaluation of their strength and creep resistance has been ongoing concurrently with this study by Jóhan Pauli Magnussen at The University of Birmingham with encouraging results. Based on the findings of this study, it is suggested that a ternary alloy of Zr-Al-Ta should be assessed. Compositions of up to 5% aluminium have been shown to be favourable here, and adding aluminium to zirconium would result in minimal change to the thermal neutron absorption cross-section of the alloy [389]. Although 2.5 at% Ta has shown to give good mechanical properties, and that 1 at% Ta has been shown as insufficient to prevent severe grain growth, a lower tantalum composition such as 1 at% would be suggested for the ternary alloy given that aluminium has been shown to be effective at preventing grain growth,

and to minimise the detrimental effect which tantalum has on the thermal neutron transparency of zirconium [389].

In addition to developing the structural alloy, it is suggested that development of coating materials is continued [390] to provide a tritium permeation barrier compatible with zirconium due to its tendency to absorb hydrogen and its isotopes, as is commonly observed in fission applications [391]. Due to the high solubility of tritium in lithium potentially reducing the driving force of hydrogen pickup by zirconium in the system, the extent of tritium permeation in to the material should be evaluated to determine the necessity of a tritium permeation barrier coating. Although zirconium has been shown to exhibit some resistance to corrosion by liquid lithium in this study, it would be advantageous for a protective barrier coating to be developed to further protect the structural metal and the tritium permeation barrier from corrosive attack.

7.2.2 Addressing material requirements

Of the material requirements set out in section 2.3.1 [80], a number have been assessed in this study:

- Strength and ductility at ambient and operating temperatures
- Phase stability at operating temperature
- Compatibility and corrosion behaviour with coolant fluid

Promising results have been demonstrated for all three of these requirements, although further investigation, alloy development, and optimisation remains necessary to fully achieve the set objectives for a fusion power plant.

Other requirements, whilst not directly assessed, have been considered based on existing knowledge:

- Thermal neutron absorption
- Hydrogen isotope retention and hydriding behaviour

And some requirements have not been addressed as part of this study:

- Effects of irradiation on strength, ductility, and phase stability
- Operating creep and fatigue performance
- Long-term activation

The importance of evaluating the creep performance of zirconium alloys for fusion applications is discussed in section 4.6.3. This evaluation was unfortunately not possible in this study due to equipment failure, and it is recommended that this property is assessed in future work. It has been shown that the small punch method may be used to compare the creep performance of materials with relatively small material sample sizes before larger-scale tests are carried out with more optimised alloys. Whilst fatigue resistance is identified as a required property, it is suggested that more detailed design requirements are sought to determine an approximate stress amplitude and number of cycles required in-service to inform material testing.

The effects of irradiation caused by the neutrons emitted by the fusion reaction upon the microstructure and properties of the zirconium alloys was outside of the scope of this study because of the time and access challenges associated with obtaining suitably irradiated specimens. In addition, due to the more resource-intensive nature of this work,

it is suggested that one (or multiple) promising alloy compositions are identified and somewhat optimised prior to undertaking irradiation testing. Furthermore, due to their extensive application within the nuclear fission industry, the effect of a neutron irradiation environment on zirconium alloys microstructure is well understood [392]–[394] and it is thought that the high operating temperature proposed for a fusion reactor may lead to minimisation of irradiation damage effects by in-situ annealing [84].

Neutron irradiation of the material will also cause transmutation and activation of the material which may be of concern. This study has not examined these effects as the relevant incident neutron spectrum has not been confirmed for future fusion reactor designs and it has been shown that these effects may be examined via computational methods with defined incident neutron spectra [169] using existing methods [79], [395]. It is also deemed that maintaining a low activation material post-service is a secondary priority with respect to producing a material which fulfils the engineering requirements of the component to provide structural integrity [85].

8 Appendix: Aqueous corrosion of Zr2.5Al and Zr2.5Ta

Although the aim of this study was not to produce materials which are resistant to the effects of aqueous corrosion, samples of the Zr2.5Al alloy and the Zr2.5Ta alloy were polished and prepared for autoclave corrosion at the University of Manchester at 300 °C for 30 days. Samples of X2 and Zirlo, both commercial zirconium alloys supplied by Westinghouse, were also prepared for equivalent testing to benchmark the results achieved of the novel alloys.

It has been widely observed in the literature that the addition of aluminium to zirconium alloys greatly reduces their resistance to corrosion [396]. This was also the case for the Zr2.5Al tested, as the metallic sample transformed completely to a flaky, white material which disintegrated easily upon examination and can be seen in Figure 8-1(a). As a result, a meaningful measurement in the mass change or oxide thickness could not be taken for comparison with the commercial alloys and it is suggested that aluminium should not be considered as an alloying addition for zirconium in aqueous environments.

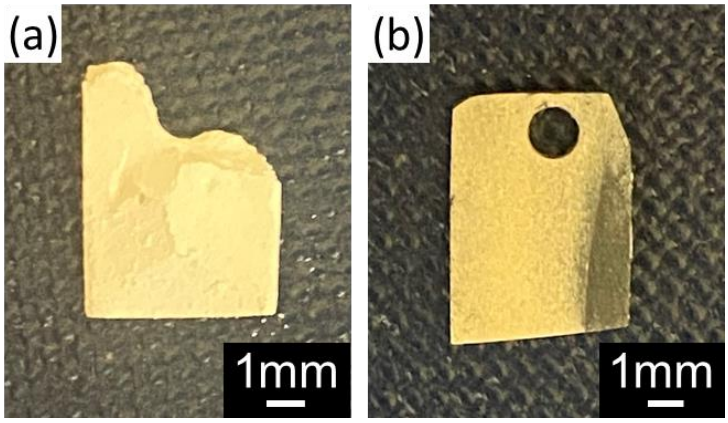


Figure 8-1: Optical images of (a) Zr2.5Al and (b) Zr2.5Ta, removed from the autoclave after 30 days at 300 °C.

In contrast, although an oxidised layer could be observed on the Zr2.5Ta sample in Figure 8-1(b), it did not fall apart as was the case for Zr2.5Al. Measurements of the oxide layer thickness on the two commercial alloys was measured by Xingzhong Liang using Fourier transform infrared (FTIR) spectroscopy with results shown in Figure 8-2. To compare the performance of the Zr2.5Ta alloy, a trench in the sample surface was made by FIB milling by Rajat Nama as shown in Figure 8-3, with the oxide layer visible as the darker layer at the surface in the cross-section, with significant horizontal cracks visible in the oxide. Measurements of the thickness of the oxide layer were taken at eleven equally spaced points along the length shown in Figure 8-3, with the average and standard deviation of these measurements shown in Figure 8-2, for comparison with the commercial alloys. Although this indicates poor aqueous corrosion resistance of Zr2.5Ta to the 300 °C autoclave exposure compared with the commercial alloys, improvements could be made to this property through optimisation of the alloy composition.

This finding, along with the observations of significant strengthening in chapter 4 and microstructural stability in chapter 5, indicates that tantalum may be considered as an

appropriate alloying element for zirconium in water-cooled fusion or advanced fission reactor designs, although further study is necessary to confirm this finding.

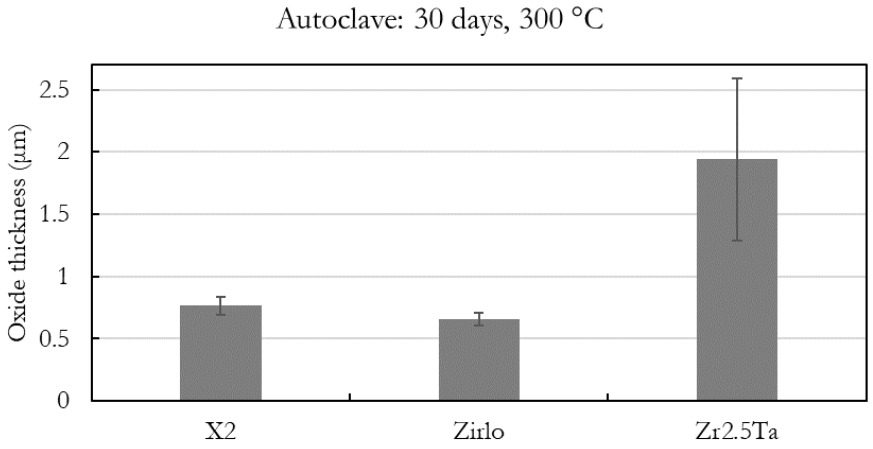


Figure 8-2: Comparison of the measured oxide thickness of zirconium alloy samples (X2, Zirlo, and Zr2.5Ta), following 30 days autoclave exposure at 300 °C. The thickness of the oxide layer on the commercial alloys were measured by FTIR spectroscopy and on the Zr2.5Ta from the FIB cross-section micrograph in Figure 8-3.

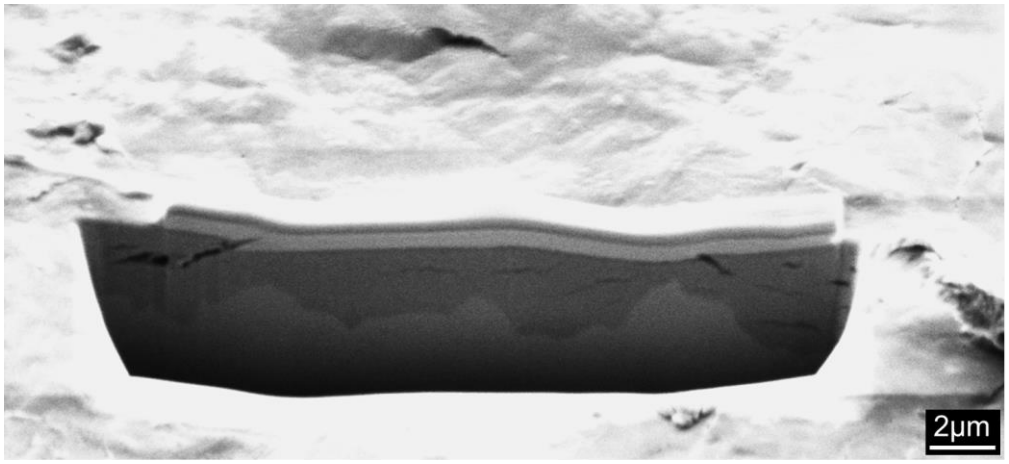


Figure 8-3: SE micrograph of a FIB cross-section of the surface of the Zr2.5Ta sample following 30 days of autoclave exposure at 300 °C, taken by Rajat Nama.

9 Appendix: Publication plans

The novel work contained in this thesis is currently unpublished in the literature. However, results and analysis have been presented at conferences including the 30th IEEE Symposium on Fusion Engineering (2023), the 21st International Conference on Fusion Reactor Materials (2023), and the 153rd TMS Annual Meeting & Exhibition (2024).

A paper containing the data relating to the corrosion of steels by liquid lithium (sections 6.4 and 6.5) has been submitted for peer review and is available on SSRN [397]. A further publication containing data of lithium corrosion of non-ferrous metals is planned which will contain sections 6.6 and 6.7 of this work, alongside other work relating to the corrosion of vanadium and tungsten by liquid lithium to which I have contributed.

As the Zr-Al and Zr-Ta systems are identified as the most promising in this work, it is planned to write two separate papers to display and discuss the findings relating to the microstructural evolution and mechanical properties of these two systems.

10 References

[1] D. O. Northwood, "The development and applications of zirconium alloys," *Mater. Des.*, vol. 6, no. 2, pp. 58–70, Apr. 1985, doi: 10.1016/0261-3069(85)90165-7.

[2] H. G. Rickover, L. D. Geiger, and B. Lustman, "History of the Development of Zirconoium Alloys for use in Nuclear Reactors," Denver, 1975.

[3] D. J. M. King *et al.*, "High temperature zirconium alloys for fusion energy," *J. Nucl. Mater.*, vol. 559, p. 153431, Feb. 2022, doi: 10.1016/j.jnucmat.2021.153431.

[4] C. B. A. Forty and P. J. Karditsas, "Uses of zirconium alloys in fusion applications," *J. Nucl. Mater.*, vol. 283–287, no. 1, pp. 607–610, 2000, doi: 10.1016/S0022-3115(00)00146-X.

[5] T. Muroga, T. Tanaka, M. Kondo, T. Nagasaka, and Q. Xu, "Characterization of liquid lithium blanket with rafm and v-alloy for tbm and demo," *Fusion Sci. Technol.*, vol. 56, no. 2, pp. 897–901, 2009, doi: 10.13182/FST09-A9024.

[6] THE INTERGOVERNMENTAL PANEL ON CLIMATE CHANGE, "AR5 Synthesis Report: Climate Change 2014," Geneva, 2015.

[7] C. Waite and UK National Statistics, "2018 UK greenhouse gas emissions, final figures," London, 2020. [Online]. Available: https://assets.publishing.service.gov.uk/government/uploads/system/uploads/a

ttachment_data/file/790626/2018-provisional-emissions-statistics-report.pdf.

[8] International Energy Agency, "Key World Energy Statistics," 2012. [Online]. Available: https://www.iea.org/reports/world-energy-outlook-2012.

[9] International Energy Agency, "Key World Energy Statistics," 2013. [Online]. Available: https://www.iea.org/reports/world-energy-outlook-2013.

[10] International Energy Agency, "Key World Energy Statistics," 2014. [Online]. Available: https://www.iea.org/reports/world-energy-outlook-2014.

[11] International Energy Agency, "Key World Energy Statistics," 2015. [Online]. Available: https://www.iea.org/reports/world-energy-outlook-2015.

[12] International Energy Agency, "Key World Energy Statistics," 2017. [Online]. Available: https://www.iea.org/reports/world-energy-outlook-2017.

[13] International Energy Agency, "Key World Energy Statistics," 2019. [Online]. Available: https://www.iea.org/events/key-world-energy-statistics-2019.

[14] US Energy Information Administration, "International Energy Outlook," 2019. [Online]. Available: https://www.eia.gov/outlooks/ieo/pdf/ieo2019.PDF.

[15] A. A. Racz, I. Muntean, and S.-D. Stan, "A Look into Electric/Hybrid Cars from an Ecological Perspective," *Procedia Technol.*, vol. 19, pp. 438–443, Jan. 2015, doi: 10.1016/J.PROTCY.2015.02.062.

[16] J. Broderick, K. Anderson, C. Jones, J. Watson, L. Falcan, and S. Glynn, "A Review of Research Relevant to New Build Nuclear Power Plants in the UK," Manchester, 2013. [Online]. Available: https://www.foe.co.uk/sites/default/files/downloads/tyndall_evidence.pdf.

[17] International Energy Agency, "India Energy Outlook 2021," Paris, 2021. doi: 10.1787/ec2fd78d-en.

[18] World Nuclear Association, "Nuclear Power in China," *World Nuclear Association, Information Library*, 2021. https://world-nuclear.org/information-library/country-profiles/countries-a-f/china-nuclear-power.aspx (accessed Aug. 23, 2021).

[19] H. Ritchie and M. Roser, "What are the safest and cleanest sources of energy?," *Our World in Data*, 2020. https://ourworldindata.org/safest-sources-of-energy (accessed Aug. 23, 2020).

[20] S. L. Cutter, "Risk cognition and the public: The case of three mile island," *Hazards, Vulnerability Environ. Justice*, pp. 167–176, 2012, doi: 10.4324/9781849771542.

[21] G. L. Brooks and E. Siddall, "An Analysis of the Three Mile Island Accident," Mississauga, Ontario, 1960.

[22] V. K. Smith and R. G. Michaels, "How did households interpret chernobyl?: A bayesian analysis of risk perceptions," *Econ. Lett.*, vol. 23, no. 4, pp. 359–364, Jan. 1987, doi: 10.1016/0165-1765(87)90145-5.

[23] W. Poortinga, M. Aoyagi, and N. F. Pidgeon, "Public perceptions of climate

change and energy futures before and after the Fukushima accident: A comparison between Britain and Japan," *Energy Policy*, vol. 62, pp. 1204–1211, Nov. 2013, doi: 10.1016/J.ENPOL.2013.08.015.

[24] MIT Energy Initiative, "The Future of Nuclear Energy in a Carbon-Constrained World," Cambridge, MA, 2018. [Online]. Available: https://energy.mit.edu/research/future-nuclear-energy-carbon-constrained-world/.

[25] the Office for Nuclear Regulation, the Environment Agency, the Scottish Environment Protection Agency, and Natural Resources Wales, "The management of higher activity radioactive waste on nuclear licensed sites," Bootle, 2015.

[26] United Nations, "JOINT CONVENTION ON THE SAFETY OF SPENT FUEL MANAGEMENT AND ON THE SAFETY OF RADIOACTIVE WASTE MANAGEMENT," *Treaties Int. agreements Regist. or filed Rec. with Secr. United Nations*, vol. 2153, no. 37605, pp. 356–377, 2003.

[27] K. Umasankari and P. Mohanakrishnan, "Types of nuclear reactors," *Phys. Nucl. React.*, pp. 155–191, Jan. 2021, doi: 10.1016/B978-0-12-822441-0.00003-0.

[28] V. Gopalakrishnan, "Introduction," *Phys. Nucl. React.*, pp. 1–86, Jan. 2021, doi: 10.1016/B978-0-12-822441-0.00001-7.

[29] B. L. Cohen, "The nuclear reactor accident at Chernobyl, USSR," *Am. J. Phys.*, vol.

55, no. 12, pp. 1076–1083, 1987, doi: 10.1119/1.15323.

[30] M. Barbarino, "A brief history of nuclear fusion," *Nat. Phys.*, vol. 16, no. 9, pp. 890–893, 2020, doi: 10.1038/s41567-020-0940-7.

[31] S. Meschini *et al.*, "Review of commercial nuclear fusion projects," *Front. Energy Res.*, vol. 11, no. June, pp. 1–21, 2023, doi: 10.3389/fenrg.2023.1157394.

[32] Y. Arikawa *et al.*, "The conceptual design of 1-ps time resolution neutron detector for fusion reaction history measurement at OMEGA and the National Ignition Facility," *Rev. Sci. Instrum.*, vol. 91, no. 6, pp. 1–10, 2020, doi: 10.1063/1.5143657.

[33] M. Abdou *et al.*, "Physics and technology considerations for the deuterium-tritium fuel cycle and conditions for tritium fuel self sufficiency," *Nucl. Fusion*, vol. 61, no. 1, 2021, doi: 10.1088/1741-4326/abbf35.

[34] M. Siccinio *et al.*, "Feasibility of D-D start-up under realistic technological assumptions for EU-DEMO," *Fusion Eng. Des.*, vol. 171, no. March, 2021, doi: 10.1016/j.fusengdes.2021.112554.

[35] C. Lecuyer, P. Gillet, and F. Robert, "The hydrogen isotope composition of seawater and the global water cycle ´ ´," 1998.

[36] T. Hoshino *et al.*, "Development of advanced tritium breeding material with added lithium for ITER-TBM," *J. Nucl. Mater.*, vol. 417, no. 1–3, pp. 684–687, Oct. 2011, doi: 10.1016/J.JNUCMAT.2010.12.128.

[37] E. Proust, L. Anzidei, M. Dalle Donne, U. Fischer, and T. Kuroda, "Solid breeder blanket design and tritium breeding," *Fusion Eng. Des.*, vol. 16, pp. 73–84, 1991, doi: 10.1016/0920-3796(91)90184-R.

[38] Oxford Sigma Ltd, "Materials for Fusion," 2024. https://oxfordsigma.com/technologies/ (accessed Jun. 20, 2024).

[39] D. Dewar, L. Harvey, and C. Vakil, "Uranium mining and health.," *Can. Fam. Physician*, vol. 59, no. 5, pp. 469–71, 2013, [Online]. Available: http://www.ncbi.nlm.nih.gov/pubmed/23673579%0Ahttp://www.pubmedcentral.nih.gov/articlerender.fcgi?artid=PMC3653646.

[40] A. M. Macfarlane and M. Miller, "Nuclear Energy and Uranium Resources," *Elements*, vol. 3, no. 3, pp. 185–192, Jun. 2007, doi: 10.2113/gselements.3.3.185.

[41] A. M. Bradshaw, T. Hamacher, and U. Fischer, "Is nuclear fusion a sustainable energy form?," *Fusion Eng. Des.*, vol. 86, no. 9–11, pp. 2770–2773, Oct. 2011, doi: 10.1016/J.FUSENGDES.2010.11.040.

[42] A. Schwenk-Ferrero, "German spent nuclear fuel legacy: Characteristics and high-level waste management issues," *Sci. Technol. Nucl. Install.*, vol. 2013, 2013, doi: 10.1155/2013/293792.

[43] United States Nuclear Regulatory Commission, "Radioactive Waste," 2019. Accessed: Aug. 23, 2021. [Online]. Available: https://www.nrc.gov/reading-rm/doc-collections/fact-sheets/radwaste.html.

[44] M. Zucchetti, L. Candido, V. Khripunov, B. Kolbasov, and R. Testoni, "Fusion power plants, fission and conventional power plants. Radioactivity, radiotoxicity, radioactive waste," *Fusion Eng. Des.*, vol. 136, pp. 1529–1533, Nov. 2018, doi: 10.1016/J.FUSENGDES.2018.05.049.

[45] Fusion Industry Association, "The global fusion industry in 2024," Washington D.C., 2024. [Online]. Available: https://www.fusionindustryassociation.org/news/from-the-fia/#industry-reports.

[46] P. H. Rebut, "ITER: the first experimental fusion reactor," *Fusion Eng. Des.*, vol. 30, no. 1–2, pp. 85–118, May 1995, doi: 10.1016/0920-3796(94)00403-T.

[47] J. Ongena, R. Koch, R. Wolf, and H. Zohm, "Magnetic-confinement fusion," *Nat. Phys.*, vol. 12, no. 5, pp. 398–410, 2016, doi: 10.1038/NPHYS3745.

[48] R. Betti and O. A. Hurricane, "Inertial-Confinement fusion with lasers," *Nat. Phys.*, vol. 12, no. 5, pp. 445–448, 2016, doi: 10.1038/NPHYS3736.

[49] R. Przybocki, "Investigation of non-normal incidence charged-particle response of CR39 nuclear track detectors , with applications in nuclear diagnostics for inertial confinement fusion by," MASSACHUSETTS INSTITUTE OF TECHNOLOGY, 2020.

[50] N. Hawker, "A simplified economic model for inertial fusion," *Philos. Trans. R. Soc. A Math. Phys. Eng. Sci.*, vol. 378, no. 2184, 2020, doi:

10.1098/rsta.2020.0053rsta20200053.

[51] D. Chapman *et al.*, "Investigating the Role of Transport in Uniaxially-Driven Conical Fusion Targets," 2020.

[52] M. Laberge, "Experimental results for an acoustic driver for MTF," *J. Fusion Energy*, vol. 28, no. 2 SPEC. ISS., pp. 179–182, 2009, doi: 10.1007/s10894-008-9181-y.

[53] N. J. Peacock, D. C. Robinson, M. J. Forrest, P. D. Wilcock, and V. V. Sannikov, "Measurement of the electron temperature by Thomson scattering in Tokamak T3," *Nature*, vol. 224, no. 5218, pp. 488–490, 1969, doi: 10.1038/224488a0.

[54] International Atomic Energy Agency, "Nuclear Fusion," in *PROCEEDINGS OF THE CONFERENCE ON PLASMA PHYSICS AND CONTROLLED NUCLEAR FUSION RESEARCH*, 1961, pp. 1–1051.

[55] I. Chapman, "Towards a fusion economy," *Phys. World*, vol. 32, no. 11, pp. 14–15, 2019, doi: 10.1088/2058-7058/32/11/20.

[56] S. McNamara *et al.*, "Achievement of ion temperatures in excess of 100 million degrees Kelvin in the compact high-field spherical tokamak ST40," *Nucl. Fusion*, vol. 63, no. 5, 2023, doi: 10.1088/1741-4326/acbec8.

[57] D. L. Smith, "Blanket materials for dt fusion reactors," *J. Nucl. Mater.*, 1981, doi: 10.1016/0022-3115(82)90570-0.

[58] UK Atomic Energy Authority, "Fusion: The Ultimate Energy Source," *Culham*

Centre for Fusion Energy, 2021. https://ccfe.ukaea.uk/ (accessed Aug. 23, 2021).

[59] N. Walkden, "Delivering Fusion Energy," 2020, [Online]. Available: https://www.youtube.com/watch?v=f0KofSsjOak.

[60] J. Linke *et al.*, "Challenges for plasma-facing components in nuclear fusion," *Matter Radiat. Extrem.*, vol. 4, no. 5, 2019, doi: 10.1063/1.5090100.

[61] D. Kumar *et al.*, "The effects of fusion reactor thermal transients on the microstructure of Eurofer-97 steel," *J. Nucl. Mater.*, vol. 554, p. 153084, Oct. 2021, doi: 10.1016/J.JNUCMAT.2021.153084.

[62] M. Abdou *et al.*, "Blanket/first wall challenges and required R&D on the pathway to DEMO," *Fusion Eng. Des.*, vol. 100, pp. 2–43, Nov. 2015, doi: 10.1016/J.FUSENGDES.2015.07.021.

[63] J. Li, X. Zhang, F. Gao, and Y. Pu, "Neutronics comparison analysis of the water cooled ceramics breeding blanket for CFETR," *Plasma Sci. Technol.*, vol. 18, no. 2, pp. 179–183, Feb. 2016, doi: 10.1088/1009-0630/18/2/14.

[64] A. Del Nevo *et al.*, "WCLL breeding blanket design and integration for DEMO 2015: status and perspectives," *Fusion Eng. Des.*, vol. 124, pp. 682–686, Nov. 2017, doi: 10.1016/j.fusengdes.2017.03.020.

[65] O. Leys, T. Bergfeldt, M. H. H. Kolb, R. Knitter, and A. A. Goraieb, "The reprocessing of advanced mixed lithium orthosilicate/metatitanate tritium breeder pebbles," *Fusion Eng. Des.*, vol. 107, pp. 70–74, Jun. 2016, doi:

10.1016/J.FUSENGDES.2016.04.025.

[66] A. W. Davies and S. T. Murphy, "Thermodynamics and phase stability of Li8XO6octalithium ceramic breeder materials (X = Pb, Ce, Ge, Zr, Sn)," *J. Phys. Condens. Matter*, vol. 34, no. 35, 2022, doi: 10.1088/1361-648X/ac762a.

[67] F. A. Hernández and P. Pereslavtsev, "First principles review of options for tritium breeder and neutron multiplier materials for breeding blankets in fusion reactors," *Fusion Eng. Des.*, vol. 137, no. May, pp. 243–256, 2018, doi: 10.1016/j.fusengdes.2018.09.014.

[68] S. Malang and R. Mattas, "Comparison of lithium and the eutectic candidate liquid metal breeder materials lead-lithium alloy, two for self-cooled blankets," *Fusion Eng. Des.*, vol. 27, pp. 399–406, 1995.

[69] D. Martelli, A. Venturini, and M. Utili, "Literature review of lead-lithium thermophysical properties," *Fusion Eng. Des.*, vol. 138, pp. 183–195, Jan. 2019, doi: 10.1016/J.FUSENGDES.2018.11.028.

[70] U. Fischer, A. Schwenk-Ferrero, and E. Wiegner, "NEUTRON MULTIPLICATION IN LEAD: A COMPARATIVE STUDY BASED ON A NEW CALCULATIONAL PROCEDURE AND NEW NUCLEAR DATA," *Fusion Eng. Des.*, vol. 10, pp. 139–144, 1989.

[71] H. Neuert and H. Pollehn, "TABLES OF CROSS-SECTIONS OF NUCLEAR REACTIONS WITH NEUTRONS IN THE 14-15 MeV ENERGY RANGE,"

Hamburg, 1963.

[72] E. Carella, C. Moreno, F. R. Urgorri, D. Rapisarda, and A. Ibarra, "Tritium modelling in HCPB breeder blanket at a system level," *Fusion Eng. Des.*, vol. 124, pp. 687–691, Nov. 2017, doi: 10.1016/J.FUSENGDES.2017.01.051.

[73] J. Aubert *et al.*, "Design and preliminary analyses of the new Water Cooled Lithium Lead TBM for ITER," *Fusion Eng. Des.*, vol. 160, p. 111921, Nov. 2020, doi: 10.1016/J.FUSENGDES.2020.111921.

[74] K. Sugiyama *et al.*, "Consequences of deuterium retention and release from Be-containing mixed materials for ITER Tritium Inventory Control," *J. Nucl. Mater.*, vol. 415, no. 1, pp. S731–S734, Aug. 2011, doi: 10.1016/J.JNUCMAT.2010.09.043.

[75] G. Federici, L. Boccaccini, F. Cismondi, M. Gasparotto, Y. Poitevin, and I. Ricapito, "An overview of the EU breeding blanket design strategy as an integral part of the DEMO design effort," *Fusion Eng. Des.*, vol. 141, pp. 30–42, Apr. 2019, doi: 10.1016/J.FUSENGDES.2019.01.141.

[76] A. Tassone, "Study on liquid metal magnetohydrodynamic flows and numerical application to a water-cooled blanket for fusion reactors," Sapienza - Universita Di Roma, 2019.

[77] H. Wang, W. Wang, Y. Bai, and H. Chen, "Preliminary thermal-hydraulics design of the dual-cooled lithium lead blanket for FDS-II," *Fusion Eng. Des.*, vol. 75–79, no. SUPPL., pp. 841–845, Nov. 2005, doi: 10.1016/J.FUSENGDES.2005.06.252.

[78] M. Green, S. Foster, A. Wisbey, A. Cole-Baker, and R. Crutchley, "Review of Titanium Alloy Development towards use in a Nuclear Fusion Environment," United Kingdom Atomic Energy Authority / Wood Nuclear Limited, 2020.

[79] M. R. Gilbert, J.-C. Sublet, and R. A. Forrest, "Handbook of activation, transmutation, and radiation damage properties of the elements simulated using FISPACT-II & TENDL-2014; Magnetic Fusion Plants," Culham Centre for Fusion Energy, 2015.

[80] A. Harte, M. Preuss, and T. Darby, "Overview and recommendations on the use of Zr and Ti as fusion materials," United Kingdom Atomic Energy Authority, 2020.

[81] R. Bullis *et al.*, "A Solid Breeder Blanket and Power Conversion System for the Mirror Advanced Reactor Study (MARS)," *Nucl. Technol. - Fusion*, vol. 4, no. 2P3, Sep. 1983, doi: 10.13182/FST83-A22948.

[82] D. P. Jackson *et al.*, "Review of Fusion Breeder Blanket Technology - Part 1: Review and Findings.," *At. Energy Canada Limited, AECL*, no. January 1985, 1985.

[83] I. . Cristescu, I. Cristescu, L. Doerr, M. Glugla, and D. Murdoch, "Tritium inventories and tritium safety design principles for the fuel cycle of ITER," *Nucl. Fusion*, vol. 47, no. 7, Jul. 2007, doi: 10.1088/0029-5515/47/7/S08.

[84] F. Barton, J. Bernard, F. Lowrie, C. Riley, and M. Rogers, "A Review into the Applicability of Zirconium Alloys for Fusion Applications," United Kingdom

Atomic Energy Authority / Rolls-Royce plc, 2020.

[85] D. J. M. King and A. J. Knowles, "STEP – Assessment of novel Zirconium alloys for fusion applications," United Kingdom Atomic Energy Authority, 2020.

[86] A.-A. . Tavassoli, "Present limits and improvements of structural materials for fusion reactors – a review," *J. Nucl. Mater.*, vol. 302, no. 2–3, pp. 73–88, Apr. 2002, doi: 10.1016/S0022-3115(02)00794-8.

[87] A. Kohyama, A. Hishinuma, D. S. Gelles, R. L. Klueh, W. Dietz, and K. Ehrlich, "Low-activation ferritic and martensitic steels for fusion application," *J. Nucl. Mater.*, vol. 233–237, pp. 138–147, Oct. 1996, doi: 10.1016/S0022-3115(96)00327-3.

[88] D. Starley, "Determining the Technological Origins of Iron and Steel," *J. Archaeol. Sci.*, vol. 26, no. 8, pp. 1127–1133, Aug. 1999, doi: 10.1006/JASC.1999.0408.

[89] E. F. Wente, J. Nutting, E. F. Wondris, and R. Curley, "Steel," *Britannica*. 2008, [Online]. Available: https://www.britannica.com/technology/steel.

[90] R. E. Gold and D. L. Harrod, "Refractory metal alloys for fusion reactor applications," *J. Nucl. Mater.*, vol. 85–86, no. PART 2, pp. 805–815, Dec. 1979, doi: 10.1016/0022-3115(79)90359-3.

[91] C. Baus *et al.*, "Kyoto Fusioneering's Mission to Accelerate Fusion Energy: Technologies, Challenges and Role in Industrialisation," *J. Fusion Energy*, vol. 42, no. 1, pp. 1–16, Jun. 2023, doi: 10.1007/S10894-023-00346-Y/FIGURES/8.

[92] A. Quadling, D. Bowden, C. Hardie, and A. Vasanthakumaran, "Developing power plant materials using the life cycle lens," *Philos. Trans. A*, vol. 382, no. 2280, Aug. 2024, doi: 10.1098/RSTA.2023.0409.

[93] A. K. Suri, N. Krishnamurthy, and I. S. Batra, "Materials issues in fusion reactors," in *Journal of Physics: Conference Series*, 2010, vol. 208, doi: 10.1088/1742-6596/208/1/012001.

[94] S. . Zinkle and N. . Ghoniem, "Operating temperature windows for fusion reactor structural materials," *Fusion Eng. Des.*, vol. 51–52, pp. 55–71, Nov. 2000, doi: 10.1016/S0920-3796(00)00320-3.

[95] S. J. Zinkle, "Advanced materials for fusion technology," *Fusion Eng. Des.*, vol. 74, no. 1–4, pp. 31–40, Nov. 2005, doi: 10.1016/J.FUSENGDES.2005.08.008.

[96] H. Tanigawa *et al.*, "Technical issues of reduced activation ferritic/martensitic steels for fabrication of ITER test blanket modules," *Fusion Eng. Des.*, vol. 83, no. 10–12, pp. 1471–1476, Dec. 2008, doi: 10.1016/J.FUSENGDES.2008.07.024.

[97] X. Meng *et al.*, "Compatibility of Molybdenum, Tungsten, and 304 Stainless Steel in Static Liquid Lithium Under High Vacuum," *Plasma Phys. Reports*, vol. 44, no. 7, pp. 671–677, Jul. 2018, doi: 10.1134/S1063780X18070036.

[98] R. L. Klueh, J. P. Shingledecker, R. W. Swindeman, and D. T. Hoelzer, "Oxide dispersion-strengthened steels: A comparison of some commercial and experimental alloys," *J. Nucl. Mater.*, vol. 341, no. 2–3, pp. 103–114, May 2005, doi:

10.1016/J.JNUCMAT.2005.01.017.

[99] T. Chikada, "Ceramic Coatings for Fusion Reactors," *Compr. Nucl. Mater.*, vol. 6, no. February 2019, pp. 274–283, 2020, doi: 10.1016/b978-0-12-803581-8.11674-1.

[100] M. Simmonds, "Liquid Lithium Corrosion of Materials for Nuclear Fusion," University of Oxford, 2023.

[101] E. Akahoshi *et al.*, "Corrosion tests of multi-layer ceramic coatings in liquid lithium-lead," *Fusion Eng. Des.*, vol. 160, no. July, p. 111874, 2020, doi: 10.1016/j.fusengdes.2020.111874.

[102] Y. Li, C. Ke, X. Liu, F. Gou, X. Duan, and Y. Zhao, "Analysis liquid lithium corrosion resistance of Er2O3 coating revealed by LIBS technique," *Fusion Eng. Des.*, vol. 136, no. September 2017, pp. 1640–1646, 2018, doi: 10.1016/j.fusengdes.2018.07.001.

[103] D. L. Smith, J. Konys, T. Muroga, and V. Evitkhin, "Development of coatings for fusion power applications," *J. Nucl. Mater.*, vol. 307–311, no. 2 SUPPL., pp. 1314–1322, 2002, doi: 10.1016/S0022-3115(02)00985-6.

[104] S. Malang, H. U. Borgstedt, E. H. Farnum, K. Natesan, and I. V. Vitkovski, "Development of insulating coatings for liquid metal blankets," *Fusion Eng. Des.*, vol. 27, no. C, pp. 570–586, 1995, doi: 10.1016/0920-3796(95)90172-8.

[105] B. A. Pint *et al.*, "Recent progress in the development of electrically insulating

coatings for a liquid lithium blanket," *J. Nucl. Mater.*, vol. 329–333, no. 1-3 PART A, pp. 119–124, 2004, doi: 10.1016/j.jnucmat.2004.04.010.

[106] B. A. Pint, K. L. More, H. M. Meyer, and J. R. Distefano, "Recent progress addressing compatibility issues relevant to fusion environments," in *Fusion Science and Technology*, 2005, vol. 47, no. 4, pp. 851–855, doi: 10.13182/FST05-A792.

[107] S. Ukai *et al.*, "Tube manufacturing and mechanical properties of oxide dispersion strengthened ferritic steel," *J. Nucl. Mater.*, vol. 204, no. C, pp. 74–80, Sep. 1993, doi: 10.1016/0022-3115(93)90201-9.

[108] K. Asano, Y. Kohno, A. Kohyama, T. Suzuki, and H. Kusanagi, "Microstructural evolution of an oxide dispersion strengthened steel under charged particle irradiation," *J. Nucl. Mater.*, vol. 155–157, no. PART 2, pp. 928–934, Jul. 1988, doi: 10.1016/0022-3115(88)90443-6.

[109] S. J. Zinkle *et al.*, "Development of next generation tempered and ODS reduced activation ferritic/martensitic steels for fusion energy applications," *Nucl. Fusion*, vol. 57, no. 9, p. 092005, Jun. 2017, doi: 10.1088/1741-4326/57/9/092005.

[110] T. P. Davis *et al.*, "Electron microscopy and atom probe tomography of nanoindentation deformation in oxide dispersion strengthened steels," *Mater. Charact.*, vol. 167, no. July, p. 110477, 2020, doi: 10.1016/j.matchar.2020.110477.

[111] M. Richardson, M. Gorley, Y. Wang, D. Andres, and H. Dawson, "Small punch creep investigation of Eurofer97 and 14Cr oxide dispersion strengthened steel,"

Nucl. Mater. Energy, vol. 29, p. 101067, Dec. 2021, doi: 10.1016/J.NME.2021.101067.

[112] P. Dubuisson, Y. De Carlan, V. Garat, and M. Blat, "ODS Ferritic/martensitic alloys for Sodium Fast Reactor fuel pin cladding," *J. Nucl. Mater.*, vol. 428, no. 1–3, pp. 6–12, 2012, doi: 10.1016/j.jnucmat.2011.10.037.

[113] G. R. Odette, "On the status and prospects for nanostructured ferritic alloys for nuclear fission and fusion application with emphasis on the underlying science," *Scr. Mater.*, vol. 143, pp. 142–148, 2018, doi: 10.1016/j.scriptamat.2017.06.021.

[114] A. J. London *et al.*, "Quantification of oxide particle composition in model oxide dispersion strengthened steel alloys," *Ultramicroscopy*, vol. 159, pp. 360–367, Dec. 2015, doi: 10.1016/J.ULTRAMIC.2015.02.013.

[115] D. Zhang *et al.*, "No ball milling needed: Alternative ODS steel manufacturing with gas atomization reaction synthesis (GARS) and friction-based processing," *J. Nucl. Mater.*, vol. 566, 2022, doi: 10.1016/j.jnucmat.2022.153768.

[116] Y. Il Jung *et al.*, "Strengthening of Zircaloy-4 using Y2O3 particles by a laser-beam-induced surface treatment process," *Mater. Des.*, vol. 116, pp. 325–330, Feb. 2017, doi: 10.1016/J.MATDES.2016.12.023.

[117] Y. Il Jung, D. J. Park, J. H. Park, H. G. Kim, J. H. Yang, and Y. H. Koo, "Effect of a surface oxide-dispersion-strengthened layer on mechanical strength of zircaloy-4 tubes," *Nucl. Eng. Technol.*, vol. 50, no. 2, pp. 218–222, Mar. 2018, doi:

10.1016/J.NET.2017.12.001.

[118] H. G. Kim, I. H. Kim, Y. Il Jung, D. J. Park, J. Y. Park, and Y. H. Koo, "Microstructure and mechanical strength of surface ODS treated Zircaloy-4 sheet using laser beam scanning," *Nucl. Eng. Technol.*, vol. 46, no. 4, pp. 521–528, 2014, doi: 10.5516/NET.07.2014.027.

[119] H. G. Kim *et al.*, "Microstructure and mechanical characteristics of surface oxide dispersion-strengthened Zircaloy-4 cladding tube," *Addit. Manuf.*, vol. 22, pp. 75–85, Aug. 2018, doi: 10.1016/J.ADDMA.2018.05.002.

[120] S. M. S. Aghamiri *et al.*, "Microstructure and mechanical properties of mechanically alloyed ODS copper alloy for fusion material application," *Nucl. Mater. Energy*, vol. 15, pp. 17–22, May 2018, doi: 10.1016/J.NME.2018.05.019.

[121] S. Spigarelli and C. Paoletti, "A new model for the description of creep behaviour of aluminium-based composites reinforced with nanosized particles," *Compos. Part A Appl. Sci. Manuf.*, vol. 112, pp. 346–355, Sep. 2018, doi: 10.1016/J.COMPOSITESA.2018.06.021.

[122] C. Si *et al.*, "Review on the Compatibility of Fusion Reactor Structural Materials with High-temperature Liquid Metals," *J. Phys. Conf. Ser.*, vol. 1637, no. 1, 2020, doi: 10.1088/1742-6596/1637/1/012037.

[123] T. S. Bray *et al.*, "Tensile and impact properties of V-4Cr-4Ti alloy heats 832665 and 832864," *J. Nucl. Mater.*, vol. 283–287, pp. 633–636, 2000, doi: 10.1016/S0022-

3115(00)00229-4.

[124] E. V. Dyomina, P. Fenici, V. P. Kolotov, and M. Zucchetti, "Low-activation characteristics of V-alloys and SiC composites," *J. Nucl. Mater.*, vol. 258–263, pp. 1784–1790, 1998, doi: 10.1016/S0022-3115(98)00133-0.

[125] S. N. Votinov *et al.*, "Prospects and problems using vanadium alloys as a structural material of the first wall and blanket of fusion reactors," *J. Nucl. Mater.*, vol. 233–237, pp. 370–375, 1996.

[126] D. L. Smith, B. A. Loomis, and D. R. Diercks, "Vanadium-base alloys for fusion reactor applications — a review," *J. Nucl. Mater.*, vol. 135, no. 2–3, pp. 125–139, Oct. 1985, doi: 10.1016/0022-3115(85)90070-4.

[127] T. W. Kerlin and B. R. Upadhyaya, "Nuclear plant instrumentation," *Dyn. Control Nucl. React.*, pp. 213–235, Jan. 2019, doi: 10.1016/B978-0-12-815261-4.00016-0.

[128] U. Ulmer *et al.*, "Cost reduction possibilities of vanadium-based solid solutions – Microstructural, thermodynamic, cyclic and environmental effects of ferrovanadium substitution," *J. Alloys Compd.*, vol. 648, pp. 1024–1030, Nov. 2015, doi: 10.1016/J.JALLCOM.2015.07.110.

[129] J. P. Smith, W. R. Johnson, R. D. Stambaugh, P. W. Trester, D. Smith, and E. Bloom, "Utilization of vanadium alloys in the DIII-D radiative divertor program," *J. Nucl. Mater.*, vol. 233–237, pp. 421–425, Oct. 1996, doi: 10.1016/S0022-3115(96)00229-2.

[130] D. Catalano and G. Scardino, "Vanadium alloys for fusion applications," *Essays Nucl. Technol.*, vol. 1, pp. 115–122, 2018.

[131] K. I. Fukumoto, H. Matsui, M. Narui, and M. Yamazaki, "Irradiation creep behavior of V–4Cr–4Ti alloys irradiated in a liquid sodium environment at the JOYO fast reactor," *J. Nucl. Mater.*, vol. 437, no. 1–3, pp. 341–349, Jun. 2013, doi: 10.1016/J.JNUCMAT.2013.02.012.

[132] R. R. Moskalyk and A. M. Alfantazi, "Processing of vanadium: a review," *Miner. Eng.*, vol. 16, no. 9, pp. 793–805, Sep. 2003, doi: 10.1016/S0892-6875(03)00213-9.

[133] M. Pistilli, "Top 4 Vanadium-producing Countries," *Investing News Network*, 2023. .

[134] D. Rappleye and R. Haun, "Production of Pure Vanadium: Industry Review and Feasibility Study of Electron Beam Melt Refining of V–Al Alloys," *J. Sustain. Metall.*, vol. 7, no. 3, pp. 755–766, 2021, doi: 10.1007/s40831-021-00407-6.

[135] M. Kaufmann and R. Neu, "Tungsten as first wall material in fusion devices," *Fusion Eng. Des.*, vol. 82, no. 5–14, pp. 521–527, Oct. 2007, doi: 10.1016/J.FUSENGDES.2007.03.045.

[136] Y. Wu, "Manufacturing of tungsten and tungsten composites for fusion application via different routes," *Tungsten*, vol. 1, no. 1, Mar. 2019, doi: 10.1007/s42864-019-00011-y.

[137] E. Gaganidze, A. Chauhan, H. C. Schneider, D. Terentyev, B. Rossaert, and J. Aktaa, "Effect of irradiation temperature on the fracture-mechanical behaviour of

tungsten irradiated to 1 dpa," *J. Nucl. Mater.*, vol. 556, p. 153200, Dec. 2021, doi: 10.1016/J.JNUCMAT.2021.153200.

[138] E. C. Miller, "Corrosion of Materials," in *Liquid-Metals Handbook*, 2nd rev., R. N. Lyon, Ed. Washington D.C.: U.S. Atomic Energy Commission, 1954, pp. 144–161.

[139] J. R. DiStefano, "Corrosion of Refractory Metals By Lithium," University of Tennessee, Oak Ridge, 1964.

[140] A. S. Kuprin *et al.*, "Vacuum-arc chromium-based coatings for protection of zirconium alloys from the high-temperature oxidation in air," *J. Nucl. Mater.*, vol. 465, pp. 400–406, Oct. 2015, doi: 10.1016/J.JNUCMAT.2015.06.016.

[141] A. S. Kuprin *et al.*, "Irradiation resistance of vacuum arc chromium coatings for zirconium alloy fuel claddings," *J. Nucl. Mater.*, vol. 510, pp. 163–167, Nov. 2018, doi: 10.1016/J.JNUCMAT.2018.07.063.

[142] J. C. Brachet *et al.*, "High temperature steam oxidation of chromium-coated zirconium-based alloys: Kinetics and process," *Corros. Sci.*, vol. 167, p. 108537, May 2020, doi: 10.1016/J.CORSCI.2020.108537.

[143] T. Yoneoka, S. Tanaka, and T. Terai, "Compatability of SiC/SiC Composite Materials with Molten Lithium Metal and Li16-Pb84 Eutectic Alloy," *Mater. Trans.*, vol. 42, no. 6, pp. 1019–1023, 2001.

[144] J. Liu *et al.*, "Liquid lithium corrosion of SiC/SiC composites," *Materialia*, vol. 34, p. 102062, May 2024, doi: 10.1016/J.MTLA.2024.102062.

[145] D. Schuppel, "Fact Sheet on Ceramic Matrix Composites," Augsburg, 2023. [Online]. Available: https://composites-united.com/wp-content/uploads/2023/08/CU_Flyer_CMC_web_verkleinert.pdf.

[146] K. M. Tynyshbayeva, K. K. Kadyrzhanov, A. L. Kozlovskiy, Y. I. Kuldeyev, V. Uglov, and M. V. Zdorovets, "Study of Helium Swelling and Embrittlement Mechanisms in SiC Ceramics," *Crystals*, vol. 12, no. 2, 2022, doi: 10.3390/cryst12020239.

[147] D. L. Smith, S. Majumdar, M. Billone, and R. Mattas, "Performance limits for fusion first-wall structural materials," *J. Nucl. Mater.*, vol. 283–287, no. PART I, pp. 716–720, Dec. 2000, doi: 10.1016/S0022-3115(00)00315-9.

[148] S. R. Soundararajan, J. Vishnu, G. Manivasagam, and N. R. Muktinutalapati, "Processing of Beta Titanium Alloys for Aerospace and Biomedical Applications," in *Titanium Alloys - Novel Aspects of Their Manufacturing and Processing*, 2018.

[149] Total Materia, "Heat Treating of Titanium and Titanium Alloys," *Total Materia*, 2004. https://www.totalmateria.com/page.aspx?ID=CheckArticle&site=ktn&NM=97 (accessed Aug. 16, 2021).

[150] A. T. Motta *et al.*, "Hydrogen in zirconium alloys: A review," *J. Nucl. Mater.*, vol. 518, pp. 440–460, May 2019, doi: 10.1016/J.JNUCMAT.2019.02.042.

[151] P. Binks, A. Cole-Baker, and G. Aspinall, "Review of Zirconium Manufacturing

and Joining," United Kingdom Atomic Energy Authority / Wood Nuclear Limited, 2020.

[152] A. Vlasov, "Five Interesting Facts to Know About Zirconium," *IAEA News*, 2023. https://www.iaea.org/newscenter/news/five-interesting-facts-to-know-about-zirconium (accessed Jan. 20, 2024).

[153] J. Peterson, M. MacDonell, L. Haroun, and F. Monette, "Radiological and Chemical Fact Sheets to Support Health Risk Analyses for Contaminated Areas," Argonne, 2007.

[154] A. S. Zaimovski, "ZIRCONIUM ALLOYS IN NUCLEAR POWER," *Sov. At. Energy*, vol. 45, no. 6, pp. 430–433, 1978, doi: 10.1007/BF01118114.

[155] C. B. A. Forty and P. J. Karditsas, "Potential use of zirconium-based alloys in fusion power plants," *Proc. - Symp. Fusion Eng.*, vol. 2, pp. 849–852, 1997, doi: 10.1109/fusion.1997.687758.

[156] D. Jeppson, J. Ballif, W. Yuan, and B. Chou, "LITHIUM LITERATURE REVIEW: LITHIUM'S PROPERTIES AND INTERACTIONS," 1978.

[157] J. Zhang *et al.*, "Experimental constraints on the phase diagram of elemental zirconium," *J. Phys. Chem. Solids*, vol. 66, no. 7, pp. 1213–1219, Jul. 2005, doi: 10.1016/j.jpcs.2005.03.004.

[158] F. Y. Zhou *et al.*, "Microstructure, mechanical property, corrosion behavior, and in vitro biocompatibility of Zr-Mo alloys," *J. Biomed. Mater. Res. - Part B Appl.*

Biomater., vol. 101 B, no. 2, pp. 237–246, 2013, doi: 10.1002/jbm.b.32833.

[159] Suyalatu *et al.*, "Microstructure and magnetic susceptibility of as-cast Zr-Mo alloys," *Acta Biomater.*, 2010, doi: 10.1016/j.actbio.2009.09.013.

[160] D. R. Lide, "Zirconium," in *CRC Handbook of Chemistry and Physics*, New York: CRC Press, 2007.

[161] A. Akhtar, "BASAL SLIP IN ZIRCONIUM," *Acta Metall.*, vol. 21, 1973.

[162] C. S. Daniel, "An Investigation into the Texture Development during Hot-Rolling of Dual-Phase Zirconium Alloys," *UoM Adm. thesis Dr. Eng.*, p. 371, 2018.

[163] R. A. Lebensohn and C. N. Tomé, "A self-consistent anisotropic approach for the simulation of plastic deformation and texture development of polycrystals: Application to zirconium alloys," *Acta Metall. Mater.*, vol. 41, no. 9, pp. 2611–2624, 1993, doi: 10.1016/0956-7151(93)90130-K.

[164] B. A. Cheadle, C. E. Ells, and W. Evans, "The development of texture in zirconium alloy tubes," *J. Nucl. Mater.*, vol. 23, no. 2, pp. 199–208, 1967, doi: 10.1016/0022-3115(67)90065-7.

[165] H. Takuda, S. Kikuchi, and N. Hatta, "Formability of a commercially pure zirconium sheet," *J. Mater. Process. Technol.*, vol. 84, no. 1–3, pp. 117–121, Dec. 1998, doi: 10.1016/S0924-0136(98)00085-5.

[166] ET-UK-Ltd, "Zirconium Data Sheet," 2011. http://www.etltd.co.uk/zirconium-

zr.html (accessed Jun. 20, 2020).

[167] E. S. Fisher and C. J. Renken, "Adiabatic elastic moduli of single crystal alpha zirconium," *J. Nucl. Mater.*, vol. 4, no. 3, pp. 311–315, Aug. 1961, doi: 10.1016/0022-3115(61)90081-2.

[168] M. K. Drake, D. A. Sargis, and T. Maung, "EVALUATED NEUTRON CROSS SECTIONS FOR ZIRCONIUM AND HAFNIUM," Palo Alto, CA, 1976. [Online]. Available: https://www.osti.gov/servlets/purl/7258830.

[169] M. R. Gilbert, M. Fleming, and J. C. Sublet, "Automated inventory and material science scoping calculations under fission and fusion conditions," *Nucl. Eng. Technol.*, vol. 49, no. 6, pp. 1346–1353, Sep. 2017, doi: 10.1016/J.NET.2017.07.005.

[170] G. Federici *et al.*, "Overview of the DEMO staged design approach in Europe," *Nucl. Fusion*, vol. 59, no. 6, 2019, doi: 10.1088/1741-4326/ab1178.

[171] W. M. Haynes, "Abundance of Elements in the Earth's Crust and in the Sea," in *CRC Handbook of Chemistry and Physics*, 97th ed., 2016, pp. 14–17.

[172] J. S. Cantrell and R. C. Bowman, "Thermal stability and phase studies of crystalline Zr2Pd hydrides," *J. Less Common Met.*, vol. 172–174, no. PART A, pp. 29–35, Aug. 1991, doi: 10.1016/0022-5088(91)90429-8.

[173] Z. H. Feng *et al.*, "Microstructure and mechanical properties of ZrBe alloys processed by hot rolling," *Mater. Sci. Eng. A*, vol. 667, Jun. 2016, doi: 10.1016/j.msea.2016.05.017.

[174] R. A. Perez, H. Nakajima, and F. Dyment, "Diffusion in α-Ti and Zr," *Mater. Trans.*, vol. 44, no. 1, pp. 2–13, 2003, doi: 10.2320/matertrans.44.2.

[175] O. S. Ivanov and V. K. Grigorovich, "Structure and Properties of Zirconium Alloys," in *PROCEEDINGS OF THE SECOND UNITED NATIONS INTERNATIONAL CONFERENCE ON THE PEACEFUL USES OF ATOMIC ENERGY, Volume 5: Properties of Reactor Materials*, 1958, pp. 34–51.

[176] H. W. Leavenworth and R. E. Cleary, "The solubility of Ni, Cr, Fe, Ti and Mo in liquid lithium," *Acta Metall.*, vol. 9, no. 5, pp. 519–520, 1961, doi: 10.1016/0001-6160(61)90151-1.

[177] M. G. Barker and T. Sample, "The solubilities of nickel, manganese and chromium in Pb17Li," *Fusion Eng. Des.*, 1991, doi: 10.1016/0920-3796(91)90005-B.

[178] M. E. Schlesinger, "The Mn-Zr (Manganese-Zirconium) system," *J. Phase Equilibria*, vol. 20, no. 1, pp. 79–83, 1999, doi: 10.1361/105497199770335983.

[179] H. Ren, X. Liu, and J. Ning, "Microstructure and mechanical properties of W-Zr reactive materials," *Mater. Sci. Eng. A*, vol. 660, pp. 205–212, Apr. 2016, doi: 10.1016/J.MSEA.2016.02.009.

[180] J. Liu *et al.*, "The role of β-Zr in a Zr-2.5Nb alloy during aqueous corrosion: A multi-technique study," *Acta Mater.*, vol. 215, p. 117042, Aug. 2021, doi: 10.1016/J.ACTAMAT.2021.117042.

[181] F. Garzarolli, R. Adamson, and K. Coleman, "Microstructure of Zirconium Alloys

and Effects on Performance," Mölnlycke, Sweden, 2015. [Online]. Available: https://www.antinternational.com/docs/samples/FM/09/ZIRAT20_IZNA15_STR_Microstructure_sample.pdf.

[182] R. J. Pérez and A. R. Massih, "Thermodynamic evaluation of the Nb–O–Zr system," *J. Nucl. Mater.*, vol. 360, no. 3, pp. 242–254, Mar. 2007, doi: 10.1016/J.JNUCMAT.2006.10.008.

[183] O. N. Senkov, D. B. Miracle, K. J. Chaput, and J.-P. Couzinie, "Development and exploration of refractory high entropy alloys—A review," *J. Mater. Res.*, vol. 33, no. 19, Oct. 2018, doi: 10.1557/jmr.2018.153.

[184] D. J. M. King, "INVESTIGATION OF HIGH-ENTROPY ALLOYS FOR USE IN ADVANCED NUCLEAR APPLICATIONS," University of Technology Sydney, Sydney, 2016.

[185] D. Ikeuchi *et al.*, "Cr-Mo-V-W: A new refractory and transition metal high-entropy alloy system," *Scr. Mater.*, vol. 158, pp. 141–145, Jan. 2019, doi: 10.1016/J.SCRIPTAMAT.2018.08.045.

[186] D. J. M. King *et al.*, "High temperature, low neutron cross-section high-entropy alloys in the Nb-Ti-V-Zr system," *Acta Mater.*, vol. 166, pp. 435–446, Mar. 2019, doi: 10.1016/j.actamat.2019.01.006.

[187] P. A. Ferreirós *et al.*, "VNbCrMo refractory high-entropy alloy for nuclear applications," *Int. J. Refract. Met. Hard Mater.*, vol. 113, p. 106200, Jun. 2023, doi:

10.1016/J.IJRMHM.2023.106200.

[188] S. C. Middleburgh, D. M. King, G. R. Lumpkin, M. Cortie, and L. Edwards, "Segregation and migration of species in the CrCoFeNi high entropy alloy," *J. Alloys Compd.*, vol. 599, pp. 179–182, 2014, doi: 10.1016/j.jallcom.2014.01.135.

[189] D. M. King, S. C. Middleburgh, L. Edwards, G. R. Lumpkin, and M. Cortie, "Predicting the Crystal Structure and Phase Transitions in High-Entropy Alloys," *Jom*, vol. 67, no. 10, pp. 2375–2380, 2015, doi: 10.1007/s11837-015-1495-4.

[190] D. J. M. King, P. A. Burr, E. G. Obbard, and S. C. Middleburgh, "DFT study of the hexagonal high-entropy alloy fission product system," *J. Nucl. Mater.*, vol. 488, pp. 70–74, 2017, doi: 10.1016/j.jnucmat.2017.02.042.

[191] D. J. M. King, S. C. Middleburgh, A. G. McGregor, and M. B. Cortie, "Predicting the formation and stability of single phase high-entropy alloys," *Acta Mater.*, vol. 104, pp. 172–179, 2016, doi: 10.1016/j.actamat.2015.11.040.

[192] X. C. He and H. S. Liu, "Determination of the isothermal section of the Cu–Zr–Y ternary system at 978 K," *J. Alloys Compd.*, vol. 475, no. 1–2, pp. 245–251, May 2009, doi: 10.1016/J.JALLCOM.2008.07.144.

[193] D. W. Bare, E. Gibson, and O. Carlson, "Tensile properties of yttrium-titanium and yttrium- zirconium alloys," Ames, 1960.

[194] J. Peng *et al.*, "Hydrogen desorption behavior of the hydrides of Zr-Y alloys under Ar and CO2atmosphere," *J. Alloys Compd.*, vol. 693, pp. 103–109, 2017, doi:

10.1016/j.jallcom.2016.09.063.

[195] B. A. Young, J. Liu, D. E. J. Armstrong, and C. R. M. Grovenor, "New Zirconium Alloys for Nuclear Fusion Applications," The Henry Royce Institute, Online, 2021.

[196] J. C. Bokros, "THE GENERAL FEATURES OF THE ZIRCONIUM RICH CORNER OF THE ZIRCONIUM-URANIUM-YTTRIUM PHASE DIAGRAM," Los Angeles, 1957.

[197] A. Jayakumar, S. Radoor, J. T. Kim, J. W. Rhim, J. Parameswaranpillai, and S. Siengchin, *Lightweight and sustainable materials—a global scenario*. LTD, 2023.

[198] A. Peruzzi and J. P. Abraita, "Al-Zr (Aluminum-Zirconium)," in *Alloy Binary Phase*, 2nd ed., T. B. Massalski, Ed. Material Park, OH: ASM International, 1990, p. 241.

[199] L. J. Swartzendruber, L. H. Ennett, L. K. Ives, and R. D. Shull, "The Ti-Al phase diagram: the alpha-alpha2 phase boundary," *Mater. Sci. Eng.*, vol. 51, pp. 1–9, 1981.

[200] F. Zhang, S. L. Chen, Y. A. Chang, and U. R. Kattner, "A thermodynamic description of the Ti-Al system," *Intermetallics*, vol. 5, no. 6, pp. 471–482, 1997, doi: 10.1016/S0966-9795(97)00030-7.

[201] E. M. Schulson, C. River, N. Laboratories, and C. River, "Atomic Energy of Canada Limited A PRELIMINARY STUDY OF CAST AND TRANSFORMED MICROSTRUCTURES OF Zr3Al-BASED ALLOYS," no. December, 1973.

[202] H. E. Rosinger, "Effect of fast neutron irradiation on the properties of Zr3Al-

based alloys," *J. Nucl. Mater.*, 1980, doi: 10.1016/0022-3115(80)90091-4.

[203] E. M. Schulson and J. A. Roy, "The notch-sensitivity of ordered Zr3Al," *J. Nucl. Mater.*, vol. 71, no. 1, pp. 124–133, 1977, doi: 10.1016/0022-3115(77)90196-9.

[204] E. M. Schulson, G. J. C. Carpenter, and L. M. Howe, "Irradiation swelling of Zr3Al," *J. Nucl. Mater.*, vol. 82, no. 1, pp. 140–147, 1979, doi: 10.1016/0022-3115(79)90046-1.

[205] S. N. Tiwari and K. Tangri, "Short-range Order Hardening in Zr-Al Solid Solutions," *Mater. Sci. Eng.*, vol. 57, pp. 31–37, 1983.

[206] X. J. Jiang, Y. Y. Zhang, C. L. Li, G. D. Liang, R. H. Han, and X. Y. Zhang, "Microstructure and mechanical properties of ZrAl binary alloys," *J. Alloys Compd.*, vol. 811, pp. 1–6, 2019, doi: 10.1016/j.jallcom.2019.152068.

[207] J. Murray, A. Peruzzi, and J. P. Abriata, "The Al-Zr (aluminum-zirconium) system," *J. Phase Equilibria*, vol. 13, no. 3, pp. 277–291, Jun. 1992, doi: 10.1007/BF02667556/METRICS.

[208] R. S. Ambartsumyan, A. A. Kiselev, R. V. Grebennikov, V. A. Myshkin, L. J. Tsuprun, and A. F. Nikulina, "Mechanical Properties and Corrosion Resistance of Zirconium and its Alloys in Water, Steam and Gases at High Temperatures," in *PROCEEDINGS OF THE SECOND UNITED NATIONS INTERNATIONAL CONFERENCE ON THE PEACEFUL USES OF ATOMIC ENERGY, Volume 5: Properties of Reactor Materials*, 1958, pp. 12–33.

[209] H. Okamoto, "Ta-Zr (tantalum-zirconium)," *J. Phase Equilibria*, vol. 17, no. 6, p. 555, 1996, doi: 10.1007/BF02666009.

[210] H. C. Dong, Z. H. Feng, M. Z. Ma, X. Y. Zhang, and R. P. Liu, "Optimization of phase composition and mechanical properties in Zr alloys by micro-alloying," *Mater. Lett.*, vol. 202, pp. 25–27, Sep. 2017, doi: 10.1016/J.MATLET.2017.05.082.

[211] J. T. A. Pollock, R. Shull, and H. C. Gatos, "Superconducting Characteristics of Zirconium-Vanadium Alloys," 1970.

[212] J. T. Williams, "Vanadium-Zirconium Alloy System," *Jom*, vol. 7, no. 2, pp. 345–350, 1955, doi: 10.1007/bf03377505.

[213] R. J. Pérez and B. Sundman, "Thermodynamic assessment of the Mo-Zr binary phase diagram," *Calphad Comput. Coupling Phase Diagrams Thermochem.*, vol. 27, no. 3, pp. 253–262, 2003, doi: 10.1016/j.calphad.2003.09.003.

[214] K. F. Ahmmed, "Microstructural Evaluation and Thermal Creep Behavior of Zr-Excel," Queen's University Kingston, Ontario, Canada, 2015.

[215] A. V. Nikulina, V. F. Konkov, M. M. Peregud, and E. E. Vorobev, "Effect of molybdenum on properties of zirconium components of nuclear reactor core," *Nucl. Mater. Energy*, vol. 14, pp. 8–13, Jan. 2018, doi: 10.1016/J.NME.2018.01.001.

[216] D. O. Northwood, "Heat treatment, transformation reactions and mechanical properties of two high strength zirconium alloys," *J. Less Common Met.*, vol. 61, no. 2, pp. 199–212, Oct. 1978, doi: 10.1016/0022-5088(78)90215-1.

[217] J. P. Magnussen, H. Swan, and A. J. Knowles, "Novel High Temperature Zirconium Alloys by Near-Alpha Titanium Analogy," 2024.

[218] D. L. Smith and G. D. Morgan, "BLANKET COMPARISON AND SELECTION STUDY FINAL REPORT vol. 1," Argonne, IL, 1984.

[219] F. Balbaud-Célérier, J. L. Courouau, D. Féron, L. Martinelli, and F. Rouillard, "Corrosion of structural materials by liquid metals used in fusion, fission, and spallation," in *Nuclear Corrosion: Research, Progress and Challenges*, S. Ritter, Ed. Elsevier Ltd, 2020, pp. 437–457.

[220] J. H. DeVan, J. E. Selle, and A. E. Morris, "Review of Lithium Iron-Base Alloy Corrosion Studies," Oak Ridge, 1976.

[221] G. DeVries, "The Corrosion of Metals by Molten Lithium," in *Corrosion by Liquid Metals: Proceedings of the Sessions on Corrosion by Liquid Metals of the 1969 Fall Meeting of the Metallurgical Society of AIME, October 13--16, 1969, Philadelphia, Pennsylvania*, J. E. Draley and J. R. Weeks, Eds. Boston, MA: Springer US, 1970, pp. 251–269.

[222] O. K. Chopra and D. L. Smith, "Corrosion of ferrous alloys in a flowing lithium environment," *J. Nucl. Mater.*, vol. 133–134, no. C, pp. 861–866, Aug. 1985, doi: 10.1016/0022-3115(85)90275-2.

[223] G. E. C. Bell, "Thermal convection loop experiments and analysis of mass-transport processes in lithium/Fe-12Cr-1MoVW systems," California Univ., Los Angeles, CA (USA), 1988.

[224] E. E. Hoffman, "CORROSION OF MATERIALS BY LITHIUM AT ELEVATED TEMPERATURES," University of Tennessee, United States, 1959.

[225] E. E. Hoffman and W. D. Manly, "Corrosion Resistance of Metals and Alloys to Sodium and Lithium," Oak Ridge, 1957. doi: 10.1021/ba-1957-0019.ch009.

[226] M. Kondo, "Forefront of liquid metal technologies for fusion reactors," *IOP Conf. Ser. Earth Environ. Sci.*, vol. 364, no. 1, 2019, doi: 10.1088/1755-1315/364/1/012012.

[227] R. J. Pulham and P. Hubberstey, "Comparison of chemical reactions in liquid lithium with those in liquid sodium," *J. Nucl. Mater.*, vol. 115, no. 2–3, pp. 239–250, 1983, doi: 10.1016/0022-3115(83)90315-X.

[228] R. L. Klueh, "Penetration of Refractory Metals by Alkali Metals," in *Corrosion by Liquid Metals*, 1969, pp. 177–196.

[229] V. Tsisar, M. Kondo, T. Muroga, T. Nagasaka, and O. Yeliseyeva, "Structural and compositional transformations in the near-surface layers of Fe-Cr based steels exposed to lithium - Effect of alloying and corrosion-assisted substructure coarsening," *Corros. Sci.*, vol. 53, no. 1, pp. 441–447, Jan. 2011, doi: 10.1016/J.CORSCI.2010.09.055.

[230] P. Hubberstey and P. G. Roberts, "Corrosion chemistry of vanadium in liquid lithium containing dissolved nitrogen," *J. Nucl. Mater.*, vol. 155–157, no. PART 2, pp. 694–697, 1988, doi: 10.1016/0022-3115(88)90397-2.

[231] S. Hammouti *et al.*, "Wetting of liquid lithium on fusion-relevant materials microtextured by femtosecond laser exposure," *J. Nucl. Mater.*, vol. 508, pp. 237–248, 2018, doi: 10.1016/j.jnucmat.2018.05.051.

[232] R. Kaita *et al.*, "Experiments with liquid metal walls: Status of the lithium tokamak experiment," *Fusion Eng. Des.*, vol. 85, no. 6, pp. 874–881, 2010, doi: 10.1016/j.fusengdes.2010.04.005.

[233] H. W. Kugel *et al.*, "The effect of lithium surface coatings on plasma performance in the National Spherical Torus Experiment," *Phys. Plasmas*, vol. 15, no. 5, 2008, doi: 10.1063/1.2906260.

[234] J. Knaster, P. Garin, H. Matsumoto, Y. Okumura, and M. Sugimoto, "Overview of the IFMIF / EVEDA project," *Nucl. Fusion*, vol. 57, no. 102016, 2017, doi: 10.1088/1741-4326/aa6a6a.

[235] P. Favuzza *et al.*, "Erosion-corrosion resistance of Reduced Activation Ferritic-Martensitic steels exposed to flowing liquid Lithium," *Fusion Eng. Des.*, vol. 136, pp. 1417–1421, Nov. 2018, doi: 10.1016/j.fusengdes.2018.05.028.

[236] X. Meng *et al.*, "Effect of temperature on the corrosion behaviors of 304 stainless steel in static liquid lithium," *Fusion Eng. Des.*, vol. 128, pp. 75–81, Mar. 2018, doi: 10.1016/J.FUSENGDES.2018.01.049.

[237] D. H. Zhang *et al.*, "Study of the corrosion characteristics of 304 and 316L stainless steel in the static liquid lithium," *J. Nucl. Mater.*, vol. 553, p. 153032, Sep. 2021, doi:

10.1016/j.jnucmat.2021.153032.

[238] C. D. Moynihan, S. Stemmley, B. Moore, R. Trendler, M. A. Hossain, and D. N. Ruzic, "Characterization of liquid lithium corrosion for fusion reactor materials," *Fusion Eng. Des.*, vol. 199, no. December 2023, p. 114102, 2024, doi: 10.1016/j.fusengdes.2023.114102.

[239] M. Kondo, M. Takahashi, T. Tanaka, V. Tsisar, and T. Muroga, "Compatibility of reduced activation ferritic martensitic steel JLF-1 with liquid metals Li and Pb–17Li," *Fusion Eng. Des.*, vol. 87, no. 10, pp. 1777–1787, Oct. 2012, doi: 10.1016/J.FUSENGDES.2011.12.013.

[240] G. E. Bell, M. A. Abdou, and P. F. Tortorelli, "Experimental and analytical investigations of mass transport processes of 12cr-1 movw steel in thermally-convected lithium systems," *Fusion Eng. Des.*, vol. 8, pp. 421–427, 1989, doi: 10.1016/S0920-3796(89)80142-5.

[241] B. A. Pint *et al.*, "Initial characterization of V-4Cr-4Ti and MHD coatings exposed to flowing Li," *J. Nucl. Mater.*, vol. 386–388, pp. 712–715, 2009, doi: 10.1016/j.jnucmat.2008.12.295.

[242] T. Hosaka, M. Kondo, S. Sato, M. Ando, and T. Nozawa, "Chemical compatibility of F82H and 316L in liquid metal heat transfer mediums Li, Na and NaK," *J. Nucl. Mater.*, vol. 561, 2022, doi: 10.1016/j.jnucmat.2022.153546.

[243] S. Gavras, S. M. Zhu, J. F. Nie, M. A. Gibson, and M. A. Easton, "On the

microstructural factors affecting creep resistance of die-cast Mg–La-rare earth (Nd, Y or Gd) alloys," *Mater. Sci. Eng. A*, vol. 675, pp. 65–75, Oct. 2016, doi: 10.1016/J.MSEA.2016.08.046.

[244] S. Karthikeyan, G. B. Viswanathan, P. I. Gouma, V. K. Vasudevan, Y. W. Kim, and M. J. Mills, "Mechanisms and effect of microstructure on creep of TiAl-based alloys," *Mater. Sci. Eng. A*, vol. 329–331, pp. 621–630, Jun. 2002, doi: 10.1016/S0921-5093(01)01659-8.

[245] R. Lässer *et al.*, "Structural materials for DEMO: The EU development, strategy, testing and modelling," *Fusion Eng. Des.*, vol. 82, no. 5–14, pp. 511–520, Oct. 2007, doi: 10.1016/J.FUSENGDES.2007.06.031.

[246] V. S. Emelyanov, Y. G. Godin, and A. I. Evstyukhin, "Mechanical Properties of Zirconium Binary and Ternary Alloys with Tantalum and Niobium at Room and Elevated Temperatures," in *PROCEEDINGS OF THE SECOND UNITED NATIONS INTERNATIONAL CONFERENCE ON THE PEACEFUL USES OF ATOMIC ENERGY, Volume 5: Properties of Reactor Materials*, 1958, pp. 69–74.

[247] S. Banerjee and R. Krishnan, "Martensitic transformation in Zr-Ti alloys," *Metall. Trans.*, vol. 4, no. 8, pp. 1811–1819, Aug. 1973, doi: 10.1007/BF02665407/METRICS.

[248] W. G. Burgers, "On the process of transition of the cubic-body-centered modification into the hexagonal-close-packed modification of zirconium," *Physica*,

vol. 1, no. 7–12, pp. 561–586, May 1934, doi: 10.1016/S0031-8914(34)80244-3.

[249] G. Bertolino, G. Meyer, and J. Perez Ipiña, "Mechanical Properties Degradation at Room Temperature in ZRY-4 by Hydrogen Brittleness," *Mater. Res.*, vol. 5, no. 2, pp. 125–129, 2002, doi: 10.1590/s1516-14392002000200007.

[250] D. Murray, "Deformation Localisation around Hydrides in Zircaloy-4," University of Oxford, Oxford, 2020.

[251] S. A. Worcester, J. P. Dougherty, and J. P. Foster, "Zircaloy-4 processing for uniform and nodular corrosion resistance," EP0446924A1, Nov. 30, 1994.

[252] S. G. McDonald III and G. P. Sabol, "Process for producing a thin-walled tubing from a zirconium-niobium alloy," EP0198570A2, Oct. 22, 1986.

[253] G. P. Sabol and S. G. McDonald II, "Process for fabricating a zirconium-niobium alloy and articles resulting therefrom," 4649023, Mar. 10, 1987.

[254] J.-P. Mardon, J. Sevenat, and D. Charquet, "Method of manufacturing a tube for a nuclear fuel assembly, and tubes obtained thereby," 5648995, Jul. 15, 1997.

[255] Y. H. Jeong *et al.*, "Niobium-containing zirconium alloy for nuclear fuel claddings," 6261516, Jul. 17, 2001.

[256] J. P. Foster, S. A. Worcester, and R. J. Cornstock, "Zirlo material composition and fabrication processing," 0475159A1, Aug. 23, 1991.

[257] J. P. Foster, J. Comstock, S. A. Worcester, and G. P. Sabol, "ZIRLO MATERIAL FOR LIGHT WATER REACTOR APPLICATIONS," 5112573, May 12, 1992.

[258] Y. Jeong *et al.*, "Method for manufacturing zirconium-based alloys containing niobium for use in nuclear fuel rod cladding," US 2003/0098105 A1, 2002.

[259] D. Charquet, J.-P. Mardon, and J. Senevat, "Zirconium based alloy and method for making a component for nuclear fuel assembly with same," WO 01/024193 A1, 2000.

[260] M. Noe, P. Beslu, J. C. Brachet, P. Parmentier, and J. Porta, "Zirconium and niobium alloy comprising erbium, preparation method and component containing said alloy," US6340536B1, 2000.

[261] P. Barberis, V. Rebeyrolle, P.-B. Hoffmann, and J.-J. Vermoyal, "Alliage de zirconium resistant a la corrosion en ombres portees pour composant d'assemblage de combustible pour reacteur a eau bouillante, composant realise en cet alliage, assemblage de combustible et son utilisation," EP2099943B2, Jul. 12, 2017.

[262] T. Isobe and Y. Suda, "Method for making Zr alloy nuclear reactor fuel cladding having excellent corrosion resistance and creep properties," US6125161A, Sep. 26, 2000.

[263] G. Bunel, D. Charquet, and J.-P. Gros, "Procede de fabrication de toles a structure homogene en zircaloy 2 ou en zircaloy 4," FR2683828A1, Aug. 26, 1994.

[264] S. G. McDonald and G. P. Sabol, "Zirconium alloy fabrication processes," EP0085553B1, Nov. 23, 1983.

[265] E. T. Andersson, S. A. Wilson, and J. H. Schemel, "Method of manufacturing tubes of zirconium alloys with improved corrosion resistance for thermal nuclear reactors," EP0196286A1, May 17, 1989.

[266] A. W. Urquhart, "Zirconium alloy heat treatment process," US4360389A, Nov. 23, 1982.

[267] S. G. McDonald and G. P. Sabol, "Zirconium alloy products and fabrication processes," US4584030A, Apr. 22, 1986.

[268] D. Charquet, "Tube, Barre ou Tole En Alliage de Zirconium, Resistant a la Fois a la corrosion uniforme et a la corrosion nodulaire et procede de fabrication correspondant," 2624136, Jun. 05, 1992.

[269] Y. T. Tang, C. Schwalbe, M. Futoma, B. Roebuck, S. Utada, and R. C. Reed, "A Comparative Study of High Temperature Tensile and Creep Testing Between Standard and Miniature Specimens: Applicability and Limits," *Metall. Mater. Trans. A Phys. Metall. Mater. Sci.*, vol. 54, no. 5, pp. 1568–1581, May 2023, doi: 10.1007/S11661-022-06869-X/FIGURES/13.

[270] Y. T. Tang, N. D'Souza, B. Roebuck, P. Karamched, C. Panwisawas, and D. M. Collins, "Ultra-high temperature deformation in a single crystal superalloy: Mesoscale process simulation and micromechanisms," *Acta Mater.*, vol. 203, p.

116468, Jan. 2021, doi: 10.1016/J.ACTAMAT.2020.11.010.

[271] S. Sulzer, E. Alabort, A. Németh, B. Roebuck, and R. Reed, "On the Rapid Assessment of Mechanical Behavior of a Prototype Nickel-Based Superalloy using Small-Scale Testing," *Metall. Mater. Trans. A Phys. Metall. Mater. Sci.*, vol. 49, no. 9, pp. 4214–4235, Sep. 2018, doi: 10.1007/S11661-018-4673-5/FIGURES/18.

[272] J. L. Vandegrift *et al.*, "Oxidation behavior of Zirconium, Zircaloy-3, Zircaloy-4, Zr-1Nb, and Zr-2.5Nb in air and oxygen," *Nucl. Mater. Energy*, vol. 20, p. 100692, Aug. 2019, doi: 10.1016/J.NME.2019.100692.

[273] S. Utada, R. Sasaki, R. C. Reed, and Y. T. Tang, "Overheating of Waspaloy: Effect of cooling rate on flow stress behavior," *Mater. Des.*, vol. 221, p. 110911, Sep. 2022, doi: 10.1016/J.MATDES.2022.110911.

[274] S. R. Kalidindi and S. Pathak, "Determination of the effective zero-point and the extraction of spherical nanoindentation stress–strain curves," *Acta Mater.*, vol. 56, no. 14, pp. 3523–3532, Aug. 2008, doi: 10.1016/J.ACTAMAT.2008.03.036.

[275] S. Pathak and S. R. Kalidindi, "Spherical nanoindentation stress–strain curves," *Mater. Sci. Eng. R Reports*, vol. 91, pp. 1–36, May 2015, doi: 10.1016/J.MSER.2015.02.001.

[276] J. E. Campbell *et al.*, "A Critical Appraisal of the Instrumented Indentation Technique and Profilometry-Based Inverse Finite Element Method Indentation Plastometry for Obtaining Stress–Strain Curves," *Adv. Eng. Mater.*, vol. 23, no. 5,

2021, doi: 10.1002/adem.202001496.

[277] A. Lodh, P. Pant, G. Kumar, K. V. Mani Krishna, R. Tewari, and I. Samajdar, "Orientation-dependent solid solution strengthening in zirconium: a nanoindentation study," *J. Mater. Sci.*, vol. 55, no. 10, pp. 4493–4503, Apr. 2020, doi: 10.1007/S10853-019-04280-3/FIGURES/10.

[278] V. Kuksenko, S. Roberts, and E. Tarleton, "The hardness and modulus of polycrystalline beryllium from nano-indentation," *Int. J. Plast.*, vol. 116, pp. 62–80, 2019, doi: 10.1016/j.ijplas.2018.12.008.

[279] A. Leitner, V. Maier-Kiener, and D. Kiener, "Essential refinements of spherical nanoindentation protocols for the reliable determination of mechanical flow curves," *Mater. Des.*, vol. 146, pp. 69–80, May 2018, doi: 10.1016/J.MATDES.2018.03.003.

[280] E. Broitman, "Indentation Hardness Measurements at Macro-, Micro-, and Nanoscale: A Critical Overview," *Tribol. Lett.*, vol. 65, no. 1, pp. 1–18, 2017, doi: 10.1007/s11249-016-0805-5.

[281] P. E. J. Flewitt and R. K. Wild, *Microstructural characterisation of metals and alloys*. Institute of Metals, 1985.

[282] S. Hamed, "Quantitative polarised light microscopy of metals," Swansea University, 2021.

[283] J. I. Goldstein, D. E. Newbury, J. R. Michael, N. W. M. Ritchie, J. H. J. Scott, and

D. C. Joy, *Scanning electron microscopy and x-ray microanalysis*, 4th ed. New York: Springer New York, 2018.

[284] J. J. Kearns, "Thermal Expansion and Preferred Orientation in Zircaloy," Pittsburgh, PA, 1965. Accessed: Jun. 21, 2024. [Online]. Available: https://ntrl.ntis.gov/NTRL/dashboard/searchResults/titleDetail/WAPDTM472.xhtml.

[285] D. O. Northwood, I. M. London, and L. E. Bähen, "Elastic constants of zirconium alloys," *J. Nucl. Mater.*, vol. 55, no. 3, pp. 299–310, 1975, doi: 10.1016/0022-3115(75)90071-9.

[286] C. E. Coleman, *The of Metallurgy of Zirconium*, vol. 2. Vienna: International Atomic Energy Agency, 2022.

[287] K. V. Mani Krishna, D. Srivastava, G. K. Dey, V. Hiwarkar, I. Samajdar, and N. Saibaba, "Comparative study of methods of the determination of Kearns parameter in zirconium," *J. Nucl. Mater.*, vol. 414, no. 3, pp. 492–497, Jul. 2011, doi: 10.1016/J.JNUCMAT.2011.04.065.

[288] J. A. Gruber, S. A. Brown, and G. A. Lucadamo, "Generalized Kearns texture factors and orientation texture measurement," *J. Nucl. Mater.*, vol. 408, no. 2, pp. 176–182, Jan. 2011, doi: 10.1016/J.JNUCMAT.2010.11.031.

[289] W. R. Tyson, "Strengthening of hcp Zr, Ti and Hf by interstitial solutes – a review," *Can. Metall. Q.*, vol. 6, no. 4, pp. 301–332, Oct. 1967, doi:

10.1179/CMQ.1967.6.4.301.

[290] L. Nie, Y. Zhan, T. Hu, X. Chen, and C. Wang, "Novel high-strength ternary Zr-Al-Sn alloys with martensite structure for nuclear applications," *J. Nucl. Mater.*, vol. 442, no. 1–3, pp. 100–105, Nov. 2013, doi: 10.1016/j.jnucmat.2013.08.045.

[291] A. J. de O. Zimmermann and A. F. Padilha, "Rolling and recrystallization behavior of pure zirconium and zircaloy-4," *Rev. Mater.*, vol. 24, no. 3, 2019, doi: 10.1590/S1517-707620190003.0767.

[292] M. Reif, F. Scherm, M. C. Galetz, and U. Glatzel, "An enhanced three-step oxidation process to improve oxide adhesion on zirconium alloys," *Oxid. Met.*, vol. 82, no. 1–2, pp. 99–112, Jun. 2014, doi: 10.1007/S11085-014-9479-2/FIGURES/11.

[293] J. P. Abriata, J. Garcés, and R. Versaci, "The O-Zr (Oxygen-Zirconium) system," *Bull. Alloy Phase Diagrams*, vol. 7, no. 2, pp. 116–124, Apr. 1986, doi: 10.1007/BF02881546/METRICS.

[294] M. Arul Kumar *et al.*, "Role of twinning on the omega-phase transformation and stability in zirconium," *Acta Mater.*, vol. 185, pp. 211–217, Feb. 2020, doi: 10.1016/J.ACTAMAT.2019.12.006.

[295] B. D. Lichter, "PRECISION LATTICE PARAMETER DETERMINATION OF ZIRCONIUM-OXYGEN SOLID SOLUTION," *Trans. Met. Soc. AIME*, vol. Vol: 218, Dec. 1960.

[296] J. C. Slater, "Atomic Radii in Crystals," *J. Chem. Phys.*, vol. 41, no. 10, pp. 3199–3204, Nov. 1964, doi: 10.1063/1.1725697.

[297] R. C. Hansen and A. Raman, "Alloy chemistry of sigma /beta-U/-related phases. III - Sigma-phases with non- transition elements," *Z. Met.*, vol. 61, pp. 115–120, 1970.

[298] M. Kucerakova, S. Vratislav, L. Kalvoda, and Z. Trojanova, "Texture analysis of zirconium samples deformed by uniaxial tension using neutron and X-ray diffraction," *IOP Conf. Ser. Mater. Sci. Eng.*, vol. 82, 2015, doi: 10.1088/1757-899X/82/1/012022.

[299] F. J. Humphreys and M. Hatherly, "Deformation Textures," in *Recrystallization and Related Annealing Phenomena*, 2nd ed., Elsevier, 2004, pp. 67–89.

[300] E. Tenckhoff, *Deformation Mechanisms, Texture, and Anisotropy in Zirconium and Zircaloy*. ASTM International, 1988.

[301] X. Yang, N. Takeichi, K. Shida, H. Tanaka, N. Kuriyama, and T. Sakai, "Novel Mg–Zr–A–H (A = Li, Na) hydrides synthesized by a high pressure technique and their hydrogen storage properties," *J. Alloys Compd.*, vol. 509, no. 4, pp. 1211–1216, Jan. 2011, doi: 10.1016/J.JALLCOM.2010.09.187.

[302] J. Bair, M. Asle Zaeem, and M. Tonks, "A review on hydride precipitation in zirconium alloys," *J. Nucl. Mater.*, vol. 466, pp. 12–20, Nov. 2015, doi: 10.1016/J.JNUCMAT.2015.07.014.

[303] P. O. Tympel, "Mechanics and micro-mechanisms of LCF and dwell fatigue in Ti-6Al-4V," Imperial College London, 2016.

[304] D. Lunt, "The effect of macrozones in Ti-6Al-4V on the strain localisation behaviour," University of Manchester, 2014.

[305] X. Li *et al.*, "Automation of intercept method for grain size measurement: A topological skeleton approach," *Mater. Des.*, vol. 224, p. 111358, 2022, doi: 10.1016/j.matdes.2022.111358.

[306] ASTM International, "Standard Test Methods for Determining Average Grain Size," West Conshohocken, PA, 1955. doi: 10.1520/E0112-13R21.1.4.

[307] W. J. Meng, J. Faber, P. R. Okamoto, L. E. Rehn, B. J. Kestel, and R. L. Hitterman, "Neutron diffraction and transmission electron microscopy study of hydrogen-induced phase transformations in Zr3Al," *J. Appl. Phys.*, vol. 67, no. 3, pp. 1312–1319, Feb. 1990, doi: 10.1063/1.345683.

[308] F. F. Dear, P. Kontis, B. Gault, J. Ilavsky, D. Rugg, and D. Dye, "Mechanisms of Ti3Al precipitation in hcp α-Ti," *Acta Mater.*, vol. 212, p. 116811, Jun. 2021, doi: 10.1016/J.ACTAMAT.2021.116811.

[309] F. F. Worsnop, S. L. M. Lea, J. Ilavsky, D. Rugg, and D. Dye, "Crystallographic ordering of Al and Sn in α-Ti," *Scr. Mater.*, vol. 226, p. 115221, Mar. 2023, doi: 10.1016/J.SCRIPTAMAT.2022.115221.

[310] J. C. Schuster and M. Palm, "Reassessment of the binary Aluminum-Titanium

phase diagram," *J. Phase Equilibria Diffus. 2006 273*, vol. 27, no. 3, pp. 255–277, Jun. 2006, doi: 10.1361/154770306X109809.

[311] Y. M. Yarmoshenko, V. N. Kozhanov, V. M. Cherkashenko, E. Z. Kurmaev, and E. P. Romanov, "X-ray emission spectra and electronic structure ZrV2 and ZrV2Dx," *Solid State Commun.*, vol. 55, no. 1, pp. 19–23, Jul. 1985, doi: 10.1016/0038-1098(85)91096-8.

[312] J. W. Edwards, R. Speiser, and H. L. Johnston, "High Temperature Structure and Thermal Expansion of Some Metals as Determined by X-Ray Diffraction Data. I. Platinum, Tantalum, Niobium, and Molybdenum," *J. Appl. Phys.*, vol. 22, no. 4, pp. 424–428, Apr. 1951, doi: 10.1063/1.1699977.

[313] S. v. Näray-Szabo, "Zur Struktur des Baddeleyits ZrO2," *Zeitschrift für Krist. - Cryst. Mater.*, vol. 94, no. 1–6, pp. 414–416, Nov. 1936, doi: 10.1524/ZKRI.1936.94.1.414.

[314] B. A. Rogers and D. F. Atkins, "Zirconium-Columbium Diagram," *Trans. Am. Inst. Mining, Metall. Pet. Eng.*, vol. 203, pp. 1034–1041, 1955.

[315] E. Gdoutos and M. Konsta-Gdoutos, *Mechanical Testing of Materials*, 1st ed., vol. 275. Cham: Springer Nature Switzerland, 2024.

[316] P. Zhang, S. X. Li, and Z. F. Zhang, "General relationship between strength and hardness," *Mater. Sci. Eng. A*, vol. 529, no. 1, pp. 62–73, Nov. 2011, doi: 10.1016/J.MSEA.2011.08.061.

[317] A. Quadling, D. Bowden, C. Hardie, and A. Vasanthakumaran, "PRE-PRINT: Developing Power Plant Materials Using the Life Cycle Lens," *Philos. Trans. A*, 2024, Accessed: Jun. 02, 2024. [Online]. Available: https://scientific-publications.ukaea.uk/wp-content/uploads/UKAEA-STEP-PR2405.PDF.

[318] E. Gaganidze, F. Gillemot, I. Szenthe, M. Gorley, M. Rieth, and E. Diegele, "Development of EUROFER97 database and material property handbook," *Fusion Eng. Des.*, vol. 135, pp. 9–14, Oct. 2018, doi: 10.1016/j.fusengdes.2018.06.027.

[319] L. M. Giancarli *et al.*, "Status of the ITER TBM Program and overview of its technical objectives," *Fusion Eng. Des.*, vol. 203, p. 114424, Jun. 2024, doi: 10.1016/J.FUSENGDES.2024.114424.

[320] B. Gómez-Ferrer, C. Dethloff, E. Gaganidze, L. Malerba, C. Hatzoglou, and C. Pareige, "Nano-hardening features in high-dose neutron irradiated Eurofer97 revealed by atom-probe tomography," *J. Nucl. Mater.*, vol. 537, p. 152228, Aug. 2020, doi: 10.1016/J.JNUCMAT.2020.152228.

[321] S. Arunkumar, "Small Punch Creep Test: An Overview," *Metals and Materials International*. Korean Institute of Metals and Materials, 2020, doi: 10.1007/s12540-020-00783-w.

[322] R. J. Lancaster and S. P. Jeffs, "Small Punch Creep," in *Creep*, T. A. Tanski, M. Sroka, and A. Zielinski, Eds. IntechOpen, 2018.

[323] R. J. Lancaster, S. P. Jeffs, B. J. Haigh, and N. C. Barnard, "Derivation of material properties using small punch and shear punch test methods," *Mater. Des.*, vol. 215, p. 110473, Mar. 2022, doi: 10.1016/J.MATDES.2022.110473.

[324] M. Zmitko *et al.*, "The European ITER Test Blanket Modules: EUROFER97 material and TBM's fabrication technologies development and qualification," *Fusion Eng. Des.*, vol. 124, pp. 767–773, Nov. 2017, doi: 10.1016/j.fusengdes.2017.04.051.

[325] H. Dawson, M. Richardson, M. Gorley, and E. Surrey, "The effect of testing environment on small punch creep," in *6th International Small Sample Test Techniques Conference*, 2018, vol. 1, no. S1, p. 15, doi: 10.5334/UPROC.15.

[326] M. Bruchhausen *et al.*, "European standard on small punch testing of metallic materials," in *American Society of Mechanical Engineers, Pressure Vessels and Piping Division (Publication) PVP*, 2017, vol. 1A-2017, pp. 1–8, doi: 10.1115/PVP2017-65396.

[327] E. Lucon, J. Benzing, and N. Hrabe, "NISTIR 8303 Development and Validation of Small Punch Testing at NIST," 2020. doi: 10.6028/NIST.IR.8303.

[328] E. Altstadt *et al.*, "Critical evaluation of the small punch test as a screening procedure for mechanical properties," *J. Nucl. Mater.*, vol. 472, pp. 186–195, Apr. 2016, doi: 10.1016/J.JNUCMAT.2015.07.029.

[329] W. J. S. Yang, R. P. Tucker, B. Cheng, and R. B. Adamson, "Precipitates in zircaloy:

Identification and the effects of irradiation and thermal treatment," *J. Nucl. Mater.*, vol. 138, no. 2–3, pp. 185–195, Apr. 1986, doi: 10.1016/0022-3115(86)90005-X.

[330] R. M. A. Jones, "The effect of niobium on the microstructural evolution of zirconium alloys during proton irradiation," University of Manchester, 2019.

[331] Q. Dong, Z. Yao, Q. Wang, H. Yu, M. A. Kirk, and M. R. Daymond, "Precipitate Stability in a Zr–2.5Nb–0.5Cu Alloy under Heavy Ion Irradiation," *Met. 2017, Vol. 7, Page 287*, vol. 7, no. 8, p. 287, Jul. 2017, doi: 10.3390/MET7080287.

[332] L. J. Chai, H. Wu, S. Y. Wang, B. F. Luan, Y. Wu, and X. Y. Huang, "Microstructural characteristics of cold-rolled Zr-2.5Nb alloy annealed near the monotectoid temperature," *Sci. China Technol. Sci.*, vol. 61, no. 4, pp. 558–566, Apr. 2018, doi: 10.1007/S11431-017-9130-4/METRICS.

[333] Y. Pushpalatha Devi, H. Donthula, N. Keskar, A. Sarkar, K. Vaibhaw, and K. V. Mani Krishna, "Microstructural evolution in (α + βZr) region of Zr-2.5 wt% Nb annealed at different temperatures: Effect on mechanical properties," *J. Nucl. Mater.*, vol. 530, p. 151978, Mar. 2020, doi: 10.1016/J.JNUCMAT.2019.151978.

[334] Z. N. Yang *et al.*, "Effect of intercritical annealing temperature on microstructure and mechanical properties of duplex Zr-2.5Nb alloy," *J. Alloys Compd.*, vol. 776, pp. 242–249, 2019, doi: 10.1016/j.jallcom.2018.10.320.

[335] X. Meng and D. Northwood, "Intermetallic Precipitates in Zirconium-Niobium Alloys," in *Zirconium in the Nuclear Industry: Eighth International Symposium, ASTM*

STP 1023, 1989, pp. 478–486, doi: 10.1520/STP18882S.

[336] B. Garrison *et al.*, "Mechanical Properties of Zircaloy Cladding Tubes and Contributions to M.E.T.A. Mechanical Property Database," Oak Ridge, TN (United States), 2023. Accessed: Jun. 29, 2024. [Online]. Available: www.osti.gov.

[337] C. L. Whitmarsh, "REVIEW OF ZIRCALOY-2 AND ZIRCALOY-4 PROPERTIES RELEVANT TO N.S. SAVANNAH REACTOR DESIGN," Oak Ridge, TN (United States), Jul. 1962. doi: 10.2172/4827123.

[338] M. Lugovy, V. Slyunyayev, and M. Brodnikovskyy, "Solid solution strengthening in multicomponent fcc and bcc alloys: Analytical approach," *Prog. Nat. Sci. Mater. Int.*, vol. 31, no. 1, pp. 95–104, Feb. 2021, doi: 10.1016/J.PNSC.2020.11.006.

[339] H. Yang *et al.*, "Effects of alloying elements (Sn, Nb, Cr, and Mo) on the microstructure and mechanical properties of zirconium alloys," *J. Nucl. Sci. Technol.*, vol. 52, no. 9, pp. 1162–1173, 2015, doi: 10.1080/00223131.2014.996622.

[340] Berkeley Lab, "ZrV2 mp-258," *The Materials Project*, 2025. https://next-gen.materialsproject.org/materials/mp-258 (accessed Feb. 22, 2025).

[341] N. N. Greenwood and A. Earnshaw, *Chemistry of the Elements*, 2nd ed. Butterworth-Heinemann, 1997.

[342] R. D. Jones, A. J. Knowles, and W. J. Clegg, "A binary beta titanium superalloy containing ordered-beta TiFe, alpha and omega," *Scr. Mater.*, vol. 200, p. 113905, Jul. 2021, doi: 10.1016/J.SCRIPTAMAT.2021.113905.

[343] P. F. Weck, E. Kim, V. Tikare, and J. A. Mitchell, "Mechanical properties of zirconium alloys and zirconium hydrides predicted from density functional perturbation theory," *Dalt. Trans.*, vol. 44, no. 43, 2015, doi: 10.1039/C5DT03403E.

[344] J. W. Connor, ; A Kirk, ; H R Wilson, A. Kirk, and H. R. Wilson, "Edge Localised Modes (ELMs): Experiments and Theory," *AIP Conf. Proc.*, vol. 1013, no. 1, pp. 174–190, May 2008, doi: 10.1063/1.2939030.

[345] A. W. Leonard, "Edge-localized-modes in tokamaks," *Phys. Plasmas*, vol. 21, no. 9, p. 90501, Sep. 2014, doi: 10.1063/1.4894742/625104.

[346] T. E. Evans, "ELM mitigation techniques," *J. Nucl. Mater.*, vol. 438, no. SUPPL, pp. S11–S18, Jul. 2013, doi: 10.1016/J.JNUCMAT.2013.01.283.

[347] A. Hassanein and V. Sizyuk, "Potential design problems for ITER fusion device," *Sci. Rep.*, vol. 11, no. 1, p. 2069, Dec. 2021, doi: 10.1038/S41598-021-81510-2.

[348] J. Hargreaves *et al.*, "The transient thermal ageing of Eurofer 97 by mitigated plasma disruptions," *Mater. Des.*, p. 113207, Jul. 2024, doi: 10.1016/J.MATDES.2024.113207.

[349] Y. Yuan, J. Du, M. Wirtz, G. N. Luo, G. H. Lu, and W. Liu, "Surface damage and structure evolution of recrystallized tungsten exposed to ELM-like transient loads," *Nucl. Fusion*, vol. 56, no. 3, p. 036021, Feb. 2016, doi: 10.1088/0029-5515/56/3/036021.

[350] G. Sinclair, S. Gonderman, J. K. Tripathi, and A. Hassanein, "Effect of ELM pacing on morphology evolution and erosion of tungsten as a plasma-facing material in a fusion environment," *J. Nucl. Mater.*, vol. 508, pp. 26–32, Sep. 2018, doi: 10.1016/J.JNUCMAT.2018.05.035.

[351] M. Reinhart *et al.*, "Latest results of Eurofusion plasma-facing components research in the areas of power loading, material erosion and fuel retention," *Nucl. Fusion*, vol. 62, no. 4, p. 042013, Feb. 2022, doi: 10.1088/1741-4326/AC2A6A.

[352] S. Pestchanyi, I. Garkusha, and I. Landman, "Simulation of tungsten armour cracking due to small ELMs in ITER," *Fusion Eng. Des.*, vol. 85, no. 7–9, pp. 1697–1701, Dec. 2010, doi: 10.1016/J.FUSENGDES.2010.05.005.

[353] T. Marchhart *et al.*, "Discovering tungsten-based composites as plasma facing materials for future high-duty cycle nuclear fusion reactors," *Sci. Reports 2024 141*, vol. 14, no. 1, pp. 1–13, Jun. 2024, doi: 10.1038/s41598-024-64614-3.

[354] H. Dominguez-Andrade, A. Croot, G. Wan, J. A. Smith, and N. A. Fox, "Characterisation of thermionic emission current with a laser-heated system," *Rev. Sci. Instrum.*, vol. 90, no. 4, p. 45110, Apr. 2019, doi: 10.1063/1.5088150/283163.

[355] J. Hargreaves, D. Kumar, H. Dawson, L. Harding, H. D. Andrade, and T. L. Martin, "Microanalysis of the Effects of Tokamak Thermal Transients on Eurofer 97 Steel," *Microsc. Microanal.*, vol. 28, no. S1, pp. 2076–2078, Aug. 2022, doi: 10.1017/S1431927622008042.

[356] F. F. Dear, "a2 , Oxygen and the Micromechanics of a-Titanium," Imperial College London, 2021.

[357] Q. Xu, T. Nagasaka, and T. Muroga, "Compatibility of Low Activation Ferritic Steels with Liquid Lithium," *Fusion Sci. Technol.*, vol. 52, no. 3, pp. 609–612, 2007, doi: 10.13182/FST07-A1555.

[358] A. Aiello *et al.*, "Lifus (lithium for fusion) 6 loop design and construction," *Fusion Eng. Des.*, vol. 88, no. 6–8, pp. 769–773, Oct. 2013, doi: 10.1016/J.FUSENGDES.2013.02.129.

[359] T. Furukawa and Y. Hirakawa, "BASIC EXPERIMENT ON LITHIUM REMOVAL TECHNIQUE," 2012, Accessed: Jun. 07, 2024. [Online]. Available: http://asmedigitalcollection.asme.org/ICONE/proceedings-pdf/ICONE20-POWER2012/44991/9/4248056/9_1.pdf.

[360] D. R. Lide, *CRC Handbook of Chemistry and Physics*, 81st ed. Boca Raton, FL: CRC Press, 2000.

[361] F. Balbaud-Célérier, J. L. Courouau, D. Féron, L. Martinelli, and F. Rouillard, "Corrosion of structural materials by liquid metals used in fusion, fission, and spallation," *Nucl. Corros. Res. Prog. Challenges*, pp. 437–457, Jan. 2020, doi: 10.1016/B978-0-12-823719-9.00013-5.

[362] M. Kondo, T. Muroga, T. Nagasaka, Q. Xu, V. Tsisar, and T. Oshima, "Mass transfer of RAFM steel in Li by simple immersion, impeller induced flow and

thermal convection," *J. Nucl. Mater.*, vol. 417, no. 1–3, pp. 1200–1204, Oct. 2011, doi: 10.1016/J.JNUCMAT.2011.01.096.

[363] X. Meng *et al.*, "Study of the corrosion behaviors of 304 austenite stainless steel specimens exposed to static liquid lithium at 600 K," *J. Nucl. Mater.*, vol. 480, pp. 25–31, Nov. 2016.

[364] X. C. Meng *et al.*, "Corrosion of 304 stainless steel in static liquid lithium under high vacuum," *Nucl. Mater. Energy*, vol. 25, p. 100823, Dec. 2020, doi: 10.1016/J.NME.2020.100823.

[365] W. P. Hagan, N. A. Hampson, and R. K. Packer, "The effect of impurities on the performance of lithium intended for lithium/thionyl chloride battery manufacture," *J. Power Sources*, vol. 24, no. 2, pp. 95–113, Sep. 1988, doi: 10.1016/0378-7753(88)80094-6.

[366] C. Cabet, F. Dalle, E. Gaganidze, J. Henry, and H. Tanigawa, "Ferritic-martensitic steels for fission and fusion applications," *J. Nucl. Mater.*, vol. 523, pp. 510–537, Sep. 2019, doi: 10.1016/J.JNUCMAT.2019.05.058.

[367] L. Tan, Y. Katoh, and L. L. Snead, "Development of castable nanostructured alloys as a new generation RAFM steels," *J. Nucl. Mater.*, vol. 511, pp. 598–604, 2018, doi: 10.1016/j.jnucmat.2018.05.024.

[368] C. Jones, "A micromechanical investigation of proton irradiated oxide dispersion strengthened steels," University of Oxford, 2016.

[369] L. Tan, T. Chen, Y. Yang, L. He, and K. Sridharan, "Development of nanoprecipitates-strengthened advanced ferritic alloys for nuclear reactor applications," Oak Ridge, TN (United States), Feb. 2019. doi: 10.2172/1526385.

[370] M. Gorley, "Powder processing of oxide dispersion strengthened steels for nuclear applications," Oxford University, UK, 2014.

[371] C. Burrows, "The irradiation resistance of oxide dispersion strengthened steels," University of Oxford, 2015.

[372] T. P. Davis, "On nanosized precipitates in steels for advanced nuclear reactors," University of Oxford, 2020.

[373] P. Fernandez, A. M. Lancha, J. Lapena, D. Gomez-Briceno, M. Serrano, and M. Hernandez-Mayoral, "Reduced Activation Ferritic/Martensitic Steel Eurofer'97 as Possible Structural Material for Fusion Devices. Metallurgical Characterization on As-Received Condition and After Simulated Service Conditions.," *Fusion Eng. Des.*, vol. 58, p. 73, 2004.

[374] S. King, "Small-angle Neutron Scattering," in *Modern Techniques for Polymer Characterisation*, 1st ed., J. V. Dawkins and R. A. Pethrick, Eds. John Wiley, 1999.

[375] P. Taylor, M. Earlman, and S. Seetharaman, "Reduction of Rare Earth Elements Through Electrochemical and Metallothermic Methods," in *Rare Earth Metals and Minerals Industries*, Y. V. Murty, M. A. Alvin, and J. Lifton, Eds. Springer, Cham, 2023.

[376] P. Julien and J. M. Bergthorson, "Enabling the metal fuel economy: Green recycling of metal fuels," *Sustain. Energy Fuels*, vol. 1, no. 3, pp. 615–625, 2017, doi: 10.1039/c7se00004a.

[377] P. Hubberstey, "Pb-17Li and lithium: A thermodynamic rationalisation of their radically different chemistry," *J. Nucl. Mater.*, vol. 247, pp. 208–214, Aug. 1997, doi: 10.1016/S0022-3115(97)00071-8.

[378] I. McCue, B. Gaskey, P. A. Geslin, A. Karma, and J. Erlebacher, "Kinetics and morphological evolution of liquid metal dealloying," *Acta Mater.*, vol. 115, pp. 10–23, 2016, doi: 10.1016/j.actamat.2016.05.032.

[379] N. Bieberdorf, M. Asta, and L. Capolungo, "Grain boundary effects in high-temperature liquid-metal dealloying: a multi-phase field study," *npj Comput. Mater.*, vol. 9, no. 1, pp. 1–11, 2023, doi: 10.1038/s41524-023-01076-7.

[380] M. G. Barker and D. J. Wood, "The corrosion of chromium, iron, and stainless steel in liquid sodium," *J. Less Common Met.*, vol. 35, no. 2, pp. 315–323, 1974, doi: 10.1016/0022-5088(74)90243-4.

[381] X. Yi, A. Ma, L. Zhang, and Y. Zheng, "Crystallographic anisotropy of corrosion rate and surface faceting of polycrystalline 90Cu-10Ni in acidic NaCl solution," *Mater. Des.*, vol. 215, p. 110429, 2022, doi: 10.1016/j.matdes.2022.110429.

[382] H. Okamoto, "Fe-Ta (Iron-tantalum)," *J. Phase Equilibria Diffus.*, vol. 34, no. 2, pp. 165–166, Apr. 2013, doi: 10.1007/S11669-012-0164-3/TABLES/1.

[383] M. G. Barker, P. Hubberstey, A. T. Dadd, and S. A. Frankham, "The interaction of chromium with nitrogen dissolved in liquid lithium," *J. Nucl. Mater.*, vol. 114, no. 2–3, pp. 143–149, Feb. 1983, doi: 10.1016/0022-3115(83)90251-9.

[384] Y. F. Bychkov, A. N. Rozanov, and V. B. Yakovleva, "DETERMINATION OF THE SOLUBILITY OF METALS IN LITHIUM," 1959.

[385] J. Isler and J. Zhang, "Examination of solubility models for the determination of transition metals within liquid alkali metals," *Metals (Basel).*, vol. 6, no. 7, 2016, doi: 10.3390/met6070144.

[386] A. Perujo and K. S. Forcey, "Tritium permeation barriers for fusion technology," *Fusion Eng. Des.*, vol. 28, pp. 252–257, 1995.

[387] A. Tassone, L. Melchiorri, and S. Siriano, "Magnetohydraulic flow in a rectangular channel filled with stream-wise obstacles," *Fusion Eng. Des.*, vol. 197, p. 114066, Dec. 2023, doi: 10.1016/J.FUSENGDES.2023.114066.

[388] E. E. Glickman, "Dissolution condensation mechanism of stress corrosion cracking in liquid metals: Driving force and crack kinetics," *Metall. Mater. Trans. A Phys. Metall. Mater. Sci.*, vol. 42, no. 2, pp. 250–266, Feb. 2011, doi: 10.1007/S11661-010-0429-6/TABLES/2.

[389] V. F. Sears, "Neutron scattering lengths and cross sections," *Neutron News*, vol. 3, no. 3, pp. 26–37, 1992, doi: 10.1080/10448639208218770.

[390] L. M. Luo, Y. L. Liu, D. G. Liu, L. Zheng, and Y. C. Wu, "Preparation technologies

and performance studies of tritium permeation barriers for future nuclear fusion reactors," *Surf. Coatings Technol.*, vol. 403, no. 126301, 2020, doi: 10.1016/j.surfcoat.2020.126301.

[391] J. Hu *et al.*, "Hydrogen pickup during oxidation in aqueous environments: The role of nano-pores and nano-pipes in zirconium oxide films," *Acta Mater.*, vol. 180, pp. 105–115, 2019, doi: 10.1016/j.actamat.2019.09.005.

[392] S. Il Choi and J. H. Kim, "RADIATION-INDUCED DISLOCATION AND GROWTH BEHAVIOR OF ZIRCONIUM AND ZIRCONIUM ALLOYS – A REVIEW," *Nucl. Eng. Technol.*, vol. 45, no. 3, pp. 385–392, Jun. 2013, doi: 10.5516/NET.07.2013.035.

[393] R. B. Adamson, C. E. Coleman, and M. Griffiths, "Irradiation creep and growth of zirconium alloys: A critical review," *J. Nucl. Mater.*, vol. 521, pp. 167–244, Aug. 2019, doi: 10.1016/J.JNUCMAT.2019.04.021.

[394] M. Griffiths, "A review of microstructure evolution in zirconium alloys during irradiation," *J. Nucl. Mater.*, vol. 159, no. C, pp. 190–218, Oct. 1988, doi: 10.1016/0022-3115(88)90093-1.

[395] R. A. Forrest, A. Tabasso, C. Danani, S. Jakhar, and A. K. Shaw, "Handbook of Activation Data Calculated Using EASY-2007," Abingdon, 2009.

[396] B. Cox, "OXIDATION OF ZIRCONIUIM-ALUMINUM ALLOYS," Chalk River, Ontario, 1967.

[397] B. Young, J. Liu, D. Honecker, S. King, T. Davis, and D. E. J. Armstrong, "High Temperature Lithium Corrosion of Fusion-grade Structural Steels," Nov. 2024. doi: 10.2139/SSRN.5034901.

11 List of Figures

Figure 2-1: Chart showing the death rate and greenhouse gas emissions associated with various sources of energy per unit of energy produced, showing how nuclear energy compares to renewable and non-renewable energy sources [19]. Credit: Hannah Ritchie and Max Roser / CC-BY-4.0 2-15

Figure 2-2: Schematic diagram showing atomic reactions that are likely to occur within a nuclear fusion reactor. After [38], reproduced with permission from Oxford Sigma Ltd., modified.....2-17

Figure 2-3: Diagram showing how each fusion atomic reaction releases more potential energy than each fission atomic reaction. Credit: User:Bdushaw / Wikimedia Commons / CC-BY-SA-4.0 / modified 2-18

Figure 2-4: The six key challenges to nuclear fusion becoming an energy source, as identified by the UK Atomic Energy Authority [59] Credit: TED / CC-BY-NC-ND-4.0.....2-20

Figure 2-5: Cross-section diagram of a nuclear fusion tokamak, breeder blanket modules highlighted in red. Credit: ITER Organization 2-20

Figure 2-6: Model of a solid breeder blanket module for the MARS reactor showing where structural material would be needed, vanadium alloys were proposed in this case: tubes, structure, spacing structure, and baffle plates. [81], [82] © copyright 1983, reprinted by permission of Informa UK Limited, trading as Taylor & Francis Group, http://www.tandfonline.com 2-23

Figure 2-7: Effective irradiation creep strain as a function of neutron dose for V-4Cr-4Ti alloys irradiated at 450 °C [131] 2-29

Figure 2-8: Schematic figure summarising the properties of materials relevant to their application as a breeder blanket structural material. Toughness is an important factor not indicated in this figure but discussed above. The region shown for novel zirconium alloys is an educated guess due to the lack of availability of data.....2-34

Figure 2-9: Allotropic phase diagram of zirconium [157] 2-35

Figure 2-10: Periodic table showing the total becquerel activity from each element after 10 years of decay cooling following a 2-fpy irradiation in a DEMO vacuum vessel environment. The colour of each element reflects the activity according to the Bq/kg legend, but the absolute values are also given beneath each element symbol. From [169]. Credit: M. R. Gilbert et al. / CC-BY-NC-ND-4.0 2-38

Figure 2-11: Zirconium-Niobium phase diagram [182] 2-42

Figure 2-12: Zirconium-Yttrium phase diagram [196] 2-45

Figure 2-13: Zirconium-Aluminium phase diagram [198], [207] Reproduced with permission from Springer Nature.....2-46

Figure 2-14: Zirconium-Tantalum phase diagram [209] Reproduced with permission from Springer Nature 2-47

Figure 2-15: Zirconium-Vanadium phase diagram [212] Reproduced with permission from Springer Nature 2-49

Figure 2-16: Zirconium-Molybdenum phase diagram showing discrepancies between research [214]. More reliable data is shown in solid lines [213]. Credit: K.F.Ahmmed / CC-BY-4.0 2-50

Figure 2-17: Schematic representation of corrosion rate evolution as a function of liquid alloy velocity. From [219] 2-53

Figure 2-18: Diagram showing the processing stages of a zirconium alloy for fission applications obtained through analysis of patents for commercial alloys. 2-56

Figure 2-19: Diagram showing the alteration of the processing route shown in Figure 2-18 specifically for commercial zirconium-niobium alloys displaying a monotectoid-type binary phase diagram. 2-56

Figure 3-1: Engineering drawing of the shape of samples produced for ETMT with dimensions marked in millimetres 3-58

Figure 3-2: Image of an ETMT sample held between the loading grips with a thermocouple attached to the centre of the sample. The scale of this image may be ascertained from the dimensions shown in Figure 3-1 3-59

Figure 3-3: (a,b) Example data from the two nanoindenter machines used in this study for the annealed Zr2.5Ta alloy at room temperature. (c,d) show the same data as in (a,b) but with the 'Load' channel raised to the power of ⅔ for determination of the elastic loading portion. 3-63

Figure 3-4: 2D isotropic elastic-perfectly plastic finite element analysis model of the Von Mises stress (shown in MPa in the scale) distribution below a 2 μm deep indentation using the commercial software ABAQUS by Charlotte Wheatley.....3-64

Figure 3-5: An example of the representation of individual indentation flow curves, (a), with an averaged flow curve (b), using the method described above using the data from the annealed Zr2.5Al alloy with the MicroMaterials machine at room temperature. 3-68

Figure 3-6: An example of the representation of individual indentation flow curves, (a), with an averaged flow curve (b), using the method described above using the data from the annealed Zr2.5Al alloy with the MicroMaterials machine at 600 °C. 3-69

Figure 3-7: Inverse pole figure colour map indicating how the colours shown in EBSD plots of the HCP α-Zr structure in this study are related to the local crystallographic orientation of the sample surface. 3-73

Figure 4-1: Images of alloy casting with (a) showing the tilted crucible with attached mould (copper-coloured), the solidifying alloy sample material (silver-coloured with some red-hot), and the tungsten electrode above the alloy. The polymer pipe connected to the vacuum pump can be seen attached to the bottom of the mould. An image of an extracted alloy sample is shown in (b).....4-78

Figure 4-2: Optical micrograph with crossed polarising filters of the Zr2.5Al alloy following quenching after a homogenisation treatment as described above 4-82

Figure 4-3: Optical images of alloy bars following the homogenisation and quenching treatment. (a) pure zirconium, (b) Zr2.5Ta, (c) Zr2.5V, (d) Zr2.5Nb, (e) Zr2.5Al, (f) Zr2.5Mo. For scale, the length of each bar imaged is approximately 9 cm. 4-83

Figure 4-4: Zirconium-Oxygen phase diagram [292], [293] Reproduced with permission from Springer Nature 4-85

Figure 4-5: Thermometric analysis of Zr-2.5at%Ta sample to determine phase transformation temperatures. The black line indicates the measured heat flow rate data from the constant heating rate test. The orange line represents the anticipated trend of heat flow rate without any phase changes of the material and the black arrows indicate the observed onset points of phase transformations ($\alpha \rightarrow \alpha+\beta$ at approximately 810 °C and $\alpha+\beta \rightarrow \beta$ at approximately 900 °C)..... 4-86

Figure 4-6: Image of zirconium alloy sample (red) being hot rolled. 4-87

Figure 4-7: Optical images of 2.5 at% alloy bars directly following the hot rolling procedure. (a) pure zirconium, (b) Zr2.5Ta, (c) Zr2.5V, (d) Zr2.5Nb, (e) Zr2.5Al 4-89

Figure 4-8: Optical images of the Zr2.5Mo sample following hot rolling 4-89

Figure 4-9: XRD data of the Zr2.5Mo sample prior to hot rolling with a simulated pattern of the ω-Zr phase indicated along with peak positions of α-Zr, from [295]. 4-90

Figure 4-10: XRD data of the Zr2.5Mo sample after hot rolling with a simulated pattern of the ω-Zr phase indicated along with peak positions of α-Zr from [295] and of $ZrMo_2$ from [297].....4-91

Figure 4-11: Optical micrograph with crossed polarising filters of the (a) pure zirconium and (b) Zr2.5Al alloy following hot rolling as described above. The arrows labelled ND and TD represent the normal and transverse rolling directions respectively. 4-92

Figure 4-12: XRD data of the pure zirconium sample (shown in blue) and the Zr2.5Al sample (shown in red) after hot rolling, along with a literature spectrum of α-Zr from [295].....4-93

Figure 4-13: (a) Optical micrograph with crossed polarising filters, (b) SE micrograph, and (c) SE micrograph of a thin lift-out by Dr Junliang Liu of the Zr2.5V alloy following hot rolling. The arrows labelled ND, TD and RD represent the normal, transverse, and rolling directions, respectively, with respect to the rolling treatment. 4-95

Figure 4-14: Optical micrograph with crossed polarising filters of the Zr2.5Ta alloy following hot rolling. The arrows labelled ND and TD represent the normal and transverse directions respectively with respect to the rolling treatment. 4-96

Figure 4-15: (a) Optical micrograph with crossed polarising filters and (b) SE micrograph of the Zr2.5Nb alloy following hot rolling. The arrows labelled ND and TD represent the normal and transverse directions respectively with respect to the rolling treatment.....4-97

Figure 4-16: Zirconium-Aluminium phase diagram [198], [207] with alloy compositions and thermo-mechanical treatment temperatures marked by purple crosses, and the homogenisation temperature marked by a green line 4-100

Figure 4-17: Zirconium-Vanadium phase diagram [212] with alloy compositions and thermo-mechanical treatment temperatures marked by purple crosses, and the homogenisation temperature marked by a green line 4-100

Figure 4-18: Zirconium-Tantalum phase diagram [209] with alloy compositions and thermo-mechanical treatment temperatures marked by purple and green crosses, and the homogenisation temperature marked by a green line 4-102

Figure 4-19: Zirconium-Niobium phase diagram [182] with alloy compositions and thermo-mechanical treatment temperatures marked by purple and green crosses, and the homogenisation temperature marked by a green line 4-103

Figure 4-20: Optical micrograph with crossed polarising filters of the pure zirconium following annealing. The arrows labelled ND and TD represent the normal and transverse directions respectively with respect to the rolling treatment. 4-106

Figure 4-21: XRD data of the pure zirconium sample after annealing, along with a peak positions from literature of the α-Zr phase from [295] and the γ-ZrH phase from [301].....4-106

Figure 4-22: Optical micrograph with crossed polarising filters of the Zr2.5Al alloy following annealing. The arrows labelled ND and TD represent the normal and transverse directions respectively with respect to the rolling treatment. 4-107

Figure 4-23: (a,b) SE micrographs of the annealed Zr2.5Al sample and (c) EDX linescan analysis across one of the black patches seen in (b) with indications of apparent concentration variations of the indicated elements.....4-108

Figure 4-24: BSE micrographs of the annealed Zr2.5Al alloy with dark spots indicating the presence of precipitates within the microstructure. The arrows labelled ND and TD represent the normal and transverse directions respectively with respect to the rolling treatment. 4-110

Figure 4-25: XRD data of the Zr2.5Al sample after annealing, along with a peak positions from literature of the α-Zr phase from [295], the $L1_2$ structure Zr_3Al phase from [307],and the γ-ZrH phase from [301]. 4-111

Figure 4-26: (a,b) BSE micrographs of the annealed Zr2.5Al sample and (c) EDX linescan analysis across one of the dark spots seen in (b) with indications of apparent concentration variations of the indicated elements.....4-112

Figure 4-27: EBSD data of the annealed Zr2.5Al sample showing the crystallographic alignment of measured pixels with (a) the rolling direction and (b) the normal direction with reference to the colour scale shown in Figure 3-7 with calculated grain boundaries overlaid in white.....4-113

Figure 4-28: APT analysis of data taken by Kieran Rivers from a sample of annealed Zr2.5Al showing Al ions as red dots indicating a homogenous distribution of aluminium within the sample volume. 4-114

Figure 4-29: (a) surface SE micrograph and (b) SE micrograph of a thin lift-out by Dr Junliang Liu of the Zr2.5V alloy following annealing. The arrows labelled ND, TD and RD represent the normal, transverse, and rolling directions respectively with respect to the rolling treatment. 4-115

Figure 4-30: (a,c) TEM micrographs by Dr Junliang Liu showing the Zr2.5V alloy and the region in this image from which EDX linescan data was taken across an area of darker contrast. EDX linescan data is shown in (b,d) with graphs displaying the relative concentrations of the three elements indicated and how these vary along the length of the line. 4-116

Figure 4-31: XRD data of the Zr2.5V sample after annealing, along with a peak positions from literature of the α-Zr phase from [295], the Laves ZrV_2 phase from [311],and the γ-ZrH phase from [301]. 4-117

Figure 4-32: EBSD data of the annealed Zr2.5V sample showing the crystallographic alignment of measured pixels with (a) the rolling direction and (b) the normal direction with reference to the colour scale shown in Figure 3-7 with calculated gran boundaries overlaid in white. 4-118

Figure 4-33: (a) Optical micrograph with crossed polarising filters and (b)BSE micrograph of the Zr2.5Ta alloy following annealing. The arrows labelled ND and TD represent the normal and transverse directions respectively with respect to the rolling treatment. 4-119

Figure 4-34: BSE micrographs of the Zr2.5Ta alloy following annealing. The arrows labelled ND and TD represent the normal and transverse directions respectively with respect to the rolling treatment.....4-120

Figure 4-35: (a) BSE micrograph of the annealed Zr2.5Ta sample and (b) EDX linescan analysis across one of the light areas seen in (a) with indications of apparent concentration variations of zirconium and tantalum.....4-121

Figure 4-36: Analysis of APT data by Wenyu Zhang of a sample of annealed Zr2.5Ta including a precipitate with red points indicating ZrO ions, blue indicating Zr ions, and purple indicating Ta ions. Chemical analysis is shown in (b) from top to bottom of the cylindrical region indicated, showing the segregation of species associated with the precipitate. 4-122

Figure 4-37: Two views of the same XRD data of the Zr2.5Ta sample after annealing, along with a peak positions from literature of the α-Zr phase from [295], the β-Ta BCC phase from [312], the ZrO_2 zirconium oxide phase from [313], and the γ-ZrH phase from [301].....4-123

Figure 4-38: EBSD data of the annealed Zr2.5Ta sample showing the crystallographic alignment of measured pixels with (a) the normal direction and (b) the rolling direction with reference to the colour scale shown in Figure 3-7 with calculated grain boundaries overlaid in white.....4-124

Figure 4-39: SE micrograph of the annealed Zr2.5Nb alloy with lighter regions indicating the presence of a second phase within the microstructure. The arrows labelled ND and TD represent the normal and transverse directions respectively with respect to the rolling treatment.....4-125

Figure 4-40: (a) SE micrograph of the annealed Zr2.5Nb sample and (b) EDX linescan analysis across one of the light regions seen in (a) with indications of apparent concentration variations of zirconium and niobium. 4-126

Figure 4-41: XRD data of the Zr2.5Nb sample after annealing, along with a peak positions from literature of the α-Zr phase from [295], the ZrNb BCC phase from [314],and the γ-ZrH phase from [301]. 4-127

Figure 4-42: An example of the stress-strain data collected by ETMT, with a section of the data collected from Zr2.5Al at room temperature shown. The collected data points are shown as orange circles with the spline smoothing of this data shown by the orange line. Analysis of the data is described in this section with indications of the fitting of the linear region, proof stress method, and yield stress identification shown.....4-130

Figure 4-43: Graph comparing the 0.2% proof stress of novel zirconium alloys with Zircaloy-4 across temperatures as measured by ETMT 4-133

Figure 4-44: Graph comparing the yield stress of novel zirconium alloys with Zircaloy-4 across temperatures as measured by ETMT and determined via a method utilising the second derivative of the stress-strain curve.....4-133

Figure 4-45: Averaged indentation flow curve comparisons between tests performed at room temperature, 300 °C and 600 °C on (a) Zr2.5Ta, (b) Zr2.5V, and (c) Zr2.5Al.....4-135

Figure 4-46: Averaged indentation flow curve comparisons between zirconium, Zr2.5V, Zr2.5Al, and Zr2.5Ta at (a) room temperature, (b) 300 °C, and (c) 600 °C.....4-136

Figure 4-47: Graphs showing the trends of alloy strength with increasing testing temperature for two different testing methods. (a) shows the 0.2% proof stress as measured by ETMT and shown previously in Figure 4-43, and (b) shows the indentation stress measured at 5% indentation strain by nanoindentation testing shown in Figure 4-46.....4-137

Figure 4-48: Averaged indentation flow curve comparisons between zirconium, Zr1V, Zr1Al, and Zr1Ta at 600 °C.....4-138

Figure 4-49: Averaged indentation flow curve comparisons of different solute percentage compositions in (a) the ZrAl system and (b) the ZrTa system, both at 600 °C.....4-139

Figure 4-50: Averaged indentation flow curve comparisons of different solute percentage compositions in the ZrV system at (a) 300 °C and (b) 600 °C.4-140

Figure 4-51: Averaged indentation flow curve comparisons between zirconium, Zr2.5Ta and Zr2.5Nb at (a) room temperature, (b) 300 °C, and (c) 600 °C.....4-142

Figure 4-52: Averaged indentation flow curve comparisons between zirconium, Zr1Ta and Zr1Nb at (a) 300 °C and (b) 600 °C.....4-143

Figure 4-53: Averaged indentation flow curve comparisons between Eurofer, Zr5Al, Zr2.5Ta, and Zr2.5Al at (a) room temperature and (b) 600 °C.. 4-145

Figure 4-54: Small Punch testing rig used for this study with heating elements surrounding the central die containing the sample disc, all contained within an argon-filled environmental chamber. 4-146

Figure 4-55: Deflection-time curve collected to evaluate the creep resistance of a 3 mm disc of Eurofer in the small punch testing geometry under a load of 70 N at 600 °C. 4-147

Figure 5-1: Backscattered electron micrographs of Eurofer 97 in the as-received condition (a) and exposed to 1 (b), 100 (c), and 500 (d) thermal transients with peak temperatures of 700 °C. e) Pyrometer measurements of sample temperature during transient thermal exposure (a subset of 10 transients). From [355] 5-168

Figure 5-2: (a,b) BSE micrographs and (b) optical micrograph with crossed polarising filters of the Zr2.5V alloy after ageing at 700 °C for 200 hours. The arrows labelled ND and TD represent the normal and transverse directions respectively with respect to the rolling treatment. 5-170

Figure 5-3: Results of ImageJ software precipitate analysis from the micrographs in Figure 5-2(a), Figure 4-29(b), and Figure 5-6(c), indicating the median precipitate area with the error indicating the interquartile range of the measured values. 5-170

Figure 5-4: Nanoindentation flow curves of the Zr2.5V alloy before (blue) and after (green) ageing at 700 °C for 200 hours, and testing at (a) room temperature, (b) 300 °C, and (c) 600 °C. 5-173

Figure 5-5: Comparison of the approximate grain sizes of Zr-V alloys of different compositions and ageing treatments, as measured by the line intercept method described in section 4.5.1 from the micrographs in Figure 4-29(b) and Figure 5-6.....5-174

Figure 5-6: (a,b,d) Optical micrographs with crossed polarising filters and (c) BSE micrograph of the Zr1V alloy (a) before and after ageing at 700 °C for (b,c) 200 hours and (d) 1343 hours. The arrows labelled ND and TD represent the normal and transverse directions respectively with respect to the rolling treatment. The red arrows in (c) indicate precipitates in the microstructure.....5-176

Figure 5-7: Nanoindentation flow curves of the Zr1V alloy before (blue) and after (green) ageing at 700 °C for 200 hours, and testing at (a) room temperature, (b) 300 °C, and (c) 600 °C. 5-177

Figure 5-8: EBSD data of the Zr2.5Ta sample following ageing at 700 °C for 1343 hours showing the crystallographic alignment of measured pixels with (a) the normal direction and (b) the rolling direction with reference to the colour scale shown in Figure 3-7 with calculated grain boundaries overlaid in white. 5-179

Figure 5-9: Comparison of the approximate grain sizes of Zr-Ta alloys of different compositions and ageing treatments, as measured by the line intercept method described in section 4.5.1 from the micrographs in Figure 5-10(a) and Figure 5-11(a) and from EBSD data shown in Figure 4-38 and Figure 5-8. ...5-179

Figure 5-10: Optical micrograph with crossed polarising filters of the Zr2.5Ta alloy after ageing at 700 °C for (a) 200 hours and (b) 1343 hours. The arrows labelled ND and TD represent the normal and transverse directions respectively with respect to the rolling treatment. 5-180

Figure 5-11: Optical micrographs with crossed polarising filters of the Zr1Ta alloy (a) before and (b,c) after ageing at 700 °C for (b) 200 hours and (c) 1343 hours. The arrows labelled ND and TD represent the normal and transverse directions respectively with respect to the rolling treatment. 5-181

Figure 5-12: BSE micrographs of (a) the annealed Zr2.5Ta alloy following ageing (b,c) at 700 °C for (b) 200 hours and (c) 1343 hours. The arrows labelled ND and TD represent the normal and transverse directions respectively with respect to the rolling treatment. 5-183

Figure 5-13: Results of ImageJ software precipitate analysis from the micrographs in Figure 5-12, indicating the median intergranular precipitate area with the error indicating the interquartile range of the measured values. 5-184

Figure 5-14: Nanoindentation flow curves of the Zr1Ta alloy before (blue) and after (green) ageing at 700 °C for 200 hours, and tested at (a) room temperature, (b) 300 °C, and (c) 600 °C. 5-185

Figure 5-15: Nanoindentation flow curves of the Zr2.5Ta alloy before (blue) and after (green) ageing at 700 °C for 200 hours, and tested at (a) room temperature, (b) 300 °C, and (c) 600 °C. 5-186

Figure 5-16: SE micrographs of Zr2.5Ta showing the microstructure (a) after annealing and no further thermal treatments, (b) after 1 transient heating cycle, (c) after 100 transient heating cycles, and (d) after 1000 transient heating cycles with the circled region indicating the area with banded intragranular precipitates remaining. 5-188

Figure 5-17: Results of ImageJ software precipitate analysis from the micrographs in Figure 5-16, indicating the median intergranular precipitate area with the error indicating the interquartile range of the measured values. 5-189

Figure 5-18: Averaged nanoindentation flow curves of the annealed Zr2.5Ta alloy at room temperature following different thermal ageing procedures including none, isothermal ageing, and transient heating cycles. 5-190

Figure 5-19: Averaged nanoindentation flow curves of the annealed Zr2.5Ta alloy at room temperature following different thermal ageing procedures including (a) none, (b) isothermal ageing at 700 °C for 200 hours, and (c) one, (d) 100, (e) 1000 thermal transient heating cycles to 850 °C. The averaged curves, using the method described in section 3.3.4, are shown as blue lines, with shaded regions around them indicating the associated standard deviation. 5-191

Figure 5-20: Calculated values of the yield stress of the annealed Zr2.5Ta alloy at room temperature following different thermal ageing procedures including none, isothermal ageing, and transient heating cycles, using the averaged nanoindentation flow curves shown above and the analysis methods described in 4.6.1. The indicated error results are from the standard deviation at the calculated point of the graph as shown in Figure 5-19. 5-191

Figure 5-21: Optical micrographs with crossed polarising filters of the Zr2.5Al alloy (a) before and (b,c) after ageing at 700 °C for (b) 200 hours and (c) 1343 hours. The arrows labelled ND and TD represent the normal and transverse directions respectively with respect to the rolling treatment. 5-194

Figure 5-22: EBSD data of the annealed Zr2.5Al sample following ageing at 700 °C for 200 hours showing the crystallographic alignment of measured pixels with (a) the rolling direction and (b) the normal direction with reference to the colour scale shown in Figure 3-7 with calculated grain boundaries overlaid in white. 5-195

Figure 5-23: BSE micrographs of Zr2.5Al following ageing at 700 °C for 200 hours with dark spots indicating the presence of precipitates within the microstructure. The arrows labelled ND and TD represent the normal and transverse directions respectively with respect to the rolling treatment.....5-197

Figure 5-24: BSE micrographs of Zr2.5Al following ageing at 700 °C for 1343 hours with dark spots indicating the presence of precipitates within the microstructure. The arrows labelled ND and TD represent the normal and transverse directions respectively with respect to the rolling treatment.....5-198

Figure 5-25: Results of ImageJ software precipitate analysis from the micrographs in Figure 4-24, Figure 5-23, and Figure 5-24, indicating the median precipitate area with the error indicating the interquartile range of the measured values.....5-199

Figure 5-26: Optical micrographs with crossed polarising filters of the Zr5Al alloy (a) before and (b,c) after ageing at 700 °C for (b) 200 hours and (c)

1343 hours. The arrows labelled ND and TD represent the normal and transverse directions respectively with respect to the rolling treatment. 5-200

Figure 5-27: BSE micrographs of (a) the annealed Zr5Al alloy following ageing (b,c) at 700 °C for (b) 200 hours and (c) 1343 hours. With dark spots and regions indicating precipitates within the microstructure. The arrows labelled ND and TD represent the normal and transverse directions respectively with respect to the rolling treatment. 5-201

Figure 5-28: Results of ImageJ software precipitate analysis from the micrographs in Figure 4-24 and Figure 5-27(a), indicating the median precipitate area with the error indicating the interquartile range of the measured values. 5-202

Figure 5-29: Results of ImageJ software precipitate analysis from the micrographs in Figure 5-27, indicating the median precipitate area with the error indicating the interquartile range of the measured values. 5-202

Figure 5-30: Examples of APT datasets by Wenyu Zhang of (a) Zr2.5Al and (b,c) Zr5Al aged at 700 °C for (b) 200 hours and (a,c) 1343 hours, showing Al ions as red dots and Zr ions as grey, indicating a non-homogenous distribution of aluminium within the sample volume.....5-204

Figure 5-31: APT datasets by Wenyu Zhang of (a) Zr2.5Al and (b,c) Zr5Al aged at 700 °C for (b) 200 hours and (a,c) 1343 hours, showing Zr ions in grey dots and Al isoconcentration surfaces in red at compositions of (a) 3.5 at%, (b) 5.5 at%, (c) 6.5 at%.....5-204

Figure 5-32: APT datasets by Wenyu Zhang of (a) Zr2.5Al and (b,c) Zr5Al aged at 700 °C for (b) 200 hours and (a,c) 1343 hours, showing Zr ions in grey dots and 5.5 at% Al isoconcentration surfaces in red.....5-205

Figure 5-33: Examples of proxigram composition profiles using the 5.5 at% Al composition isosurfaces shown in Figure 5-32 for (a) Zr2.5Al and (b,c) Zr5Al aged at 700 °C for (b) 200 hours and (a,c) 1343 hours. The horizontal axis represents the distance away from the calculated isosurface either into (positive) or away from (negative) the precipitate.....5-206

Figure 5-34: Analysis of the approximate compositions of (a) the matrix and (b) the precipitates from proxigrams of APT datasets of Zr-Al alloys as shown in Figure 5-33 with the error in (a) indicating the standard deviation of composition data points more than 2 nm from the isosurface.....5-207

Figure 5-35: Results of AP Suite software cluster analysis from APT datasets with the parameters shown in Table 5-1, indicating (a) the number of identified clusters in the calculated tip analysis volume with an error estimate based on the accuracy of the tip volume calculation, and (b) the median number of ions counted in an identified cluster with the error indicating the interquartile range of the dataset.....5-209

Figure 5-36: TEM analysis of data taken by Rajat Nama from Zr5Al following isothermal ageing at 700 °C for 1343 hours. (a) Defocussed bright field micrograph showing the size and distribution of precipitates, indicated as dark circular regions. (b) Diffraction pattern obtained from the region shown in (a),

analysed in (c) and (d) with overlaid database diffraction patterns for α-Zr (pink), $L1_2$ structure Zr_3Al (green), and $D0_{19}$ structure Zr_3Al (blue).....5-212

Figure 5-37: Nanoindentation flow curves of the Zr2.5Al alloy before (blue) and after (green) ageing at 700 °C for 200 hours, and tested at (a) room temperature, (b) 300 °C, and (c) 600 °C. 5-214

Figure 5-38: Nanoindentation flow curves of the Zr5Al alloy before (blue) and after (green) ageing at 700 °C for 200 hours, and tested at (a) room temperature, (b) 300 °C, and (c) 600 °C. 5-215

Figure 6-1: Schematic of the method developed for exposure of samples to a high-temperature, static liquid lithium corrosive environment.....6-220

Figure 6-2: Secondary electron (SE) micrographs by Dr Junliang Liu, (a) and (b) showing the polished surface of a Eurofer sample following submersion in molten lithium at 500 °C for 24 hours and the subsequent removal of residual lithium adhered to the surface.....6-230

Figure 6-3: SE micrographs by Dr Junliang Liu showing the exposed surface of the CNA sample before (a) and after (b,c) submersion in molten lithium at 500 °C for 24 hours and the subsequent removal of residual lithium adhered to the surface.....6-232

Figure 6-4: Results of SANS analysis of both corroded and uncorroded samples of the CNA material where the corroded sample was exposed to static lithium at 500 °C for 24 hours and residual lithium was chemically removed from the surface. (a) shows scattering intensity normalised for sample thickness plotted

against the neutron scattering vector for both samples and (b) shows how the ratio between the normalised scattering intensities varies with the neutron scattering vector. The highlighted regions in (a) and (b) indicate the 0.2-0.6 $Å^{-1}$ scattering vector range. 6-234

Figure 6-5: SE micrographs of the corroded surface of 14YWT ODS steel material which was polished prior to exposure in lithium at 500 °C for 24 hours followed by the removal of residual lithium adhered to the surface.....6-235

Figure 6-6: Results of SANS analysis of both corroded and uncorroded samples of the 14YWT material where the corroded sample was exposed to static lithium at 500 °C for 24 hours and residual lithium was chemically removed from the surface. (a) shows scattering intensity normalised for sample thickness plotted against the neutron scattering vector for both samples and (b) shows how the ratio between the normalised scattering intensities varies with the neutron scattering vector. The highlighted regions in (a) and (b) indicate the 0.21-0.5 $Å^{-1}$ scattering vector range. 6-236

Figure 6-7: Dark-field TEM micrograph of CNA material from [367] showing MX-type precipitates as bright white spots and $M_{23}C_6$-type precipitates labelled 'P'.....6-237

Figure 6-8: Ellingham diagrams from (a) [375] (Reproduced with permission from Springer Nature, modified) and (b) [376] indicating the relative Gibbs free energy of relevant oxides: Li_2O, Y_2O_3, and TiO_2. Their positions may be compared between the two graphs using the lines for MgO and CaO which appear on both. 6-240

Figure 6-9: EBSD map of Eurofer showing (a) the unique grains identified (encircled by a grain boundary of misorientation angle >15°) and (b) diffraction pattern quality map, from [368]. The IPF key is not included with the EBSD data presented in the source. 6-242

Figure 6-10: SE micrographs showing the surface of the Pure Zr sample following submersion in molten lithium at 500 °C for 24 hours and the subsequent removal of residual lithium adhered to the surface. 6-246

Figure 6-11: (a) BSE micrograph of the annealed Zr1V sample before corrosion and (b) EDX linescan analysis across one of the black spots seen in (a) with indications of apparent concentration variations of zirconium and vanadium. 6-247

Figure 6-12: SE micrographs showing the surface of the Zr1V sample following submersion in molten lithium at 500 °C for 24 hours and the subsequent removal of residual lithium adhered to the surface. (b) and (c) show examples of the lighter (b) and darker (c) region identified in (a) at higher magnification. 6-249

Figure 6-13: (a) SE micrograph showing a region on the surface of the Zr1V sample following corrosion and the region in this image from which EDX linescan data was taken across a circular area of dark contrast. EDX linescan data is shown in (b) with graphs displaying the relative concentrations of the two elements indicated and how these remain relatively consistent along the length of the line. 6-250

Figure 6-14: (a) SE micrograph showing a particle on the surface of the Zr1V sample following corrosion and the region in this image from which EDX

linescan data was taken. EDX linescan data is shown in (b) with graphs displaying the relative concentrations of the four elements indicated and how these vary along the length of the line. 6-251

Figure 6-15: (a) BSE micrograph of the microstructure of an annealed Zr2.5Al sample before corrosion and (b) SE micrograph of a sample of the same material following exposure to liquid lithium at 500 °C for 24 hours. 6-253

Figure 6-16: (a) SE micrograph showing a region on the surface of the Zr2.5Al sample following corrosion and the region in this image from which EDX linescan data was taken across an area of darker contrast on a grain boundary. EDX linescan data is shown in (b) with graphs displaying the relative concentrations of the three elements indicated and how these vary along the length of the line..... 6-254

Figure 6-17: (a) SE micrograph showing a region on the surface of the Zr2.5Al sample following corrosion and the region in this image from which EDX linescan data was taken across an area of very dark contrast on a grain boundary. EDX linescan data is shown in (b) with graphs displaying the relative concentrations of the three elements indicated and how these vary along the length of the line. 6-255

Figure 6-18: : (a) SE micrograph showing a region from Figure 6-15(b) on the surface of the Zr2.5Al sample following corrosion and the region in this image from which EDX linescan data was taken across a surface particle. EDX linescan data is shown in (b) with graphs displaying the relative concentrations of the four elements indicated and how these vary along the length of the line.....6-256

Figure 6-19: SE micrographs of the microstructure of annealed Zr2.5Ta samples before (a,b) and after (c) exposure to liquid lithium at 500 °C for 24 hours showing the presence of holes within the surface of both samples.....6-257

Figure 6-20: EDX linescan data from a region of the surface of the Zr2.5Ta sample shown in Figure 6-19(c) following exposure to liquid lithium at 500 °C for 24 hours with graphs displaying the relative concentrations of the seven elements indicated and how these vary along the length of the line which crosses two surface particles. 6-258

Figure 6-21: (a) SE micrograph showing a region of the surface of the Zr2.5Ta sample following corrosion and the region in this image from which EDX linescan data was taken across a surface particle. EDX linescan data is shown in (b) with graphs displaying the relative concentrations of seven elements indicated and how these vary along the length of the line. 6-260

Figure 6-22: SE micrographs of the microstructure of annealed Zr2.5Ta samples before (a) and after (b) exposure to liquid lithium at 500 °C for 24 hours showing the size and distribution of precipitates in the microstructure and the presence of intergranular holes in the sample following corrosion (b) of similar size to the intergranular precipitates.....6-262

Figure 6-23: (a) STEM micrograph by Dr Guanze He showing the Zr2.5Ta sample before corrosion and the regions in this image from which EDX linescan data was taken across precipitates. EDX linescan data is shown in (b) and (c) for the horizontal and vertical regions shown in (a) respectively, with graphs displaying

the relative concentrations of the tantalum and iron and how these vary along the length of the line. 6-264

Figure 6-24: (a) SE micrograph showing the surface of the Zr2.5Ta sample following corrosion and the region in this image from which EDX linescan data was taken across a precipitate. EDX linescan data is shown in (b) with graphs displaying the relative concentrations of the zirconium, tantalum, and iron and how these vary along the length of the line. 6-265

Figure 8-1: Optical images of (a) Zr2.5Al and (b) Zr2.5Ta, removed from the autoclave after 30 days at 300 °C. 8-282

Figure 8-2: Comparison of the measured oxide thickness of zirconium alloy samples (X2, Zirlo, and Zr2.5Ta), following 30 days autoclave exposure at 300 °C. The thickness of the oxide layer on the commercial alloys were measured by FTIR spectroscopy and on the Zr2.5Ta from the FIB cross-section micrograph in Figure 8-3. 8-283

Figure 8-3: SE micrograph of a FIB cross-section of the surface of the Zr2.5Ta sample following 30 days of autoclave exposure at 300 °C, taken by Rajat Nama. 8-283

12 List of Tables

Table 2-1: Mechanical properties data for zirconium [165]–[167].....2-36

Table 3-1: Summary of nanoindentation tip calibration constants 3-66

Table 4-1: Results of X-Ray Fluoresence analysis showing the measured compositions of the cast alloys. 'Primary Solute' refers to the main alloying element used to create the zirconium alloy, e.g. aluminium in the case of Zr1Al. The ratio between the atomic percentages of the two most abundant elements in the alloy is also shown for direct comparison with the intended ratio described by the alloy name. 4-80

Table 4-2: Summary of two-phase temperature window analysis informing choice of soak temperature for hot rolling processing. 4-86

Table 4-3: Showing details of the hot rolling processing of the alloys including the soak temperature set on the furnace and the total true strain achieved 4-88

Table 4-4: Numerical results of analysis of ETMT data by the methods described in sections 3.2 and 4.6.1. Data presented is an average of at least two tests with the standard deviation of the results shown in brackets. Strain to failure is not given at elevated temperatures due to limitations of the testing technique.4-132

Table 5-1: Parameters used for cluster analysis in AP Suite software, determined using methods of best practice for data analysis.....5-209

Table 6-1: Quantitative results of sample mass change due to corrosion at 500 °C for 24 hours following chemical removal of lithium adhered to the surface of the corroded sample. Measured or estimated densities are used to convert mass change to volume change. Volume change per surface area may be interpreted as thickness change with the assumption of uniform surface removal of material... 6-227

13 Copyright Permission

Endnotes

[i] Reprinted from Journal of Nuclear Materials, vol. 437, no. 1-3, K. I. Fukumoto, H. Matsui, M. Narui, and M. Yamazaki, Irradiation creep behavior of V–4Cr–4Ti alloys irradiated in a liquid sodium environment at the JOYO fast reactor, pp. 341-349, Copyright 2013, with permission from Elsevier

[ii] Reprinted from Journal of Physics and Chemistry of Solids, vol. 66, no. 7, J. Zhang et al., Experimental constraints on the phase diagram of elemental zirconium, pp. 1213-1219, Copyright 2005, with permission from Elsevier.

[iii] Reprinted from Journal of Nuclear Materials, vol. 360, no. 3, R. Jerlerud Pérez and A.R. Massih, Thermodynamic evaluation of the Nb–O–Zr system, pp. 242-254, Copyright 2007, with permission from Elsevier

[iv] Reprinted from Nuclear Corrosion, vol. 69, F. Balbaud-Célérier et al., 13 - Corrosion of structural materials by liquid metals used in fusion, fission, and spallation, pp. 437-457, Copyright 2020, with permission from Elsevier

[v] Reprinted from Journal of Nuclear Materials, vol. 360, no. 3, R. Jerlerud Pérez and A.R. Massih, Thermodynamic evaluation of the Nb–O–Zr system, pp. 242-254, Copyright 2007, with permission from Elsevier

[vi] J. Hargreaves et al., Microanalysis of the Effects of Tokamak Thermal Transients on Eurofer 97 Steel, Microscopy and Microanalysis, 2022, vol. 28, no. S1, pp. 2076-2078, by permission of Microscopy Society of America

[vii] Reprinted from Journal of Nuclear Materials, vol. 511, L. Tan, Y. Katoh and L.L. Snead, Development of castable nanostructured alloys as a new generation RAFM steels, pp. 598-604, Copyright 2018, with permission from Elsevier

[viii] Used with permission of The Royal Society of Chemistry, from 'Enabling the metal fuel economy: green recycling of metal fuels', P. Julien and M. Bergthorsen, vol. 1, no. 3, 2017; permission conveyed through Copyright Clearance Center, Inc.